Theoretical description of strongly correlated ultracold atoms in external confinement

D I S S E R T A T I O N

zur Erlangung des akademischen Grades

d o c t o r r e r u m n a t u r a l i u m

(Dr. rer. nat.)

im Fach Physik

eingereicht an der

Mathematisch-Naturwissenschaftlichen Fakultät I

der Humboldt-Universität zu Berlin

von

Dipl.-Phys., Dipl.-Inf. Philipp-Immanuel Schneider

Präsident der Humboldt-Universität zu Berlin:
Prof. Dr. Jan-Hendrik Olbertz

Dekan der Mathematisch-Naturwissenschaftlichen Fakultät I:
Prof. Stefan Hecht PhD

Gutachter:
1. Prof. Dr. Alejandro Saenz
2. Prof. Dr. Wolfgang Nolting
3. Prof. Achim Peters, PhD

Tag der mündlichen Prüfung: 05.09.2013

To J. B.

Abstract

Today, ultracold atoms can be confined in various optical trapping potentials, while their mutual interaction can be controlled by magnetic Feshbach resonances. The confinement and resonant interaction can lead to a strong correlation of the atoms, which allows for the quantum simulation of physical phenomena whose classical simulation is computationally intractable. A tailored control of these correlations might eventually enable the implementation of a quantum computer with ultracold atoms. In order to take advantage of the flexibility and precise control of ultracold atoms, this thesis aims to provide a precise theoretical description of strongly correlated, confined atoms at a magnetic Feshbach resonance.

Magnetic Feshbach resonances can have a strong influence on other physical processes. As an example, it is studied how a Feshbach resonance can enhance the photoassociation of a pair of unbound atoms to a molecule. On the other hand, Feshbach resonances can themselves be influenced by the confinement of the atoms. The interplay between the confinement and the Feshbach resonance is investigated by deriving from first principles a model that enables the complete analytic description of harmonically trapped ultracold atoms at a Feshbach resonance. This model is subsequently used to develop a Bose-Hubbard model of atoms in an optical lattice at a Feshbach resonance. In contrast to more elaborate numerical calculations, the model can predict the eigenenergies and the dynamical behavior of atoms in an optical lattice with high accuracy including only a small number of Bloch bands.

A comparison of the introduced Bose-Hubbard model with full numerical calculations is performed. A previously introduced numerical approach for the determination of the corresponding stationary eigenstates is shortly presented and taken as a basis for the deployment of a method that solves the time-dependent Schrödinger equation for two interacting atoms in an optical lattice.

Finally, a proposal for the implementation of a quantum computer with ultracold atoms in an optical lattice is presented. It utilizes the correlated Mott-insulator state of repulsively interacting atoms as a quantum register. Quantum operations are driven by a periodic shaking of the optical lattice.

Zusammenfassung

Heutzutage können ultrakalte Atome in unterschiedlichsten optischen Fallenpotenzialen eingefangen werden, während sich ihre Wechselwirkung durch die Ausnutzung von magnetischen Feshbachresonanzen kontrollieren lässt. Der Einschluss und die resonante Wechselwirkung können zu einer starken Korrelation der Atome führen, welche es erlaubt, mit ihnen physikalische Phänomene zu simulieren, deren Simulation mit heutigen Computern nicht durchführbar wäre. Eine maßgeschneiderte Kontrolle der Korrelationen könnte es schließlich ermöglichen, mit ultrakalten Atomen einen Quantencomputer zu implementieren. Um die Flexibilität und gute Kontrollierbarkeit ultrakalter Atome voll ausnutzen zu können, ist das Ziel dieser Dissertation die präzise theoretische Beschreibung stark korrelierter, eingeschlossener Atome an einer Feshbachresonanz.

Eine magnetische Feshbachresonanz kann einen starken Einfluss auf andere physikalische Prozesse haben. Als ein Beispiel wird untersucht, auf welche Weise eine Feshbachresonanz die Photoassoziation ungebundener Atome zu einem Molekül verstärken kann. Ebenso können Feshbachresonanzen auch selbst durch einen Einschluss der Atome beeinflusst werden. Die präzise Beschreibung dieses Wechselspiels zwischen Einschluss und Feshbachresonanz erfolgt durch ein analytisches Modell einer Feshbachresonanz zwischen Atomen in einer harmonischen Falle, welches von Grund auf hergeleitet wird. Basierend auf diesem Modell wird ein Ansatz entwickelt, wechselwirkende Atome an einer Feshbachresonanz in einem optischen Gitter über ein Bose-Hubbard-Modell zu beschreiben. Im Gegensatz zu aufwendigeren numerischen Methoden erlaubt das Bose-Hubbard-Modell mit der Einbeziehung nur weniger Blochbänder die präzise Vorhersage der Eigenenergien und des dynamischen Verhaltens der Atome im optischen Gitter.

Das Bose-Hubbard-Modell wird mit vollen numerischen Berechnungen verglichen. Eine zuvor entwickelte numerische Methode zur Bestimmung der entsprechenden stationären Eigenzustände wird kurz vorgestellt. Auf deren Basis wird eine Methode zur Lösung der zeitabhängingen Schrödingergleiung für zwei wechselwirkende Atome in einem optischen Gitter entwickelt.

Schließlich wird ein Ansatz vorgestellt, wie sich mit ultrakalten Atomen in einem optischen Gitter ein Quantencomputer implementieren ließe. Als Quantenregister dient der korrelierte Mott-Zustand von repulsiv wechselwirkenden Atomen. Quantenoperationen werden durch periodisches Wackeln des optischen Gitters getrieben.

Contents

Introduction

Since the first creation of Bose-Einstein condensates [1–3] the scientific field of ultracold quantum gases is rapidly evolving. Ultracold atoms have turned out to be a versatile tool for many applications like precision measurement, quantum simulation, and quantum information processing [4]. While in the beginning of the field the fascinating observation of macroscopic coherent matter waves was of main interest [5], the focus moved later to the creation and investigation of strongly correlated systems of ultracold atoms. A prominent example of this development is the observation of the phase transition between a superfluid and a strongly correlated Mott insulator [6]. In the last years it became even possible to detect ultracold atoms at a single-atom level, which enabled even the direct investigation of the phase transition on a single-atom level [7].

Two key techniques that were necessary for these achievements allow for the superb control over ultracold atoms: (i) Atoms can be confined in various geometries such as dipole traps, optical lattices, or atomic wave guides [8]. (ii) The atom-atom interaction that gives rise to correlations can be tuned from zero to arbitrarily large values using a magnetic Feshbach resonance (MFR) [9].

An MFR occurs if the scattering state of two atoms comes into resonance with a molecular bound state. Close to the resonance the s-wave scattering length, which completely determines the strength of the atom-atom interaction, changes and can take values between 0 and $\pm\infty$. The energy of the bound state and thus the scattering length can be manipulated by an external magnetic field. The first part of this thesis is concerned with the precise theoretical description of MFRs, their influence on various physical processes, and their interplay with the trapping potential.

One important application of MFRs is the creation of ultracold molecules out of ultracold atoms. Due to their richer internal structure and interaction, molecules are of great interest for applications in quantum information processing [10, 11], the exploration of lattices of dipolar molecules [12], precision measurement of fundamental constants [13], or ultracold chemical reactions [14, 15]. In the thesis the interplay between the MFR and the PA process is described by a two-channel (TC) approximation of the Feshbach resonance. It is shown that the dependence of the PA process on the magnetic field in the vicinity of an MFR can be fully classified by only two parameters. As a result, the magnetic field value of vanishing PA determines the enhancement of the PA due to the MFR.

The known theory of MFRs successfully describes the *free* scattering process in the limit $E \to 0$ of a zero scattering energy. While in this case the molecular bound state couples resonantly to a continuum of scattering states, the continuum is replaced by a discrete spectrum or gapped energy bands if the atoms are confined. Moreover, the extension of the trap introduces a new length scale and energy scale. For example, the molecular bound state can be in resonance to only some of the energetically sepa-

rated eigenstates of the trap. This necessitates to accurately incorporate the energy-dependence of the interaction process. As it is often the case, many important aspects of the influence of the trapping potential can be understood by first investigating its harmonic approximation, which often allows to derive analytic results. As it turns out, this is also the case for the understanding of MFRs. On the basis of the TC approximation an analytical model of MFRs in isotropic and anisotropic harmonic traps is derived from first principles. The model is compared with complete numerical solutions and is applied to shed new light on some previous experimental results.

The building block of the theoretical description of ultracold atoms in an optical lattice (OL) are Hubbard models, especially the Bose-Hubbard model (BHM) for Bosonic atoms. The model uses in its basic form a basis of single-particle Wannier functions from the first Bloch band to formulate the many-body Hamiltonian. While for weak interactions the model is very accurate, it usually breaks down for larger scattering lengths or in the presence of an MFR. The usual BHM allows via the onsite-interaction strength U either for repulsively interacting atoms ($U > 0$) or attractively interacting atoms ($U < 0$). At an MFR, however, an avoided crossing with the resonant bound state leads to the appearance of both repulsively and attractively interacting states. Moreover, the molecular bound state usually couples to scattering states in several Bloch bands in such a way that one has to include more than one Bloch band in the theoretical description. Equipped with the introduced model of MFRs in harmonic traps a multi-band BHM is introduced, which explicitly includes the resonant bound state. It is shown that the naïve approach to formulate the multi-band BHM runs into severe problems if, as usual, a zero-range coupling is considered. Indeed the variational principle does not hold and the eigenenergies can be largely underestimated. Here, the problem is approached by defining a dressed coupling strength and dressed bound-state energies, which are based on the analytic solution in the harmonic trap. By comparison with independent numerical calculations it is shown that the introduced BHM can accurately describe the energy spectrum of two atoms in an optical lattice at an MFR with only a small number of basis functions.

In the second part of the thesis aspects of the dynamical behavior of atoms in OLs are discussed. First, a numerical method is presented that solves the full time-dependent six-dimensional Schrödinger equation of two interacting atoms in a single-well or multiple-well OL. The algorithm exploits the symmetry group of the OL, which reduces the computational effort. The lattice can be perturbed by any additional time-dependent potential up to quadratic order. While the types of perturbations can be easily extended, the currently implemented ones already allow for studying many experimentally relevant situations. For example, an acceleration of an OL or a periodic driving as realized in [16, 17] results in a linear perturbation of the lattice. The manipulation of the barrier hight between two lattice sites [18] or a variation of the global confinement, e.g. by a MOT [19], can be simulated by adding a harmonic perturbation. The method is applied to the exemplary case of the scattering of ^{6}Li-^{7}Li in an OL consisting of three lattice sites perturbed by linear and quadratic perturbations. Furthermore, the method is applied to validate also the dynamical behavior of atoms at an MFR described by the BHM introduced in this thesis.

One of the most fascinating applications of ultracold atoms in OLs is the possibility

use them as a quantum simulator [20]. To this end one takes advantage of the extraordinary flexibility and precise control of ultracold atoms to emulate a large class of Hamiltonians. For example, by putting the atoms in specially designed lattice potential Simon et al. [21] were able to study magnetic phase transitions with single-atom (i.e. single-spin) resolution.

The precise theoretical description of interacting atoms in OLs discussed so far is an important requirement for exploring different possibilities of faithfully simulating other physical systems. However, the ultimate goal is the implementation of a quantum computer with ultracold atoms that is able to perform almost arbitrary unitary operations. A quantum computer can solve specific problems like integer factorization exponentially faster than classical computers. More importantly for physicists, it can be regarded as a universal quantum simulator [22].

In the end of the second part of the thesis a proposal for quantum computation with ultracold atoms in optical lattices is presented. The qubits, the counterparts of the classical bit, are represented by atoms in the correlated Mott phase of the OL. Each atom can occupy the ground or first excited state on each lattice site. Quantum operations are steered by shaking the OL thereby inducing Rabi oscillations between the qubit states. The proposal builds upon the aforementioned technological advancements that allow for a single-site resolution of the OL and as a consequence also for a manipulation of the atoms with single-site resolution [23].

Numerical simulations of a small subset of qubits by a time-propagation of a BHM indicate that the necessary qubit operations can be performed with fidelity $> 99\%$. In order to achieve these fidelities, spin refocussing techniques known from nuclear magnetic resonance are adapted to atoms in OLs. Finally, it is shown how and on which time scale one could perform Shor's algorithm in an OL for the concrete case of a factorization of 15.

The thesis is organized such that a non-expert reader should be able to follow the discussions. To this end Chapter 1 gives a short introduction to s-wave scattering, MFRs and their approximate description by the TC model. Chapter 2 explains the known analytic theory of free-atom scattering at an MFR using the TC model. Thereafter, the theory is applied to describe the process of PA at an MFR. An analytic model of MFRs in harmonic traps is derived in Chapter 3. In Chapter 4 the analytic model is used to derive a BHM for atoms in OLs at an MFR.

The second part of the thesis begins with the presentation of a numerical approach to solve the time-dependent Schrödinger equation of two interacting atoms in an OL in Chapter 5. Chapter 6 start with a basic introduction to quantum computation, especially to the notion of qubits. The proposal for performing quantum computation with ultracold atoms in OLs is explained and numerically verified. The thesis ends with a conclusion in Chapter 7.

List of publications

The theoretical approaches described in this thesis are based on the following publications:

Publication I — P.-I. Schneider and A. Saenz,
Two-channel model of photoassociation in the vicinity of a Feshbach resonance,
Phys. Rev. A **80**, 061401(R), 2009.

Publication II — P.-I. Schneider, Y. V. Vanne, and A. Saenz,
Feshbach resonances of harmonically trapped atoms,
Phys. Rev. A **83**, 030701(R), 2011.

Publication III — P.-I. Schneider and A. Saenz,
Quantum computation with ultracold atoms in a driven optical lattice,
Phys. Rev. A **85**, 050304(R), 2012.

Publication IV — P.-I. Schneider and A. Saenz,
Nonperturbative theoretical description of two atoms in an optical lattice with time-dependent perturbation,
Phys. Rev. A **87**, 053413, 2013.

Publication V — P.-I. Schneider and A. Saenz,
Two-channel Bose-Hubbard model of atoms at a Feshbach resonance,
Phys. Rev. A **87**, 052712, 2013.

Publications of the author on other subjects:

Publication VI — P.-I. Schneider, S. Grishkevich, and A. Saenz,
Ab initio determination of Bose-Hubbard parameters for two ultracold atoms in an optical lattice using a three-well potential,
Phys. Rev. A **80**, 013404 (2009).

Publication VII — S. Grishkevich, P.-I. Schneider, Y. V. Vanne, and A. Saenz,
Mimicking multichannel scattering with single-channel approaches,
Phys. Rev. A **81**, 022719 (2010).

Publication VIII — S. Sala, P.-I. Schneider, and A. Saenz,
Inelastic confinement-induced resonances in low-dimensional quantum systems,
Phys. Rev. Lett. **109**, 073201 (2012).

Part I.

Theoretical description of Feshbach resonances

1. Theoretical introduction

One of the most important advantages for the theoretical description of ultracold atoms is that their interaction is often determined by a single measure, the s-wave scattering length. In the following section a short introduction to s-wave scattering is given.

The description of the scattering process by a single length is remarkable since the interaction at short internuclear distances itself can be rather complex. Especially, in the presence of a magnetic Feshbach resonance (MFR) many spin configurations of the incoming atoms can be resonantly coupled. Sec. 1.2 introduces the concept of MFRs and their approximation by the two-channel (TC) model. A more detailed introduction to MFRs may be found in Refs. [32, 33].

1.1. Theoretical description of s-wave scattering

The scattering of two neutral atoms with coordinates $\vec{r}_1$ and $\vec{r}_2$ and masses m_1 and m_2 interacting via an isotropic potential $V_{\text{int}}(|\vec{r}_1 - \vec{r}_2\,|)$ is considered. If the atoms are confined in an isotropic harmonic trap with frequencies ω_1 and ω_2, respectively, the system is determined by the Hamiltonian

$$H = \sum_{i=1,2} \left(-\frac{\hbar^2}{2m_i}\nabla^2 + \frac{1}{2}m_i\omega_i^2 r_i^2 \right) + V_{\text{int}}(|\vec{r}_1 - \vec{r}_2\,|)\,. \tag{1.1}$$

In order to analytically treat interacting systems, it is convenient to introduce relative-distance (REL) coordinates $\vec{r} = \vec{r}_1 - \vec{r}_2$ and center-of-mass (COM) coordinates $\vec{R} = (m_1\vec{r}_1 + m_2\vec{r}_2)/(m_1 + m_2)$. By defining furthermore the total mass $M = m_1 + m_2$, the reduced mass $\mu = m_1 m_2/M$, and the COM and REL trapping frequencies

$$\Omega^2 = \frac{1}{M}\left(m_1\omega_1^2 + m_2\omega_2^2\right) \tag{1.2}$$

$$\text{and} \quad \omega^2 = \frac{1}{M}\left(m_2\omega_1^2 + m_1\omega_2^2\right)\,, \tag{1.3}$$

the Hamiltonian transforms to

$$H = -\frac{\hbar^2}{2M}\nabla_R^2 + \frac{1}{2}M\Omega^2 R^2 - \frac{\hbar^2}{2\mu}\nabla_r^2 + \frac{1}{2}\mu\omega^2 r^2 + \mu\left(\omega_1^2 - \omega_2^2\right)\vec{R}\cdot\vec{r} + V_{\text{int}}(r)\,. \tag{1.4}$$

Here, ∇_R^2 and ∇_r^2 are the Laplace operators with respect to $\vec{R}$ and $\vec{r}$, respectively. The REL and COM motion is only coupled by the term $\mu\left(\omega_1^2 - \omega_2^2\right)\vec{R}\cdot\vec{r}$. In the special cases of free scattering ($\omega_1 = \omega_2 = 0$) and the scattering of identical atoms ($\omega_1 = \omega_2$) the REL and the COM motion are decoupled. Assuming a decoupling of REL and

COM motion and supposing that the COM motion in a harmonic oscillator or in free space is well known, only the REL motion is considered in the following.

Since both the trap and the interaction are isotropic, the radial momentum $\hat{\mathrm{L}}$ is preserved. Hence, any stationary solution $\psi(\vec{r})$ can be written in as a product $\psi(\vec{r}) = f_l(r)Y_l^m(\theta,\phi)$ of a spherical harmonic function $Y_l^m(\theta,\phi)$ and a radial function $f_l(r)$. The kinetic energy of REL motion of the wave function $\psi(\vec{r})$ then evaluates to

$$-\frac{\hbar^2}{2\mu}\nabla^2\psi(\vec{r}) = \left[-\frac{\hbar^2}{2\mu}\left(\frac{d^2}{dr^2}+\frac{2}{r}\frac{d}{dr}\right)+\frac{l(l+1)\hbar^2}{2\mu r^2}\right]\psi(\vec{r})\,. \tag{1.5}$$

For sufficiently low scattering energies (specified below) all solutions with $l > 0$ are reflected by the centrifugal barrier $\frac{l(l+1)\hbar^2}{2\mu r^2}$ and are not influenced by the interaction. Only the s-wave solution with $l = 0$ is scattered by the interaction potential. In the following $\Psi(r)$ shall denote $l = 0$ wave functions $Y_0^0(\theta,\phi)f_0(r) = f_0(r)/\sqrt{4\pi}$. The kinetic-energy operator can be further simplified by introducing the radial wave function $\Phi(r) = \sqrt{4\pi}r\Psi(r)$. The prefactor $\sqrt{4\pi}$ is chosen such that the wave function and the radial wave function have the same normalization, i.e.

$$\int r^2\sin\theta dr\,d\theta\,d\phi\,|\Psi(r)|^2 = \int dr\,|\Phi(r)|^2\,. \tag{1.6}$$

The Schrödinger equation of the radial wave function simplifies to

$$\left(-\frac{\hbar^2}{2\mu}\frac{d^2}{dr^2}+\frac{1}{2}\mu\omega^2r^2+V_{\mathrm{int}}(r)-E\right)\Phi(r) = 0\,. \tag{1.7}$$

For larger internuclear distances the interaction potential of neutral atoms behaves like $V_{\mathrm{int}}(r) = -C_6/r^6$, where $C_6 > 0$ is the coefficient determining the van-der-Waals interaction. In the presence of such a short-range interaction the wave function for free scattering with energies $E > 0$ behaves asymptotically like

$$\tilde{\Phi}(r) \equiv \lim_{r\to\infty}\Phi(r) \propto \sin[kr+\delta(k)]\,. \tag{1.8}$$

Here and in the following a tilde above the wave function signifies its asymptotic behavior outside of the interaction range. The phase δ of the asymptotic wave function depends sensitively on the specific form of the interaction potential and on the scattering energy $E = \hbar^2k^2/(2\mu)$. Another measure that describes the effect of the interaction for large internuclear distances is the scattering length

$$a(k) \equiv -\frac{\tan\delta}{k}\,. \tag{1.9}$$

It can take any value from $-\infty$ to $+\infty$. More generally, one may define the scattering length by the logarithmic derivative of the asymptotic wave function, i.e.

$$-\frac{1}{a} = \lim_{r\to0}\left[\frac{d}{dr}\log(\tilde{\Phi})\right] = \frac{\tilde{\Phi}'(0)}{\tilde{\Phi}(0)}\,. \tag{1.10}$$

For confined atoms the asymptotic behavior of the wave function differs from that of Eq. (1.8). Nevertheless, the scattering length can be also defined for confined atoms by using Eq. (1.10). However, in order to do so, there needs to be an internuclear distance r_0, where both the interaction and the trap can be neglected since otherwise the interaction cannot be subsumed by a trap-independent scattering length. A semi-classical treatment of free scattering with $E > 0$ shows that the interaction can be neglected for $r \gg \beta_6 = \left(\frac{2\mu C_6}{\hbar^2}\right)^{1/4}$ [34]. The value of β_6, which can be regarded as the range of the interaction, varies for alkali-metal atom scattering between 65 a.u. for ^{7}Li-^{7}Li and 93 a.u. for ^{7}Li-^{133}Cs [35]. On the other hand, the length scale of the harmonic trap is given by the trap length $a_{\mathrm{ho}} = \sqrt{\frac{\hbar}{\mu\omega}}$. For $r \ll a_{\mathrm{ho}}$ the influence of the harmonic trap is negligible, which becomes especially apparent regarding the Schrödinger equation for the asymptotic wave function

$$\tilde{\Phi}''(\rho) = \left(\rho^2 - 2\epsilon\right)\tilde{\Phi}(\rho)\,. \tag{1.11}$$

in dimensionless units $\rho = r/a_{\mathrm{ho}}$ and $\epsilon = E/(\hbar\omega)$. Typical trap lengths are on the order of some 1 000 a.u. so that there indeed exists usually an interatomic distance r_0 of several 100 a.u. where to a good approximation both the trap and the interaction can be neglected.

Finally, one can also quantify the regime of pure s-wave scattering. It requires that the scattering energy E is much smaller than the centrifugal $\hbar^2 l(l+1)/(2\mu r_0)$ barrier at $r = r_0$, so that partial waves with $l > 0$ sufficiently decay before entering the interaction range at $r \approx \beta_6$. This condition is equivalent to demanding $kr_0 \ll 1$. In this case, one can approximate the wave function for internuclear distances $r \approx r_0$ by a linear expansion. Using $\sin(kr + \delta) = k\cos\delta\,(r + \tan\delta/k) + \mathcal{O}([kr]^2)$, this yields

$$\tilde{\Phi}(r) \propto r - a\,. \tag{1.12}$$

Eq. (1.12) provides an intuitive physical picture of the scattering length. If a is positive and $ka \ll 1$, the asymptotic wave function has a node at $r = a$ and is thus equivalent to a wave function that was scattered by a hard sphere of radius a. The scattering length is therefore a measure of the strength of the interaction. For negative scattering lengths the picture is less transparent. However, in the limit $k \to 0$ the total scattering cross section $\sigma = 4\pi a^2$ depends only on the absolute value of a [32]. In the trap the equivalence to hard-sphere scattering is limited to small scattering lengths $a \ll a_{\mathrm{ho}}$.

One has to note that in literature the scattering length is often only defined in the limit of zero scattering energy. That is, only the measure

$$a_0 = -\lim_{k\to 0}\frac{\tan\delta(k)}{k} \tag{1.13}$$

is denoted as the scattering length. However, in a later section it will be shown that an accurate description of the scattering process often requires to take the energy dependence of the scattering length into account.

Since the interaction range is usually short compared with the trap length the concrete interaction potential is often irrelevant as long as it reproduces the same scattering length a. If furthermore the energy dependence of the scattering length is irrelevant, one may replace the interaction potential by a zero-range pseudo potential V_{ps}. In order to define V_{ps} for a given scattering length a, one demands that the Schrödinger equation of the s-wave REL motion for free scattering at a pseudo potential V_{ps},

$$\left(\nabla^2 + k^2\right) \Psi(r) = \frac{2\mu}{\hbar^2} V_{\mathrm{ps}}(\vec{r}) \Psi(r)\,, \tag{1.14}$$

has the solution $\tilde{\Psi}(r) = C \sin(kr + \delta)/r = \tilde{C} \left[\sin(kr) + \tan(\delta)\cos(kr)\right]/r$, which is identical to the asymptotic behavior of a wave function with scattering length $a = -\tan(\delta)/k$ [see Eqs. (1.8) and (1.9)]. Using the identity $\nabla^2(1/r) = -4\pi\delta(\vec{r})$, where $\delta(\vec{r})$ is the Dirac-delta function[1] the wave function fulfils

$$\left(\nabla^2 + k^2\right) \Psi(\vec{r}) = -4\pi\delta(\vec{r})\tilde{C}\tan(\delta)\,. \tag{1.15}$$

$\tilde{C}$ can be eliminated using

$$\frac{1}{k}\frac{\partial}{\partial r}\left[r\Psi(r)\right]\Big|_{r=0} = \tilde{C}\,, \tag{1.16}$$

which yields finally

$$\left(\nabla^2 + k^2\right) \Psi(r) = 4\pi \frac{\tan\delta}{k}\, \delta(\vec{r}) \frac{\partial}{\partial r}\left[r\Psi(r)\right]\,. \tag{1.17}$$

Assuming that the energy dependence of the scattering length is negligible one may replace $a = -\tan(\delta)/k$ by a_0 defined in Eq. (1.13). Comparing Eqs. (1.14) and (1.17) one finds

$$V_{\mathrm{ps}}(\vec{r}) = \frac{4\pi\hbar^2 a_0}{2\mu}\, \delta(\vec{r}) \frac{\partial}{\partial r} r\,, \tag{1.18}$$

which is known as the Fermi-Huang pseudo potential for s-wave scattering [36].

1.2. Two-channel model of a Feshbach resonance

The s-wave radial wave function of two colliding ground-state alkali-metal atoms in a harmonic trap of frequency ω is determined by the REL-motion Hamiltonian [37]

$$\hat{\mathrm{H}} = -\frac{\hbar^2}{2\mu}\frac{d^2}{dr^2} + \frac{1}{2}\mu\omega^2 r^2 + \sum_{j=1}^{2}(\hat{\mathrm{V}}_j^{\mathrm{hf}} + \hat{\mathrm{V}}_j^{\mathrm{Z}}) + \hat{\mathrm{V}}_{\mathrm{int}}(r)\,. \tag{1.19}$$

[1] The Dirac-delta function $\delta(\vec{r})$ and the phase shift $\delta(k)$ can be well distinguished by their dependence on $\vec{r}$ and k, respectively. If this is not the case, it is explicitly stated, which of the two is meant.

The hyperfine operator $\hat{\mathrm{V}}_j^{\mathrm{hf}} = a_{\mathrm{hf}}^j/\hbar^2\ \vec{s}_j \cdot \vec{i}_j$ and the Zeeman operator $\hat{\mathrm{V}}_j^{\mathrm{Z}} = (\gamma_e \vec{s}_j - \gamma_n \vec{i}_j) \cdot \vec{B}$ in the presence of a magnetic field $\vec{B}$ depend on the electronic spin $\vec{s}_j$, the nuclear spin $\vec{i}_j$, the hyperfine constant a_{hf}^j of atom $j = 1, 2$, and on the nuclear and electronic gyromagnetic factors γ_n and γ_e. Within Born-Oppenheimer approximation the interaction $\hat{\mathrm{V}}_{\mathrm{int}}(r)$ depends on the electronic spin configuration of the colliding atoms, which is determined by the quantum number S of the total electronic spin $\vec{S} = \vec{s}_1 + \vec{s}_2$. Let $V_{\mathrm{S}}(r)$ be the spin-singlet (i.e. $S = 0$) Born-Oppenheimer interaction potential and $V_{\mathrm{T}}(r)$ the spin-triplet (i.e. $S = 1$) interaction potential, then the interaction can be expressed as $\hat{\mathrm{V}}_{\mathrm{int}}(r) = V_{\mathrm{S}}(r)\hat{\mathrm{P}}_{\mathrm{S}} + V_{\mathrm{T}}(r)\hat{\mathrm{P}}_{\mathrm{T}}$ where $\hat{\mathrm{P}}_{\mathrm{S}}$ and $\hat{\mathrm{P}}_{\mathrm{T}}$ project on the singlet and triplet components of the scattering wave function, respectively. The exchange interaction $V_{\mathrm{S}}(r) - V_{\mathrm{T}}(r)$ between the electrons vanishes rapidly for large internuclear distances such that $V_{\mathrm{S}}(r)$ and $V_{\mathrm{T}}(r)$ become identical. Defining $\hat{\mathrm{V}}_{\pm} = (\hat{\mathrm{V}}_{\mathrm{S}} \pm \hat{\mathrm{V}}_{\mathrm{T}})/2$, the interaction evaluates to

$$\hat{\mathrm{V}}_{\mathrm{int}}(r) = V_+(r) + V_-(r)(\hat{\mathrm{P}}_{\mathrm{S}} - \hat{\mathrm{P}}_{\mathrm{T}}) \overset{r\to\infty}{=} V_+(r)\,. \tag{1.20}$$

Since for large interatomic distances the interaction does not depend of the spin-configuration of the atoms, MFRs are conveniently described in the atomic basis $\{|\alpha\rangle\}$ consisting of eigenstates of the hyperfine and Zeeman operator $\hat{\mathrm{V}}_{\mathrm{ZHf}} = \hat{\mathrm{V}}_1^{\mathrm{hf}} + \hat{\mathrm{V}}_1^{\mathrm{Z}} + \hat{\mathrm{V}}_2^{\mathrm{hf}} + \hat{\mathrm{V}}_2^{\mathrm{Z}}$. The eigenenergies $E_{\mathrm{ZHf}}^{(\alpha)}$ of the eigenequation $\hat{\mathrm{V}}_{\mathrm{ZHf}}|\alpha\rangle = E_{\mathrm{ZHf}}^{(\alpha)}|\alpha\rangle$ can be directly obtained from the Breit-Rabi formula [38]. For weak magnetic fields, where the hyperfine coupling dominates over the coupling to the magnetic field, the eigenstates of the atomic basis $|\alpha\rangle$ are equal to spin states $|f_1, m_{f_1}\rangle|f_2, m_{f_2}\rangle$, where $\vec{f}_j = \vec{s}_j + \vec{i}_j$ is the total spin of atom j and m_f its projection onto the B-field axis. Since each eigenstate for stronger magnetic fields is adiabatically connected to a weak-field basis state, the weak-field basis is used to label the atomic basis states $|\alpha\rangle$. Independently of the magnetic field the total spin projection $M_f = m_{f_1} + m_{f_2}$ is preserved during the collision.

The eigenfunctions of Hamiltonian (1.19) can be written as a superposition

$$|\Phi\rangle = \sum_\alpha \Phi_\alpha(r)|\alpha\rangle \tag{1.21}$$

of channel functions $\Phi_\alpha(r)$ belonging to a specific atomic basis state $|\alpha\rangle$. In the basis of these channel functions the Schrödinger equation evaluates to the multi-channel (MC) differential equation

$$\left(-\frac{\hbar^2}{2\mu}\frac{d^2}{dr^2} + \frac{1}{2}\mu\omega^2 r^2 + V_{\alpha,\alpha}(r) - E\right)\Phi_\alpha(r) + \sum_{\alpha'\neq\alpha} V_{\alpha,\alpha'}(r)\Phi_\alpha(r) = 0 \tag{1.22}$$

with the matrix elements

$$V_{\alpha,\alpha'}(r) = V_-(r)\left\langle\alpha\middle|\,\hat{\mathrm{P}}_{\mathrm{S}} - \hat{\mathrm{P}}_{\mathrm{T}}\,\middle|\alpha'\right\rangle + \left(V_+(r) + E_{\mathrm{ZHf}}^{(\alpha)}\right)\delta_{\alpha,\alpha'}\,. \tag{1.23}$$

In the atomic basis different channels are coupled by the exchange interaction $V_{\mathrm{ex}}(r) = 2V_-(r)$ between the two valence electrons of the alkali atoms.

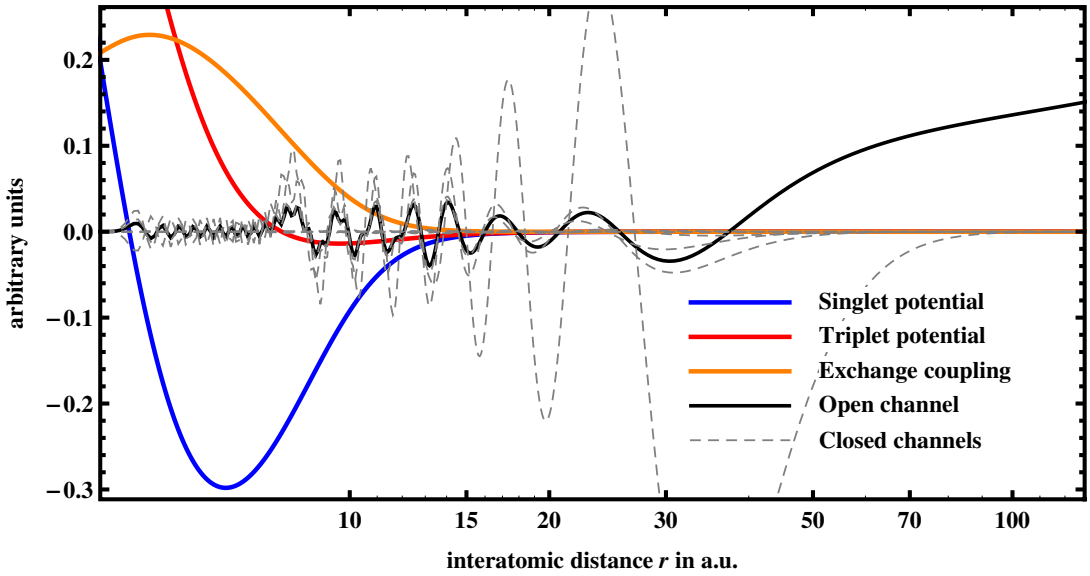

Figure 1.1: Exemplary solution of the MC equation (1.22) for the scattering of ^{6}Li (atom 1) and ^{87}Rb (atom 2) and a total spin projection $M_F = 3/2$ close to an MFR at $B = 1067\,\mathrm{G}$. For the chosen scattering energy only one channel $|\alpha_0\rangle = |1/2, 1/2\rangle|1, 1\rangle$ is open while the seven other channels are closed. For about $r < 8\,\mathrm{a.u.}$ the triplet potential of the electronic state $a^3\Sigma^+$ has a positive energy so that the triplet admixture to the channel wavefunctions vanishes and the system is well described by a pure singlet interaction of the electronic state $X^1\Sigma^+$. For $r > 8\,\mathrm{a.u.}$ the channel wavefunctions show a more complex behavior since they are superpositions of singlet and triplet wave functions. Already for $r > 16\,\mathrm{a.u.}$ the coupling between the channels by the exchange interaction is negligible.

In this thesis solely elastic collisions are considered, where only the channel with the lowest threshold energy $E_{\mathrm{ZHf}}^{(\alpha_0)}$ with spin configuration $|\alpha_0\rangle$ is open and all other coupled channels are closed. That is, all channel functions $\Phi_\alpha(r)$ apart from a single channel function decay exponentially for large r. If more than one channel is open, inelastic spin-changing collision are possible. During these inelastic collisions the atoms gain usually a sufficiently large kinetic energy, such that they are immediately lost from the experimental setup.

In Fig. 1.1 a solution of the MC equation (1.22) for the exemplary case of the scattering of ^{6}Li-^{87}Rb with one open channel is shown. The numerical MC solutions were provided by Yulian V. Vanne. More details on the calculations are given in Publication VII. ^{6}Li (atom 1) and ^{87}Rb (atom 2) have nuclear spins $i_1 = 1$ and $i_2 = 3/2$, respectively. The channel with the lowest hyperfine and Zeeman energy is $|f_1, m_{f_1}\rangle|f_2, m_{f_2}\rangle = |1/2, 1/2\rangle|1, 1\rangle$, which has a total spin projection $M_F = 3/2$. Considering low-energy scattering events, where this is the only open channel, seven other closed channels with $M_F = 3/2$ are coupled to the open channel.

Within the TC approximation of the scattering process one projects the full MC Hilbert space onto two subspaces, the one of the open entrance channel (with projection operator $\hat{\mathrm{P}} = |\alpha_0\rangle\langle\alpha_0|$) and the one of the closed channels (with projection operator $\hat{\mathrm{Q}} = 1 - \hat{\mathrm{P}}$) [39]. The resulting TC Schrödinger equation reads

$$(\hat{\mathrm{H}}_P - E)|\Phi_P\rangle + \hat{\mathrm{W}}|\Phi_Q\rangle = 0 \tag{1.24}$$

$$(\hat{\mathrm{H}}_Q - E)|\Phi_Q\rangle + \hat{\mathrm{W}}^\dagger|\Phi_P\rangle = 0\,, \tag{1.25}$$

where $\hat{\mathrm{H}}_P = \hat{\mathrm{P}}\hat{\mathrm{H}}\hat{\mathrm{P}}$, $\hat{\mathrm{H}}_Q = \hat{\mathrm{Q}}\hat{\mathrm{H}}\hat{\mathrm{Q}}$, $\hat{\mathrm{W}} = \hat{\mathrm{P}}\hat{\mathrm{H}}\hat{\mathrm{Q}}$, $|\Phi_P\rangle = \hat{\mathrm{P}}|\Phi\rangle$ and $|\Phi_Q\rangle = \hat{\mathrm{Q}}|\Phi\rangle$.

An MFR occurs if the energy E of the system is close to the eigenenergy E_b of a bound state $|\Phi_b\rangle$ of the closed-channel subspace. By a variation of the magnetic field B, $E_b = E_b(B)$ can be brought to resonance with the energy E. In the remainder of the thesis the bound state that is responsible for the occurrence of a specific MFR is denoted as the resonant bound state (RBS).

Eq. (1.25) may be formally solved using the Greens operator $\hat{\mathrm{G}}_Q = (E^+ - \hat{\mathrm{H}}_Q)^{-1}$, where $E^+ = E + i0$ is infinitesimally shifted to the positive complex plane. $\hat{\mathrm{G}}_Q$ can be expanded in discrete eigenstates $|\phi_m\rangle$ and continuum states $|\phi(E)\rangle$ of $\hat{\mathrm{H}}_Q$,

$$\hat{\mathrm{G}}_Q = \sum_m \frac{|\phi_m\rangle\langle\phi_m|}{E - E_m} + \int d\epsilon \frac{|\phi(\epsilon)\rangle\langle\phi(\epsilon)|}{E^+ - \epsilon}\,. \tag{1.26}$$

Close to the resonance with the n-th bound state the sum is dominated by the contribution $\frac{|\phi_n\rangle\langle\phi_n|}{E-E_n}$. Within the one-pole approximation one neglects the contribution of all other eigenstates, such that the closed-channel wave function

$$|\Phi_Q\rangle = \hat{\mathrm{G}}_Q\hat{\mathrm{W}}^\dagger|\Phi_P\rangle \approx \frac{\left\langle\phi_n\right|\hat{\mathrm{W}}\left|\Phi_Q\right\rangle}{E - E_n}|\phi_n\rangle = A|\phi_n\rangle \tag{1.27}$$

is equal to a multiple A of a the RBS $|\Phi_b\rangle \equiv |\phi_n\rangle$. Applying the one-pole approximation of Eqs. (1.24) and (1.25) yields the coupled equations

$$(\hat{\mathrm{H}}_P - E)|\Phi_P\rangle + A\hat{\mathrm{W}}|\Phi_b\rangle = 0 \tag{1.28}$$

$$(E_b - E)A|\Phi_b\rangle + \hat{\mathrm{W}}^\dagger|\Phi_P\rangle = 0\,, \tag{1.29}$$

which are the starting point of the following considerations of free and trapped atoms at an MFR.

2. Free atoms at a magnetic Feshbach resonance

In Sec. 2.1 the TC model is applied in order to determine the scattering states in the vicinity of an MFR by solving the coupled equations (1.28) and (1.29). The discussion follows in large parts the derivation of Friedrich [32] and Moerdijk and Verhaar [37], and is extended by a more accurate estimation of the energy-dependence of the scattering length.

In Sec. 2.2 the TC solutions are applied in order to determine the enhancement of the PA rate at an MFR. This approach was also taken by Pellegrini et al. [40]. However, here some inconsistencies in the derivation in Ref. [40] are corrected, leading to a different and simplified expression for the PA rate. It is shown that the magnetic field position of vanishing PA rate determines the enhancement of the PA rate at an MFR. The results are validated by a comparison with MC calculations.

The discussion of Sec. 2.2 was published in Ref. [24] (Publication I). In parts the results were also discussed in the diploma thesis [41] of the author.

2.1. Two-channel solution in free space

A convenient way to solve equation (1.28) in the case of free scattering ($\omega = 0$) is to employ the Greens operator $\hat{\mathrm{G}}_P = (E^+ - \hat{\mathrm{H}}_P)^{-1}$ with $E^+ = E + i0$. In position space the Greens operator $\hat{\mathrm{G}}_P$ is given as [32]

$$\langle r|\hat{\mathrm{G}}_P|r'\rangle = -\pi \begin{cases} \Phi_{\mathrm{reg}}(r)\Phi_{\mathrm{irr}}(r') & \text{for } r \leq r' \\ \Phi_{\mathrm{reg}}(r')\Phi_{\mathrm{irr}}(r) & \text{for } r > r' \,, \end{cases} \tag{2.1}$$

where $|\Phi_{\mathrm{reg}}\rangle$ and $|\Phi_{\mathrm{irr}}\rangle$ are two linearly independent solutions of $\hat{\mathrm{H}}_P|\Phi\rangle = E|\Phi\rangle$. While the regular solution $|\Phi_{\mathrm{reg}}\rangle$ vanishes at $r = 0$, the irregular solution $|\Phi_{\mathrm{irr}}\rangle$ does not. Hence, the corresponding irregular wave function $\Psi_{\mathrm{irr}}(r) = \Phi_{\mathrm{irr}}(r)/(\sqrt{4\pi}r)$ diverges for $r \to 0$. The asymptotic behaviour of the two solutions is given as

$$\tilde{\Phi}_{\mathrm{reg}}(r) = \sqrt{\frac{2\mu}{\pi\hbar^2 k}}\sin(kr + \delta_{\mathrm{bg}})|\alpha_0\rangle \tag{2.2}$$

$$\tilde{\Phi}_{\mathrm{irr}}(r) = \sqrt{\frac{2\mu}{\pi\hbar^2 k}}\cos(kr + \delta_{\mathrm{bg}})|\alpha_0\rangle \,. \tag{2.3}$$

The phase shift of these solutions determines the background scattering length $a_{\mathrm{bg}} = -\tan(\delta_{\mathrm{bg}})/k$. The prefactor $\sqrt{2\mu/(\pi\hbar^2 k)}$ ensures that the solutions are energy-normalized, i.e. it holds $\langle\Phi(E)|\,\Phi(E')\rangle = \delta(E - E')$, where $|\Phi(E)\rangle$ shall denote a wave function with

a scattering energy $E = \hbar^2 k^2/(2\mu)$ and $\delta(E - E')$ the Dirac-delta function.

In free space the general open-channel solution consist of a superposition of the regular solution of the homogeneous problem and a solution of the inhomogeneous problem. The general solution employing the Greens operator $\hat{\mathrm{G}}_P$ thus reads

$$|\Phi_P\rangle = C|\Phi_{\mathrm{reg}}\rangle + A\hat{\mathrm{G}}_P\hat{\mathrm{W}}|\Phi_b\rangle \tag{2.4}$$

$$|\Phi_Q\rangle = A|\Phi_b\rangle\,, \tag{2.5}$$

where C is a normalization constant.

Inserting Eqs. (2.4) and (2.5) in Eq. (1.29) and multiplying by $\langle\Phi_b|$ yields the closed channel admixture

$$A = C \cdot \frac{\langle\Phi_b|\hat{\mathrm{W}}|\Phi_{\mathrm{reg}}\rangle}{E - E_b - \langle\Phi_b|\hat{\mathrm{W}}^\dagger\hat{\mathrm{G}}_P\hat{\mathrm{W}}|\Phi_b\rangle}\,. \tag{2.6}$$

If r_{ex} is the internuclear distance where the exchange energy and with this the coupling operator $\hat{\mathrm{W}}$ becomes negligible, then with Eq. (2.1) the open-channel function for $r > r_{\mathrm{ex}}$ reads

$$\Phi_P(r) = C\Phi_{\mathrm{reg}}(r) - \pi A\langle\Phi_{\mathrm{reg}}|\hat{\mathrm{W}}|\Phi_b\rangle\Phi_{\mathrm{irr}}(r) = C\left[\Phi_{\mathrm{reg}}(r) + \tan(\delta_{\mathrm{res}})\Phi_{\mathrm{irr}}(r)\right]\,. \tag{2.7}$$

With Eq. (2.6) the resonant phase shift evaluates to

$$\tan\delta_{\mathrm{res}} = -\frac{\Gamma/2}{E - E_b - \delta E}\,. \tag{2.8}$$

The position of this Breit-Wigner resonance is shifted from the bound state energy E_b by the detuning $\delta E = \langle\Phi_b|\hat{\mathrm{W}}^\dagger\hat{\mathrm{G}}_P\hat{\mathrm{W}}|\Phi_b\rangle$. The width of the resonance is $\Gamma = 2\pi|\langle\Phi_b|\hat{\mathrm{W}}|\Phi_{\mathrm{reg}}\rangle|^2$.

The asymptotic behaviour of Eqs. (2.2) and (2.3) determines the asymptotic behavior

$$\tilde{\Phi}_P(r) = \tilde{C}\sqrt{\frac{2\mu}{\pi\hbar^2 k}}\sin(kr + \delta_{\mathrm{bg}} + \delta_{\mathrm{res}})|\alpha_0\rangle \tag{2.9}$$

of the open-channel wave function, where $\tilde{C} = C/\cos\delta_{\mathrm{res}}$ is a normalization constant. An energy-normalization of the open channel corresponds to setting $\tilde{C} = 1$.

Introducing the definition of the resonant phase shift into Eq. (2.10), the closed channel admixture

$$A = -\tilde{C}\sqrt{\frac{2}{\pi\Gamma}}\sin\delta_{\mathrm{res}}\,, \tag{2.10}$$

can be directly related to the phase shift $\delta = \delta_{\mathrm{bg}} + \delta_{\mathrm{res}}$ and thus to the scattering length $a = -\tan(\delta)/k$ of the open channel.

With Eq. (2.8) the scattering length evaluates to

$$a \equiv -\frac{\tan(\delta_{\mathrm{bg}} + \delta_{\mathrm{res}})}{k} = a_{\mathrm{bg}}\left(1 - \frac{\left(1 + a_{\mathrm{bg}}^2 k^2\right)\Delta E}{E_b + \delta E - E + a_{\mathrm{bg}}^2 k^2 \Delta E}\right)\,, \tag{2.11}$$

where $\Delta E = \Gamma/(2ka_{\mathrm{bg}})$. Since the energy-dependent scattering length depends explic-

itly on $E \propto k^2$, care has to be taken to estimate the energy dependence of ΔE and δE up to terms on the order $\mathcal{O}(k^2)$. In literature this is usually neglected and δE and ΔE are assumed to be constant [42–45]. This leads necessarily to the conclusion that the width of the resonance $\left(1 + a_{\mathrm{bg}}^2 k^2\right) \Delta E$ increases linearly with the energy E for large background scattering lengths a_{bg}.

Since in the region of the overlap with the bound state $\Phi_b(r)$ the energy of the Born-Oppenheimer interaction is much larger than the scattering energy, the nodal structure of the $\Phi_{\mathrm{reg}}(r)$ and $\Phi_{\mathrm{irr}}(r)$ does hardly depend on the energy. However, the overall amplitude of $\Phi_{\mathrm{reg}}(r)$ and $\Phi_{\mathrm{irr}}(r)$ changes with k since for $r \to \infty$ one has

$$\begin{aligned}\tilde{\Phi}_{\mathrm{reg}}(r) &= \sqrt{\frac{2\mu}{\pi\hbar^2 k}} \sin\left[kr - \arctan(k a_{\mathrm{bg}})\right] |\alpha_0\rangle \\ &\propto (r - a_{\mathrm{bg}}) k^{1/2} + \left(2a_{\mathrm{bg}}^3 + (a_{\mathrm{bg}} - r)^3\right) \frac{k^{5/2}}{6} + \mathcal{O}(k^{7/2}) \qquad (2.12) \\ \tilde{\Phi}_{\mathrm{irr}}(r) &= \sqrt{\frac{2\mu}{\pi\hbar^2 k}} \cos\left[kr - \arctan(k a_{\mathrm{bg}})\right] |\alpha_0\rangle \\ &\propto k^{-1/2} - (a_{\mathrm{bg}} - r)^2 \frac{k^{3/2}}{2} + \mathcal{O}(k^{7/2}) \,. \qquad (2.13)\end{aligned}$$

Matrix elements like $\left\langle \Phi_b \middle| \hat{W} \middle| \Phi_{\mathrm{reg}} \right\rangle$ are approximately equal to $\gamma_1 \tilde{\Phi}_{\mathrm{reg}}(r_0)$, where γ_1 is a proportionality constant and r_0 is some internuclear distance close to, but not in the interaction range (see Sec. 1.1). That is, for ultracold s-wave scattering it still holds $r_0 k \ll 1$. The detuning energy $\delta E = \langle \Phi_b | \hat{\mathrm{W}}^\dagger \hat{\mathrm{G}}_P \hat{\mathrm{W}} | \Phi_b \rangle$ is accordingly approximately equal to $\gamma_2 \tilde{\Phi}_{\mathrm{reg}}(r_0) \tilde{\Phi}_{\mathrm{irr}}(r_0)$ with the proportionality constant γ_2. Using Eqs. (2.12) and (2.13) the energy dependence of the total resonance width and the total resonance detuning can be estimated as

$$\Delta E_{\mathrm{tot}} \equiv \left(1 + a_{\mathrm{bg}}^2 k^2\right) \Delta E \approx \gamma_1 a_{\mathrm{bg}} \left(1 - \frac{r_0}{a_{\mathrm{bg}}}\right)^2 + \mathcal{O}(k^4) \qquad (2.14)$$

$$\begin{aligned}\delta E_{\mathrm{tot}} \equiv &\delta E - a_{\mathrm{bg}}^2 k^2 \Delta E \approx \gamma_2 r_0 - a_{\mathrm{bg}} \left(\gamma_1 r_0^2 k^2 + \gamma_2\right) + \\ &a_{\mathrm{bg}}^2 k^2 \left(a_{\mathrm{bg}} - 2r_0\right) (\gamma_2 - \gamma_1) + \mathcal{O}(k^4) \,. \qquad (2.15)\end{aligned}$$

As one can see, the energy dependence of the matrix elements crucially influences the energy dependence of the scattering length:

(i) The total width of the resonance ΔE_{tot} is not proportional to $a_{\mathrm{bg}}^2 k^2$ for large background scattering lengths, but the term $a_{\mathrm{bg}}^2 k^2$ drops out completely.

(ii) The energy dependence of the total resonance detuning δE_{tot} depends on all three parameters γ_1, γ_2, and r_0. However, if $\gamma_1 \approx \gamma_2$, the total detuning simplifies to $\delta E_{\mathrm{tot}} \approx \gamma_1 (r_0 - a_{\mathrm{bg}})$. Since γ_2 depends on the nodal structure of both the irregular and the regular solution, while γ_1 depends only on the regular solution, one has to expect that in general the detuning is strongly energy dependent for large background scattering lengths.

In Sec. 3 the energy-dependent scattering length is derived by a different approach. There it will be shown that the scattering length does indeed not depend on terms proportional to $a_{\mathrm{bg}}^2 k^2$. Furthermore, the scattering length will be determined not by three parameters (here γ_1, γ_2, and r_0) but only by two.

The scattering length a can be related to the magnetic field by assuming a linear dependence $E_b(B) = \sigma(B - B_0)$ of the bound-state energy on the magnetic field B. The relative magnetic moment σ the closed-channel and the open-channel subspaces is known for many MFRs [46]. The scattering length

$$a = a_{\mathrm{bg}} \left(1 - \frac{\left(1 + a_{\mathrm{bg}}^2 k^2\right) \Delta B}{B - B_0 + \delta B - E/\sigma + a_{\mathrm{bg}}^2 k^2 \Delta B} \right) , \tag{2.16}$$

is then determined by the magnetic resonance width $\Delta B = \Delta E/\sigma$ and the magnetic resonance detuning $\delta B = \delta E/\sigma$. In the following Section 2.2 the limit $k \to 0$ of zero scattering energy is considered. In this case one obtains the well known relation [47]

$$a = a_{\mathrm{bg}} \left(1 - \frac{\Delta B}{B - B_R} \right) \tag{2.17}$$

with the resonant magnetic-field position $B_R = B_0 - \delta B$. The relation between the resonant phase shift and the magnetic field for $k \to 0$ is then correspondingly given as

$$\tan \delta_{\mathrm{res}} = \frac{k a_{\mathrm{bg}} \Delta B}{B_R - B} \tag{2.18}$$

and can be obtained from the experimentally accessible quantities B_R, a_{bg}, and ΔB.

2.2. Photoassociation of untrapped atoms

As an application of the TC solution derived in the last section the process of associating deeply bound molecules from the scattering atoms by photoassociation (PA) is considered.

Cooling schemes, such as laser cooling that work well for atoms, are usually not suitable to cool molecules. On the other hand, the rates of molecule production by a photoassociation of a sample of dilute atoms is usually very small. It has been shown, both theoretically and experimentally, that the PA transfer rate can be significantly increased in the vicinity of an MFR [40, 48–51]. This leads to the prospect of creating a large number of ultracold molecules out of a sample of ultracold atoms.

Deeply bound molecules are localized at internuclear distances where the coupling between the channels in the atomic basis by the exchange coupling is large (see Fig. 1.1). Therefore, the bound states are better described in the molecular basis specified as $|\chi\rangle = |S, M_S\rangle|m_{i_1}, m_{i_2}\rangle$, where S is the quantum numbers of the total electronic spin $\vec{S} = \vec{s}_1 + \vec{s}_2$ of the two valence electrons of the alkali-metal atoms, M_S is its projection along the magnetic field, and m_{i_1}, m_{i_2} are the nuclear spin projections of the individual atoms. In the molecular basis the channels are coupled by the weak hyperfine interaction $\hat{\mathrm{V}}_1^{\mathrm{hf}} + \hat{\mathrm{V}}_2^{\mathrm{hf}}$ [see Eq. (1.19)] so that the bound states are to a good approximation pure singlet ($S = 0$) or triplet ($S = 1$) wave functions.

Equipped with the solution of the MC equation (1.22) a convenient way to calculate PA transition rates to molecular bound states is therefore to transform the scattering wave function of Eq. (1.21) to the molecular basis. Within the dipole approximation with electronic dipole transition moment $D(r)$ the transition rate $\Gamma_{\mathrm{PA}}(B)$ to the final molecular state $|\Psi_{\mathrm{f}}\rangle = \frac{1}{r}\Phi_\nu(r)Y_J^M(\Theta, \Phi)|\chi_{\mathrm{f}}\rangle$ with vibrational quantum number ν and rotational quantum number J is proportional to the squared dipole transition moment [52]

$$I_{\mathrm{MC}}(B) = \left| \int_0^\infty \Phi_\nu(r) D(r) \phi_{\chi_{\mathrm{f}}}(r) dr \right|^2 . \tag{2.19}$$

Selection rules allow only transitions from the s-wave scattering function to a final state with $J = 1$. In the following a transition to the vibrational ground state ($\nu = 1$) is considered. Due to the orthogonality of the molecular basis, only one molecular channel $|\chi_{\mathrm{f}}\rangle$ with the same spin state as the final state with radial wave function $\phi_{\chi_{\mathrm{f}}}(r)$ takes part in the PA. A sketch of the scattering states that are photo associated to molecular bound states is shown in Fig. 2.1.

The solutions (2.4) and (2.5) of the TC approximation formulated in the atomic basis yield together with the behavior of the closed channel admixture in Eq. (2.10) a squared dipole transition moment

$$I_{\mathrm{TC}}(B) = |\langle\Phi_{\mathrm{f}}|\hat{\mathrm{D}}|\Psi\rangle|^2 = |\tilde{C}|^2 \left|C_1 \cos\delta_{\mathrm{res}} - C_2 \sin\delta_{\mathrm{res}}\right|^2 \tag{2.20}$$

to the final state $|\Phi_{\mathrm{f}}\rangle = \Phi_\nu(r)|\chi_{\mathrm{f}}\rangle$, where

$$C_1 = \langle\Phi_{\mathrm{f}}|\hat{\mathrm{D}}|\Phi_{\mathrm{reg}}\rangle \qquad \text{and} \qquad C_2 = \sqrt{\frac{2}{\pi\Gamma}} \left(\langle\Phi_{\mathrm{f}}|\hat{\mathrm{D}}\hat{\mathrm{G}}_P\hat{\mathrm{W}}|\Phi_b\rangle + \langle\Phi_{\mathrm{f}}|\hat{\mathrm{D}}|\Phi_b\rangle\right) \tag{2.21}$$

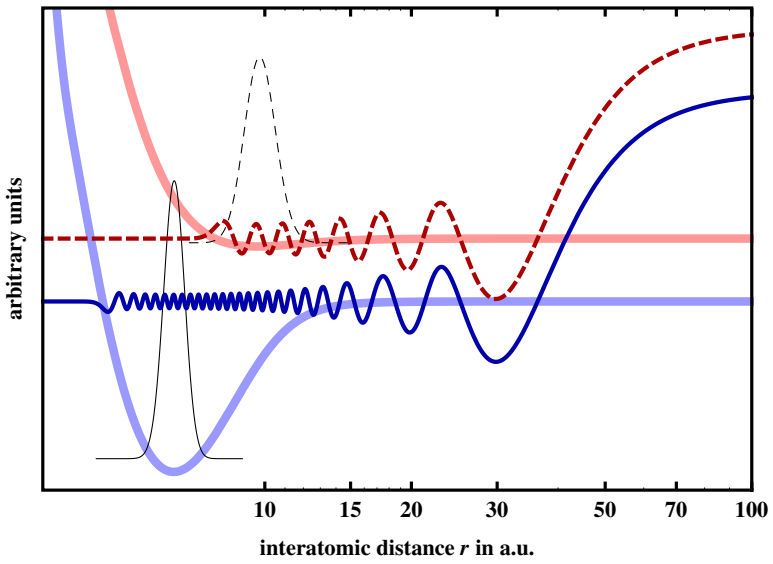

Figure 2.1: Schematic sketch of a singlet wave function (dark blue) and a triplet wave function (dashed red) that can be coupled during the PA to the singlet ground state (thin, solid) and the triplet ground state (thin, dashed), respectively. For better visibility, the singlet potential (light blue), the triplet potential (red dashed) and the corresponding wave functions are shifted along the y-axis.

do not vary with the magnetic field B. Depending on the chosen normalization the prefactor $\tilde{C}$ may vary with a. However, in the following energy-normalized scattering solutions with $\tilde{C} \equiv 1$ are considered [see Eq. (2.9)]. Introducing $\beta = (C_1^2 + C_2^2)$ and $\tan\delta_0 = C_1/C_2$ one can further simplify Eq. (2.20) to

$$I_{\mathrm{TC}}(B) = \beta \sin^2(\delta_{\mathrm{res}} - \delta_0) \ . \tag{2.22}$$

In analogy to the discussion in Sec. 2.1 one can study the behavior of $\tan\delta_0$ for $k \to 0$. According to Eqs. (2.12) and (2.13) one has $\Gamma \propto k$ and $\langle \Phi_{\mathrm{f}} | \hat{\mathrm{D}} | \Phi_{\mathrm{reg}} \rangle \propto \sqrt{k}$. In the limit $k \to 0$ the matrix element $\langle \Phi_{\mathrm{f}} | \hat{\mathrm{D}} \hat{\mathrm{G}}_P \hat{\mathrm{W}} | \Phi_b \rangle$ is constant and $\langle \Phi_{\mathrm{f}} | \hat{\mathrm{D}} | \Phi_b \rangle$ does not depend on k. Altogether, one has $\tan\delta_0 \propto k$ so that one can associate a finite length

$$a_e \equiv -\lim_{k\to 0} \frac{\tan\delta_0}{k} \tag{2.23}$$

with the phase shift δ_0.

At this point the derived result shall be compared to the previously derived dipole transition moment in [40]. In the notation of the current work Eq. (8) in [40] gives

$$I_{\mathrm{TC}}(B) = K|1 + C_1 \tan\delta_{\mathrm{res}} + C_2 \sin\delta_{\mathrm{res}}|^2 \tag{2.24}$$

with

$$K = |\langle\Phi_\mathrm{f}|\hat{\mathrm{D}}|\Phi_\mathrm{reg}\rangle|^2, \qquad C_1 = \frac{\langle\Phi_\mathrm{f}|\hat{\mathrm{D}}|\Phi_\mathrm{irr}\rangle}{\langle\Phi_\mathrm{f}|\hat{\mathrm{D}}|\Phi_\mathrm{reg}\rangle}, \quad \text{and} \quad C_2 = -\sqrt{\frac{2}{\pi\Gamma}}\frac{\langle\Phi_\mathrm{f}|\hat{\mathrm{D}}|\Phi_b\rangle}{\langle\Phi_\mathrm{f}|\hat{\mathrm{D}}|\Phi_\mathrm{reg}\rangle}\,. \quad (2.25)$$

The most obvious difference to Eq. (2.20) is the dependence on three parameters K, C_1 and C_2 and not just two. This is a result of an inconsistent normalization of open and closed channels in [40]. The open channel was not energy normalized and leads thus to a term proportional to $\tan\delta_\mathrm{res}$. Furthermore, in contrast to the coefficients in Eq. (2.21) the value of C_2 in Eq. (2.25) depends explicitly on the irregular solution $|\Phi_\mathrm{irr}\rangle$. This is due to the description of the open channel in [40] as a pure sum of regular and irregular solution. This may, however, only be done for interatomic distances $r > r_\mathrm{ex}$, were the coupling to the closed channels induced by the exchange energy is negligible. A transition to states within the same electronic configuration as considered in [40] depends, however, on the scattering wave function at distances where the exchange energy is considerable. Nevertheless, a fit of Eq. (2.24) to a full MC calculation seemed to be possible, which is probably due to the freedom of three fitting parameters.

The universal dependence of the PA transition moment on just two parameters in Eq. (2.22) suggests that not all physical observables like the enhancement of the PA rate, the magnetic-field position of vanishing PA rate, and the resonance position of the scattering length can be independent. According to Eq. (2.22) the transition rate vanishes where $\delta_\mathrm{res} = \delta_0$. For $k \to 0$ this corresponds to vanishing transition rate at a scattering length $a_\mathrm{min} = a_\mathrm{bg} + a_e$ or correspondingly at a magnetic field

$$B_\mathrm{min} = B_R + \Delta B\frac{a_\mathrm{bg}}{a_e}\,. \quad (2.26)$$

The point of vanishing transition rate can be related to the enhancement ratio of the maximum transition rate Γ_max and the background rate Γ_bg in the presence of an off-resonant magnetic field (i.e. where $\delta_\mathrm{res} = 0$ and $a = a_\mathrm{bg}$). In the limit $k \to 0$ on finds

$$\frac{\Gamma_\mathrm{max}}{\Gamma_\mathrm{bg}} = \frac{1}{\sin^2\delta_0} = \frac{1}{k^2 a_e^2} = \left(\frac{B_\mathrm{min} - B_R}{k\, a_\mathrm{bg}\Delta B}\right)^2\,. \quad (2.27)$$

In order to verify the TC description of the PA process, the exemplary case of an elastic collision of ^{6}Li-^{87}Rb (^{6}Li is atom 1, ^{87}Rb is atom 2) in the initial atomic basis state $|\alpha_0\rangle = |f_1 = 1/2, m_{f_1} = 1/2\rangle|f_2 = 1, m_{f_2} = 1\rangle$ is considered (see Fig. 1.1 for an exemplary solution of the corresponding MC problem). For an energy just 50 Hz above the threshold of the entrance channel, which admits the comparison with the $k \to 0$ limit, the MC solution was calculated for different magnetic fields B in Ref. [30] (Publication VII). For $B < 1500\,\mathrm{G}$ two s-wave resonances occur, a broad one at $B = 1066,917\,\mathrm{G}$ which was also observed experimentally [53], and a narrow one at $B = 1282.576\,\mathrm{G}$. The dependence of the scattering length a on the magnetic field strength is shown in Fig. 2.2.

Assuming that the two resonances are sufficiently separated in order to describe the

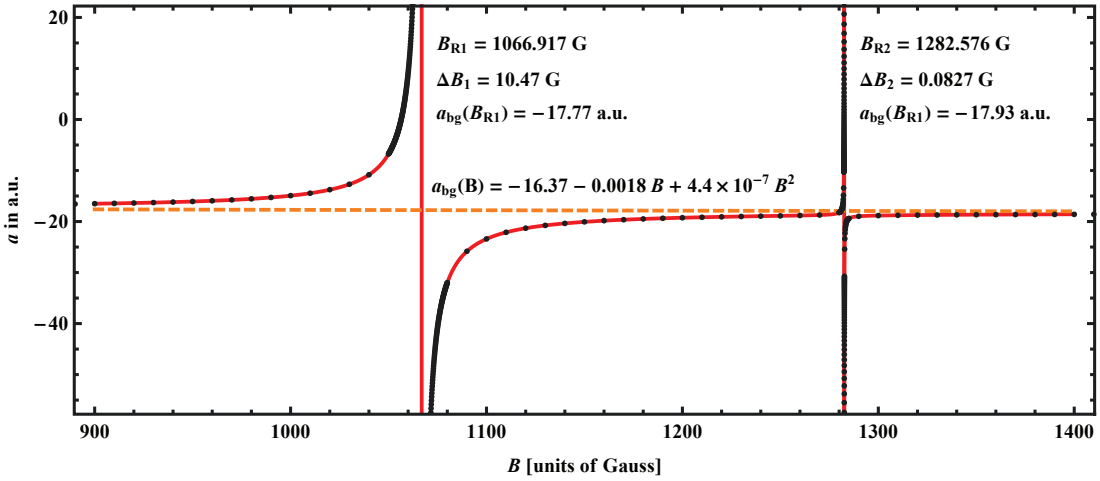

Figure 2.2: Scattering length a as a function of the external magnetic field value B for ^{6}Li-^{87}Rb scattering at $E = 50\,\mathrm{Hz}$ (dots). A fit according to Eq. (2.28) is depicted by the solid red line. The value of $a_{\mathrm{bg}}(B)$ is shown by the dashed orange line. All fitting parameters are shown in the plot.

process by two independent resonances one may generalize Eq. (2.17) to

$$a(B) = a_{\mathrm{bg}}\left(1 + \frac{\Delta B_1}{B - B_{R1}} + \frac{\Delta B_2}{B - B_{R2}}\right). \tag{2.28}$$

Additionally, effects beyond the one-pole approximation are accounted for by permitting a_{bg} to vary slowly with B as $a_{\mathrm{bg}}(B) = a_0 + a_1 \cdot B + a_2 \cdot B^2$. As shown in Fig. 2.2, with this quadratic expansion a fit according to Eq. (2.28) excellently reflects the MC behavior.

The exemplary case of a dipole transitions of the scattering state to the absolute vibrational ground state of the electronic singlet configuration $X^1\Sigma^+$ and the triplet configuration $a^3\Sigma^+$ is considered. Since these transitions take place at internuclear distances, where the coupling between all atomic channels is strong, it is probable that any deficiency of the TC approximation becomes obvious. The MC rate was calculated in Ref. [30] (Publication VII) for an electronic dipole moment in the linear approximation $D(r) = D_0 + D_1 \cdot R$, where D_0 could be neglected. In the following $D_0 = 0$ and $D_1 = E_h/a_0$ is used. The magnetic field dependence of the according dipole transition moment to ground states in different spin configurations is shown in Fig. 2.3.

The MC behavior is fitted by assuming again that the two resonances are sufficiently separated, such that one can add the transition amplitudes $A^{(j)}_{\mathrm{TC}}(B) = C_1 \cos(\delta^{(j)}_{\mathrm{res}}) - C_2^{(j)} \sin(\delta^{(j)}_{\mathrm{res}})$ of both resonances $j = 1, 2$ independently and take the absolute square of the sum

$$I^{(1,2)}_{\mathrm{TC}}(B) = |A^{(1)}_{\mathrm{TC}}(B) + A^{(2)}_{\mathrm{TC}}(B)|^2 \tag{2.29}$$

in order to determine the dipole transition moment. The resonant phase shifts $\tan \delta^{(j)}_{\mathrm{res}} =$

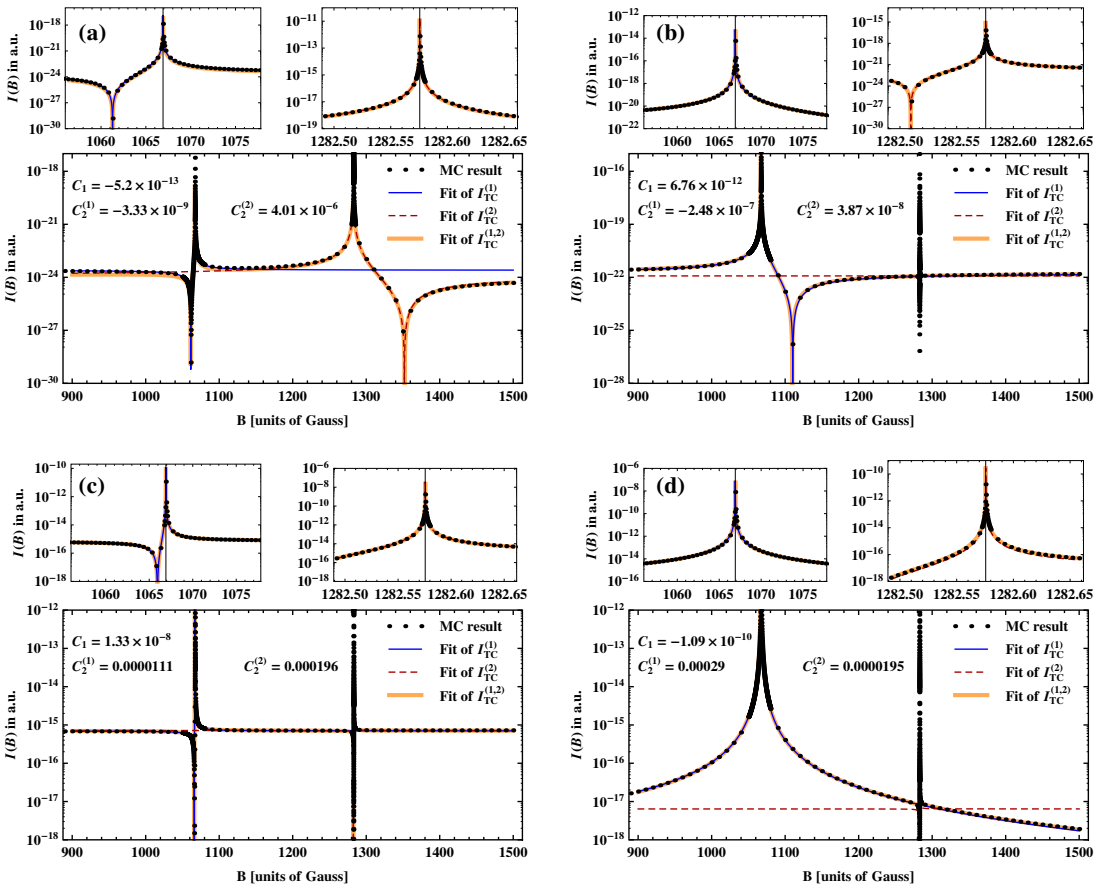

Figure 2.3: Squared dipole transition moment as a function of the external magnetic field for ^{6}Li-^{87}Rb scattering at $E = 50\,\mathrm{Hz}$ (dots). Transitions to the molecular singlet ground states $|S, M_S\rangle|m_{i_1}, m_{i_2}\rangle = |0,0\rangle|0,3/2\rangle$ **(a)** and $|0,0\rangle|1,1/2\rangle$ **(b)** and the triplet ground states $|1,-1\rangle|1,3/2\rangle$ **(c)** and $|1,1\rangle|1,-1/2\rangle$ **(d)** are considered. In each graph a fit according to Eqs. (2.29) and (2.30) is performed and the resulting fitting parameters for Eq. (2.29) are shown. The smaller graphs on top focus on the regions $B_{R1} - 2\Delta B_1 \leq B \leq B_{R1} + 2\Delta B_1$ and $B_{R2} - 2\Delta B_2 \leq B \leq B_{R2} + 2\Delta B_2$, respectively.

$ka_{\mathrm{bg}}(B)\Delta B_j/(B_{Rj} - B)$ for $j = 1, 2$ are in analogy to Eq. (2.18) associated to the resonant coupling to two different closed-channel bound states $|\Phi_{b1}\rangle$ and $|\Phi_{b2}\rangle$. Since C_1 does not depend on either of the bound states $|\Phi_{b1}\rangle$ and $|\Phi_{b2}\rangle$, it is independent of the magnetic field B. Hence, for describing a transition process to a specific molecular state for two well separated resonances, one needs only three independent parameters.

Additionally a fit to the behavior

$$I_{\mathrm{TC}}^{(j)}(B) = \beta_j \sin^2(\delta_{\mathrm{res}}^{(j)} - \delta_0^{(j)}) \tag{2.30}$$

Table 2.1: Enhancement of the dipole transition rate between off-resonant and resonant magnetic field in MC and TC description for transitions to all eight possible spin states $|S, M_S\rangle|m_{i_1}, m_{i_2}\rangle$ at the two resonances at $B_{R1} = 1066,917\,\mathrm{G}$ and $B_{R2} = 1282.576\,\mathrm{G}$.

Molecular state	Resonance 1		Resonance 2	
	$I_{\mathrm{MC}}^{\mathrm{max}}/I_{\mathrm{MC}}^{\mathrm{off}}$	$(k\,a_e^{(1)})^{-2}$	$I_{\mathrm{MC}}^{\mathrm{max}}/I_{\mathrm{MC}}^{\mathrm{off}}$	$(k\,a_e^{(2)})^{-2}$
$\|0,0\rangle\|0,\frac{3}{2}\rangle$	$5.81 \cdot 10^6$	$5.83 \cdot 10^6$	$6.85 \cdot 10^{12}$	$1.39 \cdot 10^{13}$
$\|0,0\rangle\|1,\frac{1}{2}\rangle$	$2.62 \cdot 10^8$	$3.49 \cdot 10^8$	$6.57 \cdot 10^6$	$1.27 \cdot 10^7$
$\|1,-1\rangle\|1,\frac{3}{2}\rangle$	$1.80 \cdot 10^5$	$1.75 \cdot 10^5$	$5.73 \cdot 10^7$	$5.41 \cdot 10^7$
$\|1,0\rangle\|0,\frac{3}{2}\rangle$	$8.86 \cdot 10^6$	$8.69 \cdot 10^6$	$1.63 \cdot 10^{13}$	$5.93 \cdot 10^{13}$
$\|1,0\rangle\|1,\frac{1}{2}\rangle$	$5.04 \cdot 10^9$	$2.14 \cdot 10^9$	$2.15 \cdot 10^8$	$4.71 \cdot 10^7$
$\|1,1\rangle\|-1,\frac{3}{2}\rangle$	$5.77 \cdot 10^6$	$8.41 \cdot 10^6$	$7.76 \cdot 10^{12}$	$5.21 \cdot 10^{13}$
$\|1,1\rangle\|0,\frac{1}{2}\rangle$	$1.88 \cdot 10^7$	$2.13 \cdot 10^7$	$1.32 \cdot 10^{13}$	$6.57 \cdot 10^{13}$
$\|1,1\rangle\|1,-\frac{1}{2}\rangle$	$1.09 \cdot 10^{10}$	$1.18 \cdot 10^{12}$	$3.66 \cdot 10^7$	$4.41 \cdot 10^7$

for $j = 1, 2$ is performed, which neglects respectively one resonance. Again one can relate the phase shifts $\delta_0^{(j)}$ to the corresponding lengths $a_e^{(j)}$ via Eq. (2.23), which allows also for validating the applicability of Eq. (2.27) for both resonances separately.

Considering Fig. 2.3 one finds that for all shown transitions the TC approximation for two well separated resonances excellently describes the magnetic-field dependence of the MC transition rate. The behavior of Eq. (2.30) reproduces each of the MC resonances $j = 1, 2$ in an interval of several ΔB_j around the resonant magnetic fields B_{Rj}. With only one parameter more than for the description of a single resonance, both resonances can be also accurately described by Eq. (2.29). This is remarkable, since the behavior of the transition rates to all four different spin configurations are quite different.

The good description of the MC transition rates by Eq. (2.30) suggests that Eq. (2.27) indeed reflects the dependence of the PA enhancement on the position of vanishing transition rate. In Eq. (2.27) the enhancement was defined relative to the transition rate at the background scattering length. However, this point is only reached at infinite detuning from the resonant magnetic field B_R. In order to nevertheless verify the validity of Eq. (2.27), the maximal transition rate $I_{\mathrm{MC}}^{\mathrm{max}}$ at each resonance is separately related to the transition rate $I_{\mathrm{MC}}^{\mathrm{off}} = I_{\mathrm{MC}}(800\,\mathrm{G})$ far away from both resonances. A magnetic field with larger detuning is not chosen in order to avoid effects of other molecular bound states of the closed-channel subspace. In Tab. 2.1 the ratio $I_{\mathrm{MC}}^{\mathrm{max}}/I_{\mathrm{MC}}^{\mathrm{off}}$ is compared for both resonances to the prediction of Eq. (2.27) for transitions to the vibrational ground states of all eight possible spin configurations in the molecular basis. One finds that the order of magnitude generally agrees excellently. Only for few transitions, such as

the one to the molecular states $|1,1\rangle|1,-1/2\rangle$ at the first (broad) resonance, the orders of magnitude differ significantly. A view on Fig. 2.3 (d) reveals that this is not related to a break down of Eq. (2.27), but that the absence of a vanishing transition rate leads to a comparably slow degradation of the transition rate such that $I_{\mathrm{MC}}^{\mathrm{off}}$ is not a good representation for the background transition rate. On the other hand, for transitions for which the background transition rate is quickly approached away from the resonance, the two estimates of the enhancement agree even to the first significant digit [see the third row in Tab. 2.1 and the corresponding Fig. 2.3 (b)]. This and the results shown in Fig. 2.3 demonstrate that the TC approximation provides an excellent basis to understand the PA processes in the presence of an external magnetic field inducing an MFR.

3. Two-channel solution in a harmonic trap

In this chapter an approach to analytically describe MFRs of harmonically confined atoms is presented. The system can be specified by an eigenenergy equation, whose solutions determine the open-channel wave function and the admixture of the RBS. The eigenenergy equation also yields a parametrization of the energy-dependent scattering length $a(E, B)$. The validity of the approach is verified by comparing with a system of coupled square-well potentials and full MC calculations for ^{6}Li-^{87}Rb in harmonic confinement. Furthermore, regarding several experiments, the model is applied in order to explain divers trap-induced phenomena of MFRs.

Since MFRs are one of the most important tools for the control of ultracold atoms the case of MFRs in harmonic traps has been discussed in several previous publications. The most common approach is to consider the known solution of atoms in a harmonic trap interacting with a constant scattering length a discussed by Busch et al. [54] for isotropic traps and extended to anisotropic traps by Idziaszek and Calarco [45]. The extension to MFRs is done by simply replacing the constant scattering length by the energy-dependent one given in Eq. (2.16) [42–45]. As will be derived in this chapter, this approach is in principle correct. However, the parametrization of the scattering length in free space suggests a wrong energy-dependence for large a_{bg}. Moreover, the RBS admixture is left undetermined by this approach.

There are also more fundamental approaches that seek to solve a specific two-channel problem in the harmonic trap, which incorporates the RBS admixture. For example, Moore [55] solves the TC problem by replacing the RBS with a regularized delta function. However, he derives the solution by setting the open-channel interaction potential to zero, thereby neglecting the influence of the background scattering length on observables like the resonance width and the resonance detuning. The same is also true for other approaches that expand the solution in non-interacting harmonic oscillator eigenfunctions [56, 57]. These approaches lead furthermore to the appearance of ultraviolet divergences that are dealt with by a renormalization of the bound-state energy.

Here, an approach is taken that incorporates the influence of arbitrarily large background scattering lengths. Nevertheless, the theory is free of divergent terms that have to be compensated for by a renormalization.

Large parts of the following considerations were published in Ref. [25] (Publication II) and Ref. [28] (Publication V).

3.1. Derivation of the analytic model

In order to determine the TC solution in a harmonic trap, the general coupled Eqs. (1.28) and (1.29) are again considered, however, this time with a non-vanishing trap frequency $\omega > 0$.

The great advantage of solving the coupled equations in a trap is that, in contrast to free-space scattering, the open-channel wave function is square integrable. Thus, one can introduce the normalized solution of the open channel $|\Phi_E\rangle$ with $\langle\Phi_E|\ \Phi_E\rangle = 1$ and $|\Psi_P\rangle = C|\Phi_E\rangle$. Since the RBS is also normalized to one and the full solution is given as $|\Phi\rangle = |\Phi_P\rangle + |\Phi_Q\rangle = C|\Phi_E\rangle + A|\Phi_b\rangle$, it holds $C^2 + A^2 = 1$. This allows one to define a phase $\delta_{\mathrm{RBS}} = \arctan(A/C)$ associated with the admixture of the RBS. Introducing $|\Psi_P\rangle = C|\Phi_E\rangle$ and $|\Psi_Q\rangle = A|\Phi_b\rangle$ into Eq. (1.29) and multiplying by $\langle\Phi_b|$ gives

$$\tan\delta_{\mathrm{RBS}} = \frac{\langle\Phi_E|\hat{\mathrm{W}}|\Phi_b\rangle}{(E - E_b)}\,. \tag{3.1}$$

For infinite detuning $|E - E_b| \to \infty$ the open channel is in some background eigenstate $|\Phi_{\mathrm{bg}}\rangle$ of $\hat{\mathrm{H}}_P$ with eigenenergy E_{bg}. Fig. 3.1 sketches how these background states are coupled to the RBS. In the free-space theory the background states correspond to regular solutions $|\Phi_{\mathrm{reg}}\rangle$ with continuous scattering energies and with the background scattering phase δ_{bg}. Multiplying Eq. (1.28) by $\langle\Phi_{\mathrm{bg}}|$ and using Eq. (3.1) yields an equation

$$(E - E_b)(E - E_{\mathrm{bg}}) = \frac{\langle\Phi_{\mathrm{bg}}|\hat{\mathrm{W}}|\Phi_b\rangle\langle\Phi_E|\hat{\mathrm{W}}|\Phi_b\rangle}{\langle\Phi_{\mathrm{bg}}|\ \Phi_E\rangle}\,, \tag{3.2}$$

whose solutions determine the eigenenergies of the system. In free space the same approach would have failed, again, because the open-channel wave function is not square integrable. For an energy-normalized open-channel scattering wave function the overlap $\langle\Phi_{\mathrm{bg}}|\ \Phi_E\rangle$ would correspond in free space to $\langle\Phi_{\mathrm{reg}}|\ \Psi_P\rangle$, which is proportional to the Dirac-delta function $\delta(E - E_{\mathrm{bg}})$. This would allow only for a trivial solution $E_{\mathrm{bg}} = E$.

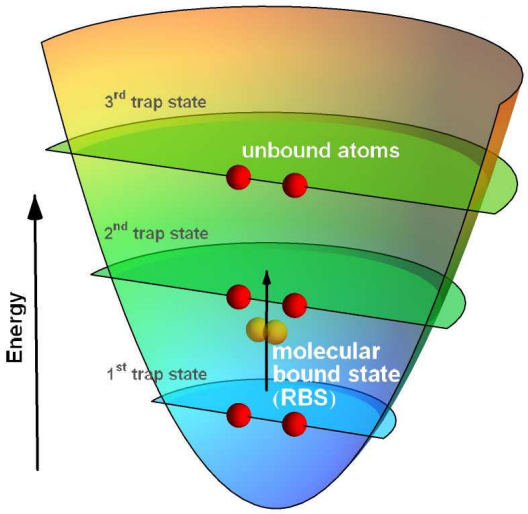

Figure 3.1: Sketch of the relative-motion unbound trap states (background eigenstates of the open-channel Hamiltonian) in a harmonic trap that are coupled to the RBS, whose energy can be manipulated by an external magnetic field.

3.1.1. Short-range approximation

In order to solve Eq. (3.2), one has to find simplified expressions for the matrix elements $\langle\Phi_{\mathrm{bg}}|\hat{\mathrm{W}}|\Phi_b\rangle$, $\langle\Phi_E|\hat{\mathrm{W}}|\Phi_b\rangle$, and $\langle\Phi_{\mathrm{bg}}|\,\Phi_E\rangle$. To this end one can exploit that the interaction acts only in some small range $r < r_0$. As discussed in Sec. 1.1, for almost all atomic systems and optical traps, the interaction range r_0 is much smaller than the extensions of the trap a_{ho}. In a harmonic trap the open-channel solution $|\Phi_E\rangle$ is known analytically for $r > r_0$. Denoting again the asymptotic behaviour of $\Phi_E(r)$ for $r > r_0$ by $\tilde{\Phi}_E(r)$ one has

$$\tilde{\Phi}_E(r) \equiv \lim_{r\to\infty} \Phi_E(r) = A_\nu D_\nu(\rho)\,, \tag{3.3}$$

where $D_\nu(\rho)$ is the parabolic cylinder function, $\rho = \sqrt{2}r/a_{\mathrm{ho}}$, $\nu = E/(\hbar\omega) - 1/2$, and A_ν is a normalization constant. Fig. 3.2 (a) shows a plot of $\tilde{\Phi}_E(\rho)$ for different energies E.

The short-range behavior of the parabolic cylinder function is given as [58]

$$D_\nu(\rho) = D_\nu(0)\left(1 - \frac{\rho}{\sqrt{2}f(E)}\right) + \mathcal{O}(\rho^2) \tag{3.4}$$

with

$$f(E) = \frac{\Gamma\left(\frac{1}{4} - \frac{E}{2\hbar\omega}\right)}{2\Gamma\left(\frac{3}{4} - \frac{E}{2\hbar\omega}\right)}. \tag{3.5}$$

Using Eq. (1.10) one obtains the scattering length $a(E) = a_{\mathrm{ho}}f(E)$ of the open-channel solution as a function of the eigenenergy E. The like holds for $|\Phi_{\mathrm{bg}}\rangle$, i.e the background scattering length is given as $a_{\mathrm{bg}} = a_{\mathrm{ho}}f(E_{\mathrm{bg}})$.

The function $f(E)$ contains many important information about the wave function in an isotropic harmonic trap. For example, if one neglected at this point the RBS admixture and the energy dependence of the scattering length a, the eigenenergies and thus the asymptotic wave function $\tilde{\Phi}_E(r)$ would be already fully specified by roots of $a = a_{\mathrm{ho}}f(E)$, which is equivalent to the result derived by Busch et al. [54].

The function $f(E)$ can be well approximated for $E > \hbar\omega/2$ and $E < -\hbar\omega/2$ by

$$f_>(E) = \sqrt{\frac{\hbar\omega}{2E}}\tan\left(\frac{\pi E}{2\hbar\omega} + \frac{\pi}{4}\right) \tag{3.6}$$

$$\text{and}\quad f_<(E) = \sqrt{-\frac{\hbar\omega}{2E}}\,, \tag{3.7}$$

respectively[1]. The functions $f(E)$, $f_>(E)$, and $f_<(E)$ are shown in Fig. 3.2. As one can

[1]The asymptotic behavior $f(E) \to f_<(E)$ for $E \to -\infty$ follows directly from the asymptotic behavior of the ratio of gamma functions $\Gamma(z+a)/\Gamma(z+b) \to z^{a-b}$ for $z \to \infty$ [59]. Using the reflection property of the gamma functions $\Gamma(z)\Gamma(1-z) = \pi/\sin(\pi z)$ [59] one finds $f(E) = \tan\left(\frac{\pi E}{2\hbar\omega} + \frac{\pi}{4}\right) f(-E)$. Hence, $f(E) \to f_>(E)$ for $E \to +\infty$.

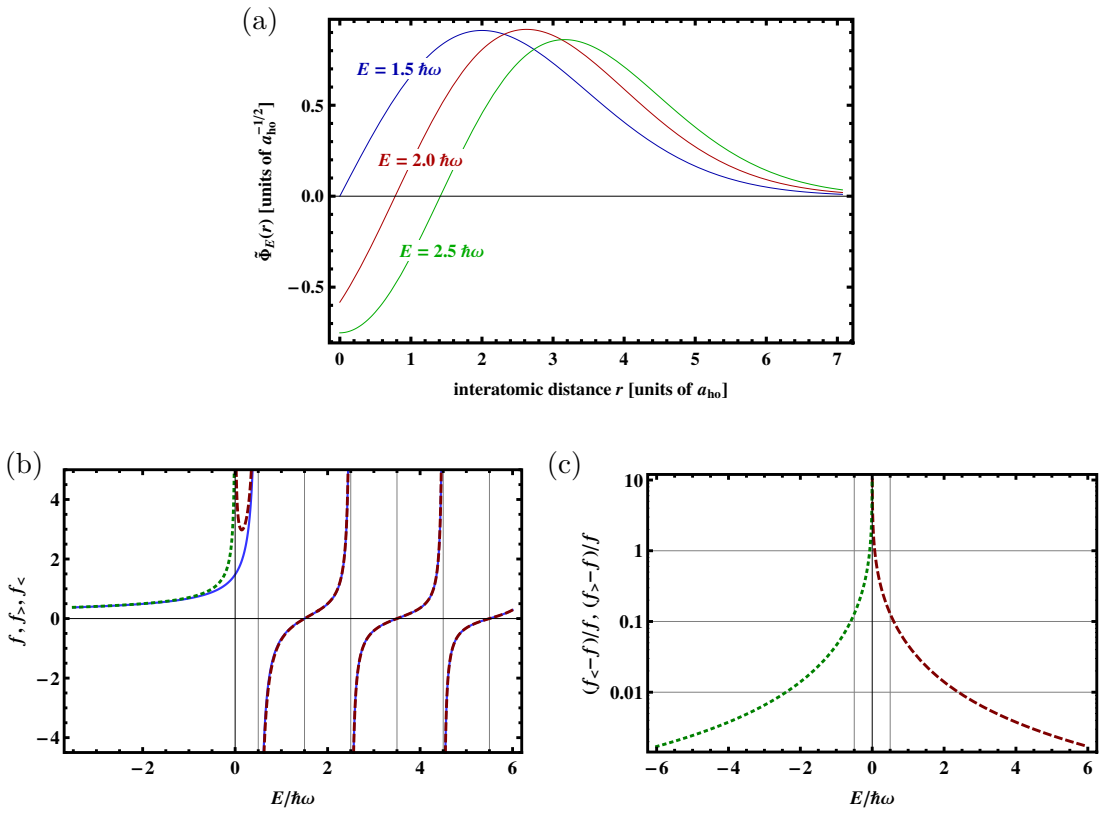

Figure 3.2: **(a)** Asymptotic behaviour of the open-channel wave function $\tilde{\Phi}_E(r)$ for $E = 1.5\hbar\omega$ (scattering length $a = 0$), $E = 2.0\,\hbar\omega$ ($a = 0.49\,a_{\mathrm{ho}}$), and $E = 2.5\,\hbar\omega$ ($|a| = \infty$). **(b)** Comparison of the function $f(E)$ [blue solid] to its approximations $f_>(E)$ [red dashed] and $f_<(E)$ [green dotted]. **(c)** Relative difference between $f(E)$ and $f_>(E)$ or $f_>(E)$ defined in Eqs. (3.5), (3.6), and (3.7).

expect, for the $l = 0$ harmonic oscillator eigenenergies $E = (3/2 + 2n)\hbar\omega$ of the non-interacting system the scattering length vanishes. On the other hand, the scattering length diverges approaching an energy $E = (1/2 + 2n)\hbar\omega$.

In the case of free-space scattering the energy dependence of $\langle\Phi_b|\hat{\mathrm{W}}|\Phi_{\mathrm{reg}}\rangle$ was evaluated by considering the energy behavior of the regular solution $|\Phi_{\mathrm{reg}}\rangle$ for some small internuclear distance r_0 for which the interaction could be neglected. A similar approach is taken here, i.e. it is assumed that the matrix element $\langle\Phi_E|\hat{\mathrm{W}}|\Phi_b\rangle$ is approximately equal to $\gamma\tilde{\Phi}_E(r_0) \approx \gamma\left[\tilde{\Phi}_E(0) + r_0\tilde{\Phi}'_E(0)\right]$, where γ is a proportionality constant parametrizing the coupling strength. In order to be able to accurately describe a large class of MFRs, the interaction range r_0 is replaced by a length a^* that is allowed to take arbitrary positive and negative values. Accordingly, the matrix element $\langle\Phi_E|\hat{\mathrm{W}}|\Phi_b\rangle$ is

parametrized as

$$\begin{aligned}\langle\Phi_E|\hat{\mathrm{W}}|\Phi_b\rangle &= \gamma\,\left[\tilde{\Phi}_E(0) + a^*\,\tilde{\Phi}'_E(0)\right] \\ &= \gamma\,\tilde{\Phi}_E(0)\left(1 + a^*\,\frac{\tilde{\Phi}'_E(0)}{\tilde{\Phi}_E(0)}\right) \\ &= \gamma\,\tilde{\Phi}_E(0)\left(1 - \frac{a^*}{a}\right).\end{aligned} \tag{3.8}$$

The parametrization of Eq. (3.8) can be interpreted in a different way by considering the wave functions (and not the radial wave functions) of the system. Be $\Psi_b(r) = \Phi_b(r)/(\sqrt{4\pi}r)$ the wave function describing the RBS and $\tilde{\Psi}_E(r) = \tilde{\Phi}_E(r)/(\sqrt{4\pi}r)$ the asymptotic wave function of the open channel then

$$\begin{aligned}\gamma\,\left[\tilde{\Phi}_E(0) + a^*\,\tilde{\Phi}'_E(0)\right] &= \int dr\tilde{\Phi}_E(r)\gamma\,\left[\delta(r) - a^*\delta'(r)\right] \\ &= \int dr\sqrt{4\pi}\tilde{\Psi}_E(r)\gamma\,(r + a^*)\,\delta(r) \\ &= \int r^2 dr\,d\Omega\,\tilde{\Psi}_E(r)\sqrt{4\pi}\gamma\,(r + a^*)\,\delta(\vec{r})\,.\end{aligned} \tag{3.9}$$

Here one uses that $r\delta'(r) = -\delta(r)$ and $\delta(r) = 4\pi r^2\delta(\vec{r})$. In this sense, the parametrization of Eq. (3.8) is equivalent to replacing the short-range coupling to the RBS by a zero-range coupling, i.e. $W(r)\Psi_b(r) \to \sqrt{4\pi}\gamma(r+a^*)\delta(\vec{r})$, that acts not on the full wave function $\Psi_E(r)$ but only on its asymptotic form $\tilde{\Psi}_E(r)$. Although, only two parameters are used, the parametrization of the short-range coupling by a zero-range coupling is already quite general. While the asymptotic form of the wave function $\tilde{\Psi}_E(r)$ can exhibit a $1/r$ divergence for $r \to 0$ ($\tilde{\Phi}_E(0) \neq 0$ for $a \neq 0$), such that $\int r^2 dr\tilde{\Psi}_E(r)r\delta(\vec{r})$ is non-zero, all higher order couplings proportional to $r^2\delta(\vec{r}), r^3\delta(\vec{r}), \ldots$ automatically vanish for any asymptotic solution of the harmonic oscillator $\tilde{\Psi}_E(r)$.

Within the TC model the RBS is assumed to be constant. Therefore, within the zero-range coupling approximation the parameters a^* and γ describing the coupling to the RBS should be also constant. However, considering realistic MC solutions, both the RBS wave function and the open-channel wave function at the resonance differ slightly from the off-resonant ones (see Fig. 3.3). To account for this effect one can introduce background-coupling parameters a^*_{bg} and γ_{bg} in order to parametrize the coupling to the background state, i.e. $\langle\Phi_{\mathrm{bg}}|\hat{\mathrm{W}}|\Phi_b\rangle = \gamma_{\mathrm{bg}}\left(1 - a^*_{\mathrm{bg}}/a_{\mathrm{bg}}\right)$. Since the variations should be small, it suffices to introduce only a different background-coupling strength γ_{bg}. If $a^*_{\mathrm{bg}} = a^* + \delta a^*$, then δa^* can be absorbed into the definition of γ_{bg}, i.e. $\gamma_{\mathrm{bg}}\left(1 - a^*_{\mathrm{bg}}/a_{\mathrm{bg}}\right) \to \gamma_{\mathrm{bg}}\,(1 - a^*/a_{\mathrm{bg}})$ for $\gamma_{\mathrm{bg}} \to \gamma_{\mathrm{bg}}\,(1 + \delta a^*/[a_{\mathrm{bg}} - a^*])$. Accordingly, the coupling between the bound state and the background state is parametrized as

$$\langle\Phi_{\mathrm{bg}}|\hat{\mathrm{W}}|\Phi_b\rangle = \gamma_{\mathrm{bg}}\tilde{\Phi}_{E_{\mathrm{bg}}}(0)\left(1 - \frac{a^*}{a_{\mathrm{bg}}}\right). \tag{3.10}$$

Finally, one has to evaluate the overlap $\langle\Phi_{\mathrm{bg}}|\,\Phi_E\rangle$ appearing in Eq. (3.2). Since the

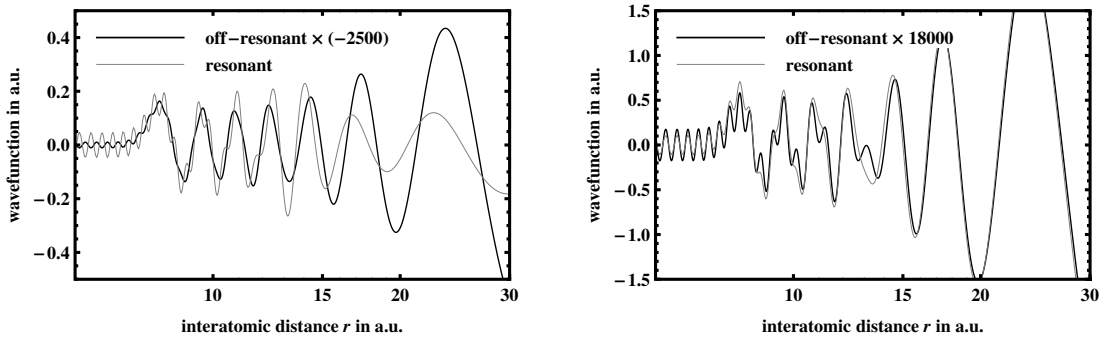

Figure 3.3: Channel wave functions for ^{6}Li-^{87}Rb scattering in the atomic basis at an off-resonant magnetic field of $B = 1000\,\text{Gauss}$ and close to the resonance at $B = 1066.92\,\text{Gauss}$ (see also Fig. 2.2). **Left:** Open-channel wave function ($|f_1, m_{f_1}\rangle|f_2, m_{f_2}\rangle = |1/2, 1/2\rangle|1, 1\rangle$). **Right:** Exemplary closed-channel wave function ($|3/2, 3/2\rangle|1, 0\rangle$). Clearly, the resonant wave functions are similar but not equal to the scaled off-resonant ones.

integral is predominantly determined by the asymptotic form of $|\Phi_E\rangle$ and $|\Phi_{\text{bg}}\rangle$, one has to a very good approximation $\langle\Phi_{\text{bg}}|\,\Phi_E\rangle = \left\langle\tilde{\Phi}_{\text{bg}}\right|\,\tilde{\Phi}_E\big\rangle$. Only if $|\tilde{\Phi}_E\rangle$ and $|\tilde{\Phi}_{\text{bg}}\rangle$ are almost orthogonal, the overlap for small internuclear distances $r < r_0$ is decisive, such that in general $\langle\Phi_{\text{bg}}|\,\Phi_E\rangle \neq \left\langle\tilde{\Phi}_{\text{bg}}\right|\,\tilde{\Phi}_E\big\rangle$. As all background solutions form a complete set of orthogonal functions the proximate orthogonality would imply that $|\tilde{\Phi}_E\rangle$ is itself almost identical to a different background solution $|\Phi'_{\text{bg}}\rangle$ with energy $E'_{\text{bg}} \approx E$ and $E'_{\text{bg}} \neq E_{\text{bg}}$. In this case one is free to chose $|\Phi'_{\text{bg}}\rangle$ instead of $|\Phi_{\text{bg}}\rangle$ as a background solution such that any part of the energy spectrum can be described. Using the analytic properties of the integral $\langle D_\nu|\,D_{\nu'}\rangle$ of two parabolic cylinder functions [60] one finds

$$\begin{aligned}\langle\Phi_E|\,\Phi_{\text{bg}}\rangle &= A_{\nu_{\text{bg}}}A_\nu\int dR D_{\nu_{\text{bg}}}\left(\sqrt{2}\frac{R}{a_{\text{ho}}}\right)D_\nu\left(\sqrt{2}\frac{R}{a_{\text{ho}}}\right)\\ &= A_{\nu_{\text{bg}}}A_\nu\frac{a_{\text{ho}}}{\sqrt{2}}\int d\rho D_{\nu_{\text{bg}}}(\rho)\,D_\nu(\rho)\\ &= A_{\nu_{\text{bg}}}A_\nu\frac{a_{\text{ho}}}{\sqrt{2}}\frac{\pi 2^{(\nu_{\text{bg}}+\nu+1)/2}}{\nu-\nu_{\text{bg}}}\left(\frac{1}{\Gamma\left(\frac{1}{2}-\frac{\nu}{2}\right)\Gamma\left(-\frac{\nu_{\text{bg}}}{2}\right)}-\frac{1}{\Gamma\left(\frac{1}{2}-\frac{\nu_{\text{bg}}}{2}\right)\Gamma\left(-\frac{\nu}{2}\right)}\right).\end{aligned} \tag{3.11}$$

Plugging Eqs. (3.8), (3.10), and (3.11) into Eq. (3.2) and using

$$\tilde{\Phi}_E(0) = \frac{2^{\nu/2}A_\nu\sqrt{\pi}}{\Gamma\left(\frac{1}{2}-\frac{\nu}{2}\right)} \tag{3.12}$$

one has

$$
\begin{aligned}
(E-E_b)(E-E_{\mathrm{bg}}) &= \frac{\langle\Phi_{\mathrm{bg}}|\hat{\mathrm{W}}|\Phi_b\rangle\langle\Phi_E|\hat{\mathrm{W}}|\Phi_b\rangle}{\langle\Phi_{\mathrm{bg}}|\,\Phi_E\rangle} \\
&= \frac{\gamma_{\mathrm{bg}}\gamma\left(1-\dfrac{a^*}{a_{\mathrm{ho}}f(E_{\mathrm{bg}})}\right)\left(1-\dfrac{a^*}{a_{\mathrm{ho}}f(E)}\right)\dfrac{2^{\nu_{\mathrm{bg}}/2}A_{\nu_{\mathrm{bg}}}\sqrt{\pi}}{\Gamma\left(\frac{1}{2}-\frac{\nu_{\mathrm{bg}}}{2}\right)}\,\dfrac{2^{\nu/2}A_{\nu}\sqrt{\pi}}{\Gamma\left(\frac{1}{2}-\frac{\nu}{2}\right)}}{A_\nu A_{\nu_{\mathrm{bg}}}\dfrac{a_{\mathrm{ho}}}{\sqrt{2}}\dfrac{\pi 2^{(\nu+\nu_{\mathrm{bg}}+1)/2}}{\nu-\nu_{\mathrm{bg}}}\left(\dfrac{1}{\Gamma\left(\frac{1}{2}-\frac{\nu}{2}\right)\Gamma\left(-\frac{\nu_{\mathrm{bg}}}{2}\right)}-\dfrac{1}{\Gamma\left(\frac{1}{2}-\frac{\nu_{\mathrm{bg}}}{2}\right)\Gamma\left(-\frac{\nu}{2}\right)}\right)} \\
&= \frac{\gamma_{\mathrm{bg}}\gamma\left(1-\dfrac{a^*}{a_{\mathrm{ho}}f(E_{\mathrm{bg}})}\right)\left(1-\dfrac{a^*}{a_{\mathrm{ho}}f(E)}\right)}{\dfrac{a_{\mathrm{ho}}}{\sqrt{2}}\hbar\omega\dfrac{2^{1/2}}{E-E_{\mathrm{bg}}}\left(\dfrac{\Gamma\left(\frac{1}{2}-\frac{\nu_{\mathrm{bg}}}{2}\right)}{\Gamma\left(-\frac{\nu_{\mathrm{bg}}}{2}\right)}-\dfrac{\Gamma\left(\frac{1}{2}-\frac{\nu}{2}\right)}{\Gamma\left(-\frac{\nu}{2}\right)}\right)} \\
&= (E-E_{\mathrm{bg}})\frac{2\gamma_{\mathrm{bg}}\gamma}{a_{\mathrm{ho}}\hbar\omega}\,\frac{\left(f(E_{\mathrm{bg}})-\dfrac{a^*}{a_{\mathrm{ho}}}\right)\left(f(E)-\dfrac{a^*}{a_{\mathrm{ho}}}\right)}{f(E)-f(E_{\mathrm{bg}})}\,.
\end{aligned}
$$

Dividing both sides by $(E-E_{\mathrm{bg}})$ yields an eigenenergy equation

$$
E-E_b = \frac{2\gamma\gamma_{\mathrm{bg}}}{a_{\mathrm{ho}}\hbar\omega}\,\frac{\left(f(E)-\frac{a^*}{a_{\mathrm{ho}}}\right)\left(f(E_{\mathrm{bg}})-\frac{a^*}{a_{\mathrm{ho}}}\right)}{f(E)-f(E_{\mathrm{bg}})}\,, \tag{3.13}
$$

which finally depends only on constants and analytic functions.

3.1.2. Background scattering length

The value of $f(E_{\mathrm{bg}})$ in Eq. (3.13) is determined by the value of the background scattering length a_{bg}, i.e. E_{bg} must be a root of $a_{\mathrm{ho}}f(E_{\mathrm{bg}}) = a_{\mathrm{bg}}$. However, the background scattering length is not a constant, but does itself depend on the energy E_{bg} of the chosen background state. Within the effective-range expansion

$$
a_{\mathrm{bg}}(k)^{-1} = a_0^{-1} - \frac{1}{2}k^2 r_{\mathrm{eff}} \tag{3.14}
$$

with $k^2 = 2\mu E/\hbar^2$ and a_0 the zero-energy background scattering length, the energy dependence of the background scattering length is determined by the effective range $r_{\mathrm{eff}} > 0$. An analysis of the low-energy scattering process of ultracold atoms shows that r_{eff} can be accurately estimated from a_0 and the van der Waals coefficient C_6 by [61]

$$
r_{\mathrm{eff}} \approx \frac{\sqrt{2}\beta_6}{3}\left[\frac{\Gamma(1/4)}{\Gamma(3/4)} - 2\frac{\sqrt{2}\beta_6}{a_0} + \frac{\Gamma(3/4)}{\Gamma(1/4)}\frac{4\beta_6^2}{a_0^2}\right], \tag{3.15}
$$

where $\beta_6 = \left(\frac{2\mu C_6}{\hbar^2}\right)^{1/4}$ is the range of the van der Waals interaction.

The question arises, which root of $a_{\mathrm{ho}}f(E_{\mathrm{bg}}) = a_{\mathrm{bg}}$ must be chosen to determine

the value of $f(E_{\mathrm{bg}})$. While deriving Eq. (3.13) it was demanded that one chooses the background state that is closest to the energy E. The larger the energy difference of the chosen energy of the background state E_{bg} to the eigenenergy E, the less accurate is the approximation $\langle \Phi_{\mathrm{bg}} | \, \Phi_E \rangle = \left\langle \tilde{\Phi}_{\mathrm{bg}} \middle| \, \tilde{\Phi}_E \right\rangle$ used for the derivation. Fortunately, within the model the trap itself has no influence on the scattering length, which solely depends on the interaction for $r < r_0 \ll a_{\mathrm{ho}}$. One can therefore use the $\omega \to 0$ limit to determine the value of $f(E_{\mathrm{bg}})$. In this case the energy separation of all solutions of $a_{\mathrm{bg}}(E_{\mathrm{bg}}) = a_{\mathrm{ho}} f(E_{\mathrm{bg}})$ goes to zero such that one can set

$$f(E_{\mathrm{bg}}) \equiv a_{\mathrm{bg}}(E)/a_{\mathrm{ho}} \tag{3.16}$$

in Eq. (3.13), where $a_{\mathrm{bg}}(E)$ is determined by Eq. (3.14).

3.1.3. Energy dependent scattering length

One can rewrite Eq. (3.13) in the more intuitive form of a matching condition: The scattering length $a(E, E_b)$ due to the short-range coupling to the RBS must be equal to the scattering length $a_{\mathrm{ho}} f(E)$ of the long-range wave function $\tilde{\Phi}_E(r)$. Rearranging Eq. (3.13) to $a_{\mathrm{ho}} f(E)$ yields

$$a_{\mathrm{ho}} f(E) = a(E, E_b) \quad \text{where} \quad a(E, E_b) = a_{\mathrm{bg}}(E) \left(1 - \frac{\Delta E}{E_b + \delta E - E} \right) . \tag{3.17}$$

The energy dependence of the scattering length $a(E, E_b)$ depends on the background

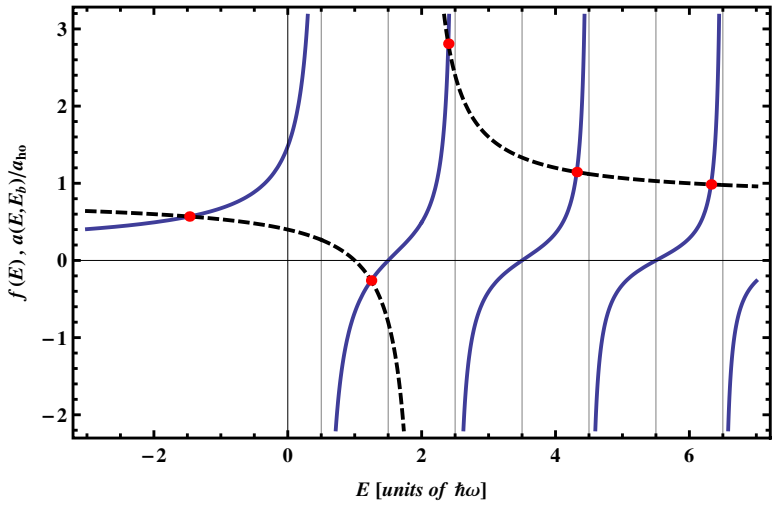

Figure 3.4: Solution of Eq. (3.17) (red dots) are given as intersections of $f(E)$ (blue line) and $a(E, E_b)$ (black dashed line). As an example the parameters of the scattering length are $a_{\mathrm{bg}} = 0.8 a_{\mathrm{ho}}$, $\Delta E = 1\hbar\omega$, $E_{\mathrm{res}} = E_b + \delta E = 2\hbar\omega$. The energies of the solutions are given by the horizontal position of the intersections and their scattering lengths by the vertical positions.

scattering length $a_{\mathrm{bg}}(E)$ and the resonance width

$$\Delta E = \frac{2\gamma\gamma_{\mathrm{bg}}\mu a_{\mathrm{bg}}}{\hbar^2}\left(1-\frac{a^*}{a_{\mathrm{bg}}}\right)^2 . \tag{3.18}$$

The resonance energy $E_{\mathrm{res}} = E_b + \delta E$ is shifted from the bound-state energy E_b by the resonance detuning

$$\delta E = \frac{a_{\mathrm{bg}}\Delta E}{a_{\mathrm{bg}} - a^*} . \tag{3.19}$$

The graphical solution of Eq. (3.17) is shown for an exemplary case in Fig. 3.4.

By assuming, as in the case of free scattering, a linear dependence $E_b = \sigma(B - B_0)$ of the bound-state energy on the magnetic field the eigenenergy equation can be expressed as

$$a_{\mathrm{ho}} f(E) = a(E,B) = a_{\mathrm{bg}}(E)\left(1-\frac{\Delta B}{B - B0 + \delta B - E/\sigma}\right) , \tag{3.20}$$

with the magnetic resonance width $\Delta B = \Delta E/\sigma$ and the detuning $\delta B = \delta E/\sigma$.

According to Ref. [62] one can show based on the ideas of a multi-channel quantum defect theory that in the limit $E \to 0$ the resonance detuning can be excellently approximated by

$$\delta B = \Delta B \frac{\frac{a_0}{\overline{a}}\left(1-\frac{a_0}{\overline{a}}\right)}{1+\left(1-\frac{a_0}{\overline{a}}\right)^2} , \tag{3.21}$$

where

$$\overline{a} = \frac{1}{\sqrt{2}}\frac{\Gamma(3/4)}{\Gamma(5/4)}\frac{\beta_6}{2} \approx 0.956\,\frac{\beta_6}{2} \tag{3.22}$$

is the so-called mean scattering length [63]. Within the developed model in the limit $E \to 0$ the resonance detuning is related to the resonance width by $\delta B = \Delta B a_0/(a_0 - a^*)$. Hence, the length a^* can be expressed as a function of a_0 and $\overline{a}$,

$$a^* = \overline{a}\left(1+\frac{\overline{a}}{\overline{a}-a_0}\right) . \tag{3.23}$$

Both, for $|a_0| \ll \overline{a}$, where $a^* \approx 2\overline{a} \approx \beta_6$ and for $|a_0| \gg \overline{a}$, where $a^* \approx \overline{a} \approx \beta_6/2$, the length a^* is on the order of the range of the interaction, which is in agreement with its initial interpretation as r_0. However, if $a_0 \approx \overline{a}$ the value of a^* can be large and both positive or negative.

The eigenenergy relation can be easily extended also to anisotropic harmonic traps with $\omega_x = \omega_y = \eta\omega_z$. For a given scattering length a the eigenenergy relation in this case is known to be $a = -\sqrt{\pi}d/\mathcal{F}(u)$, where $d = \sqrt{\hbar/(\mu\omega_z)}$ is the harmonic trap length in z direction and $u = \frac{1}{4}(1 + 2\eta - 2E/\hbar\omega_z)$. As derived in Ref. [45] for $u > 0$ one has

$$\mathcal{F}(u) = \int dt \left(\frac{\eta e^{-ut}}{\sqrt{1-e^{-t}}(1-e^{-\eta t})} - \frac{1}{t^{3/2}}\right) . \tag{3.24}$$

If $u \leq 0$ one has to apply, possibly several times, the recurrence relation

$$\mathcal{F}(u) = \mathcal{F}(u+\eta) + \eta\sqrt{\pi}\frac{\Gamma(u)}{\Gamma(u+\frac{1}{2})}\,. \tag{3.25}$$

Since the function $a(E,B)$ is trap-independent, one has to simply replace for $\eta \neq 1$ in the eigenenergy relation $a_{\mathrm{ho}}f(E)$ by $-\sqrt{\pi}d/\mathcal{F}(u)$ yielding the more general eigenenergy relation

$$-\frac{\sqrt{\pi}d}{\mathcal{F}(u)} = a_{\mathrm{bg}}\left(1 - \frac{\Delta E}{E_b + \delta E - E}\right) \tag{3.26}$$

3.1.4. Bound-state admixture at narrow and broad Feshbach resonances

In the established theory of MFRs in free space one generally distinguishes between open-channel dominated and closed-channel dominated MFRs [9]. For an open-channel dominated MFR the closed channel admixture A is negligible over a large range of the MFR. In this case the MFR is called universal since its properties are solely determined by the scattering length. On the other hand, at a closed-channel dominated MFR the bound-state admixture cannot be neglected and thus influences the properties of the MFR. Closed and open-channel dominated MFRs are conventionally called narrow MFR and broad MFR, respectively.

The concept of narrow and broad MFRs can be also extended to MFRs in harmonic traps. In the case of a broad MFR the coupling strength to the bound state is relatively large such that it is admixed to unbound trap states in a large energy domain. Consequently, its admixture to a specific eigenstate is small. On the other hand, in the case of a narrow resonance the RBS is only admixed to the background state that is in resonance. If no background state is in resonance, the RBS is almost an eigenstate of the system and can be strongly occupied (see Fig. 3.5).

In the formal limit $E_{\mathrm{bg}} \to E$ of Eq. (3.13) with $f(E_{\mathrm{bg}}) = f(E) + (E_{\mathrm{bg}} - E)f'(E)$ one has

$$(E - E_{\mathrm{bg}})(E - E_b) = \frac{2\gamma\gamma_{\mathrm{bg}}}{a_{\mathrm{ho}}\hbar\omega}\frac{\left(f(E) - \frac{a^*}{a_{\mathrm{ho}}}\right)^2}{f'(E)}\,. \tag{3.27}$$

On the other hand, in the same limit Eq. (3.2) and its short-range approximation give

$$(E - E_b)(E - E_{\mathrm{bg}}) = \langle\Phi_E|\hat{\mathrm{W}}|\Phi_b\rangle^2 = \gamma\gamma_{\mathrm{bg}}\,\tilde{\Phi}_E^2(0)\left(1 - \frac{a^*}{a_{\mathrm{ho}}f(E)}\right)^2\,. \tag{3.28}$$

By combining the two results one can obtain an expression for $\tilde{\Phi}_E(0)$ as a function of $f(E)$ and $f'(E)$,

$$\tilde{\Phi}_E^2(0) = \frac{2}{a_{\mathrm{ho}}\hbar\omega}\frac{f^2(E)}{f'(E)} \tag{3.29}$$

Using Eqs. (3.13) and (3.29) the short-range approximation of Eq. (3.1) can be written as

$$\tan^2\delta_{\mathrm{RBS}} = \frac{\gamma}{\gamma_{\mathrm{bg}}}\frac{a_{\mathrm{ho}}}{a_{\mathrm{bg}}\Delta E}\frac{\left(f(E) - a_{\mathrm{bg}}/a_{\mathrm{ho}}\right)^2}{f'(E)}\,. \tag{3.30}$$

The derivation of this result is equally valid in an anisotropic trap. Therefore, as in the case of the eigenenergy relation, Eq. (3.30) can be applied to traps with $\omega_x = \omega_y = \eta\omega_z$ by replacing $a_{\mathrm{ho}} f(E)$ by $-\sqrt{\pi} d/\mathcal{F}(u)$ defined in Eqs. (3.24) and (3.25).

The eigenenergies and RBS admixtures of two atoms in an isotropic harmonic trap at two exemplary narrow and broad MFRs are shown Fig. 3.5.

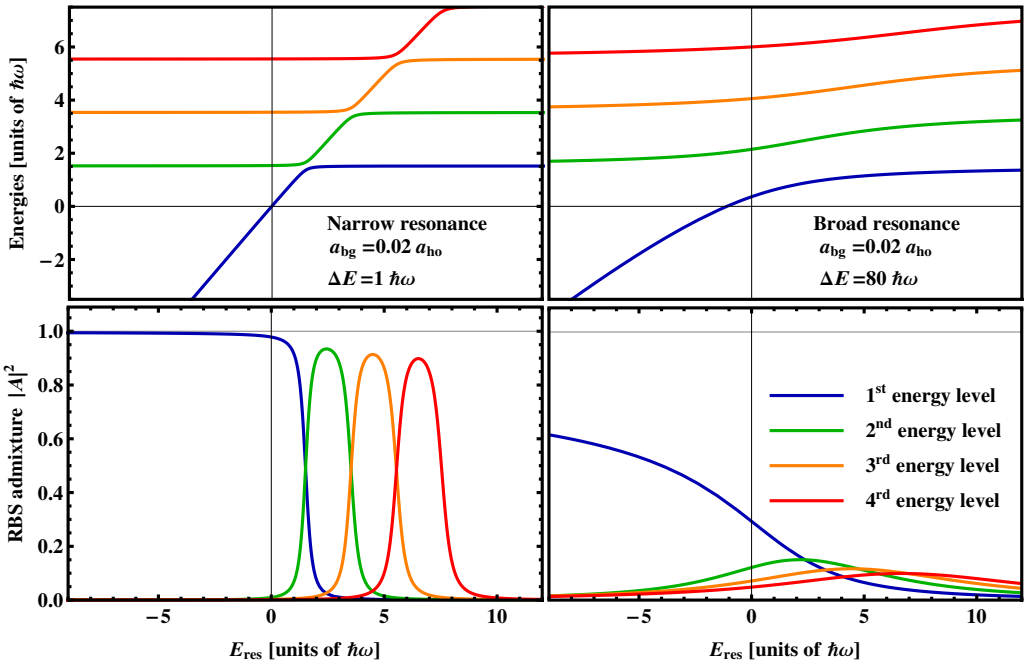

Figure 3.5: **Top:** Energies of the eigenstates at a narrow MFR (left) and a broad MFR (right). The chosen parameters of the MFRs are given in the graphs. **Bottom:** Corresponding RBS admixtures of several eigenstates. At a narrow MFR the weak coupling of the bound state to the trap states leads to small avoided crossings in the spectrum. Away from any avoided crossing the RBS is almost an eigenstate of the system and can be strongly occupied. At a broad MFR the RBS couples strongly to all trap states and is admixed to many eigenstates. Hence, the admixture to a specific eigenstate is smaller.

In order to get a quantitative estimate of the RBS admixture, Eq. (3.30) is approximated for $E > \hbar\omega/2$ using $f(E) = f_>(E)$ [see Eqs. (3.5) and (3.6)]. With the short notations $\epsilon = E/(\hbar\omega)$ and $\alpha = a_{\mathrm{bg}}/a_{\mathrm{ho}}$ this yields

$$\tan^2 \delta_{\mathrm{RBS}} \approx \frac{\gamma}{\gamma_{\mathrm{bg}}} \frac{\hbar\omega}{\Delta E} \frac{1}{\alpha} \left(\frac{\sqrt{2\epsilon}\left([1+\sin(\pi\epsilon)] + 2\alpha^2\epsilon\,[1-\sin(\pi\epsilon)]\right) - 4\alpha\epsilon\cos(\pi\epsilon)}{2\pi\epsilon - \cos(\pi\epsilon)} \right). \tag{3.31}$$

One can further simplify Eq. (3.31) using $[2\pi\epsilon - \cos(\pi\epsilon)] \approx 2\pi\epsilon$ for $E > \hbar\omega/2$. In the

two limits of large or small background scattering length one finds

$$\tan^2\delta_{\mathrm{RBS}} \approx \frac{\gamma}{\gamma_{\mathrm{bg}}}\frac{\hbar\omega}{\Delta E}\frac{1}{\pi}\begin{cases}\dfrac{1}{\sqrt{2\epsilon}\alpha}\left[1+\sin(\pi\epsilon)\right] & \text{for} \quad |a_{\mathrm{bg}}| \ll a_{\mathrm{ho}} \\ \sqrt{2\epsilon}\alpha\left[1-\sin(\pi\epsilon)\right] & \text{for} \quad |a_{\mathrm{bg}}| \gg a_{\mathrm{ho}}\,.\end{cases} \tag{3.32}$$

Of course for negative energies the bound state is stronger and stronger occupied. For $E < -\hbar\omega/2$ one can approximate Eq.(3.30) by

$$\tan^2\delta_{\mathrm{RBS}} \approx \frac{\gamma}{\gamma_{\mathrm{bg}}}\frac{\hbar\omega}{\Delta E}\begin{cases}\dfrac{1}{\alpha}\sqrt{-2\epsilon} & \text{for} \quad |a_{\mathrm{bg}}| \ll a_{\mathrm{ho}} \\ \alpha(-2\epsilon)^{3/2} & \text{for} \quad |a_{\mathrm{bg}}| \gg a_{\mathrm{ho}}\end{cases} \tag{3.33}$$

using $f(E) \approx f_<(E)$ [see Eq.(3.7)].

Regarding Eqs. (3.32) and (3.33) for energies on the order of $\hbar\omega$ and for $\gamma_{\mathrm{bg}} \approx \gamma$ [see discussion below Eq.(3.8)] one can summarize that an MFR is broad (narrow) if for small background scattering length $\Delta E a_{\mathrm{bg}} \gg \hbar\omega a_{\mathrm{ho}}$ ($\Delta E a_{\mathrm{bg}} \ll \hbar\omega a_{\mathrm{ho}}$) and for large background scattering length $\Delta E/a_{\mathrm{bg}} \gg \hbar\omega/a_{\mathrm{ho}}$ ($\Delta E/a_{\mathrm{bg}} \ll \hbar\omega/a_{\mathrm{ho}}$).

Especially for large a_{bg} the properties of the MFR are quite different in free space and in the trap. According to Eq. (2.8) the bound-state admixture to the scattering wave function in free space is maximal at the resonance position $E = E_b + \delta E$ of the scattering length. According to Eq. (3.32) for $|a_{\mathrm{bg}}| \gg a_{\mathrm{ho}}$ the bound-state admixture is maximal where $\sin(\pi\epsilon) = -1$ or equivalently for $E = (3/2 + 2n)\hbar\omega$. However, at these energies the scattering length vanishes (see Fig. 3.2). In contrast, for $|a_{\mathrm{bg}}| \ll a_{\mathrm{ho}}$ the bound-state admixture is maximal where $\sin(\pi\epsilon) = 1$ or accordingly for $E = (1/2 + 2n)\hbar\omega$ which coincides with the resonance position of the scattering length.

Of course, the case $|a_{\mathrm{bg}}| \ll a_{\mathrm{ho}}$ is much more common since background scattering lengths are usually on the order of 100 a.u. while trap lengths are at least about 1000 a.u. For some MFRs of ^{6}Li and ^{133}Cs the background scattering length can reach up to -1727 a.u. and 2500 a.u., respectively [46]. For these MFRs features of the formulas for the limit $|a_{\mathrm{bg}}| \gg a_{\mathrm{ho}}$ can become apparent. That is, although the MFRs are broad in free space, they become in fact significantly narrower in sufficiently strong confinement.

The width of the avoided crossings and thus the width of the MFR are crucial parameters, which determines the behavior of the atoms if the magnetic field and thus the energy of the RBS is varied. Provided that at an avoided crossing the energy difference between the two corresponding eigenstates is small compared to the energy difference to other eigenstates, the dynamical behavior of the system is mainly determined by these two states while all other eigenstates can be neglected.

Expanding $f(E) \approx f(E_{\mathrm{bg}}) + f'(E_{\mathrm{bg}})(E - E_{\mathrm{bg}})$ in Eq. (3.13) around some background energy E_{bg} yields the eigenenergy equation

$$(E - E_b - \delta E)(E - E_{\mathrm{bg}}) = \delta^2\,, \tag{3.34}$$

which describes the coupling of a molecular eigenstate with energy $E_1 = E_b + \delta E$ to a background state with energy $E_2 = E_{\mathrm{bg}}$ with coupling strength $\delta^2 = \Delta E f(E_{\mathrm{bg}})/f'(E_{\mathrm{bg}})$.

Approximating $f(E_{\mathrm{bg}})$ by $f_>(E_{\mathrm{bg}})$ [see Eq. (3.6)] one obtains for the n^{th} avoided

crossing

$$\delta^2 \approx \Delta E \hbar\omega \frac{2}{\pi} \begin{cases} \alpha\sqrt{3+4n} & \text{for} \quad |a_{\mathrm{bg}}| \ll a_{\mathrm{ho}} \\ \dfrac{1}{\alpha\sqrt{3+4n}} & \text{for} \quad |a_{\mathrm{bg}}| \gg a_{\mathrm{ho}} \,. \end{cases} \tag{3.35}$$

According to the Landau-Zener formula the probability of a diabatic transition through the avoided crossing, i.e. the probability of finding the system after the transition still in its initial state, is given as $P = e^{-2\pi G}$ with

$$G = \left| \frac{\delta^2}{\hbar \frac{\partial}{\partial t}(E_2 - E_1)} \right| = \left| \frac{\delta^2}{\hbar\sigma\dot{B}} \right| \approx \left| \frac{2\Delta B \hbar\omega}{\pi\hbar\dot{B}} \begin{cases} \alpha\sqrt{3+4n} & \text{for} \quad |a_{\mathrm{bg}}| \ll a_{\mathrm{ho}} \\ \dfrac{1}{\alpha\sqrt{3+4n}} & \text{for} \quad |a_{\mathrm{bg}}| \gg a_{\mathrm{ho}} \end{cases} \right| \tag{3.36}$$

The experimentally selectable value of $\dot{B}$ thus determines whether a transition is diabatic ($G \ll 1$) or adiabatic ($G \gg 1$). Ideally, sequences of diabatic and adiabatic transitions allow for bringing the system to an arbitrary eigenstate. Of course, only for $|\delta| \ll \hbar\omega$ the Landau-Zener theory can give exact results while otherwise two coupled states offer only a quantitative approximation.

3.1.5. Summary of the model

In order to provide a better overview of the model of MFRs in harmonic traps, the most important equations derived in the previous sections shall be shortly summarized for the special case of an isotropic harmonic trap.

The eigenenergies as a function of the external magnetic field B are determined by

$$a_{\mathrm{ho}} f(E) = a_{\mathrm{bg}} \left(1 - \frac{\Delta B}{B - B_0 + \delta B - E/\sigma} \right)$$

with

$$\Delta B = \frac{2\gamma\gamma_{\mathrm{bg}}\mu a_{\mathrm{bg}}}{\hbar^2\sigma} \left(1 - \frac{a^*}{a_{\mathrm{bg}}} \right)^2, \quad \delta B = \frac{a_{\mathrm{bg}}\Delta B}{a_{\mathrm{bg}} - a^*}, \quad \text{and} \quad a^* = \overline{a} \left(1 + \frac{\overline{a}}{\overline{a} - a_0} \right).$$

For many MFRs the mean scattering length $\overline{a}$, the relative magnetic moment σ, the zero-energy resonance width $\Delta B|_{E=0}$, the zero-energy resonance position $B_R = B_0 - \delta B|_{E=0}$, the zero-energy background scattering length a_0, and the energy-dependent background scattering length a_{bg} in effective-range approximation are known [46]. The values of $\gamma\gamma_{\mathrm{bg}}$ and B_0 can then be easily determined from $\Delta B|_{E=0}$ and B_R, such that there is often no free parameter in the eigenenergy relation.

For a given eigenenergy the ratio of the RBS admixture A and the open-channel admixture C is given as

$$\frac{A^2}{C^2} \equiv \tan^2 \delta_{\mathrm{RBS}} = \frac{\gamma}{\gamma_{\mathrm{bg}}} \frac{a_{\mathrm{ho}}}{a_{\mathrm{bg}}\sigma\Delta B} \frac{\left(f(E) - a_{\mathrm{bg}}/a_{\mathrm{ho}}\right)^2}{f'(E)} \,.$$

The ratio $\frac{\gamma}{\gamma_{\mathrm{bg}}}$ is not directly related to the energy-dependence of the scattering length

and is usually unknown. However, for many MFRs the one-pole approximation is well applicable such that the coupling strength of the RBS to the background eigenstate and to the eigenstate at the resonance are almost equal and $\frac{\gamma}{\gamma_{\mathrm{bg}}} \approx 1$. Below in Sec. 3.2.2 the model is compared to full numerical MC calculations for the ^{6}Li-^{87}Rb MFR at 1066.9 G. In this case it is found that $\frac{\gamma}{\gamma_{\mathrm{bg}}} = 1.05$.

3.2. Comparison with numerical calculations

3.2.1. Comparison to a coupled square-well resonance model

The energy-dependent scattering length $a(E, E_b)$ of Eq. (3.17),

$$a(E, E_b) = a_{\mathrm{bg}} \left(1 - \frac{\Delta E}{E_b + \delta E - E}\right)$$

differs significantly from that of the theory of the scattering of free atoms, where

$$a(E, E_b) = a_{\mathrm{bg}} \left(1 - \frac{\left(1 + a_{\mathrm{bg}}^2 k^2\right) \Delta E_f}{E_b + \delta E_f - E + a_{\mathrm{bg}}^2 k^2 \Delta E_f}\right)$$

[see Eq. (2.11)]. The index "f" shall indicate that the resonance width and resonance detuning in free space is defined differently from those in the harmonic trap. The energy dependence of the total resonance width $\Delta E_{\mathrm{tot}} = \left(1 + a_{\mathrm{bg}}^2 k^2\right) \Delta E_f$ and the total resonance detuning $\delta E_{\mathrm{tot}} = \delta E_f + a_{\mathrm{bg}}^2 k^2 \Delta E_f$ in the case of free scattering is considered in Eqs. (2.14) and (2.15), respectively. They depend on three parameters γ_1, γ_2, and r_0. Remarkably, within the introduced model in the harmonic trap $a(E, E_b)$ depends effectively only on two parameters, the product of the coupling strength $\gamma\gamma_{\mathrm{bg}}$ and the length a^* that has initially replaced the interaction range r_0 [see Eq. (3.8)]. Indeed replacing r_0 by a^* also in Eq. (2.14) both theories agree, i.e. the resonance width in free space and in the harmonic trap are parametrized in the same way. Nevertheless, both models disagree regarding the parametrization of the total resonance detuning given in Eqs. (2.15). In the free-scattering theory the detuning is proportional to $(a_{\mathrm{bg}} k)^2$ for large background scattering length, which is in stark contrast to the theory of MFRs in harmonic traps where no dependence on $(a_{\mathrm{bg}} k)^2$ appears [see Eq. (3.19)]. Also for other two-channel models of MFRs in the presence of a trapping potential the dependence on $(a_{\mathrm{bg}} k)^2$ is absent [55, 64, 65].

In order to determine whether the description in free space or in the trap offers a more accurate determination of the scattering length, a simple model of an MFR is considered. It consists of an open and a closed channel whose potentials are square wells of range d. In the remainder of this section all lengths are given in units of d and all energies in units of $E_0 = \hbar^2/(2\mu d^2)$. The square-well potentials have the general form

$$V_{a,b}(\rho) = \begin{cases} -a & \text{for} \quad \rho < 1 \\ b & \text{for} \quad \rho \geq 1\,. \end{cases} \tag{3.37}$$

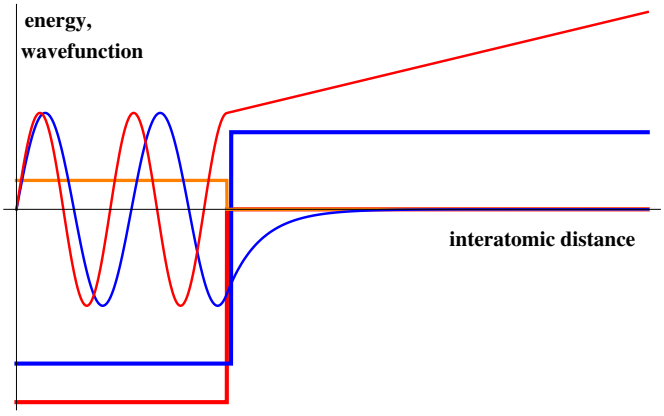

Figure 3.6: Sketch of the used coupled square-well potentials and wave functions of the closed channel (blue) and the open channel (red). Both channels are coupled by a constant coupling potential (orange) within the interaction range.

Also the coupling is considered to be constant within the interaction range $0 \leq \rho < 1$ (see Fig. 3.6). The MFR is described by the dimensionless coupled equations

$$\begin{aligned} -\Phi_P''(\rho) + (V_{a_P,0}(\rho) - E)\,\Phi_P(\rho) + V_{\delta,0}(\rho)\Phi_Q(\rho) &= 0 \\ -\Phi_Q''(\rho) + \left(V_{a_Q,b_Q}(\rho) - E\right)\Phi_Q(\rho) + V_{\delta,0}(\rho)\Phi_P(\rho) &= 0\,, \end{aligned} \tag{3.38}$$

which are visualized in Fig. 3.6. For scattering energies $E \ll a_P$ the background scattering length of the open channel is given as $a_{\mathrm{bg}} = d[1-\tan(\sqrt{a_P})/\sqrt{a_P}]$ and can be chosen arbitrarily large. The width of the MFR is determined by the coupling strength δ. In the following the case $\delta = -0.1\,E_0$ and $a_{\mathrm{bg}} = -400\,d$ (i.e. $a_P = 22.2016\,E_0$) are considered. The depth of the closed-channel potential is chosen to be $a_Q + b_Q = 100\,E_0$. One bound state of the closed-channel potential has an energy $E_b = b_Q - 29.05\,E_0$.

As discussed above, the theory of free scattering suggests that for a given scattering energy E the energy of the bound state $E_b^{(\mathrm{res})} = E - \delta E_f - (a_{\mathrm{bg}}k)^2\Delta E_f$ for which the scattering length diverges [see Eq. (2.11)] can strongly depend on the energy if the background scattering length is large. On the other hand, the theory of an MFR in the harmonic trap suggest no such strong energy dependence, i.e. according to Eq. (3.17) it holds $E_b^{(\mathrm{res})} = E - \delta E$.

In Fig. 3.7 the results of a numerical solution of Eq. (3.38) are shown. As one can see, the value of $E_b^{(\mathrm{res})} - E$ does hardly depend on the energy, although the value of $(a_{\mathrm{bg}}k)^2$ is on the order of one. The invisible change on the order of $10^{-5}E_0$ can be well explained by the energy dependence of the background scattering length, which changes over the shown energy range on the order of 10^{-4} relative to the value of a_{bg} for $E = 0$. To ensure that the stability of the resonance position is no coincidence of the chosen parameters, the same calculations have been performed for other potential depths of the closed channel, always showing similar results. The numerical results imply that

one has to chose $\gamma_1 = \gamma_2$ in Eq. (2.14) in order to realistically describe MFRs. In this case both models parametrize consistently not only the resonance width but also the resonance detuning in the same way. Replacing r_0 by a^* in the theory of free scattering the ratio of resonance width and resonance detuning is given as $(1 - \frac{a^*}{a_{\mathrm{bg}}})$ which is in accordance with Eqs. (3.18) and (3.19).

As one can also see in Fig. 3.7, the numerically determined scattering length $a(E_b, E = 0)$ can be very well described by the parametrization of the scattering length according to Eq. (3.17) with $\Delta E = -0.0565 E_0$, $\delta E = -0.0563 E_0$ and $a_{\mathrm{bg}} = -383d$. The value of the observed background scattering length does not exactly agree with the background scattering length of the uncoupled open channel. Since the scattering length can be influenced by relatively small perturbations, the coupling to the closed channel has a significant influence even if any bound state is far from resonance. For real MFRs this significant off-resonant coupling is one of the reasons for a slight magnetic-field dependence of the background scattering length (see also Fig. 2.2).

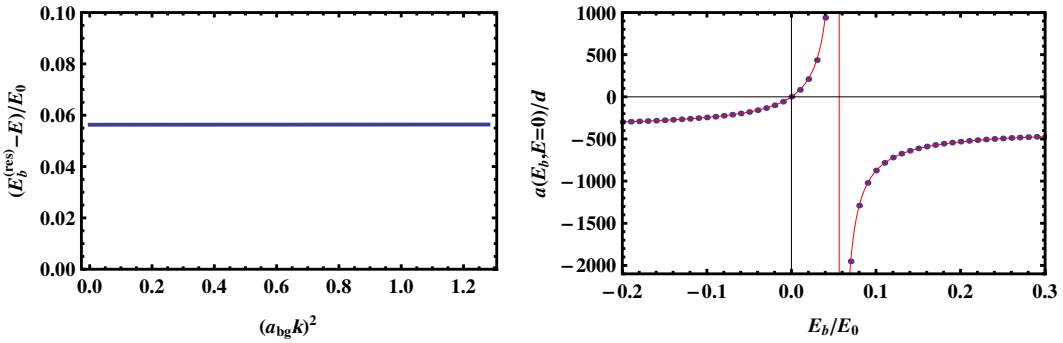

Figure 3.7: **Left:** Value of $E_b^{(\mathrm{res})} - E$ (for the bound-state energy $E_b^{(\mathrm{res})}$ the scattering length diverges) as a function of $(ka_{\mathrm{bg}})^2$. **Right:** Scattering length for $E = 0$ as a function of the bound-state energy E_b. The numerical results are shown as dots while the red solid line shows the behavior according to Eq. (3.17) with $\Delta E = -0.0565 E_0$, $\delta E = -0.0563 E_0$ and $a_{\mathrm{bg}} = -383d$.

3.2.2. Comparison to multi-channel calculations for Li-Rb

For the case of ^{6}Li-^{87}Rb that was already regarded in Sec. 2.2 Yulian V. Vanne has performed full numerical MC calculations in order to obtain eigenenergies and channel admixtures in isotropic harmonic traps with different trap frequencies ω as a function of the magnetic field[2].

In order to compare the results with the introduced model, the model parameters have to be determined. The zero-energy background scattering length is determined

[2]Both in the numerical calculations and in the model a possible coupling of REL and COM motion for different atomic species appearing in Eq. (1.4) is ignored.

from the numerically determined scattering length $a(B)$ in the $E \to 0$ limit in free space (i.e. $\omega = 0$), yielding $a_0 = -17.77\,\text{a.u.}$ The effective range $r_{\text{eff}} = 1899.9\,\text{a.u.}$ of the background scattering length is determined with Eq. (3.15) by the coefficient $C_6 = 2543\,\text{a.u.}$ Using Eq. (3.23) one finds $a^* = 68.88\,\text{a.u.}$ The magnetic field positions of vanishing and resonant scattering length of the first two trap states in a shallow trap with $\omega = 2\pi \times 20\,\text{kHz}$ yield $\gamma\gamma_{\text{bg}} = 2.52 \times 10^{-8}\,\text{a.u.}$, $\sigma = 2.468\,\mu_B$, and $B_0 = 1064.77\,\text{G}$. Finally, by comparing the channel admixtures with Eq. (3.30) one obtains $\gamma = 2.58 \times 10^{-8}\,\text{a.u.}$ and correspondingly $\gamma_{\text{bg}} = 2.46 \times 10^{-8}\,\text{a.u.}$

The parameters are no applied to describe the behavior in a much deeper trap with $\omega = 2\pi \times 200\,\text{kHz}$. Figure 3.8 shows a comparison of the eigenenergies and RBS admixture obtained from the full MC calculation and from the introduced model for both the shallow and the deep trap. The results are in very good agreement with energy deviations smaller than $0.002\,\hbar\omega$ and errors in the RBS admixture smaller than $< 0.1\%$ (see Fig. 3.9). This shows that the model accurately reproduces the E and B dependence of the scattering process. Only for energies E well below zero the model fails to reproduce E and A correctly. Here, the open-channel wave function gets more and more bound. If the range of the open-channel wave function is on the same order as the range of the RBS, the approximation of a zero-range coupling between both channels breaks down.

The value of a^* does not only determine the ratio of resonance width ΔB and resonance detuning δB but also the energy dependence of ΔB and δB, which is induced by the energy dependence of the background scattering length. According to Eqs. (3.18) and (3.19) for $|a_{\text{bg}}| \gg |a^*|$ one has $\Delta B = \delta B \propto a_{\text{bg}}$ while for $|a_{\text{bg}}| \ll |a^*|$ one has $\Delta B \propto a_{\text{bg}}^{-1}$ and $\delta B = 0$. For the present MFR one has $a^* = 3.9|a_{\text{bg}}|$ and indeed one accurately reproduces a significant broadening of ΔB by 0.2 G between the first and the fourth eigenstate of the $\omega = 2\pi \times 200\,\text{kHz}$ trap while the magnitude of the background scattering length decreases for larger energies.

3.3. Comparison with experimental results

3.3.1. Three-body losses induced by the resonant bound state

The bound-state admixture is not only decisive for the creation of molecules, e.g. via PA (see Sec. 2.2), but also for the lifetime of the atoms in the harmonic trap. In the presence of a single open channel two-body collisions are usually elastic, i.e. the kinetic energy is conserved during the collision. Atoms are then predominantly lost from the trap by undergoing inelastic three-body collisions. In the presence of a third atom the state of two unbound or weakly bound atoms can be coupled to a deeply bound molecular state. Due to the large REL motion binding energy of the molecule the state of the molecule and the third atom must have a large COM energy to be in resonance with the scattering state of the three atoms. Since the trapping potentials are much shallower than the molecular binging energy, the molecule and the third atom are lost from the trap at such a three-body resonance.

Usually, atom-loss processes are attributed to a resonance of the scattering length, which leads to a higher probability of finding three atoms within close distance [9].

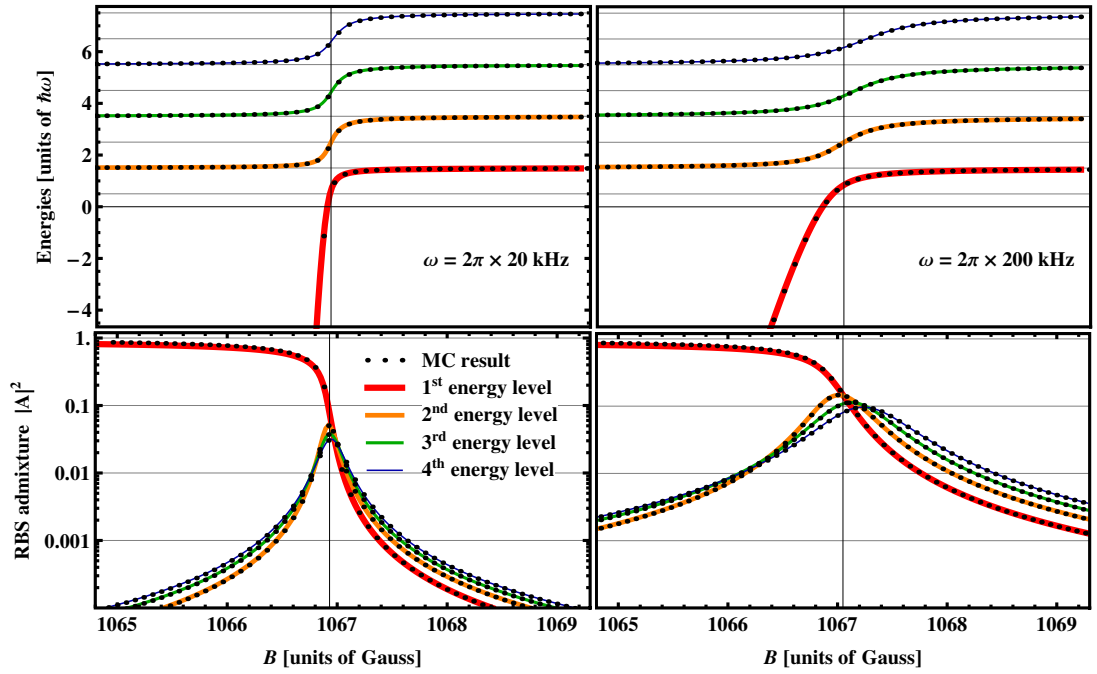

Figure 3.8: **Top:** Energy spectrum of ^{6}Li-^{87}Rb as a function of the magnetic field B in a trap with $\omega = 2\pi \times 20\,\mathrm{kHz}$ (left) and $\omega = 2\pi \times 200\,\mathrm{kHz}$ (right). Dots indicate MC calculations while lines indicate solutions of Eq. (3.20). **Bottom:** Corresponding admixtures $|A|^2$ of the RBS for each energy level as a function of the magnetic field B. Dots indicate MC calculations while lines indicate results of Eq. (3.30).

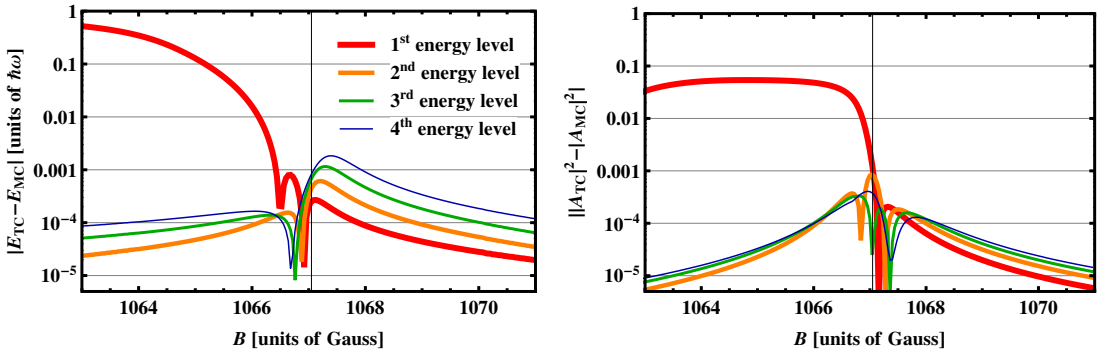

Figure 3.9: **Left:** Absolute difference between TC model and complete MC calculations of the eigenenergies of ^{6}Li-^{87}Rb in a trap with $\omega = 2\pi \times 200\,\mathrm{kHz}$ (see right column in Fig. 3.8). **Right:** Corresponding differences of the RBS admixtures. Apart from energies well below zero, where the lowest state forms a bound state, the energy differences are smaller than $0.002\,\hbar\omega$ and the difference of the RBS admixtures are smaller than $< 0.1\%$.

However, the losses are also influenced by the admixture of the RBS [66]. Since the RBS is already a bound state one can assume that it is stronger coupled to deeply bound states than the unbound open-channel wave function. Unfortunately, in free space the resonance of the scattering length and the maximal RBS admixture coincide such that it is hard to determine whether the value of the scattering length of the open channel or the admixture of the RBS leads dominantly to losses.

In the trap, however, according to Eq. (3.31) the bound-state admixture is shifted from the resonance if $a_{\mathrm{bg}}/a_{\mathrm{ho}}$ and $E/(\hbar\omega)$ are large. Accordingly, the shift should be well observable in a system of two species of Fermionic atoms with a large background scattering length that fill up many trap states. Such a system was, e.g., regarded in an experiment performed by Bourdel et al. [67] with $2N = 7 \times 10^4$ ^{6}Li atoms in two different hyperfine states with a large mutual zero-energy background scattering length of $a_0 = -1405\,\mathrm{a.u.}$ The atoms were confined in a harmonic trap with $\omega_z = 2\pi \times 0.78\,\mathrm{kHz}$ and $\omega_x \approx \omega_y \approx 2\pi \times 2.2\,\mathrm{kHz}$. The atom loss was determined as a function of the magnetic field. A *local* maximum of atom loss was found close to the resonance position B_R of the scattering length. However, the *global* loss maximum was observed at a surprisingly large shift of about $-80\,\mathrm{G}$ from B_R (see Fig. 3.10).

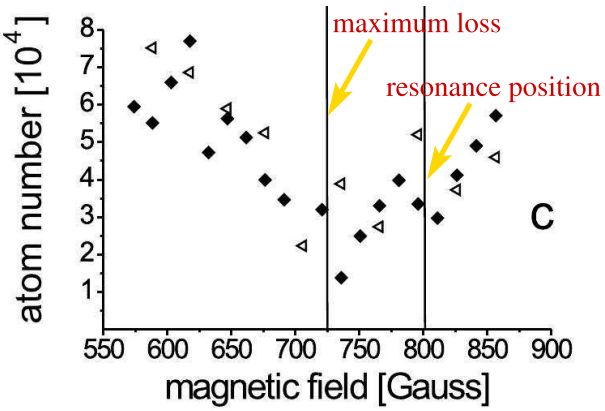

Figure 3.10: Bourdel et al. [67] determined the atom loss of initially 4×10^4 ^{6}Li atoms in a harmonic trap. While a local maximum of atom-loss is found at the free resonance position, the global maximum appears at the maximal admixture of the RBS, $-80\,\mathrm{Gauss}$ shifted from the resonance (plot derived from Ref. [67]).

Ultracold atoms scatter predominantly at the Fermi edge where they have a relative-motion energy equal to the Fermi energy. In a harmonic trap with $\omega_x = \omega_y = \eta\omega_z$ one has $E_F = \hbar\omega_z(6N\eta^2)^{1/3}$ [68]. Employing Eq. (3.30) for an anisotropic trap with $\eta \approx 3$ one can determine at which energy E_{max} close to E_F the RBS admixture reaches its maximum. Knowing E_{max} and the corresponding scattering length of the open-channel wave function a_{max} one can determine the magnetic field of the maximal RBS admixture B_{max} at which $a(E_{\mathrm{max}}, B_{\mathrm{max}}) = a_{\mathrm{max}}$ [see Eq. (3.20)].

Since the Fermi energy is large, the energy dependence of the background scattering length in Eq. (3.30) has to be taken into account, which is determined by the van der

Waals coefficient C_6 [see Eqs. (3.14) and (3.15)]. For $C_6 = 1393.4\,\text{a.u.}$, $\Delta B|_{E=0} = -300\,\text{G}$ and $\sigma = 2\mu_B$ [46] the model predicts a maximal RBS admixture at $B_{\max} = B_R - 80.8\,\text{G}$.

This agrees well with the maximum loss position, which can be an indication that the RBS admixture enhances transitions to deeper bound states and thereby influences atom-loss processes. However, the MFR is broad the RBS admixture $|A|^2$ itself is only on the order of 10^{-6}, which raises the question if such a small admixture can influence loss processes. On the other hand, the ordinary loss process of a three-body scattering event in the open channel is strongly suppressed. Because only two Fermionic species of ^{6}Li are present, two of the three scattering atoms must be identical Fermions such that s-wave scattering between them is impossible while the scattering of higher partial waves is hindered by the centrifugal barrier (see Sec. 1.2). The RBS consist on the other hand of two atoms in a superposition of hyperfine states that differ from the open channel such that s-wave scattering of the third atom with the RBS should be possible. Consequently, despite its small magnitude the RBS admixture could be the dominant reason for atom losses.

There exists yet another qualitative explanation of the off-resonant loss. In Ref. [67] it is argued that for some scattering length $a \geq 0$ a weakly bound molecule can be formed, whose binding energy is just sufficient to lead to a loss of the molecule and the third atom. A decisive answer on the question whether the RBS admixture or the formation of a weakly bound molecule leads to the loss could be given experimentally. If the experiment in [67] would be performed in a deeper trap the gain of binding energy from the weakly bound molecule would not suffice to overcome the trap. In this case the persistence of the atoms loss would be a strong indication that even at a broad MFR the relatively small RBS admixture can be responsible for losses.

3.3.2. Confinement-induced molecules in exited states

While in free space the RBS would decay for an energy $E > 0$ since it is coupled to scattering states[3], it can be stable if the atoms are confined. In a harmonic trap the RBS admixture is present for each energy level [see Figs. 3.5 and 3.8]. Therefore, RBS molecules can be created not only in the bound state as in free space [69] but also in exited states, e.g. exited bands of an optical lattice.

Indeed, these confinement-induced molecules have been experimentally observed in Ref. [70] in a deep optical lattice with two ^{87}Rb atoms per lattice site at an MFR with a zero-energy background scattering length $a_0 = 100.8\,\text{a.u.}$, a zero-energy resonance width $\Delta B|_{E=0} = 18\,\text{mG}$, and $\sigma = 0.08\mu_B$. Considering the harmonic approximation of a single site, the lattice consisted of harmonic traps with frequency $\omega = 2\pi \times 33\,\text{kHz}$ and trap length $a_{\text{ho}} = 1580\,\text{a.u.}$ Because the background scattering length is small compared to a_{ho}, the resonance can be considered very narrow, i.e. $\frac{\Delta B \sigma}{\hbar\omega}\frac{a_0}{a_{\text{ho}}} = 1/260 \ll 1$. Hence, the RBS admixture can be very close to unity (see Sec. 3.1.4).

[3] This is also in agreement with the derived model. The RBS admixture of the stationary states vanishes according to Eq. (3.30) for $\omega \to 0$ and $E > 0$.

By inducing Rabi oscillations at the narrow avoided crossing between the RBS and the first trap state, a large number of RBS molecules could be created from the unbound atoms. Starting with a sample of RBS molecules, after a sudden change of the magnetic field the number of unbound atoms was measured. As shown in Fig. 3.11 the atom number featured pronounced maxima and broad minima as a function of the magnetic field. The suppressed dissociation of the molecules at the minima can be attributed to a strong RBS admixture of excited trap states. Assuming that $\gamma \approx \gamma_{\mathrm{bg}}$ the RBS admixture can be estimated using Eq. (3.30). Additionally to the parameters specified above, the energy dependence of the RBS admixture is determined by the zero-energy resonance position $B_R = 413.9\,\mathrm{G}$ [70] and the van der Waals coefficient $C_6 = 4660\,\mathrm{a.u.}$ [71]. In Fig. 3.11 the RBS admixtures for excited eigenstates at different magnetic fields are charted. Clearly, a large RBS admixture coincides with a suppressed dissociation. Here, the initially prepared RBS molecules survive as part of an eigenstate of the new Hamiltonian. For magnetic fields where the RBS admixtures are small, the RBS quickly decays into a superposition of unbound eigenstates.

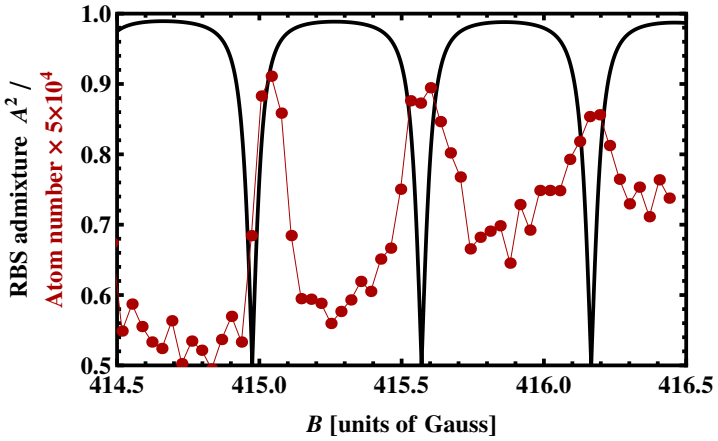

Figure 3.11: Atom number vs. magnetic field (dots) as measured in Ref. [70]. RBS admixture of eigenstates according to Eq. (3.30) with parameters specified in the text (black line). A large RBS admixture coincides with the minima of the molecule dissociation.

3.3.3. Resonance position in the harmonic trap

The resonances of the scattering length $a = a_{\mathrm{ho}} f(E)$ in an isotropic trap appear for eigenenergies $E_{\mathrm{res}}^{(n)} = \hbar\omega(2n + \frac{1}{2})$. More generally, in an anisotropic trap the resonant eigenenergy $E_{\mathrm{res}}^{(n)}$ is determined by the n-th root of $\mathcal{F}(u)$ [see Eq. (3.26)]. Hence, the magnetic field positions of the resonance of the scattering length are not located at the resonance position $B_R = B_0 - \delta B$ in free space but according to Eq. (3.17) at

$$B = B_{\mathrm{res}}^{(n)} = B_0 - \delta B + E_{\mathrm{res}}^{(n)}/\sigma\,. \tag{3.39}$$

In general, not only the last term in Eq. (3.39) but also δB depend on the energy. The strongest energy dependence of δB appears in the case of $|a_{\mathrm{bg}}| \gg |a^*|$ where $d\,\delta B/dE|_{E=0} \approx m a_0 r_{\mathrm{eff}} \Delta B/\hbar^2$.

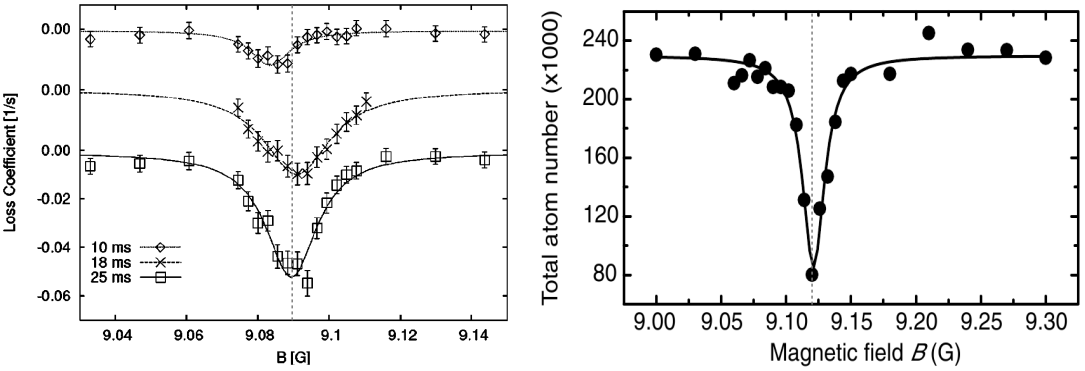

Figure 3.12: Atom losses of ^{87}Rb in a negligibly weak trap (left, extracted from Ref. [72]) and a trap with $\omega_x = 2\pi \times 33\,\mathrm{kHz}$, $\omega_y \approx \omega_z \approx 2\pi \times 42\,\mathrm{kHz}$ (right, extracted from Ref. [73]). The resonance positions differ by 0.031 G.

Applying Eq. (3.39) one is able to explain the disagreement of an experimentally observed resonance position of an MFR of ^{87}Rb close to 9 G. As shown in Fig. 3.12, in a negligibly weak trap the resonant magnetic field position $B_{\mathrm{res}} = 9.09(1)\,\mathrm{G}$ as measured by Erhard et al. [72] differs by about 31 mG from the $B_{\mathrm{res}} = 9.121(9)\,\mathrm{G}$ measured in a trap of frequency $\omega_x = 2\pi \times 33\,\mathrm{kHz}$, $\omega_y \approx \omega_z \approx 2\pi \times 42\,\mathrm{kHz}$ by Widera et al. [73]. The difference can be well explained by Eq. (3.39). For the magnetic field sweep to the resonance performed in [73] the state with $E^{(1)}_{\mathrm{res}} = 2.92\hbar\omega_x$ is predominantly occupied.

The energy dependence of δB is very small. With $C_6 = 4660\,\mathrm{a.u.}$ $\Delta B|_{E=0} = 0.015\,\mathrm{G}$ and $a_0 = 99.8\,\mathrm{a.u.}$ [46] one finds $\delta B_{E=E^{(1)}_{\mathrm{res}}} - \delta B_{E=0} = 4.25 \cdot 10^{-6}\,\mathrm{G}$. The remaining resonance shift $E^{(2)}_{\mathrm{res}}/\sigma = 0.034\,\mathrm{G}$ is much larger and is in good agreement with the experimental results.

The difference of the resonance position for each energy level n might open the possibility to tune the magnetic field to a resonance of a specific trap state, which in turn enhances inelastic collisions depopulating this level. By successively adjusting the magnetic field at different resonance positions one might be able to engineer an ensemble of ultracold atoms in an excited state or cool the system to its relative-motion ground state. A good candidate for this approach would be the narrow ^{87}Rb MFR considered in the discussion on confinement-induced molecules in Sec. 3.3.2, which admits to address single levels in reasonably deep traps.

4. Two-channel model of Feshbach resonances in an optical lattice

If an atom with polarizability $\alpha(\nu)$ is placed in the standing wave of a laser field, which oscillates with frequency ν_0, the electric field component $\vec{E}$ induces a dipole moment $\vec{d} = \alpha(\nu_0)\vec{E}$. The time-averaged dipole potential, which the atom experiences is given as

$$V_{\mathrm{OL}}(\vec{r}) = -\frac{1}{2}\left\langle \vec{d}\cdot\vec{E}\right\rangle = -\frac{1}{2\epsilon_0 c}\mathrm{Re}\left\{\alpha(\nu_0)\right\} I(\vec{r})\,, \tag{4.1}$$

where ϵ_0 is the vacuum permittivity, c the speed of light, and $I(\vec{r})$ the intensity distribution of the laser field. An intensity distribution $I(\vec{r}) = I_x \sin^2(k_0 x) + I_y \sin^2(k_0 y) + I_z \sin^2(k_0 z)$ formed by three standing laser fields with wave vector $k_0 = 2\pi\nu_0/c$ and with perpendicular linear polarization and perpendicular direction creates an optical-lattice (OL) potential

$$V_{\mathrm{OL}}(\vec{r}) = V_x \sin^2(k_0 x) + V_y \sin^2(k_0 y) + V_z \sin^2(k_0 z)\,, \tag{4.2}$$

with the potential depths $V_u = -\frac{1}{2\epsilon_0 c}\mathrm{Re}\left\{\alpha(\nu_0)\right\} I_u$ in direction $u = x, y, z$.

Just like electrons in solids also atoms in OLs are typically described by Hubbard models. In the following, the case of the Hubbard model for Bosonic atoms, the Bose-Hubbard model (BHM), is considered. The extension to a Hubbard model for two species of interacting Fermions is straight forward. The usual BHM allows via the onsite interaction strength U either for repulsively interacting atoms ($U > 0$) or attractively interacting atoms ($U < 0$). As shown in the previous Chapter, especially at a narrow MFR an avoided crossing with the RBS leads to the appearance of both repulsively and attractively interacting states (see Fig. 3.5). In this situation the RBS must be explicitly included into the BHM.

Several different kinds of these extended models have been introduced and debated [56, 74–76] and applied to map out the phase diagramm [56, 77, 78] or to investigate lattice solitons [79]. These investigations consider the extended Hubbard model within a single-band approximation that is only applicable in the rather exceptional situation that the coupling energy to the resonant bound state is small compared to the band gap. In order to generalize the applicability, one can introduce the notion of dressed molecules with effective bound-state energies and coupling strengths obtained from elaborate numerical calculations [80].

A convenient approach to generalize Hubbard models to describe broader MFRs or systems with a large scattering length is to simply include more Bloch bands. For example, Duan [81] has derived an effective single-band Hubbard model for the case of interacting fermions at a broad MFR starting from a multi-band Hubbard model in the Wannier basis and a zero-range coupling between atoms and molecules. How-

ever, as will be discussed below, severe numerical problems arise for the description of a system with a zero-range coupling, e.g., if expanding the solution in products of single-particle basis functions. Especially for large scattering lengths all of these basis functions behave completely differently for internuclear distances $r \to 0$ compared with the correct solution. This poses a problem especially for positive scattering lengths where the open channel supports a bound state. In fact, the obtained energies are lower than the correct ones so that an increase of the basis leads to an even larger disagreement. A similar problem also appears when replacing the interaction potential by the delta-like Fermi-Huang pseudo-potential [82] [see Eq. (1.18)]. And even within analytical treatments of MFRs in harmonic traps that use non-interacting basis states the eigenenergies do not converge [56, 57]. In this case, after an infinite summation, the diverging terms can be absorbed by introducing a renormalized RBS energy. In numerical approaches the problem is usually circumvented by replacing the delta-like potential by a regularized short-range potential [83–85]. However, in order to resolve the potential, a large basis is necessary.

In the following Chapter, an extended BHM is introduced that avoids the numerical problems in the presence of a delta-like coupling without the need of regularization and inclusion of many Bloch bands. Along the lines of Ref. [28] (Publication V), the model is derived from first principles on the basis of the analytic microscopic theory of MFRs in a harmonic trap discussed in the last Chapter. While in the harmonic trap the MFR could be treated analytically, in the OL especially the coupling of the REL motion to the COM motion hinders an analytical approach. The analytic solution in the harmonic trap is nevertheless helpful as it allows to define dressed bound-state energies and couplings that correct for the problems due to the deficiency of the basis states in the presence of a zero-range coupling to the RBS.

Given the numerous different proposals to describe MFRs within a BHM one has to compare the predictions of the introduced BHM with non-perturbative calculations. In the standard description of MFRs this requires to solve at least a two-channel problem of two interacting atoms in an optical lattice coupled at short distance to a molecular bound state. This problem is numerically very demanding. However, it is shown that one can largely simplify the problem by introducing a square-well interaction potential that realistically mimics the behavior at an MFR. Using this single-channel interaction potential, an approach introduced by Grishkevich et al. [86] is applied in order to obtain the correct energies and wave functions of two atoms in a small OL at an MFR. By a direct comparison it is shown that, with only a small number of Bloch bands included, the BHM is able to accurately describe MFRs with coupling energies up to the depth of the OL.

4.1. Derivation of the two-channel Bose-Hubbard model

In order to avoid unneeded complexity, in the following an OL is considered, in which two directions of movement are effectively frozen out by using strong harmonic confinement. Nevertheless, the following discussions can be easily extended to 2D and 3D lattices.

An atom of mass m in such an OL of depth V_L and periodicity $d = \pi/k_0$ in the spacial direction x and transversal harmonic confinement with frequency $\omega_\perp$ in y and z direction is described by the Hamiltonian

$$\mathcal{H}_\mathrm{A}(x,y,z) = -\frac{\hbar^2\nabla^2}{2m} + V_\mathrm{L}\sin^2(k_0 x) + \frac{1}{2}m\omega_\perp^2(y^2+z^2) \tag{4.3}$$

Eigensolutions of $\mathcal{H}_\mathrm{A}$ with quasi momentum k can be expressed in the form

$$\Phi_{k,n,m_y,m_z}(x,y,z) = e^{ikx}\phi_{n,k}(x)\,h_{m_y}(y)\,h_{m_z}(z), \tag{4.4}$$

where $\phi_{n,k}$ are analytically known Bloch solutions with band index $n = 1,2,3,\ldots$ and quasi momentum k of the periodic lattice. h_m is the m-th solution of the one-dimensional harmonic oscillator in y and z direction, respectively.

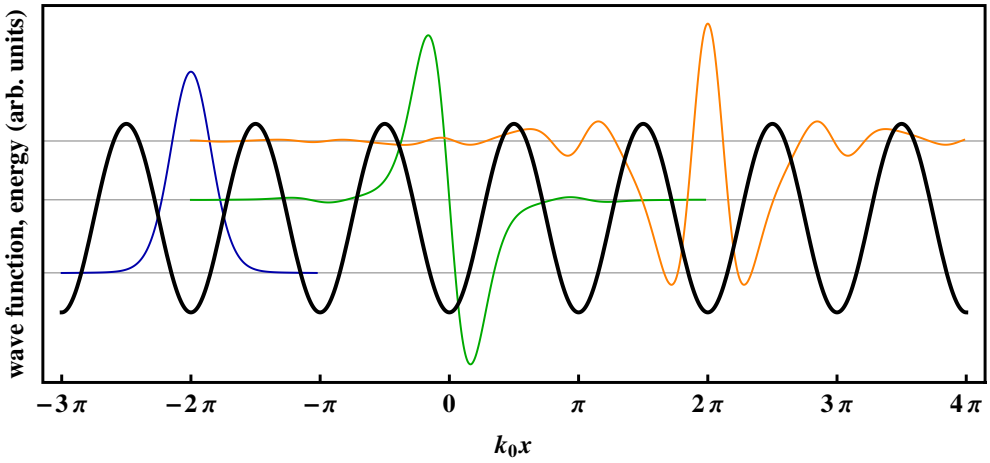

Figure 4.1: Wannier functions of atoms in a deep OL (black) with depth $V_\mathrm{L} = 20\,E_r$ of the first Bloch band (blue, localized around $k_0x = -2\pi$), the second Bloch band (green, localized around $k_0x = 0$), and the third Bloch band (orange, localized around $k_0x = 2\pi$).

In order to describe more than one atom in an OL, interactions have to be taken into account. Since neutral atoms interact only on short distances it is convenient to transform the basis (4.4) into localized functions. This is done by the usual transformation to Wannier functions [87]

$$W_{i,n,m_y,m_z}(x,y,z) = \mathcal{W}_{i,n}(x)\,h_{m_y}(y)\,h_{m_z}(z)\,. \tag{4.5}$$

Here, $\mathcal{W}_{i,n}$ denotes the Wannier function localized at lattice site i and band n. Some exemplary Wannier functions are shown in Fig. 4.1.

Due to the anharmonicity of the OL the relative-motion (REL) coordinates $\vec{r} = \vec{r}_1 - \vec{r}_2$ and center-of-mass (COM) coordinates $\vec{R} = (\vec{r}_1 + \vec{r}_2)/2$ are coupled. Therefore, the Eqs. (1.28) and (1.29) for REL motion have to be extended to include also the COM energies of the two atoms and the RBS. To this end $\Psi_P(\vec{r}_1,\vec{r}_2\,)$ shall describe the

wave function of the two atoms in the open channel with kinetic and potential energies $\mathcal{H}_\mathrm{A}(\vec{r}_1) + \mathcal{H}_\mathrm{A}(\vec{r}_2)$ interacting via a short-range potential $V(r)$. The open channel is coupled by some real-valued short-range coupling $W(r)$ to the closed-channel wave function $\Psi_Q(\vec{R},\vec{r})$. I is assumed that the RBS in REL motion has an extension small enough not to probe the external trapping potential. Therefore, the closed-channel wave function can be written as a product state $\Psi_Q(\vec{R},\vec{r}) = \psi_b(\vec{r})\Psi_\mathrm{COM}(\vec{R})$ of the RBS $\psi_b(\vec{r})$ with binding energy E_b, which is equal to the one introduced in Sec. 3, and the COM wave function $\Psi_\mathrm{COM}(\vec{R})$. The kinetic and potential energy $\mathcal{H}_\mathrm{M}(\vec{R})$ of the COM motion of a molecule with double the mass and polarizability of an atom is obtained by replacing m by $2m$, V_L by $2V_\mathrm{L}$, and $\omega_\perp^2$ by $2\omega_\perp^2$ in the atomic Hamiltonian (4.3). A molecular Wannier function of $\mathcal{H}_\mathrm{M}$ shall be denoted as $\tilde{W}_{i,n,m_y,m_z}$.

Summing up, two atoms in an OL at a Feshbach resonance are described by the coupled equations

$$\begin{pmatrix} \mathcal{H}_\mathrm{A}(\vec{r}_1) + \mathcal{H}_\mathrm{A}(\vec{r}_2) + V(r) - E & W(r) \\ W(r) & \mathcal{H}_\mathrm{M}(\vec{R}) + E_b - E \end{pmatrix} \begin{pmatrix} \psi_\mathrm{P}(\vec{r}_1,\vec{r}_2) \\ \psi_b(\vec{r})\Psi_\mathrm{COM}(\vec{R}) \end{pmatrix} = 0\,. \quad (4.6)$$

As usual for Hubbard models the Hamiltonian is reformulated in the basis of Wannier functions of the OL. However, in order to include effects of higher Bloch bands and their couplings due to the presence of the RBS the basis is not restricted to the first Bloch band. In the following, the simplification of strong transversal confinement is considered, i.e. the ultracold atoms only occupy the ground state of transversal motion. Let $a_{i,n}^\dagger$ ($a_{i,n}$) be the creation (annihilation) operator of a bosonic atom with Wannier function $w_{i,n} \equiv W_{i,n,0,0}$ and $b_{i,n}^\dagger$ ($b_{i,n}$) the creation (annihilation) operator of the bosonic RBS with COM Wannier function $\tilde{w}_{i,n} \equiv \tilde{W}_{i,n,0,0}$. The Hamiltonian in second quantization that leads for a two-particle system to the coupled equations (4.6) expanded in the Wannier basis is given as

$$\begin{aligned} \hat{\mathrm{H}} = &\sum_{i,j}\sum_{n,m} \left\langle w_{i,n}\right| \hat{\mathcal{H}}_\mathrm{A} \left|w_{j,m}\right\rangle a_{i,n}^\dagger a_{j,m} \\ &+ \frac{1}{2}\sum_{i,j,k,l}\sum_{n,m,p,q} \left\langle w_{i,n}w_{j,m}\right| \hat{\mathrm{V}} \left|w_{k,p}w_{l,q}\right\rangle a_{i,n}^\dagger a_{j,m}^\dagger a_{k,p} a_{l,q} \\ &+ \sum_{i,j}\sum_{n,m} \left(\left\langle \tilde{w}_{i,n}\right| \hat{\mathcal{H}}_\mathrm{M} \left|\tilde{w}_{j,m}\right\rangle + E_b\right) b_{i,n}^\dagger b_{j,m} \\ &+ \frac{1}{\sqrt{2}}\sum_{i,j,k}\sum_{n,m,p} \left\langle w_{i,n}w_{j,m}\right| \hat{\mathrm{W}} \left|\tilde{w}_{k,p}\,\psi_b\right\rangle \left(a_{i,n}^\dagger a_{j,m}^\dagger b_{k,p} + h.c.\right)\,. \end{aligned} \quad (4.7)$$

Note the factor $1/\sqrt{2}$ before the atom-molecule coupling, which has to be included to ensure that the matrix elements of the Hamiltonian are equal in first and second quantization [88].

It must be emphasized that Eq. (4.6) and thus the second quantized Hamiltonian (4.7) are only valid if not more than two atoms interact. If the probability of finding three or more atoms within the interaction range cannot be neglected, effects such as

three-body losses or the appearance of Efimov states are not correctly reproduced. The same is, however, also true for ordinary Hubbard models for ultracold atoms and does not hinder the general applicability of the approach to model atoms in OLs with a sufficiently small filling rate.

The following simplifications and approximations are introduced:

1. The Hamiltonians $\mathcal{H}_\mathrm{A}$ and $\mathcal{H}_\mathrm{M}$ do not couple different Bloch bands, since the Wannier functions $w_{i,n}$ and $\tilde{w}_{i,n}$ are superpositions of eigenstates of $\mathcal{H}_\mathrm{A}$ and $\mathcal{H}_\mathrm{M}$ that belong to the same band. For example, for $\mathcal{H}_\mathrm{A}$ holds $\left\langle w_{i,n}\right| \hat{\mathcal{H}}_\mathrm{A} \left|w_{j,k}\right\rangle = \left\langle w_{i,n}\right| \hat{\mathcal{H}}_\mathrm{A} \left|w_{j,n}\right\rangle \delta_{nk}$.

2. Only next-neighbor coupling is considered, i.e.

$$\begin{aligned}
&\sum_{i,j}\sum_{n}\left\langle w_{i,n}\right| \hat{\mathcal{H}}_\mathrm{A} \left|w_{j,n}\right\rangle a_{i,n}^\dagger a_{j,n} + \sum_{i,j}\sum_{n,m}\left(\left\langle \tilde{w}_{i,n}\right| \hat{\mathcal{H}}_\mathrm{M} \left|\tilde{w}_{j,m}\right\rangle + E_b\right) b_{i,n}^\dagger b_{j,m} \\
&\approx \sum_{i}\sum_{n}\epsilon_n a_{i,n}^\dagger a_{i,n} - \sum_{\langle i,j\rangle}\sum_{n} J_n a_{i,n}^\dagger a_{j,n} + \sum_{i}\sum_{n}(\mathcal{E}_n + E_b) b_{i,n}^\dagger b_{i,n} \\
&\quad - \sum_{\langle i,j\rangle}\sum_{n}\mathcal{J}_n b_{i,n}^\dagger b_{j,n}
\end{aligned} \tag{4.8}$$

   where $\epsilon_n = \left\langle w_{1,n}\right| \hat{\mathcal{H}}_\mathrm{A} \left|w_{1,n}\right\rangle$, $\mathcal{E}_n = \langle \tilde{w}_{1,n}| \mathcal{H}_\mathrm{M} |\tilde{w}_{1,n}\rangle$, $J_n = -\left\langle w_{1,n}\right| \hat{\mathcal{H}}_\mathrm{A} \left|w_{2,n}\right\rangle$, $\mathcal{J}_n = -\left\langle \tilde{w}_{1,n}\right| \hat{\mathcal{H}}_\mathrm{M} \left|\tilde{w}_{2,n}\right\rangle$, and $\langle\cdots\rangle$ below the sums denotes summation over nearest-neighbor lattice sites.

3. The interaction potential is replaced by the Fermi-Huang pseudo potential (1.18),

$$V(r) \to \frac{4\pi\hbar^2 a_0}{m}\delta(\vec{r})\frac{\partial}{\partial r}r \tag{4.9}$$

   that reproduces the same zero-energy background scattering length a_0 as the full open-channel interaction potential. As discussed in Chap. 1 this approximation neglects the influence of the energy dependence of the scattering length. Moreover, the approximation is only applicable for small background scattering lengths, as has been investigated in Publication VI.

   For small background scattering length only onsite-interaction is taken into account, i.e.

$$\begin{aligned}
&\sum_{i,j,k,l}\sum_{n,m,p,q}\left\langle w_{i,n}w_{j,m}\right| \hat{\mathrm{V}} \left|w_{k,p}w_{l,q}\right\rangle a_{i,n}^\dagger a_{j,m}^\dagger a_{k,p} a_{l,q} \\
&\approx \sum_{i}\sum_{n,m,p,q} U_{n,m,p,q} a_{i,n}^\dagger a_{i,m}^\dagger a_{i,p} a_{i,q}
\end{aligned} \tag{4.10}$$

   with $U_{n,m,p,q} = \left\langle w_{1,n}w_{1,m}\right| \hat{\mathrm{V}} \left|w_{1,p}w_{1,q}\right\rangle = \frac{4\pi\hbar^2 a_0}{m}\int dx\, dy\, dz\; w_{0,n}\, w_{0,m}\, w_{0,p}\, w_{0,q}$.

4. The coupling to the molecule happens only at short distances. On the length

scale of the lattice and the transverse harmonic confinement one can replace

$$W(\vec{r})\psi_b(\vec{r}) \to g\delta(\vec{r})\,, \tag{4.11}$$

where the coupling strength g has to be adapted to match the behavior of the system under consideration. Including only next-neighbor coupling leads to the simplification

$$\begin{aligned}\sum_{i,j,k}\sum_{n,l,p}&\left\langle w_{i,n}w_{j,l}\right|\hat{\mathrm{W}}\left|\tilde{w}_{k,p}\;\psi_b\right\rangle\left(a^\dagger_{i,n}a^\dagger_{j,l}b_{k,p}+h.c.\right)\\ &\approx\sum_{\langle i,j,k\rangle}\sum_{n,l,p} g^{(i-k,j-k)}_{n,m,p}\left(a^\dagger_{i,n}a^\dagger_{j,l}b_{k,p}+h.c.\right)\,,\end{aligned} \tag{4.12}$$

with

$$g^{(i,j)}_{n,l,p} = g\int dx\;dy\;dz\;w_{i,n}\;w_{j,l}\;\tilde{w}_{0,p}\,. \tag{4.13}$$

Due to the symmetry of the Wannier functions the onsite coupling obeys the selection rule

$$g^{(0,0)}_{n,l,p} = 0 \quad \text{for} \quad n+l+p \quad \text{even}. \tag{4.14}$$

Employing the above simplifications and approximations the BHM Hamiltonian reduced to the first N Bloch bands reads

$$\begin{aligned}\hat{\mathrm{H}}_{\mathrm{BH}} =&\sum_i\sum_{n=1}^{N}\epsilon_n\;a^\dagger_{i,n}a_{i,n}-\sum_{\langle i,j\rangle}\sum_{n=1}^{N}J_n\;a^\dagger_{i,n}a_{j,n}\\ &+\frac{1}{2}\sum_i\sum_{n,l,p,q=1}^{N}U_{n,l,p,q}\;a^\dagger_{i,n}a^\dagger_{i,l}a_{i,p}a_{i,q}\\ &+\sum_i\sum_{n=1}^{N}(\mathcal{E}_n+E_b)\;b^\dagger_{i,n}b_{i,n}-\sum_{\langle i,j\rangle}\sum_{n=1}^{N}\mathcal{J}_n\;b^\dagger_{i,n}b_{j,n}\\ &+\frac{1}{\sqrt{2}}\sum_{\langle i,j,k\rangle}\sum_{n,l,p=1}^{N}g^{(i-k,j-k)}_{n,m,p}\left(a^\dagger_{i,n}a^\dagger_{j,l}b_{k,p}+h.c.\right)\,.\end{aligned} \tag{4.15}$$

4.2. Problem of the zero-range coupling

The coupling of the open channel to the bound state as described by Eq. (4.11) seems to be a crude approximation. Indeed, as discussed in Sec. 3, a more general form of a short-range coupling to the bound state is of the form $W(\vec{r})\psi_b(\vec{r}) = \sqrt{4\pi}\gamma(r+a^*)\delta(\vec{r})$. While one can associate g with $\sqrt{4\pi}a^*\gamma$ the coupling $\sqrt{4\pi}\gamma r\delta(\vec{r})$ automatically vanishes for the chosen single-atom basis states. In fact it vanishes for any basis that conforms to a scattering length $a = 0$. Hence, the presented BHM can only conform to an MFR with $\gamma \to 0$, $a^* \to \infty$, and $\gamma a^* = const.$ This results according to Eqs. (3.18) and (3.19) in a resonance width $\Delta E = 2\mu\gamma\gamma_{\mathrm{bg}}(a^*)^2/(\hbar^2 a_{\mathrm{bg}}) = \mu g^2/(2\pi\hbar^2 a_{\mathrm{bg}})$ and a resonance detuning $\delta E = 0$. For MFRs with $\gamma \neq 0$ one can easily account for the altered resonance

parameters by introducing an effective coupling strength and an effective bound-state energy,

$$g \to g_{\text{eff}} = \sqrt{\frac{4\pi\hbar^2 a_{\text{bg}} \Delta E}{2\mu}}\Bigg|_{E=0} \tag{4.16}$$

$$E_b \to E_{b,\text{eff}} = E_{\text{res}} = E_b + \delta E|_{E=0} \tag{4.17}$$

that lead, apart from the influence of the energy dependence of the background scattering length, to the correct resonance width ΔE and resonance energy E_{res}. In the following, the index "eff" will be suppressed keeping however in mind that g and E_b are not equivalent to the physical coupling strength and the physical energy of the RBS.

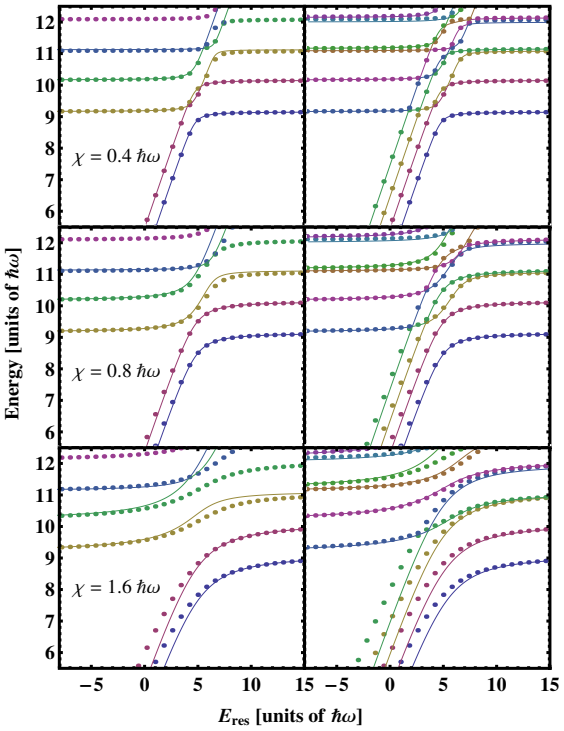

Figure 4.2: Energy spectrum as a function of the resonance energy E_{res} for $\eta = 4$, $a_{\text{bg}} = 0.04\, a_{\text{ho}}$ and from top to bottom $\Delta E = (1, 4, 16)\,\hbar\omega$. This results in the coupling energies χ [see Eqs. (4.11) and (4.18)] given in the graphs. The analytic eigenenergies (dots) obtained by Eq. (3.26) are compared to the eigenenergies of the BHM (lines) for two Bloch bands (left column) and four Bloch bands (right column) included. With only two Bloch bands (left column) the analytic eigenstate with energy $\approx 12\,\hbar\omega$ is not reproduced by the BH model.

In Fig. 4.2 the energy spectra in an anisotropic harmonic trap of several MFRs of different widths are compared to the corresponding result of the effective BHM. The trapping frequencies are $\omega_\perp = \eta\omega$, with $\eta = 4$ and ω the trapping frequency in x

direction. In the harmonic trap the Wannier functions of the BHM are replaced by harmonic oscillator eigenfunctions. On the left side of Fig. 4.2 two Bloch bands are included and the RBS appears in two different COM states, while the unbound atoms can occupy three different trap states [(i) both atoms in the first band at $9\,\hbar\omega$, (ii) one atom in the first and one in the second band at $10\,\hbar\omega$ and (iii) two atoms in the second band at $11\,\hbar\omega$]. On the right side four Bloch bands are included with correspondingly more molecular states and trap states. As a measure for the coupling strength the energy

$$\chi = g_{1,1,1}^{(0,0)} \tag{4.18}$$

is introduced [see Eq. (4.13)]. The avoided crossing between the lowest bound state and the first trap state has a splitting energy of approximately 2χ.

For a relatively narrow MFR with an effective coupling strength $\chi = 0.4\,\hbar\omega$ the agreement between the BHM and the analytic result is very good independently of the number of Bloch bands included. For the broader MFRs with $\chi = 0.8\,\hbar\omega$ and $\chi = 1.6\,\hbar\omega$ one can make two observations: (i) Trap states (i.e. states above the bound state threshold of $9\,\hbar\omega$) quickly approach to the analytic results for an increasing number of Bloch bands. (ii) The disagreement between analytic and BHM results of the bound states does not decrease with the number of Bloch bands.

Obviously, the variational principle does not hold for the bound states as an insufficient basis leads to an energy *lower* than the correct bound-state energies. Moreover, by increasing the basis the incorrect bound-state energies becomes even lower and the disagreement to the correct result increases. Though less severe, the same problem also appears for trap states. For example, the first trap state in the last row in Fig. 4.2 lies below the correct energy if four Bloch bands are included.

The reason for this insufficiency of the basis to conform to the behavior of a delta-like coupling is related to the problem of a missing coupling of the form $\sqrt{4\pi}\gamma r\delta(\vec{r})$: the two-particle basis states are $a = 0$ wave functions. However, as shown in Fig. 4.3 $a = 0$ basis functions can represent the full wave function only for $r > 0$ but not for $r \to 0$. While for ordinary interaction potentials the value of the wave function at the single point $r = 0$ is irrelevant, for zero-range potentials it is decisive. The problem is especially severe for the open-channel bound state, which appears for positive scattering lengths. For $E \to -\infty$ one has $|\tilde{\phi}_E(0)| \propto (-E)^{1/4}$ making its representation by $a = 0$ basis functions for decreasing energy more and more problematic.

For weak coupling the problem is less severe. Here, eigenstates which differ significantly from the background trap states are predominantly bound states (see discussion of Sec. 3.1.4) with different COM excitations. These states are explicitly included in the BHM and are therefore well reproduced. On the other hand, for strong coupling the bound-state admixture is lower, such that a good representation of the open-channel wavefunction would be important for large scattering lengths.

The described problem does not only arise when using non-interacting $a = 0$ basis states. For any finite expansion of the radial wave function $\phi_{\text{exp}}(r) = \sum c_n \phi_n(r)$ in a superposition of basis functions with a specific scattering length a_b [i.e. $a_b =$

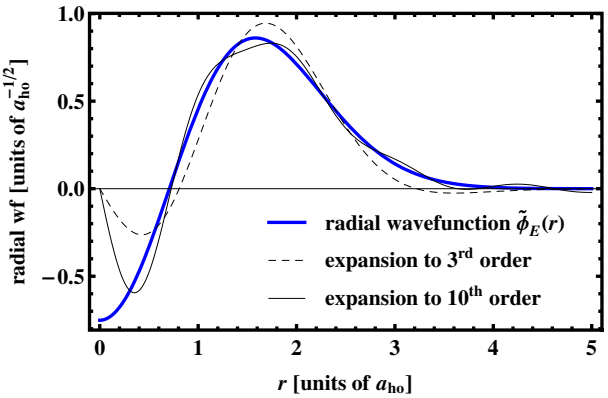

Figure 4.3: The radial wave function $\tilde{\phi}_E(r)$ in a spherical harmonic trap introduced in Eq. (3.3) is compared for the REL energy $E = 2.5\,\hbar\omega$ to its expansion $\phi_{\text{exp}} = \sum_{n=0}^{N-1} \langle \phi_n | \phi_E \rangle \phi_n(r)$ to different orders N, where ϕ_n is the radial wave function of the non-interacting system with radial momentum $l = 0$ and energy $(2n + \frac{3}{2})\hbar\omega$. Since all non-interacting radial basis functions are zero for $r = 0$ the expansion cannot reproduce the behavior of $\tilde{\phi}_E(r)$ for $r \to 0$. This is important since the coupling to the bound state is proportional to $\tilde{\phi}'_E(0)$ or $\phi'_{\text{exp}}(0)$, respectively.

$-\phi_n(0)/\phi'_n(0)]$ the scattering length of the expansion also evaluates to

$$a_{\text{exp}} = -\frac{\phi_{\text{exp}}(0)}{\phi'_{\text{exp}}(0)} = \frac{\sum c_n a_b \phi'_n(0)}{\sum c_n \phi'_n(0)} = a_b\,. \tag{4.19}$$

Hence, the wave function $\phi_{\text{exp}}(r)$ cannot adapt to a change of the scattering length induced by a short-range coupling. Especially since the scattering length at an MFR is energy dependent, these kind of finite expansions cannot reproduce the correct eigenenergies and eigenstates.

4.3. Dressing of coupling strength and bound-state energies

To circumvent the problem of the wrong representation of a zero-range coupling one can replace it by a finite-range coupling. To this end one usually considers the problem in the momentum representation and introduces a high-momentum cut-off Λ. This regularizes the zero-range coupling $g\delta(\vec{r}) = g/(4\pi r^2)\ \delta(r)$. That is, by effectively replacing $\delta(r) \to \frac{1}{2\pi}\int_{-\Lambda}^{\Lambda} dk e^{ikr} = \sin(\Lambda r)/(\pi r)$ the zero range coupling is replaced by a finite-range coupling

$$g\delta(\vec{r}) \to \frac{g}{4\pi r^2}\frac{\sin(\Lambda r)}{\pi r}\,. \tag{4.20}$$

Upon the regularization, the coupling parameter g has to be renormalized in order to absorb terms diverging in the limit $\Lambda \to \infty$ [89]. In numerical approaches only a finite cut-off can be considered, which leads to a coupling with an extension on the

order of $1/\Lambda$ which should be small compared to the lattice spacing d. However, for an interaction with a range of $1/\Lambda = d/N$ more than N Bloch bands have to be included to converge the energies [84]. Since for two atoms in a one dimensional lattice the number of basis functions scales quadratically with the number of Bloch bands and the number of sites the solution can quickly become numerically very demanding.

Here, a different approach is taken with no need to include more Bloch bands to reproduce the correct bound-state energies. Provided with the analytic solution in the harmonic trap a dressed bound state is introduced, which reproduces the correct energy spectrum in the harmonic trap at least in the important energy range of the first Bloch band. The applicability of the dressed parameters also for anharmonic OLs builds upon the fact that the full bound state (i.e. the combination of the closed-channel and open-channel bound state) falls off rapidly for increasing internuclear separation. Hence, the bound state does hardly probe the anharmonic parts of the OL potential.

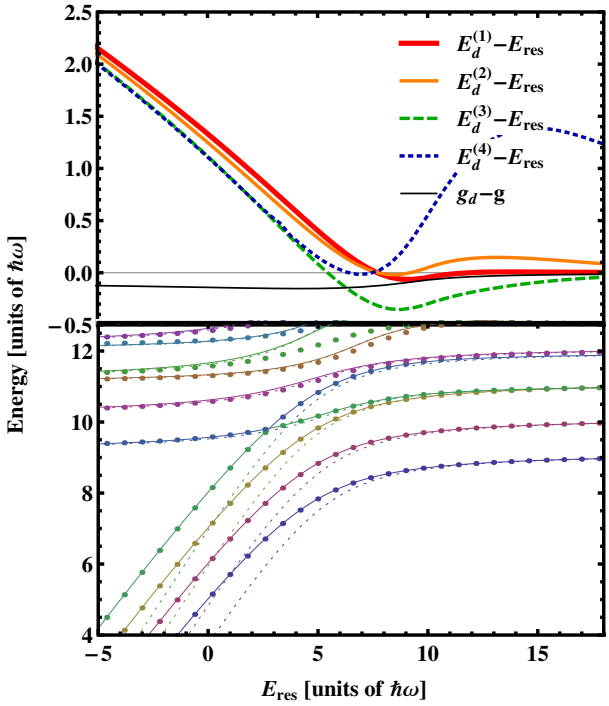

Figure 4.4: Results of the dressed BHM for four Bloch bands with $a_{\rm bg} = 0.04\, a_{\rm ho}$ and $\Delta E = 16\,\hbar\omega$. **Top**: Dressed bound-state energies and dressed coupling strength as a function of $E_{\rm res}$. **Bottom**: Comparison of the analytic energy spectrum (dots) with the energies of the dressed BHM (solid lines) and the undressed BHM (dotted lines).

More concretely, the dressed bound state is introduced in the following way: The RBS in the first band (for which the COM wave function is a Wannier function of the first band) couples predominantly to two atoms in the first band leading to the lowest avoided crossing in the spectrum. The two corresponding eigenenergies are given by a sum of the lowest COM energy $E_1^{\rm COM}$ $[E_n^{\rm COM} = \hbar\omega(n - \frac{1}{2} + \eta)]$ and the two

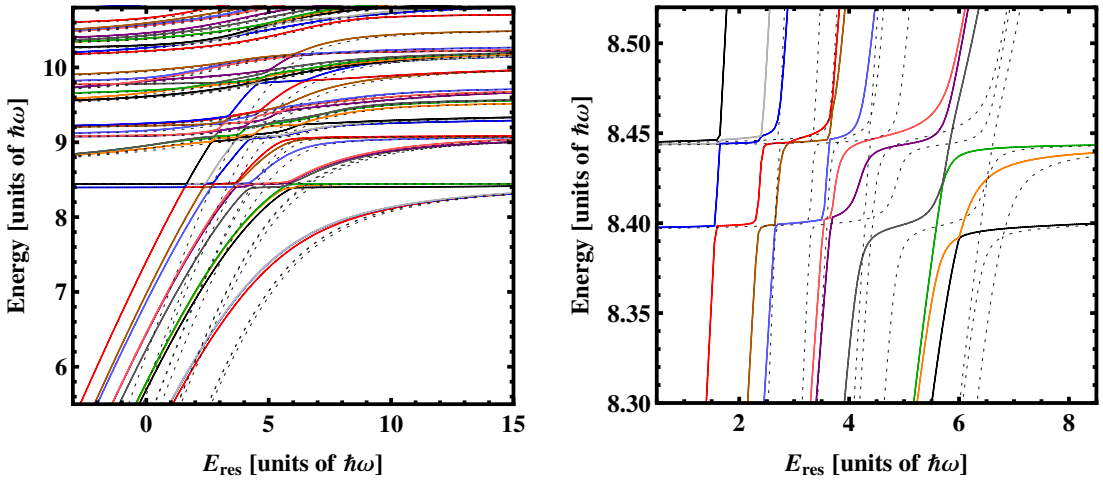

Figure 4.5: Energy spectrum of two atoms in an OL with lattice depth $V_\mathrm{L} = 5E_r = 1.1\,\hbar\omega$ consisting of three lattice sites with periodic boundary conditions. Excitations in transversal direction are frozen out by choosing transversal trapping frequencies $\omega_y = \omega_z = 3.8\omega$, where ω is the frequency of the harmonic approximation of a lattice site in x direction. The resonance parameters are $a_\mathrm{bg} = 85\,\mathrm{a.u.} = 9.0 \cdot 10^{-3} d$ and $\Delta E = 24.2\,\hbar\omega$, which corresponds to a coupling strength of $\chi = 1.66\,\hbar\omega = 1.48\,V_\mathrm{L}$ (See also the right graph in Fig. 4.9 with the same lattice parameters and resonance parameters). The comparison of the eigenenergies of the dressed BHM (solid lines) and the undressed BHM (dashed lines) each with four Bloch bands included, shows that again both models disagree especially for the bound states, while the differences for the trap states are small. The right graph shows a magnification of the spectrum close to the crossing of excited bound states with the lowest Bloch band.

lowest solutions E_1, E_2 of the REL motion eigenenergy relation (3.26), which depend on the bound-state energy $E_b = E_\mathrm{res}$. In order to match the energies of this avoided crossing, the bound-state energy E_b and the coupling strength g are replaced by dressed parameters $E_b \to E_d^{(1)}(E_\mathrm{res})$ and $g \to g_d(E_\mathrm{res})$. The two parameters are determined by a least-square fit to the energies $E_1 + E_0^\mathrm{COM}$ and $E_2 + E_0^\mathrm{COM}$.

To match the energies $E_1 + E_n^\mathrm{COM}$ with $n = 2, 3, \ldots$ of bound states in higher Bloch bands, dressed bound-state energies $E_d^{(2)}(E_\mathrm{res}), E_d^{(3)}(E_\mathrm{res}), \ldots$ are introduced, which are also determined by a least square fit. The upper branches of the avoided crossings with bound states in higher Bloch bands lay above the first Bloch band. Therefore, their correct representation is less relevant and there is no need to introduce also band-dependent dressed coupling strengths.

In Fig. 4.4 the dressed parameters $E_d^{(1)}, E_d^{(2)}, E_d^{(3)}, E_d^{(4)}$, and g_d and the corresponding corrected spectrum are shown for the four-band BHM with $a_\mathrm{bg} = 0.04\,a_\mathrm{ho}$ and $\Delta E = 16\,\hbar\omega$ (parameters of the right bottom graph in Fig. 4.2). Evidently, the dressing of the bound states becomes relevant for a resonance energy $E_\mathrm{res} < 5\,\hbar\omega$. Since only

a band-independent dressed coupling strength is introduced, the repulsive branches above the first Bloch band with an energy above $10\,\hbar\omega$ are not fitted to the exact results. Correspondingly, slight deviations between the exact energies and the dressed BHM energies appear for these states, while the first repulsive branch is correctly reproduced.

The introduced dressed parameters can now be used to determine the energy spectrum of two atoms in an OL. In Fig. 4.5 the spectrum of the dressed and undressed BHM of two atoms in a small OL consisting of three lattice sites are compared for a coupling energy of $\chi = 1.66\,\hbar\omega = 1.48\,V_\mathrm{L}$. In contrast to the purely harmonic trap, the energies of the bound states and trap states split due to tunnelling. If the molecular bound states are not in resonance, i.e. for $E_\mathrm{res} < 0$, the trap-state energies form bands around $8.4\,\hbar\omega$, $9.1\,\hbar\omega$, $9.8\,\hbar\omega$, and $10.4\,\hbar\omega$. For resonance energies $E_\mathrm{res} > 0$ the bound states cross with the trap states leading to a plethora of avoided crossings. In the ultracold regime especially the avoided crossings with the first band are of relevance. These appear due to the next-neighbor coupling of the molecular state with the atomic states [90]. As shown in the inset of Fig. 4.5 the width of those avoided crossings decreases with the COM excitation energy of the RBS. The comparison between the dressed and the undressed BHM shows that also in the OL the energies disagree especially for the bound states, while the energy differences for the trap states are small.

4.4. Non-perturbative determination of stationary states

In the following, the results of the BHM shall be compared to non-perturbative calculations for two atoms at an MFR in an OL consisting of two lattice sites. The corresponding numerical method, which is described in Ref. [86] will be further discussed in Sec. 5. At this point it is important to note that the method allows to find the stationary solutions of the two-body problem with arbitrary isotropic *single-channel* interaction potentials.

Since the lattice potential couples REL and COM motion and the interaction couples the motion in x, y and z direction, all six coordinates of the problem are coupled. An extension of the numerical approach to the coupling to an additional channel describing the COM and REL motion of the molecular bound state would make the solution very cumbersome. Instead, the freedom of the interaction potential is used to realistically mimic a two-channel problem by a square-well interaction potential. The potential supports bound states, which are weakly coupled by a barrier to the scattering states. As will be shown, this potential leads to an energy dependence of the scattering length, which is in very good agreement to the one of a two-channel description [see Eq. (3.17)]. This is already sufficient to realistically mimic an MFR since, as shown in Sec. 3, the energy dependence of the scattering length fully determines the energy spectrum and the wave function outside of the interaction range.

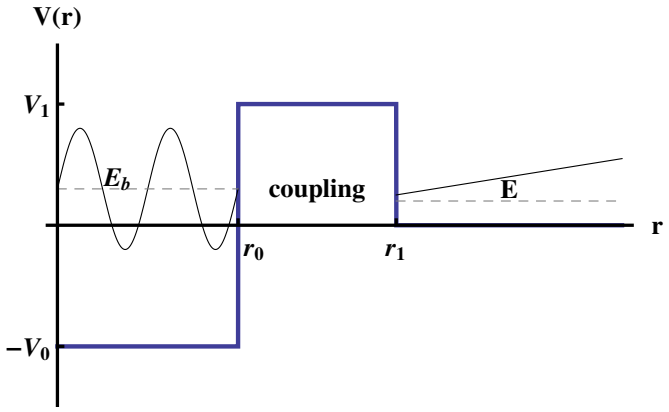

Figure 4.6: Sketch of the square well potential (thick blue). The resonant character of the potential is due to the coupling of a bound state with energy E_b (gray dashed) to an unbound state with energy E (gray dashed). The according wave functions are sketched by black thin lines. For $E_b \approx E$ the scattering length changes resonantly.

The square-well potential is defined as

$$V(r) = \begin{cases} -V_0 & \text{for } r \leq r_0 \\ +V_1 & \text{for } r_0 < r \leq r_1 \\ 0 & \text{for } r > r_1 \end{cases} \tag{4.21}$$

with $V_0, V_1 > 0$ (see Fig. 4.6). This potential has been previously used to study effects of the energy-dependence of the scattering length on the BEC-BCS crossover [91]. For sufficiently large V_0 the potential supports bound states behind a potential barrier of height V_1 and width $r_1 - r_0$. An atom pair that collides with an energy $E = \hbar^2 k^2/(2\mu)$ scatters resonantly, if E is close to a bound-state energy.

Introducing dimensionless variables $\rho = r/r_1$, $d = r_0/r_1$, $\kappa = kr_1$, $v_0 = V_0/E_0$, and $v_1 = V_1/E_0$ with $E_0 = \frac{\hbar^2}{2\mu r_1^2}$ the general solution of the Schrödinger equation for $E > 0$ is given as

$$\phi(\rho) = \begin{cases} C\sin[k_0\rho] & \text{for } \rho \leq d \\ Ae^{k_1\rho} + Be^{-k_1\rho} & \text{for } d < \rho \leq 1 \\ \sin\left[\kappa\rho + \delta(k)\right] & \text{for } \rho > 1 \end{cases} \tag{4.22}$$

with $k_0 = \sqrt{v_0 + \kappa^2}$ and $k_1 = \sqrt{v_1 - \kappa^2}$.

In the case of pure s-wave scattering one has $\kappa \ll 1$ so that one can make, e.g., the replacements $\sin(\kappa) \to \kappa$ and $\cos(\kappa) \to 1$. Eliminating A, B, and C by demanding that the wavefunction is continuous and differentiable the scattering length in the limit $\kappa \ll 1$ evaluates to

$$\frac{a(\kappa^2)}{r_1} \equiv -\frac{\tan\delta}{\kappa} = \frac{1 + \epsilon_{\text{res}}}{\epsilon_{\text{res}} - \kappa^2} \tag{4.23}$$

with

$$\epsilon_{\mathrm{res}} = k_1 \frac{\alpha+\beta}{\alpha-\beta}, \tag{4.24}$$

$$\alpha = e^{2dk_1}\left[k_0\cos(dk_0) - k_1\sin(dk_0)\right], \tag{4.25}$$

$$\beta = e^{2k_1}\left[k_0\cos(dk_0) + k_1\sin(dk_0)\right]. \tag{4.26}$$

From the functional behavior of Eq. (4.23) one can determine the corresponding parameters of the MFR, i.e. E_{res}, ΔE, and a_{bg}. The resonance positions of $a(\kappa^2)$ are given by the roots of $\kappa^2 = \epsilon_{\mathrm{res}}(\kappa^2)$. The smallest root shall be called $\kappa^2_{\mathrm{res}} = \epsilon(\kappa^2_{\mathrm{res}})$. Hence, the resonance position evaluates to

$$E_{\mathrm{res}} = E_0\kappa^2_{\mathrm{res}}. \tag{4.27}$$

According to Eq. (3.17) the scattering length is zero if $E = E_{\mathrm{res}} - \Delta E$. Be κ_0 the solution of $1 + \epsilon_{\mathrm{res}}(\kappa_0) = 0$ that is closest to κ_{res} then

$$\Delta E = E_0(\kappa^2_{\mathrm{res}} - \kappa^2_0). \tag{4.28}$$

In order to determine the value of the background scattering length a_{bg}, ϵ_{res} is expanded linearly in κ^2 around the resonance position, yielding

$$\epsilon_{\mathrm{res}}(\kappa^2) \approx \kappa^2_{\mathrm{res}} + \lambda(\kappa^2 - \kappa^2_{\mathrm{res}}) \tag{4.29}$$

$$\text{with} \quad \lambda = \left.\frac{\partial\epsilon_{\mathrm{res}}}{\partial(\kappa^2)}\right|_{\kappa=\kappa_{\mathrm{res}}}. \tag{4.30}$$

For $\kappa \to \kappa_{\mathrm{res}}$ the scattering length evaluates according to Eqs. (4.23) and (4.29) to

$$\frac{a(\kappa^2)}{r_1} = \frac{\frac{1}{\lambda-1}\left(\kappa^2_{\mathrm{res}}+1\right)}{\kappa^2_{\mathrm{res}} - \kappa^2}. \tag{4.31}$$

By comparing this with the behavior $a = a_{\mathrm{bg}}\Delta E/(E_{\mathrm{res}} - E)$ of Eq. (3.17) for $E \to E_{\mathrm{res}}$, one finds

$$a_{\mathrm{bg}} = r_1 \frac{E_{\mathrm{res}} + E_0}{\Delta E(\lambda-1)}. \tag{4.32}$$

For non-resonant background scattering the wavefunction simply falls off exponentially for $r < r_1$. Therefore, $a_{\mathrm{bg}} \lessapprox r_1$. Since the potential mimics an s-wave resonance, the choice for r_1 is limited to $kr_1 \ll 1$ and for energies $E \approx \hbar\omega$ to $r_1 \ll a_{\mathrm{ho}}$, allowing only for rather small positive background scattering lengths. On the other hand, one can freely choose E_{res} and ΔE by an appropriate choice of the parameters v_0 and v_1, respectively. In order to also control the background scattering length, one could add another square well with $V(r) < 0$ in front of the potential in Eq. (4.21). However, here the focus lies on the coupling to the RBS and not on the value of a_{bg}.

In Fig. 4.7 $a(\kappa^2)$ is shown for an exemplary square-well potential with $d = 0.6$ and

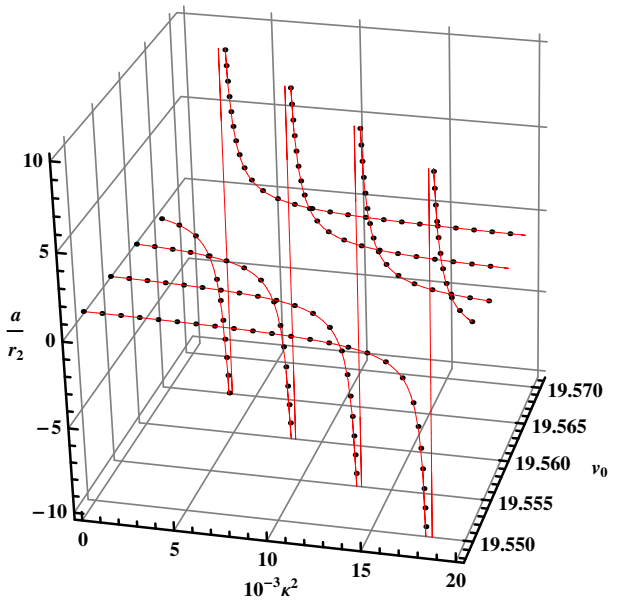

Figure 4.7: Energy-dependent scattering length of the square-well potential (dots) and approximation according to Feshbach theory (thin red) for $V_1 = 70\,E_0$ and $r_0/r_1 = 0.6$.

$v_1 = 70$. The values of $a(\kappa^2)$ according to Eq. (4.23) and its approximation

$$a = a_{\mathrm{bg}} \left(1 - \frac{\Delta E}{E_{\mathrm{res}} - E}\right) \tag{4.33}$$

with the parameters according to the equations (4.27), (4.28), and (4.32) agree almost perfectly, showing that the square-well potential reproduces very well the behavior of an MFR.

4.5. Comparison to non-perturbative calculations

Provided with the possibility to model MFRs with a single-channel potential one can apply the non-perturbative approach introduced in [86] to determine the energy spectrum of two atoms at an MFR in a small OL with a lattice spacing of $d = 500$ nm. Within the numerical approach one can expand the OL potential in all directions to some arbitrary order. Again, to avoid unnecessary complexity the OL is expanded to harmonic order around $y = z = 0$ in y and z direction and to 12-th order around $x = \pi/2$ in x direction. The lattice depth in y and z direction is chosen sufficiently large ($\omega_y = \omega_z = 3.8\omega$ where ω is the trap frequency of the harmonic approximation of the lattice wells in x direction) such that excitations in these directions can be ignored. The resulting double-well potential in x-direction is shown in Fig. 4.8.

While this system is relatively simple, it features all important properties of the optical lattice: the atoms and molecules can tunnel from one well to the other and also

onsite and nearest-neighbor interaction is present. Therefore, any flaw of the BHM regarding the interaction of two atoms should become apparent in the double well.

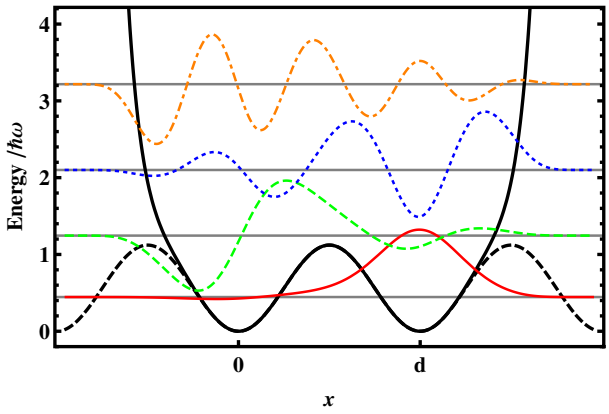

Figure 4.8: Double well potential (thick, solid) used in the *ab initio* calculations and corresponding full lattice potential $V_\mathrm{L}\sin^2(k_0x)$ (thick, dashed). The Wannier functions of the atoms in the BHM are depicted for bands one to four (red solid, green dashed, blue dotted and orange dot-dashed) alternately for the right and the left well. Already above the first band they clearly probe regions, where the double-well potential significantly differs from the full lattice potential. Horizontal lines mark the onsite energies of bands one to four.

For large lattice depths the spectrum converges to the one of two uncoupled harmonic traps. In order to probe the accuracy of the BHM, a relatively small lattice depth of $V_\mathrm{L} = 5\,E_r = 1.1\,\hbar\omega$ is chosen in x direction. For this low lattice depth excited states in higher Bloch bands probe parts of the potential, which significantly deviate from an ordinary lattice potential $V_\mathrm{L}\sin^2(k_0x)$. Therefore, the correct single-atom states deviate significantly from ordinary Wannier functions. This insufficiency can be corrected for by replacing the ordinary Wannier basis by a basis constructed from single-atom eigenstates in the double well. For each band n the left and right Wannier functions are constructed by superpositions of the n-th symmetric eigenstate with energy $E_n^{(\mathrm{even})}$ and the n-th anti-symmetric eigenstate with energy $E_n^{(\mathrm{odd})}$. The corresponding atomic Wannier functions of the first four Bloch bands are shown in Fig. 4.8. As one can see they are neither symmetric nor anti-symmetric so that any selection rule for the BHM parameters (such as that of the coupling between the open and the closed channel) of the OL does not apply. The onsite energies are given as $\epsilon_n = \frac{1}{2}(E_n^{(\mathrm{odd})} + E_n^{(\mathrm{even})})$ and the hopping parameters as $J_n = \frac{1}{2}(E_n^{(\mathrm{odd})} - E_n^{(\mathrm{even})})$. The molecular Wannier functions and BHM parameters $\mathcal{E}_n$ and $\mathcal{J}_n$ are obtained in the same manner. Furthermore, to be sure that all errors are solely due to deficiencies of the representation of the Feshbach resonance in the BHM, also next-neighbor background interaction is included.

The spectrum of the non-perturbative calculation for three different coupling strengths is compared in Fig. 4.9 to the corresponding dressed and non-dressed BHM spectrum.

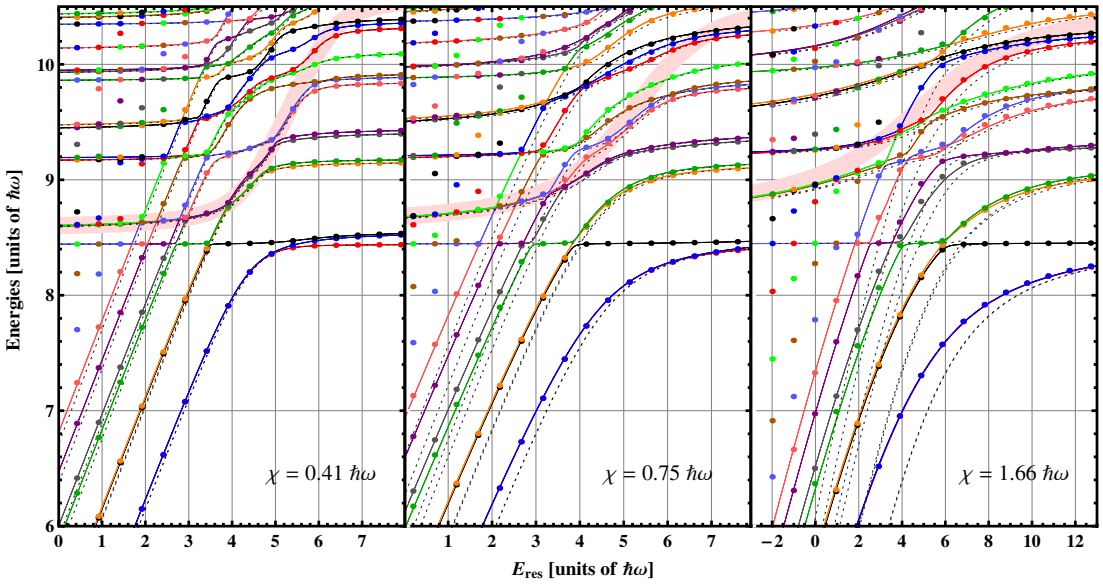

Figure 4.9: Spectra of the non-perturbative calculations (dots), the dressed BHM (lines) and the undressed BHM (dotted lines). The non-perturbative calculations include the representation of bound states with many COM excitations. Of course, not all of these bound states can be represented by the BHM that only includes four Bloch bands. For example, in the right graph all non-perturbative energies for $7.4\,\hbar\omega < E < 8.4\,\hbar\omega$ and $E_{\mathrm{res}} < 0$ are not covered by the BHM. From left to right the parameters $a_{\mathrm{bg}} = (88, 87, 85)\,\mathrm{a.u.} = (9.3, 9.2, 9.0) \cdot 10^{-3} d$, $\Delta E = (1.4, 4.9, 24.2)\,\hbar\omega$ are chosen. This corresponds to a coupling strength of $\chi = (0.41, 0.75, 1.66)\,\hbar\omega = (0.36, 0.67, 1.48)\,V_{\mathrm{L}}$. The red shading marks the energy of the repulsively interacting atoms within a single-band approximation. From left to right the energy of this state is significantly influenced by the bound state in the second, third and fourth Bloch band demonstrating that for stronger coupling bound states in more and more Bloch bands have to be included to obtain accurate eigenenergies.

In contrast to Fig. 4.5 the trap states do not form energy bands due to the reduced size of the system. The bound states appear as duplets with one symmetric and one antisymmetric COM excitation in x direction. Again, excited bound states in higher Bloch bands are able to couple to the first trap state (lowest horizontal line) by next-neighbor coupling, i.e. the bound state couples to a state of one atom in the same well and one in the neighboring well. For symmetry reasons only the lower bound state of each dublet can couple to the lowest symmetric trap state [90].

Fig. 4.10 shows a detailed view onto two of these avoided crossings around $E = 8.4\,\hbar\omega$ for a resonance energy of $E_{\mathrm{res}} = 2.9\,\hbar\omega$ and $E_{\mathrm{res}} = 3.9\,\hbar\omega$, respectively. Clearly, the splitting of the avoided crossing and hence also the next-neighbor coupling strength is

well reproduced by the BHM.

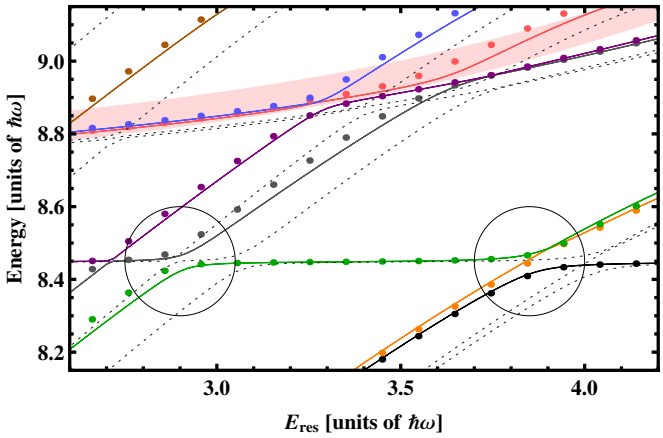

Figure 4.10: Zoom on the resonance of the bound state in the second Bloch band (right circle) and third Bloch band (left circle) with the state of two separated atoms in the ground state for $\chi = 0.75\,\hbar\omega$. The splitting energies of the left resonance ($0.04\,\hbar\omega$) and that of the right resonance ($\Delta = 0.06\,\hbar\omega$) are well reproduced by the dressed BHMs.

Given the large degree of anharmonicity of the lattice potential the agreement between the non-perturbative spectra and BHM spectra in Figs. 4.9 and 4.10 is surprisingly good. The dressed bound-state energies are obtained from a harmonic approximation of the two lattice sites. Already in the second Bloch band the potential and therefore the states and energies differ significantly from their harmonic counterparts (see Fig. 4.8). Nevertheless, the dressed bound-state energies and the dressed coupling strength lead to a significant improvement of the undressed results in all three cases shown in Fig. 4.9.

In general, the dressed parameters should lead to an improvement as long as the couplings of the bound states to trap states that probe anharmonic parts of the potential, i.e. with energies above $E = V_\mathrm{L}$, is negligible. Approximately, for $\chi \geq V_\mathrm{L}$ this is not the case any more since at the avoided crossing of the lowest bound state with the lowest trap state an energy regime above V_L is entered. Indeed, considering the spectrum with the largest coupling energy $\chi = 1.48 V_\mathrm{L} = 1.66\,\hbar\omega$, the lowest bound-state energy of the BHM is slightly lower than that of the non-perturbative calculations. But still the disagreement is surprisingly small. As one can expect, the correction of the bound-state energies in the third and fourth Bloch band is less accurate than that of the first and second Bloch band. Already for the lower coupling energies of $\chi = 0.36 V_\mathrm{L} = 0.41\,\hbar\omega$ and $\chi = 0.67\,V_\mathrm{L} = 0.75\,\hbar\omega$ small disagreements between the corresponding eigenenergies of the non-perturbative calculations and the corrected BHM appear.

The requirement of a maximal coupling energy $\chi \sim V_\mathrm{L}$ for the dressed BHM to be valid corresponds usually to MFRs of small up to medium width. As derived in Sec. 3.1.4, in the more usual case of $a_\mathrm{bg} \ll a_\mathrm{ho}$ an MFR in a harmonic trap is broad if $a_\mathrm{bg}\Delta E \gg a_\mathrm{ho}\hbar\omega$. Since χ is a measure for the coupling strength leading to the

avoided crossing of the lowest bound state with the first band, it is comparable to $\sqrt{a_{\mathrm{bg}}\Delta E\hbar\omega/a_{\mathrm{ho}}}$ in the harmonic trap [see Eq. (3.35)]. Therefore, an MFR is broad if $[\chi/(\hbar\omega)]^2 \gg 1$. Since the BHM is valid for $\chi \sim V_{\mathrm{L}}$ it can only accurately describe broad MFRs in a very deep lattice with $[V_{\mathrm{L}}/(\hbar\omega)]^2 = V_{\mathrm{L}}/(4E_r) \gg 1$.

The coupling of the two atoms in the lowest Bloch band to the bound state in the lowest Bloch band leads to the appearance of both attractively and repulsively interacting states. The energy of the repulsively interacting state is marked by the red shading in Figs. 4.9 and 4.10. For the medium coupling energy $\chi = 0.75\,\hbar\omega$ Fig. 4.10 shows that the dressed BHM reproduces correctly the energy of the repulsively interacting state while the undressed model underestimates its energy. As one can see in Fig. 4.9, for larger and larger coupling energy χ the repulsively interacting state is strongly influenced by bound states in increasingly higher Bloch bands. If the energy range of the repulsively interacting states shall be correctly reproduced at the resonance, this sets a lower limit for the number of Bloch bands that must be included in the BHM. Already for $\chi = 1.66\,\hbar\omega$ COM-excited bound states in all four included Bloch bands influence the repulsively interacting atoms highlighting again the importance of a multi-band description of atoms at an MFR.

Part II.

Dynamic behavior of atoms in an optical lattice

5. Time propagation of two atoms in an optical lattice

The knowledge of the stationary solutions of interacting atoms already gives some insights also into the dynamical behavior of the system. If a system parameter changes sufficiently slowly, i.e. adiabatically, the system always stays in the same eigenstate. As shown in Sec. 3.1.4, applying the Landau-Zener formula at a narrow avoided crossing, also diabatic changes can be described with the knowledge of the eigenenergies. In general, however, a perturbation of the system couples many eigenstates and requires to solve the time-dependent Schrödinger equation.

In the following a numerical method is introduced that solves the full time-dependent six-dimensional Schrödinger equation of two interacting atoms in a single-well or multiple-well OL that can be perturbed by any additional time-dependent potential up to quadratic order in the spacial coordinates. The numerical method was published in Ref. [27] (Publication IV).

The general problem of a precise description of interacting atoms in trapping potentials is the existence of two very distinct length scales: that of the short-range interaction (100 a.u.) and that of the trapping potential (10 000 a.u.). Within the Born-Oppenheimer approximation the employed basis functions have to cover the highly oscillating behavior in the interaction range [see Fig. 2.1 for exemplary singlet and triplet wave functions in the interaction range of ^{6}Li-^{87}Rb] and the slow variation due to the trap. The use of an uncorrelated basis such as a regular grid or products of single-particle solutions is therefore impractical. The numerical demands can be reduced to some extend if one replaces the Born-Oppenheimer potential by the appropriate Fermi-Huang pseudo potential, which supports only a single bound state. In this case one ignores the energy-dependence of the scattering length induced by the long-range behavior of the Born-Oppenheimer potential [see Eq. (3.14) in Sec. 3.1.2]. However, even then the use of an uncorrelated basis necessitates to regularize the delta-like potential [e.g., like in Eq. 4.20 in Sec. 4.3], which requires to resolve a short-range potential by the chosen basis functions.

The problem of describing both the short-range interaction and the behavior in the trap is approached by expanding the time-dependent wave functions in a basis of stationary solutions of two atoms in the lattice potential. Within the approach the atoms are allowed to interact via any central interaction potential. The stationary solutions are obtained by a procedure introduced by Grishkevich et al. [86]. Within this procedure the Hamiltonian is first separated into REL and COM motion. The different length scales are covered by expanding the REL and COM wave functions in spherical harmonics and a flexible basis of B splines for the radial part. In a configuration-interaction procedure the eigenfunctions of the REL and COM part are used to determine the

eigenfunctions of the full lattice Hamiltonian. These eigenfunctions are subsequently used as a basis for the propagation of the time-dependent wave function.

After the introduction of the stationary-lattice Hamiltonian the basis functions used to determine the stationary solutions are shortly introduced. A more exhaustive discussion on this subject is given in Ref. [86]. In Sec. 5.2 the time-propagation method is described. Afterwards the results of the time propagation are validated by a comparison to problems that possess an analytical solution. The numerical method is used to analyse a system of ^{6}Li-^{7}Li within Born-Oppenheimer approximation in a three-well OL that is perturbed by an acceleration and an additional harmonic confinement. Finally, the method is applied to validate the dynamical behavior of two atoms at an MFR predicted by a time propagation of the BHM introduced in Chapter 4.

5.1. Stationary Hamiltonian and its eigensolutions

The Hamiltonian

$$\hat{\mathrm{H}}(t) = \hat{\mathrm{H}}_0 + \hat{\mathrm{W}}(t) \tag{5.1}$$

considered in the following consists of a time-dependent part $\hat{\mathrm{W}}(t)$ (specified below) and a stationary part

$$H_0(\vec{r}_1, \vec{r}_2) = -\frac{\hbar^2 \nabla^2_{r_1}}{2m_1} - \frac{\hbar^2 \nabla^2_{r_2}}{2m_2} + V^{(1)}_{\mathrm{lat}}(\vec{r}_1) + V^{(2)}_{\mathrm{lat}}(\vec{r}_2) + V_{\mathrm{int}}(\vec{r}_1 - \vec{r}_2), \tag{5.2}$$

which describes two particles $i = 1, 2$ with mass m_i interacting via the potential $\hat{\mathrm{V}}_{\mathrm{int}}$. $\nabla^2_{r_i}$ is the Laplace operator with respect to $\vec{r}_i$. Within Born-Oppenheimer approximation the isotropic interaction potential $V_{\mathrm{int}}(\vec{r}_1 - \vec{r}_2) = V_{\mathrm{int}}(|\vec{r}_1 - \vec{r}_2|)$ is described by an often only numerically given Born-Oppenheimer potential. The trapping potential

$$V^{(i)}_{\mathrm{lat}}(\vec{r}_i) = \sum_{u=x,y,z} V^{(i)}_u \sin^2(k_u u_i) \tag{5.3}$$

is that of an OL formed by three counter-propagating laser beams with wave vector k_u in u direction ($u = x, y, z$). As discussed in Chap. 4 the lattice depth $V^{(i)}_u$ is proportional to the laser intensity in direction u and the polarizability of particle i.

The eigenfunctions of the lattice potential V_{lat} spread over infinitely many lattice sites. However, within the numerical approach only wave functions with finite extension can be expressed. Therefore, a potential $\tilde{V}_{\mathrm{lat}}$ is considered, which is defined by an expansion of V_{lat} to some specific order into a Taylor series in all three directions. Only expansions of order $2(2n+1)$ are relevant, since they lead to lattice potentials $\tilde{V}_{\mathrm{lat}}$ with $\tilde{V}_{\mathrm{lat}}(\vec{r}) \to \infty$ for $|\vec{r}| \to \infty$. Hence, all eigenfunctions occupy only a limited number of lattice sites and decay exponentially for $|\vec{r}| \to \infty$. Fig. 5.1 shows the case of a 22-nd order expansion of $V_x \sin^2(k_x x)$, which results in a triple-well potential.

The trapping potential V_{lat} of an OL (and also $\tilde{V}_{\mathrm{lat}}$) has orthorhombic symmetry, which is characterized by the point group D_{2h}. By adapting the basis functions to this symmetry, the eigenfunctions and the time-dependent wave function can be determined more efficiently. The symmetry of the problem is discussed in depth in Ref. [86]. Here,

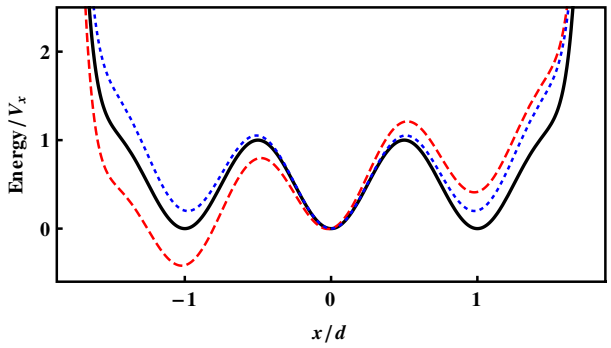

Figure 5.1: The 22nd-order expansion $\tilde{V}_{\rm lat}(x, y = 0, z = 0)$ of the lattice potential $V_{\rm lat}(x, y = 0, z = 0)$ in x-direction (solid line). Lengths are given in units of the lattice spacing $d = \pi/k_x$. A linear perturbation as it appears, e.g., for an acceleration of the lattice in x direction leads to an inclination of the lattice sketched by the red dashed line, while an additional harmonic confinement raises the left and right lattice site (blue dotted line).

only the essential points are repeated.

The symmetry operations of D_{2h} are

$$\mathcal{S} = \{E,\ C_2(x),\ C_2(y),\ C_2(z),\ \sigma(xy),\ \sigma(xz),\ \sigma(yz),\ i\}\ , \tag{5.4}$$

where E is the identity, $C_n(u)$ is the rotation about $\frac{2\pi}{n}$ around the u axis ($u = x, y, z$), $\sigma(u_1u_2)$ the reflection on the (u_1, u_2) plane and i the inversion (i.e. point reflection at the origin). The group D_{2h} possesses eight irreducible representations Γ_σ with

$$\sigma \in \{A_g, B_{1g}, B_{2g}, B_{3g}, A_u, B_{1u}, B_{2u}, B_{3u}\}\ . \tag{5.5}$$

The characters of these irreducible representations are listed in Table 5.1. Since the interaction potential $V_{\rm int}(\vec{r})$ is invariant under any operation in $\mathcal{S}$, also the full unperturbed Hamiltonian $\hat{\rm H}_0$ belongs to the D_{2h} point group if the symmetry operations are performed on both coordinates $\vec{r}_1$ and $\vec{r}_2$ simultaneously.

In order to find the eigensolutions of $\hat{\rm H}_0$, the system is split into REL and COM coordinates,

$$\vec{r} = (r_x, r_y, r_z)^T = \vec{r_1} - \vec{r_2}\ , \quad \vec{R} = (R_x, R_y, R_z)^T = \frac{m_1\vec{r_1} + m_2\vec{r_2}}{m_1 + m_2}. \tag{5.6}$$

With this separation, the Hamiltonian is written as

$$H_0(\vec{R}, \vec{r}) = H_{\rm COM}(\vec{R}) + H_{\rm REL}(\vec{r}) + H_{\rm coupl}(\vec{R}, \vec{r})\ , \tag{5.7}$$

where $\hat{\rm H}_{\rm COM}$, $\hat{\rm H}_{\rm REL}$, and $\hat{\rm H}_{\rm coupl}$ still have D_{2h}-symmetry [86]. Since the symmetry operations of D_{2h} commute with the Hamiltonians, the eigenfunctions can be chosen such that their symmetry properties correspond to some irreducible representation Γ_σ of D_{2h}. In the following the REL [COM] eigenfunctions are denoted as $\phi_j^{(\sigma)}(\vec{r})$ [$\Psi_j^{(\sigma)}(\vec{R})$]

D_{2h}	E	$C_2(z)$	$C_2(y)$	$C_2(x)$	i	$\sigma(xy)$	$\sigma(xz)$	$\sigma(yz)$
A_g	1	1	1	1	1	1	1	1
B_{1g}	1	1	-1	-1	1	1	-1	-1
B_{2g}	1	-1	1	-1	1	-1	1	-1
B_{3g}	1	-1	-1	1	1	-1	-1	1
A_u	1	1	1	1	-1	-1	-1	-1
B_{1u}	1	1	-1	-1	-1	-1	1	1
B_{2u}	1	-1	1	-1	-1	1	-1	1
B_{3u}	1	-1	-1	1	-1	1	1	-1

Table 5.1: Character table of the D_{2h} point group.

with $j = 1, 2, 3, \ldots$

The eigenfunctions of REL and COM are described in spherical coordinates and expanded in a basis of B splines B_α and symmetry-adapted superpositions of spherical harmonics Y_l^m and Y_l^{-m}. The B spline basis is characterized by their order and a flexible knot-sequence [92], which determines the density of the basis functions in a specific range. The implementation of Grishkevich et al. [86] allows for linear distributions, geometrical distributions and certain combinations of both. For example, the REL radial wave function in the presence of a Born-Oppenheimer interaction and an OL potential can be well represented by a linear sequence in the highly oscillatory interaction range ($0 \leq r \leq 15\,\text{a.u.}$), a geometrically descending sequence in the van der Waals tail ($15\,\text{a.u.} < r \lessapprox 200\,\text{a.u.}$), and again a linear sequence for larger interatomic distances. In order to be able to represent the wave function in the square-well interaction potential that was introduced in Sec. 4.4 for mimicking the behavior at an MFR, the implementation of possible knot sequences had to be extended. Especially the discontinuities of the square-well potential have to be well resolved by the basis functions since they crucially influence the energy dependence of the scattering length. Combinations of 5 linear zones with high and low B-spline density in the interaction range allow for converging the wave function with only about 35 B splines of order 8. A Born-Oppenheimer interaction of alkali-metal atoms requires usually more than 60 B splines of the same order to reach convergence.

In a configuration-interaction procedure products of eigensolutions of $\hat{\mathrm{H}}_{\mathrm{COM}}$ and $\hat{\mathrm{H}}_{\mathrm{REL}}$, i.e. configurations, are used to diagonalize the full Hamiltonian $\hat{\mathrm{H}}_0$. Because all irreducible representations of D_{2h} are one dimensional, the direct product of two irreducible representations $\Gamma_\kappa \otimes \Gamma_\lambda$ is again an irreducible representation Γ_σ that can be determined from the product table 5.2. Hence, each configuration $\Psi_i^{(\kappa)}(\vec{R})\phi_j^{(\lambda)}(\vec{r})$ has the symmetry properties of the related irreducible representation $\Gamma_\sigma = \Gamma_\kappa \otimes \Gamma_\lambda$.

The full solutions of a given symmetry σ has the form of a superposition

$$\Phi_\sigma(\vec{R},\vec{r}) = \sum_{\{\kappa,\lambda\}\in\sigma} \sum_{ij} \mathcal{C}_{ij}^{(\kappa,\lambda)} \Psi_i^{(\kappa)}(\vec{R}) \phi_j^{(\lambda)}(\vec{r}\,)\,, \tag{5.8}$$

where $\{\kappa,\lambda\} \in \sigma$ should indicate that the summation is performed over irreducible representations that fulfill $\Gamma_\kappa \otimes \Gamma_\lambda = \Gamma_\sigma$.

When considering identical bosonic (fermionic) particles the REL wave function has to be symmetric (antisymmetric) under inversion, i.e. only basis functions of REL motion with $\lambda \in \{A_g, B_{1g}, B_{2g}, B_{3g}\}$ ($\lambda \in \{A_u, B_{1u}, B_{2u}, B_{3u}\}$) are used to form configurations. The wave functions, i.e. the coefficients $C_{ij}^{(\kappa,\lambda)}$ in Eq. (5.8), are finally determined by solving the eigenvalue problem

$$\hat{\mathrm{H}}_0 |\Phi_i^{(\sigma)}\rangle = E_i^{(\sigma)} |\Phi_i^{(\sigma)}\rangle \tag{5.9}$$

of $\hat{\mathrm{H}}_0$ in the configuration basis.

$\otimes$	A_g	B_{1g}	B_{2g}	B_{3g}	A_u	B_{1u}	B_{2u}	B_{3u}
A_g	A_g	B_{1g}	B_{2g}	B_{3g}	A_u	B_{1u}	B_{2u}	B_{3u}
B_{1g}	B_{1g}	A_g	B_{3g}	B_{2g}	B_{1u}	A_u	B_{3u}	B_{2u}
B_{2g}	B_{2g}	B_{3g}	A_g	B_{1g}	B_{2u}	B_{3u}	A_u	B_{1u}
B_{3g}	B_{3g}	B_{2g}	B_{1g}	A_g	B_{3u}	B_{2u}	B_{1u}	A_u
A_u	A_u	B_{1u}	B_{2u}	B_{3u}	A_g	B_{1g}	B_{2g}	B_{3g}
B_{1u}	B_{1u}	A_u	B_{3u}	B_{2u}	B_{1g}	A_g	B_{3g}	B_{2g}
B_{2u}	B_{2u}	B_{3u}	A_u	B_{1u}	B_{2g}	B_{3g}	A_g	B_{1g}
B_{3u}	B_{3u}	B_{2u}	B_{1u}	A_u	B_{3g}	B_{2g}	B_{1g}	A_g

Table 5.2: Product table of irreducible representations of the D_{2h} point group.

5.2. Solution of the time-dependent Schrödinger equation

The time-dependent Schrödinger equation

$$\begin{gathered}\left(\hat{\mathrm{H}}_0 + \hat{\mathrm{W}}(t)\right) |\Psi(t)\rangle = i\hbar \frac{\partial}{\partial t} |\Psi(t)\rangle \\ \text{with} \quad |\Psi(t=0)\rangle = |\Psi_0\rangle\end{gathered} \tag{5.10}$$

is solved in the basis $\{\Phi_i^{(\sigma)}\}$ of eigenfunctions of $\hat{\mathrm{H}}_0$ of Eq. (5.9),

$$|\Psi(t)\rangle = \sum_{\sigma i} \mathcal{B}_{\sigma i}(t) |\Phi_i^{(\sigma)}\rangle\,. \tag{5.11}$$

Plugging Eq. (5.11) into Eq. (5.10) and multiplying from the left by $\langle\Phi_j^{(\kappa)}|$ leads to the equation

$$i\hbar\frac{\partial\mathcal{B}_{\kappa j}(t)}{\partial t} = E_j^{(\kappa)}\mathcal{B}_{\kappa j}(t) + \sum_{\sigma i}\mathcal{B}_{\sigma i}(t)\langle\Phi_j^{(\kappa)}|\hat{\mathrm{W}}(t)|\Phi_i^{(\sigma)}\rangle \tag{5.12}$$

for the evolution of the time-dependent coefficients $\mathcal{B}_{\kappa j}(t)$, which is governed by the matrix elements $\mathcal{P}_{ij}^{(\kappa,\sigma)} = \langle\Phi_j^{(\kappa)}|\hat{\mathrm{W}}(t)|\Phi_i^{(\sigma)}\rangle$ of the perturbation. An important part of the numerical method consists of calculating all non-zero matrix elements $\mathcal{P}_{ij}^{(\kappa,\sigma)}$

Considering the expansions of the m-th and n-th eigenstate

$$\begin{aligned}|\Phi_m^{(\tau)}\rangle &= \sum_{\{\kappa,\lambda\}\in\tau}\sum_{ij}\mathcal{C}_{ij}^{(\kappa,\lambda)}|\Psi_i^{(\kappa)}\rangle|\phi_j^{(\lambda)}\rangle \\ |\Phi_n^{(\sigma)}\rangle &= \sum_{\{\mu,\nu\}\in\sigma}\sum_{kl}\mathcal{C}'^{(\mu,\nu)}_{kl}|\Psi_k^{(\mu)}\rangle|\phi_l^{(\nu)}\rangle\,,\end{aligned} \tag{5.13}$$

which depend on the coefficients $\mathcal{C}_{ij}^{(\kappa,\lambda)}$ and $\mathcal{C}'^{(\mu,\nu)}_{kl}$, respectively, the matrix elements of a perturbation are

$$\begin{aligned}\mathcal{P}_{mn}^{(\tau,\sigma)} =&\langle\Phi_m^{(\tau)}|\hat{\mathrm{W}}(t)|\Phi_n^{(\sigma)}\rangle \\ =&\sum_{\{\kappa,\lambda\}\in\tau}\sum_{ij}\sum_{\{\mu,\nu\}\in\sigma}\sum_{kl}\left(\mathcal{C}_{ij}^{(\kappa,\lambda)}\right)^*\mathcal{C}'^{(\mu,\nu)}_{kl} \\ &\times\langle\phi_j^{(\lambda)}|\langle\Psi_i^{(\kappa)}|\hat{\mathrm{W}}(t)|\Psi_k^{(\mu)}\rangle|\phi_l^{(\nu)}\rangle\,.\end{aligned} \tag{5.14}$$

In general, the perturbation $\hat{\mathrm{W}}(t)$ can be expanded in a time-dependent Taylor series of its spacial coordinates

$$\hat{\mathrm{W}}(t) = \sum_{ij}\sum_{u=x,y,z}\sum_{u'=x,y,z} f_{nm}^{(u,u')}(t)\,\hat{\mathrm{R}}_u^n\,\hat{\mathrm{r}}_{u'}^m\,, \tag{5.15}$$

where r_u (R_u) is the component of the REL (COM) motion in u direction ($u = x, y, z$).

At the present stage perturbations in x direction of the general form

$$\begin{aligned}\hat{\mathrm{W}}(t) =&f_{01}(t)\,\hat{\mathrm{r}}_x + f_{10}(t)\,\hat{\mathrm{R}}_x + f_{11}(t)\,\hat{\mathrm{r}}_x\hat{\mathrm{R}}_x \\ &+ f_{02}(t)\,\hat{\mathrm{r}}_x^2 + f_{20}(t)\,\hat{\mathrm{R}}_x^2\end{aligned} \tag{5.16}$$

are implemented. The method can be easily extended to allow for perturbations in other directions and of higher orders.

In order to illustrate how the perturbation matrix is computed, the case of a linear perturbation $\hat{\mathrm{W}} = f_{10}(t)\hat{\mathrm{R}}_x$ is discussed in more detail. This perturbation does not couple the orthonormal REL basis functions $|\phi_j^{(\lambda)}\rangle$. Thus, the summations in Eq. (5.14)

reduce to

$$\begin{aligned}\mathcal{P}_{mn}^{(\tau,\sigma)} =& f_{10}(t) \sum_{\{\kappa,\lambda\}\in\tau} \sum_{ij} \sum_{\{\mu,\lambda\}\in\sigma} \sum_{k} \left(\mathcal{C}_{ij}^{(\kappa,\lambda)}\right)^* \mathcal{C}'^{(\mu,\lambda)}_{kj} \\ & \langle \Psi_i^{(\kappa)} | \hat{\mathrm{R}}_x | \Psi_k^{(\mu)} \rangle \,.\end{aligned} \tag{5.17}$$

In the following the term $\langle \Psi_i^{(\kappa)} | \hat{\mathrm{R}}_x | \Psi_k^{(\mu)} \rangle$ is considered for the exemplary case of $\kappa = A_g$. In this case the wave function $\Psi_i^{(\kappa)}(\vec{R}\,)$ is totally symmetric (see Table 5.1). Hence, $\Psi_k^{(\mu)}(\vec{R}\,)$ needs to be anti-symmetric in x direction and symmetric otherwise, which is fulfilled solely for $\mu = B_{3u}$. In all other cases the integral vanishes. The according COM basis functions are represented as

$$\begin{aligned}\Psi_i^{(A_g)}(R,\Theta,\Phi) &= \sum_{\alpha=1}^{N_\alpha} \sum_{l=0,\{2\}}^{N_l} \sum_{m=0,\{2\}}^{l} c_{i,\alpha lm}^{(A_g)} \frac{B_\alpha(R)}{R} \mathscr{Y}_{lm}^{+}(\Theta,\Phi) \\ \Psi_k^{(B_{3u})}(R,\Theta,\Phi) &= \sum_{\alpha=1}^{N_\alpha} \sum_{l=1,\{2\}}^{N_l} \sum_{m=1,\{2\}}^{l} c_{k,\alpha lm}^{(B_{3u})} \frac{B_\alpha(R)}{R} \mathscr{Y}_{lm}^{-}(\Theta,\Phi)\,,\end{aligned} \tag{5.18}$$

where $\mathscr{Y}_{lm}^{\pm}(\Theta,\Phi) = Y_l^m(\Theta,\Phi) \pm Y_l^{-m}(\Theta,\Phi)$ are a sum of spherical harmonics for $m \neq 0$, $\mathscr{Y}_{l0}^{\pm}(\Theta,\Phi) = Y_l^0(\Theta,\Phi)$, and B_α are B splines (see Ref. [86] for details). The number in curly brackets below the sums indicates the summation step. N_l and N_α are variable values of maximal angular momentum and the number of B splines, respectively. With $R_x = R\sin\Theta\cos\Phi$ one finds

$$\begin{aligned}&\langle \Psi_i^{(\kappa)} | \hat{\mathrm{R}}_x | \Psi_k^{(\mu)} \rangle \\ &\quad= \sum_{l=0,\{2\}}^{l} \sum_{m=0,\{2\}} \sum_{l'=1,\{2\}}^{l'} \sum_{m'=1,\{2\}} \sum_{\alpha\alpha'} \left(c_{i,\alpha lm}^{(A_g)}\right)^* c_{k,\alpha lm}^{(B_{3u})} \\ &\qquad\times \int \mathrm{d}R\; B_\alpha(R) R B_{\alpha'}(R) \\ &\qquad\times \int_0^\pi \sin\Theta\,\mathrm{d}\Theta \int_0^{2\pi} \mathrm{d}\Phi \left(\mathscr{Y}_{lm}^{+}\right)^* \sin\Theta\cos\Phi \mathscr{Y}_{lm}^{-}\,.\end{aligned} \tag{5.19}$$

The integral over the angles Θ and Φ can be simplified by using

$$\begin{aligned}&\int_0^\pi \sin\Theta\,\mathrm{d}\Theta \int_0^{2\pi} \mathrm{d}\Phi\; Y_{l_1}^{m_1}(\Theta,\Phi) Y_{l_2}^{m_2}(\Theta,\Phi) Y_{l_3}^{m_3}(\Theta,\Phi) \\ &\quad= \sqrt{\frac{(2l_1+1)(2l_3+1)(2l_3+1)}{4\pi}} \begin{pmatrix} l_1 & l_2 & l_3 \\ 0 & 0 & 0 \end{pmatrix} \begin{pmatrix} l_1 & l_2 & l_3 \\ m_1 & m_2 & m_3 \end{pmatrix},\end{aligned} \tag{5.20}$$

where $\begin{pmatrix} l_1 & l_2 & l_3 \\ m_1 & m_2 & m_3 \end{pmatrix}$ is the Wigner 3j-symbol. With $(Y_l^m)^* = (-1)^m Y_l^{-m}$ and

$$\sin\Theta\cos\Phi = \sqrt{\frac{2\pi}{3}}\left[Y_1^{-1}(\Theta,\Phi) - Y_1^1(\Theta,\Phi)\right] \tag{5.21}$$

this yields

$$\begin{aligned}\int_0^\pi \sin\Theta\,\mathrm{d}\Theta \int_0^{2\pi} \mathrm{d}\Phi\ \left[Y_{l_1}^{m_1}(\Theta,\Phi)\right]^* \sin\Theta\cos\Phi\ Y_{l_2}^{m_2}(\Theta,\Phi)& \\ =(-1)^{m_1}\sqrt{\frac{(2l_1+1)(2l_2+1)}{2}}\begin{pmatrix} l_1 & l_2 & 1 \\ 0 & 0 & 0\end{pmatrix}& \\ \times\left[\begin{pmatrix} l_1 & l_2 & 1 \\ -m_1 & m_2 & -1\end{pmatrix} - \begin{pmatrix} l_1 & l_2 & 1 \\ -m_1 & m_2 & 1\end{pmatrix}\right],&\end{aligned} \tag{5.22}$$

which can be efficiently computed. The other types of perturbations in Eq. (5.16) are treated in an analogous way.

Since the system is six dimensional the analysis in terms of the full time-dependent wave function is nontrivial. However, equipped with the matrix elements of all perturbations, $\langle\Phi_i^{(\kappa)}|\hat{\mathrm{R}}_x|\Phi_k^{(\mu)}\rangle$, $\langle\Phi_i^{(\kappa)}|\hat{\mathrm{R}}_x^2|\Phi_k^{(\mu)}\rangle$, $\langle\Phi_i^{(\kappa)}|\hat{\mathrm{r}}_x|\Phi_k^{(\mu)}\rangle$, $\langle\Phi_i^{(\kappa)}|\hat{\mathrm{r}}_x^2|\Phi_k^{(\mu)}\rangle$, and $\langle\Phi_i^{(\kappa)}|\hat{\mathrm{R}}_x\hat{\mathrm{r}}_x|\Phi_k^{(\mu)}\rangle$ one can easily determine the expectation values of some of the most important observables. For example, the squared mean particle distance in x direction is given as

$$\begin{aligned}\left\langle r_x^2\right\rangle &= \left\langle\Psi(t)\right|\hat{\mathrm{r}}_x^2\left|\Psi(t)\right\rangle \\ &= \sum_{\sigma i}\sum_{\kappa j}\left[\mathcal{B}_{\sigma i}(t)\right]^*\mathcal{B}_{\kappa j}(t)\langle\Phi_i^{(\sigma)}|\hat{\mathrm{r}}_x^2|\Phi_j^{(\kappa)}\rangle\,.\end{aligned} \tag{5.23}$$

Likewise, one can determine the mean particle position or the uncertainty of the position in x direction.

5.3. Comparison with analytical results

In order to validate the numerical procedure, a comparison with analytical results is necessary, which are available for the harmonic approximation of the OL potential. In the case of two identical particles of mass m in a harmonic trap the system decouples into REL and COM motion with Hamiltonian [see Eq. 1.4 in Sec. 1.1]

$$H_0(\vec{R},\vec{r}) = -\frac{\hbar^2\nabla_R^2}{2M} + \frac{1}{2}M\omega^2R^2 - \frac{\hbar^2\nabla_r^2}{2\mu} + \frac{1}{2}m\omega^2r^2 + V_{\mathrm{int}}(r)\,, \tag{5.24}$$

where $M = 2m$ and $\mu = m/2$. In the following a linear perturbation $\hat{\mathrm{W}}_1(t) = f(t)\hat{\mathrm{R}}_x$ and a quadratic perturbation $\hat{\mathrm{W}}_2(t) = f(t)\hat{\mathrm{R}}_x^2$ are considered. This corresponds to

a time-dependent acceleration and a variation of the trapping frequency, respectively. Since the COM part of H_0 decouples into x, y, and z direction, only the COM harmonic oscillator in x direction with Hamiltonian

$$H_{\mathrm{ho}}(R_x) = -\frac{\hbar^2}{2M}\frac{\partial^2}{\partial R_x^2} + \frac{1}{2}M\omega^2 R_x^2 = \hbar\omega\left(-\frac{A_{\mathrm{ho}}^2}{2}\frac{\partial^2}{\partial R_x^2} + \frac{1}{2}\frac{R_x^2}{A_{\mathrm{ho}}^2}\right) \tag{5.25}$$

is affected by the perturbations. Here, $A_{\mathrm{ho}} = \sqrt{\hbar/(M\omega)}$ is the length of the COM harmonic oscillator.

Obviously, the interaction does not enter Eq. (5.25) and hence its correct implementation cannot be checked. However, the advantage of the applied spectral method is that the effect of the interaction is already fully included in the stationary eigenfunctions used as a basis in the time propagation. Since the correctness of these basis functions has been already checked in Ref. [86], it suffices to ensure the correct implementation of the perturbations and the convergence of the time propagation. In addition to the here presented perturbations in COM motion also perturbation in REL motion have been checked for non-interacting systems with results comparable to the ones shown below.

The comparisons are performed for expectation values of the position

$$\bar{X}(t) = \left\langle \hat{\mathrm{R}}_x \right\rangle = \left\langle \Psi(t) \middle| \hat{\mathrm{R}}_x \middle| \Psi(t) \right\rangle \tag{5.26}$$

and the mean deviation from $\bar{X}$

$$\sigma(t) = \sqrt{\left\langle \hat{\mathrm{R}}_x^2 \right\rangle - \left\langle \hat{\mathrm{R}}_x \right\rangle^2}\,. \tag{5.27}$$

5.3.1. Periodic driving

For the case of a periodically driven harmonic oscillator with driving strength C_{shake} and frequency ω_0, i.e.

$$\hat{\mathrm{W}}_1(t) = \hbar\omega\, C_{\mathrm{shake}}\, \cos(\omega_0 t)\, \frac{\hat{\mathrm{R}}_x}{A_{\mathrm{ho}}}\,, \tag{5.28}$$

there exists an analytic solution [93]

$$\psi_n(R_x, t) = e^{i\varphi(R_x,t)} h_n(R_x - \xi(t))\,, \tag{5.29}$$

where $\varphi(R_x, t)$ is a phase, which vanishes for $t = 0$, h_n is the n-th harmonic oscillator eigenstate of $\hat{\mathrm{H}}_{\mathrm{ho}}$, and

$$\xi(t) = \frac{A_{\mathrm{ho}} C_{\mathrm{shake}}}{1 - \omega_0^2/\omega^2}\cos(\omega_0 t). \tag{5.30}$$

In order to conform with the initial condition

$$\psi_n(R_x, 0) = h_n(R_x - \xi(0)) \tag{5.31}$$

the trap is shifted at $t = 0$ to $\xi(0)$ by instantly adding a constant linear perturbation

$$\hat{\mathrm{W}}_2 = -\hbar\omega\, C_{\mathrm{shake}}\, \frac{1}{1-\omega_0^2/\omega^2}\, \frac{\hat{\mathrm{R}}_x}{A_{\mathrm{ho}}}\,. \tag{5.32}$$

From the analytic solution one obtains straightforwardly

$$\bar{X}(t) = -A_{\mathrm{ho}} C_{\mathrm{shake}}\,[1-\cos(\omega_0 t)]\,, \quad \sigma(t) = \frac{A_{\mathrm{ho}}}{\sqrt{2}}. \tag{5.33}$$

In Fig. 5.2 a comparison of a numerical calculation of $\bar{X}(t)$ to the result in Eq. (5.33) shows very good agreement with deviations on the order of 10^{-10}. A similar accuracy is obtained for the value of $\sigma(t)$. The deviations are due to the finiteness of the basis which, in the shown calculation, only includes basis functions with an eigenenergy below the chosen cutoff of $20\,\hbar\omega$. The energy cutoff can be adapted to reach higher accuracies, if needed.

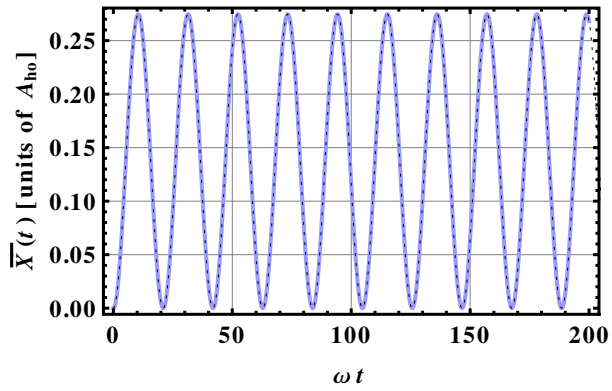

Figure 5.2: Comparison of analytical (blue solid) and numerical (black dashed) results for $\bar{X}(t)$ [see Eqs. (5.26) and (5.33)] for $C_{\mathrm{shake}} = 0.5$ and $\omega_0 = 0.3\,\omega$. The difference of the results is below 10^{-10} and therefore invisible. The width of the wave function $\sigma(t) = A_{\mathrm{ho}}/\sqrt{2}$ is numerically reproduced with the same level of accuracy.

5.3.2. Adiabatic deepening

The mean width of the wave function σ for an harmonic oscillator with oscillator length A_{ho} is given as $A_{\mathrm{ho}}/\sqrt{2}$ [see Eq. (5.33)]. Considering a time-dependent perturbation $\hat{\mathrm{W}}(t) = C_{\mathrm{harm}}\hbar\omega\hat{\mathrm{R}}_x^2/A_{\mathrm{ho}}^2\;\omega t$, the full potential is given as $\frac{1}{2}\hbar\omega R_x^2/A_{\mathrm{ho}}^2(1+2C_{\mathrm{harm}}\omega t)$. If C_{harm} is sufficiently small, the wave function will always remains in an eigenstate of a harmonic oscillator with a trap length

$$A_{\mathrm{ho}}(t) = A_{\mathrm{ho}}(t=0)/\sqrt{1+2C_{\mathrm{harm}}\omega t}\,. \tag{5.34}$$

Thus, assuming perfect adiabaticity, the width of the wave function behaves like

$$\sigma(t) = A_{\mathrm{ho}}/\sqrt{2(1 + 2C_{\mathrm{harm}}\omega t)}\,. \tag{5.35}$$

In Fig. 5.3 a comparison to the numerical calculations shows good agreement to this result with an error of about 5×10^{-5} for $C_{\mathrm{harm}} = 0.002$, which is due to nonadiabatic effects. For example, reducing the speed of the perturbation by setting $C_{\mathrm{harm}} = 0.001$ reduced the error to about 2×10^{-5}.

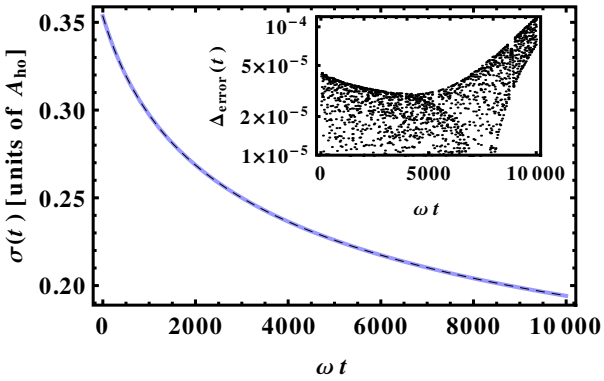

Figure 5.3: Comparison of analytical (blue solid) and numerical (black dashed) results for $\sigma(t)$ [see Eqs. (5.27) and (5.35)] for $C_{\mathrm{harm}} = 0.002$. The error $\Delta_{\mathrm{error}} = |\sigma - \sigma_{\mathrm{num}}|$ is shown in the inset. The relatively large error in comparison to the results shown in Fig. 5.2 is due to nonadiabatic effects. These effects get smaller for larger t since the change of $A_{\mathrm{ho}}(t)$ is reduced [see Eq. (5.34)]. For $\omega t > 5000$, however, the incompleteness of the basis used for the numerical calculations (only states with energies below $E = 20\,\hbar\omega$ are included) leads finally to an increase of Δ_{error}.

5.4. Example calculations for Li-Li

In order to demonstrate the possibility to perform time propagations within the Born-Oppenheimer approximation, a system of two distinguishable atoms, ^{6}Li and ^{7}Li, which interact via the Born-Oppenheimer potential for the scattering of spin-polarized lithium, is considered. As in Ref. [50] the data given in Ref. [94] are used for the short-range part of the corresponding $a^3\Sigma_u^+$ potential as well as the van der Waals coefficients and exchange coefficients cited in Ref. [94]. The atoms are confined in a three-site lattice potential $\tilde{V}_{\mathrm{lat}}$, which is realized by a 22nd order expansion of V_{lat} in Eq. (5.3) in x direction (see Fig. 5.1) and a harmonic approximation in y and z direction. The chosen wave vectors $k_x = k_y = k_z = 2\pi/(1000\,\mathrm{nm})$ lead to a lattice spacing of $d = 500\,\mathrm{nm} = 9450\,\mathrm{a.u.}$ A lattice depth in x direction of $V_x = 1.36\hbar\omega_1$, where ω_1 is the frequency of the harmonic approximation of the lattice for atom 1 (^{6}Li), results in the relatively small hopping energies $J_1 = 0.0066\hbar\omega_1$ of atom 1 and $J_2 = 0.0042\hbar\omega_1$ of atom 2 in the corresponding Hubbard model for the infinite lattice. Hence, even for

the relatively small s-wave scattering length of 41 a.u. of ^{6}Li-^{7}Li a correlated Mott-like state is formed, i.e. the atoms do not occupy the same lattice site in the ground state[1]. Since no unit filling of the lattice is considered, the atoms are nevertheless mobile in x direction. This enables the observation of a correlated motion of the distinguishable atoms. The lattice depths in y and z direction are given as $V_y = V_z \approx 8V_x$ such that for low-lying states motion in these directions is frozen out.

Despite the reduction to only three lattice sites, the considered system exhibits the basic mechanisms of hopping and onsite-interaction of atoms in an OL. Similar systems of only a few lattice sites appear also experimentally in superlattices [18].

5.4.1. Linear perturbation

First, the system is adiabatically inclined by a perturbation of the type $\hat{\mathrm{W}}(t) = At\hat{\mathrm{R}}_x$. Experimentally this can be realized by slowly increasing the acceleration of the lattice in x direction. In the co-moving frame of the lattice an acceleration leads to a conservative inertial force in $-x$ direction that can be represented by an additional potential that is proportional $m_1x_1 + m_2x_2$ and thus to the COM coordinate R_x.

The system starts in the ground state, where the atoms spread symmetrically over the lattice [see Fig. 5.4 (a)]. As a consequence, the mean atom position is exactly in the middle of the triple-well potential, i.e. at $x/d = 0$. Due to their repulsion the atoms never occupy the same lattice site. In this case their mean distance $\sqrt{\langle\, r_x^2 \,\rangle}$ is approximately d. The corresponding probability density along the x axis is shown in Fig. 5.4 (c).

Upon the slow inclination the system stays in the state of minimal energy. Thus, the heavier ^{7}Li atom slowly moves into the lower left lattice site (i.e. $\bar{x}_2 = \langle\, \hat{\mathrm{x}}_2 \,\rangle$ approaches $-d$) while the lighter ^{6}Li atom moves to the central site (i.e. $\bar{x}_1 = \langle\, \hat{\mathrm{x}}_1 \,\rangle$ approaches zero), where it avoids an energy gain due to the interatomic repulsion. With much smaller probability the same process with exchanged ^{6}Li and ^{7}Li appears [see of Fig. 5.4 (d)]. During the process the mean distance is unchanged while the uncertainty of the position $\sqrt{\langle\, (x_i - \bar{x}_i)^2 \,\rangle}$ of atom i ($i = 1, 2$) decreases [see Fig. 5.4 (a)]. Stopping at a final inclination that results in an energy difference of $0.04\hbar\omega$ between neighboring wells, the atoms are well separated. For a further inclination both ^{6}Li and ^{7}Li would move to the left well.

Starting from the system of separated atoms, one can induce a collision process. To this end the linear perturbation, i.e. the acceleration, is suddenly switched off. As shown Fig. 5.4 (d) in this case the heavier atom tunnels back and forth between the left and the right well leading to strong oscillations of $\bar{x}_2$. Due to the small initial population of the state where ^{6}Li is in the left well and ^{7}Li in the central well, also ^{6}Li tunnels back and forth and $\bar{x}_1$ oscillates slightly around zero. Owing to the mass difference both tunneling processes of ^{6}Li and ^{7}Li happen with different frequencies. Due to the repulsion the atoms do still not occupy the same lattice site during the tunneling process, which is obvious from the unchanged particle distance.

[1] The occupation of the deeply bound molecular states can be neglected during the calculation.

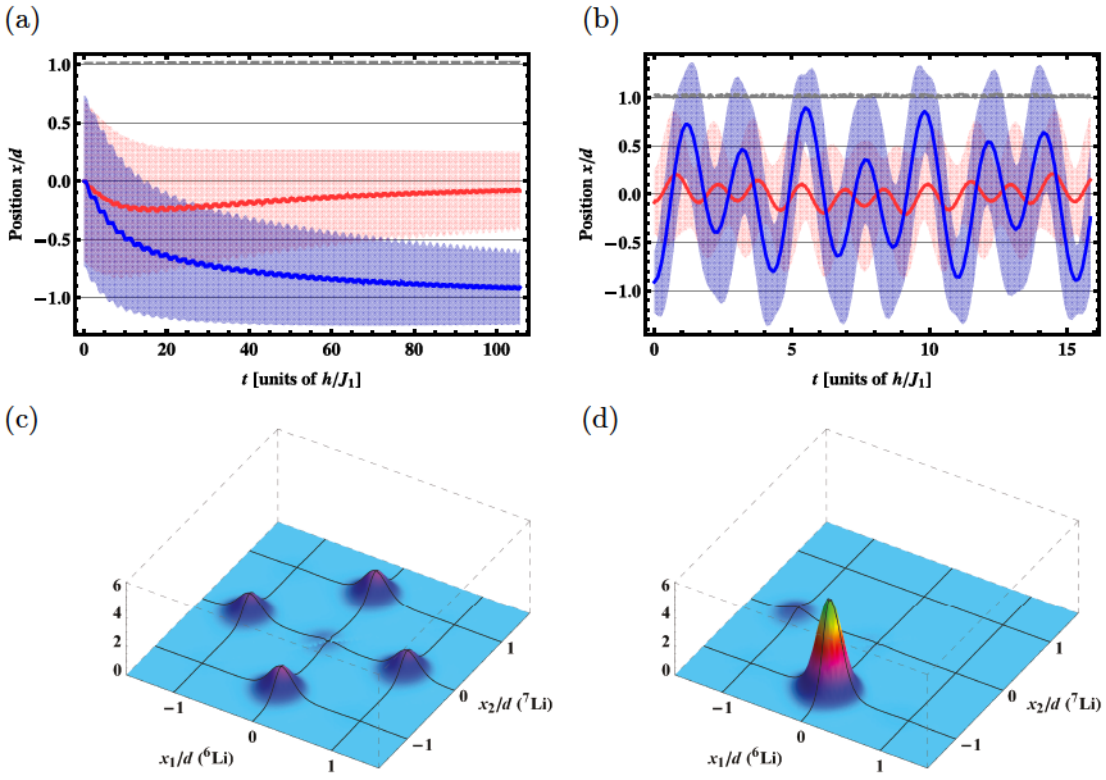

Figure 5.4: Mean particle position $\bar{x}_i = \langle x_i \rangle$ of ^{6}Li (thick red line) and of ^{7}Li (thick blue line) and mean distance $\sqrt{\langle r_x^2 \rangle}$ (grey dashed line). The corresponding red, and blue shading illustrates the uncertainty of the position $\bar{x}_i \pm \sqrt{\langle (x_i - \bar{x}_i)^2 \rangle}$ of ^{6}Li and ^{7}Li, respectively. Time is given in units of the hopping time h/J_1 of ^{6}Li. **(a)** Time dependent behavior for a linear inclination with a final perturbation $\hat{\mathrm{W}} = 5.1 J_1 \hat{\mathrm{R}}_x/d = 0.063\,\hbar\omega_1 \hat{\mathrm{R}}_x/d$. **(b)** Free evolution of the system (i.e. $\hat{\mathrm{W}} = 0$) with the initial state being the final state after the inclination of (a). **(c)** Probability density $|\Psi(x_1, x_2)|^2$ for $y_1 = y_2 = z_1 = z_2 = 0$ of the initial state of (a). There is an almost equal probability of finding ^{6}Li in the central well and ^{7}Li in the outer wells and vice versa. **(d)** The same probability density for the final state of (a), i.e. the initial state of (b). Clearly, after the linear inclination ^{7}Li is predominantly situated in the left well and ^{6}Li in the central well. However, the situation with exchanged ^{6}Li and ^{7}Li has a small but non-vanishing probability.

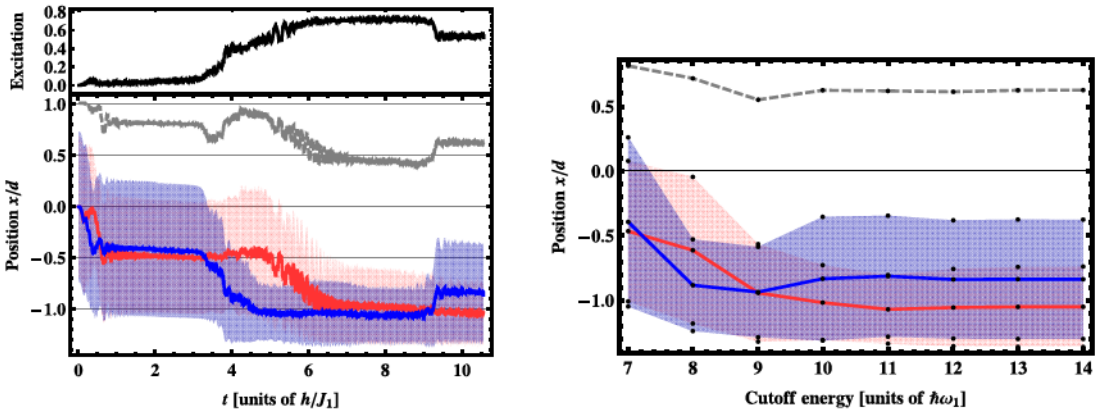

Figure 5.5: **Left:** Time dependent behavior for a linear inclination with a final perturbation $\hat{W} = 563\,J_1\hat{R}_x/d = 3.6\,\hbar\omega_1\hat{R}_x/d$. The total occupation probability of states above the first Bloch band (top) is shown together with the mean particle positions (bottom, legend as in Fig. 5.4). **Right:** Convergence of the mean particle positions for $t = 10h/J_1$ (Legend as in Fig. 5.4) as a function of the cutoff energy. The results are well converged for $E_{\text{cutoff}} \geq 12\,\hbar\omega_1$.

While a weak adiabatic inclination can be easily described also within the standard Hubbard model, a fast inclination couples states of different Bloch bands. In Fig. 5.5 the behavior for a stronger and faster inclination than the one in Fig. 5.4 (a) is presented. In this case the behavior is harder to predict. For example, it is unclear whether either first the heavier atom or the lighter atom moves to the left lattice site. Although one could expect that the lighter atom with its larger tunneling rate is more mobile and will move first, indeed the heavier atom tunnels first to the left well. During the fast inclination also states with two atoms at the same lattice site are occupied, which is accompanied by a reduction of the mean distance $\sqrt{\langle r_x^2 \rangle}$. The occupation probability of states above the first Bloch band is high, and thus the behavior cannot be described within a single-band approximation of the Hubbard model. This is also supported by studying the convergence of the dynamical behavior. By including only stationary basis states with an eigenenergy $E < E_{\text{cutoff}}$ one can determine the importance of basis states of a certain energy range. As can be observed in the right graph of Fig. 5.4, basis states up to an eigenenergy $E \approx 12\,\hbar\omega_1$ have to be included to reach convergence. These states lay $5.12\hbar\omega_1 = 3.77\,V_0$ above the eigenenergy $6.88\,\hbar\omega_1$ of the initial state.

5.4.2. Harmonic perturbation

In experiments OLs are not infinite but the atoms are normally confined by an additional weak harmonic potential. In the following the effect of the sudden activation of such a harmonic potential $\hat{\mathrm{W}} = A(\hat{\mathrm{x}}_1^2 + \hat{\mathrm{x}}_2^2)/d^2$ is studied. This perturbation does not break the symmetry of the potential and the mean position of the atoms remains at $x/d = 0$. However, as one can see in the left graph of Fig. 5.6, for a certain strength of the harmonic perturbation the system oscillates between unbound states ($\sqrt{\langle r_x^2 \rangle} \approx d$)

and repulsively bound states ($\sqrt{\langle r_x^2 \rangle} \approx 0.5\,d$) that are in resonance. These oscillations are also visible in the uncertainty of the atoms' positions. For an increased harmonic perturbation no repulsively bound state is in resonance with the unbound state. Hence, as shown in the right graph of Fig. 5.6, the atoms oscillate predominantly between delocalized states and states localized at the central lattice site. Since the atoms repel each other, the oscillations are exactly opposing each other. The off-resonant coupling to the bound state leads to small and fast oscillations of the mean distance $\sqrt{\langle r_x^2 \rangle}$ between $0.8\,d$ and $1.0\,d$.

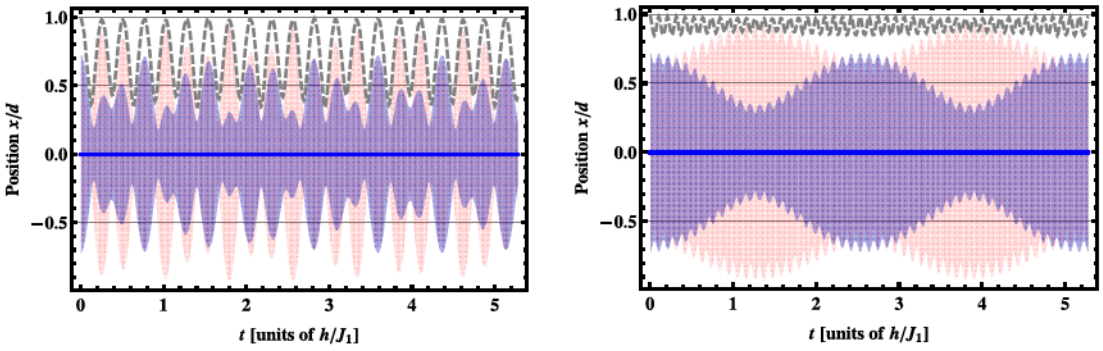

Figure 5.6: Time-dependent behavior for the sudden turn-on of an additional harmonic confinement. **Left:** For $\hat{\mathrm{W}} = 5.3\,J_1(\hat{\mathrm{x}}_1^2 + \hat{\mathrm{x}}_2^2)/d^2 = 0.034\,\hbar\omega_1(\hat{\mathrm{x}}_1^2 + \hat{\mathrm{x}}_2^2)/d^2$ oscillations between bound and unbound states appear. **Right:** For stronger confinement $\hat{\mathrm{W}} = 10.5\,J_1(\hat{\mathrm{x}}_1^2 + \hat{x}_2^2)/d^2 = 0.067\,\hbar\omega_1(\hat{x}_1^2 + \hat{x}_2^2)/d^2$ the bound-state occupation is much weaker, however the particles tunnel alternating between the central and outer wells. Legend as in Fig. 5.4.

5.5. Dynamic behavior at a Feshbach resonance

By replacing the Born-Oppenheimer interaction potential by the square-well potential defined in Sec. 4.4, the dynamical behavior in the presence of an MFR can be realistically numerically simulated. This allows for studying the validity of the BHM not only for a stationary but also for a dynamically perturbed OL. For M identical atoms any time-dependent perturbation

$$W(t, \vec{r}_1, \cdots, \vec{r}_M) = f(t) \sum_{i=1}^{M} V_{\mathrm{pert}}(\vec{r}_i) \tag{5.36}$$

acts on each atom in the same way.

Normally, any external perturbation $V_{\mathrm{pert}}(\vec{r}_i)$ is approximately constant on the length scale of the bound state. Hence, the perturbation cannot couple the orthogonal closed and open-channel states at an MFR. The matrix elements of the perturbation of the

closed channel evaluate to

$$\begin{aligned}
&\left\langle \psi_b \tilde{w}_{i,n} \middle| \sum_{i=1}^{M} V_{\mathrm{pert}}(\vec{r}_i\,) \middle| \tilde{w}_{j,m} \psi_b \right\rangle = \int d\vec{R} \int d\vec{r}\, |\psi_b(\vec{r})|^2 \times \\
&\times \tilde{w}_{i,n}(\vec{R}) \left[V_{\mathrm{pert}}\left(\vec{R} + \frac{1}{2}\vec{r}\right) + V_{\mathrm{pert}}\left(\vec{R} - \frac{1}{2}\vec{r}\right) \right] \tilde{w}_{j,m}(\vec{R}) \\
&\approx \int d\vec{R}\, \tilde{w}_{i,n}(\vec{R}) \int d\vec{r}\, |\psi_b(\vec{r})|^2\, 2V_{\mathrm{pert}}(\vec{R}) \tilde{w}_{j,m}(\vec{R}) \\
&= 2 \left\langle \tilde{w}_{i,n} \middle| \hat{\mathrm{V}}_{\mathrm{pert}} \middle| \tilde{w}_{j,m} \right\rangle .
\end{aligned} \tag{5.37}$$

Hence, in second quantization the perturbation is expressed as

$$\begin{aligned}
\hat{\mathrm{W}}(t) = f(t) \Bigg(&\sum_{\langle i,j \rangle} \sum_{n,m=1}^{N} \left\langle w_{i,n} \middle| \hat{\mathrm{V}}_{\mathrm{pert}} \middle| w_{j,m} \right\rangle a_{i,n}^{\dagger} a_{j,m} \\
&+ 2 \sum_{\langle i,j \rangle} \sum_{n,m=1}^{N} \left\langle \tilde{w}_{i,n} \middle| \hat{\mathrm{V}}_{\mathrm{pert}} \middle| \tilde{w}_{j,m} \right\rangle b_{i,n}^{\dagger} b_{j,m} \Bigg) .
\end{aligned} \tag{5.38}$$

As usual, only next-neighbor coupling and on-site coupling are considered and the basis is restricted to the first N Bloch bands.

In the following the case of a linear perturbation in x direction with increasing strength is considered. That is, $V_{\mathrm{pert}}(\vec{r}_i) = x_i$ and $f(t) = \lambda t$.

Of course, like the eigenenergies in Chap. 4 also the dynamical behavior depends crucially on the value of the resonance energy E_{res}, i.e. the energy of the bound state in the BHM. For the dynamical studies a resonance energy is chosen such that an inclination leads to the resonant next-neighbor coupling of two separated atoms in the ground state to a bound state in the first and second Bloch band. The corresponding dynamical behavior is sketched in Fig. 5.7. As one can see, the COM movement of the system upon accelerating the lattice depends crucially on the energy of the bound states. Depending on the bound state and its COM excitation that comes into resonance, the system can move against the direction or in direction of the acceleration. A precise representation of the system is thus necessary to predict the mobility behavior of two atoms at an MFR.

Fig. 5.8 shows the projections $|\langle n|\,\Psi(t)\rangle\,|^2$ of the time-dependent wave functions $|\Psi(t)\rangle$ onto the eigenstates $|n\rangle$ of the unperturbed system for a slow inclination with $\lambda = 0.0003 \frac{E_r}{\hbar} \frac{\hbar\omega}{d}$. If the perturbation would be suddenly switched off, the projections give the probability of finding the system in the corresponding eigenstate. For the same three coupling energies as shown in Fig. 4.9 the qualitative agreement between the result of the non-perturbative approach (upper row) and the dressed BHM (middle row) is very good. As described in Fig. 5.7 initially the bound state in the second Bloch band is slowly occupied. After $t \approx 1300\hbar/E_r$ this bound state gets into resonance with the bound state in the first Bloch band, which is then occupied. After $t \approx 1500\hbar/E_r$ the main occupation moves back to the initial state. Additionally to the behavior described in Fig. 5.7 the inclination leads to a strong coupling of the bound states in the first and second Bloch bands. Due to the large energy separation of these states this coupling

leads to fast oscillations of the population of the eigenstates. These oscillations appear, once the excited bound state in the left well comes into resonance with the lowest bound state in the right well at $t \approx 1300\hbar/E_r$.

In order to examine the quantitative agreement between the non-perturbative and BHM results, the time-dependent COM motion of the system $\left\langle \Psi(t) \right| \hat{\mathrm{R}}_x \left| \Psi(t) \right\rangle$ is regarded. As one can see in the lower row in Fig. 5.7, the overall quantitative agreement between the non-perturbative calculations and the dressed BHM is good. Especially for the smallest coupling energy $\chi = 0.41\,\hbar\omega$ the dressed BHM accurately recovers the correct dynamical behavior. For the larger coupling energies the fast oscillations appearing after $t \approx 1300\hbar/E_r$ are less accurately reproduced by the dressed BHM. The phase shift and altered frequency of the oscillations is mainly due to a small underestimation of the coupling strength between the stationary eigenstates within the dressed BHM by about 1% . In contrast to the dressed BHM, the undressed BHM leads even for small coupling energies to a dynamical behavior significantly disagreeing from the one of the non-perturbative calculations.

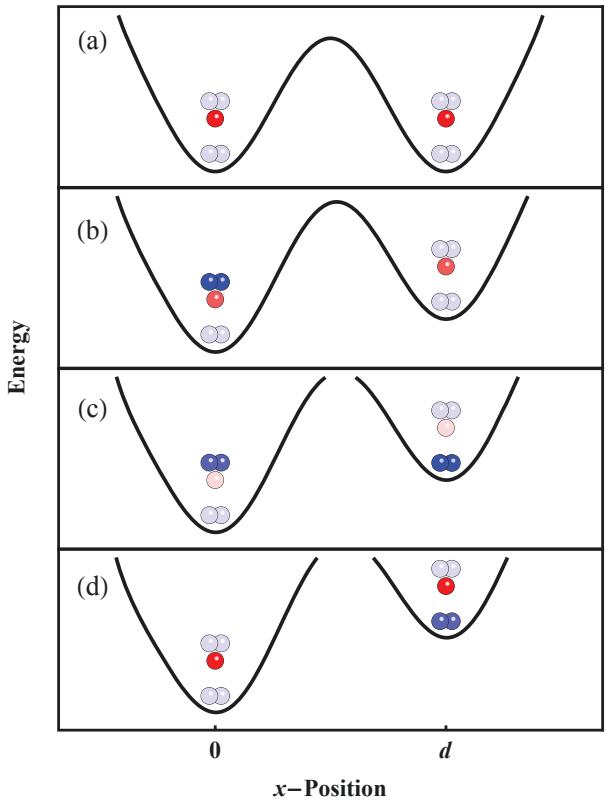

Figure 5.7: Sketch of the dynamical behavior while accelerating (inclining) the double-well. **(a)** The initial state consists of separated atoms (red disks) in the ground state of the left and right well. The four molecular states in the COM ground state (blue double disk below red disks) and in the first excited COM state (blue double disk above red disks) are not in resonance. **(b)** Upon inclining the potential the energy of an excited molecular state in the left well (dark blue) comes in resonance with the energy of the separated atoms. The molecular state is occupied and the COM of the system moves to the left. **(c)** After a further inclination the energy of the excited molecule in the left well comes into resonance with the ground-state molecule in the right well. By occupying this state the COM of the system moves to the right. **(d)** Finally, the molecule on the right well comes into resonance with the initial state of two separated atoms and the COM of the system moves again to the left.

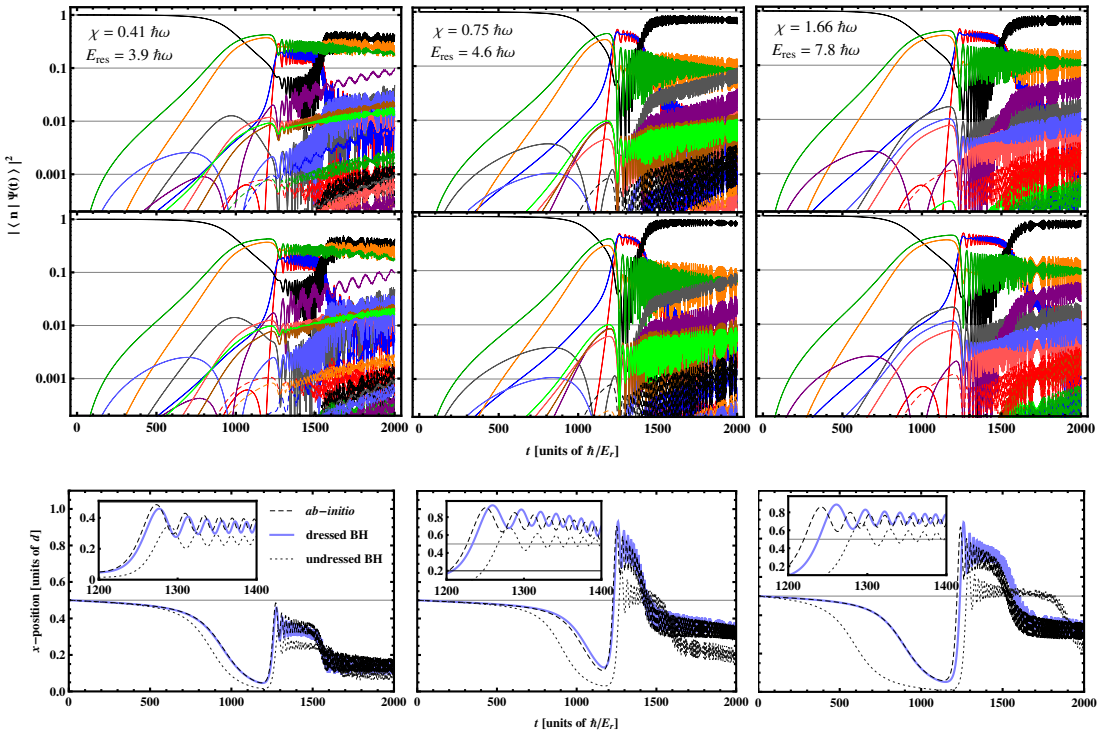

Figure 5.8: Dynamic behavior of two initially separated atoms in the ground state of the double-well potential during an inclination of the lattice for different coupling energies χ and resonance energies E_{res}. At $t = t_{\mathrm{end}} = 2000\,\hbar/E_r$ each atom experiences a perturbation of $\hat{W} = 0.7\,\hbar\omega\hat{x}/d$, which suffice to bring both the first and second bound state into resonance (see Fig. 5.7). The projection of the time-dependent wave function $|\Psi(t)\rangle$ onto the eigenstates $|n\rangle$ of the unperturbed system is shown in the first row (non-perturbative results) and the second row (results of the dressed BHM) using the same color coding as in Figs. 4.9 and 4.10. In the lowest row the mean COM position $\left\langle \Psi(t) \middle| \hat{\mathrm{R}}_x \middle| \Psi(t) \right\rangle$ is shown for the non-perturbative calculations and the time propagation of the dressed and undressed BHM. The insets show a magnified region of the beginning of the fast oscillations between $1200\hbar/E_r$ and $1400\hbar/E_r$.

6. Quantum computation with ultracold atoms in optical lattices

In the last years tremendous progress has been made in controlling and observing ultracold atoms in OL potentials [95]. One of the latest developments has been the optical detection of atoms with single-site resolution in lattices of increasingly smaller periodicity [96–99] (see also Fig. 6.1). This technological advancement allowed, e.g., for a direct observation of the superfluid to Mott-insulator transition [7]. Along with these detection schemes comes the possibility to also control the lattice potential with single-site resolution. For example, this has been used to manipulate the spin of single atoms in an OL [23].

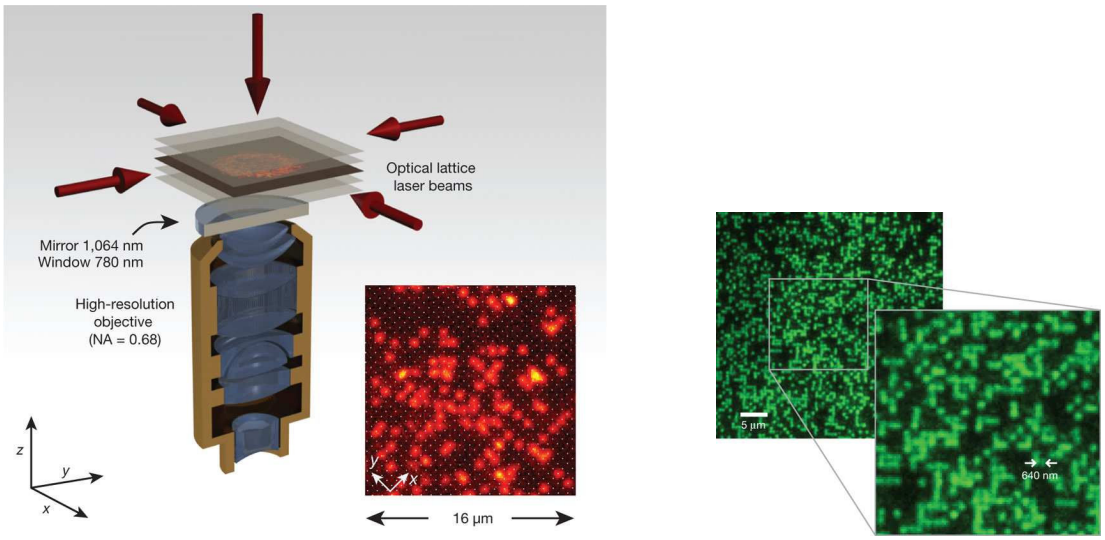

Figure 6.1: **Left:** Sketch of the experimental setup for observing atoms in a two-dimensional OL by a high aperture optical system. The inset shows a site-resolved imaging of single atoms in a 532-nm-period OL. (extracted from Sherson et al. [99]) **Right:** Site-resolved imaging of single atoms in a 640-nm-period OL with the quantum gas microscope (extracted from Bakr et al. [98]).

These technological advancements once more raise the hope to build quantum computers with ultracold atoms in optical lattices. A quantum computer makes use of quantum mechanical phenomena, such as superposition and entanglement, in order to solve specific tasks with decisively fewer computational steps than a classical computer. Prominent examples for quantum algorithms are Grover search and Shor's algorithm.

The former allows for finding an element in an unsorted quantum database with N elements saved on a $\mathcal{O}(\log N)$ large storage space in $\mathcal{O}(\sqrt{N})$ time, which offers a quadratic speed-up compared to the classical search [100]. Shor's algorithm, which performs integer factorization, offers even an exponential speed-up compared to all known algorithms on classical computers [101]. However, in the field of quantum physics (and quantum chemistry) the most relevant application of a quantum computer is probably that as a universal quantum simulator that may efficiently compute the time-dependent wave function of a quantum system [102]. For large quantum systems this is infeasible on a classical computer since an N-particle system has an exponentially large Hilbert space with dimensionality $\mathcal{O}(2^N)$. Therefore, a classical computer would in general have to keep track of exponentially many coefficients describing the time-dependent wave function.

Many different candidates are being pursued for the physical implementation of a quantum computer, among them trapped ions, nuclear magnetic resonance (NMR) on molecules, and cavity quantum electrodynamics [102]. Compared to other possible candidate systems for the implementation of a quantum computer, atoms in OLs have the advantage of a natural scalability to a large number of atoms encoding qubits and a weak coupling to the environment leading to long decoherence times [103]. Single-site addressability of large qubit systems may be one of the last important technologies on the way to the first experimental implementation of an OL quantum computer.

Many schemes proposed for quantum computation in OLs rely on encoding the qubits by atomic spin states [104–107]. Although single-qubit operations [96] and collective two-qubit operations [18] have been demonstrated, spin qubit states are generally disturbed by barely avoidable external magnetic fields, which lead to their decoherence. This source of decoherence can be avoided by encoding the qubits in the spacial wave function of the ground and first excited state of bosonic atoms localized at single sites of an OL [107–109].

In the following it is shown that a periodic modulation of the lattice position, i.e. a shaking of the lattice, suffices to drive all quantum operations needed for quantum computation. The shaking of the OL can be studied in the context of Floquet theory showing that it effectively changes the hopping parameter of the system [110]. This effect has been verified experimentally, while also revealing that the shaking drives transitions from the first to the second Bloch band [111]. Within the proposed scheme, these band transitions are used to drive qubit operations, while the qubit addressability is provided by manipulating the OL with single-site resolution. This enables the selective change of the energy spacing of specific sites and the driving of local transitions. The cancellation of additional z rotations induced by the lattice manipulation is approached by adapting refocusing schemes known from NMR quantum control [112].

After the introduction of the proposal, which was published in Ref. [26] (Publication III), it is shown how in principle an integer factorization of 15 can be performed with ultracold atoms in optical lattices. Based on this example the practicability of the implementation is discussed.

6.1. Theoretical introduction

This section gives a very short introduction to the notion of qubits, qubit operations and the requirements of the implementation of a quantum computer. The discussion is far from being exhaustive. For a very good introduction to quantum computers the reader is referred to the book of Nielsen and Chuang [102].

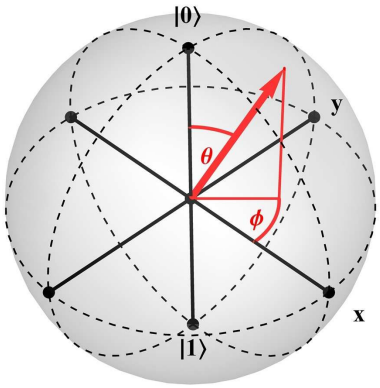

Figure 6.2: Any qubit state $|\Psi\rangle = \cos\left(\frac{\theta}{2}\right)|0\rangle + e^{i\phi}\sin\left(\frac{\theta}{2}\right)|1\rangle$ can be visualized as a unit vector (red arrow) pointing anywhere at the Bloch sphere (gray). Unitary operations on a qubit can be imagined as rotations of this vector in the Bloch sphere.

Quantum computers do not operate on bits that can take the values 0 and 1, but on quantum bits (qubits). These are represented by two-level quantum systems, which can be in a state

$$|\Psi\rangle = \cos\left(\frac{\theta}{2}\right)|0\rangle + e^{i\phi}\sin\left(\frac{\theta}{2}\right)|1\rangle \tag{6.1}$$

that is determined by two angles θ and ϕ. The coefficient in front of the state $|0\rangle$ can be chosen real since the overall phase of the qubit is not observable. As shown in Fig. 6.2 the possible qubit states can be visualized by a unit vector in the so-called Bloch sphere. Any unitary operation $\hat{\mathrm{U}}$ on the qubit can then be regarded as a rotation of the unit vector by an angle θ around some vector $\vec{n}$ in the Bloch sphere. Again, the operations are only defined up to a global phase, i.e. $e^{i\varphi}\hat{\mathrm{U}}$ is equivalent to $\hat{\mathrm{U}}$.

Any rotations in the Bloch sphere can be represented by a sum of four 2×2 matrices, the identity $\hat{\mathrm{I}}$ and the Pauli matrices

$$\hat{\sigma}_x = \begin{pmatrix} 0 & 1 \\ 1 & 0 \end{pmatrix} \qquad \hat{\sigma}_y = \begin{pmatrix} 0 & -i \\ i & 0 \end{pmatrix} \qquad \hat{\sigma}_z = \begin{pmatrix} 1 & 0 \\ 0 & -1 \end{pmatrix}. \tag{6.2}$$

A rotation $\hat{\mathcal{R}}_{\vec{n}}(\theta)$ about the $\vec{n}$ axis by an angle θ can be expressed as

$$\hat{\mathcal{R}}_{\vec{n}}(\theta) = e^{-i\theta\vec{n}\cdot\vec{\sigma}/2} = \cos\left(\frac{\theta}{2}\right)\hat{\mathrm{I}} - i\sin\left(\frac{\theta}{2}\right)\vec{n}\cdot\vec{\sigma}\,, \tag{6.3}$$

where $\vec{\sigma}$ denotes the three component vector $(\hat{\sigma}_x, \hat{\sigma}_y, \hat{\sigma}_z)$ [102]. The operators

$$\hat{\mathrm{X}}(\theta) \equiv \hat{\mathrm{X}}_\theta = e^{-i\theta\hat{\sigma}_x/2} = \begin{pmatrix} \cos\frac{\theta}{2} & -i\sin\frac{\theta}{2} \\ -i\sin\frac{\theta}{2} & \cos\frac{\theta}{2} \end{pmatrix} \tag{6.4}$$

$$\hat{\mathrm{Y}}(\theta) \equiv \hat{\mathrm{Y}}_\theta = e^{-i\theta\hat{\sigma}_y/2} = \begin{pmatrix} \cos\frac{\theta}{2} & -\sin\frac{\theta}{2} \\ \sin\frac{\theta}{2} & \cos\frac{\theta}{2} \end{pmatrix} \tag{6.5}$$

$$\hat{\mathrm{Z}}(\theta) \equiv \hat{\mathrm{Z}}_\theta = e^{-i\theta\hat{\sigma}_z/2} = \begin{pmatrix} e^{-i\frac{\theta}{2}} & 0 \\ 0 & e^{i\frac{\theta}{2}} \end{pmatrix} \tag{6.6}$$

correspond to the three special cases of rotations about the x, y, and z axes.

In order to implement a universal quantum computer by a specific physical system the following requirements have to be met [102]:

Qubit register: The physical system can be mapped onto a scalable register of n qubits. The corresponding $N = 2^n$ dimensional Hilbert space is spanned by product states of the form $|x_1, \ldots, x_n\rangle$, where $x_i = 0, 1$, that are known as the computational basis.

Preparation: Any computational basis state, e.g. $|0 \ldots 0\rangle$, can be efficiently prepared.

Universal gate set: One must be able to perform a universal set of quantum operations on any subset of qubits. For example, single-qubit rotations together with controlled rotation of two qubits discussed below form a universal gate set [113].

Readout: Measurements may be performed in the computational basis of one or more of the qubits.

Of course, there are also more practical requirements, that have to be met. For example, the physical system that implements the quantum computer must be well isolated from the environment since a coupling to the environment leads to the decoherence of the quantum state. In general the quantum operations can be only performed with limited accuracy. For longer and longer computations small errors can accumulate and would eventually spoil the computation. Fortunately, there exist ways to correct small errors using quantum error correction schemes [102]. Nevertheless, the operations should be performed as accurately as possible. A measure for the accuracy of an operation is the fidelity. Supposing $\hat{\mathrm{U}}$ is a quantum operation performed on the qubits that should ideally correspond to an operation $\hat{\mathrm{U}}_0$. The fidelity $\mathcal{F}$ of the operation $\hat{\mathrm{U}}$ is then defined as the overlap of the state $\hat{\mathrm{U}}|\Psi\rangle$ with the state $\hat{\mathrm{U}}_0|\Psi\rangle$ averaged over all possible states $|\Psi\rangle$ of the qubit register [114], i.e.

$$\mathcal{F} = \int d\Psi \left\langle \Psi \middle| \hat{\mathrm{U}}^\dagger \hat{\mathrm{U}}_0 \middle| \Psi \right\rangle . \tag{6.7}$$

In a theoretical treatment one is usually able to determine $\hat{\mathrm{U}}|\Psi\rangle$ numerically for any state $|\Psi\rangle$. Nevertheless, the determination of the fidelity using directly definition (6.7)

is numerically extremely demanding as one would have to sample the integrand for many states $|\Psi\rangle$. Fortunately, it can be shown that in an $N = 2^n$ dimensional Hilbert space the fidelity is equally determined by

$$\mathcal{F} = \frac{1}{N(N+1)} \left(\mathrm{Tr}\left(\hat{\mathrm{M}}\hat{\mathrm{M}}^\dagger\right) + \left|\mathrm{Tr}(\hat{\mathrm{M}})\right|^2 \right) , \tag{6.8}$$

where $\hat{\mathrm{M}} = \hat{\mathrm{U}}^\dagger \hat{\mathrm{U}}_0$ (see Ref. [115] and references therein). The operator $\hat{\mathrm{U}}$ is fully determined by its action $\hat{\mathrm{U}}|x_1 \dots x_n\rangle$ on the N states of the computational basis. Hence, for small qubit systems the fidelity can be efficiently determined.

6.2. Addressable qubit register in an optical lattice

For sufficiently strong confinement in the transversal directions the OL potential can be represented by a one-dimensional OL in x direction with a potential $V_\mathrm{L} \sin^2(k_0 x)$. In the remainder of this chapter lengths are given in units of $1/k_0$ and energies in units of the recoil energy $E_r = \hbar^2 k_0^2/(2m)$, where m is the mass of the atoms. In this system of units the lattice spacing is given as $d = \pi$ and the oscillator energy of the harmonic approximation of a single lattice site as $\hbar\omega_\mathrm{L} = 2\sqrt{V_\mathrm{L}}$. As in Sec. 4.1 the ultracold Bosons in the OL are described by a multi-band Bose-Hubbard model in the basis of Wannier functions $w_{i,b}(x)$ of sites $i = 1 \dots S$ and bands $b = 1 \dots N$. However, the inclusion of a coupled resonant bound state that leads to a Feshbach resonance is not necessary. The atom-atom interaction is simply described by a zero-range interaction potential $V_\mathrm{int}(x_1, x_2) = g\delta(x_1 - x_2)$ with a relatively weak coupling strength g that depends on the scattering length and the transversal confinement. Generally, atoms in different Bloch bands are coupled by the interaction. By means of a sufficiently broad MFR[1] or by adjusting the transversal confinement one can make g sufficiently large to form a Mott-insulator state in the first two Bloch bands, i.e. for a lattice with unit filling there is exactly one atom at each lattice site. The lattice then realizes a quantum register with $|0\rangle$ encoded by an atom in the excited state, and $|1\rangle$ encoded by one in the ground state [see Fig. 6.3 (a)]. In the following

$$\left\| \begin{array}{cccc} n_{2,1} & n_{2,2} & n_{2,3} & \cdots \\ n_{1,1} & n_{1,2} & n_{1,3} & \cdots \end{array} \right\rangle \tag{6.9}$$

shall denote a Fock state in the extended Wannier basis with occupation number $n_{i,j}$ of band i and site j. If the coupling between the bands and sites is small and no avoided crossing appears, all important eigenstates can be characterized by their dominantly contributing Fock state. In this notation the qubits state $|001\rangle$ is encoded by the eigenstate with maximal overlap to $\left\|{}^{110}_{001}\right\rangle$.

[1] The MFR must be broad enough, such that the attractively interacting bound state is sufficiently off-resonant from the transitions discussed below

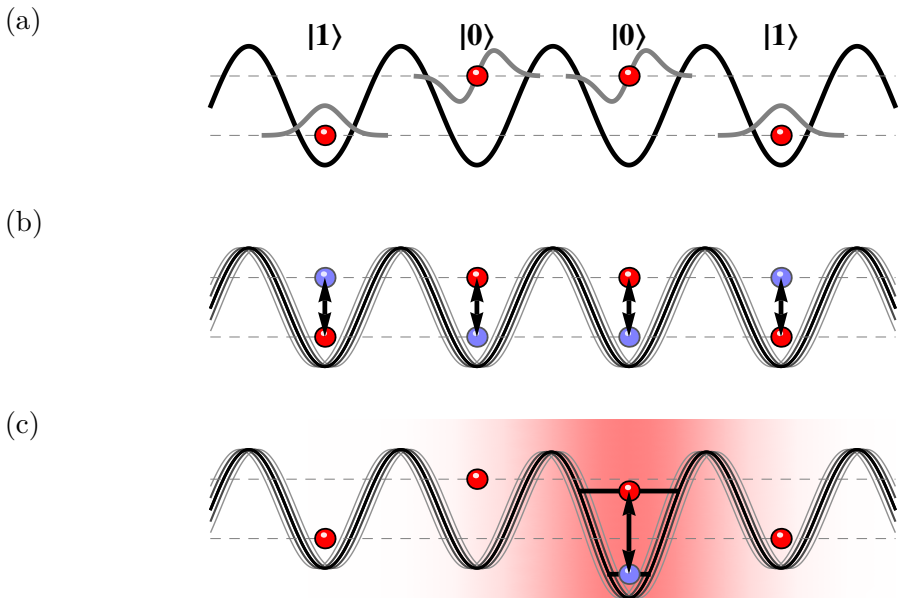

Figure 6.3: **(a)** Qubit register with atoms (circles) in the ground state $\left\|{}^{0}_{1}\right\rangle = |1\rangle$ or the excited state $\left\|{}^{1}_{0}\right\rangle = |0\rangle$ of each lattice site. **(b)** A shaking of the lattice with an appropriate frequency couples predominantly ground and excited states in each lattice site (indicated by arrows). **(c)** By shining a laser with waist on the order of the lattice spacing (red shading) onto one site a local transition between $|0\rangle$ and $|1\rangle$ can be driven by shaking the lattice.

Within the presented approach the qubits are manipulated by a global periodic acceleration, i.e. a shaking of the lattice. In the co-moving frame of the lattice this leads to an oscillating additional potential $\hat{\mathrm{V}}_{\mathrm{sh}}(t) = f_{\mathrm{sh}}(t)\hat{\mathrm{x}}\cos(\omega_{\mathrm{sh}}t - \varphi)$, where ω_{sh} is the frequency, φ the phase, and $f_{\mathrm{sh}}(t)$ is the slowly varying force amplitude of the shaking. This perturbation undulates the onsite energies of the lattice and leads to a coupling between Bloch bands with symmetric and antisymmetric Wannier functions [see Fig. 6.3 (b)]. In passing, it is noted that transitions between the ground and excited states can also be achieved by two-photon Raman transitions [116].

6.3. Qubit operations in the rotating frame

By means of $\hat{\mathrm{V}}_{\mathrm{sh}}$ one is generally able to drive transitions between different eigenstates of the lattice Hamiltonian $\hat{\mathrm{H}}_0$.

For a better understanding of this approach first the effect of the shaking on a single qubit shall be discussed. Choosing the zero point of the energy in the middle of the eigenenergies of the two qubit states, the Hamiltonian of a single lattice site can be written as

$$\hat{\mathrm{H}}_0 = \frac{1}{2}\hbar\omega_0\hat{\sigma}_z + \hat{\mathrm{W}}(t)\,, \tag{6.10}$$

where $\hbar\omega_0$ is the energy difference between the qubit states and $\hat{\mathrm{W}}(t)$ is a general perturbation of the lattice. In the following the qubits are defined in the frame rotating with $-\omega_0 t$ around the z axis of the Bloch sphere. That is, the system is transformed from the Schrödinger picture to the interaction picture. In this picture the state vector is defined as

$$|\Psi_I(t)\rangle = e^{i\hat{\mathrm{H}}_0 t/\hbar}|\Psi_S(t)\rangle = e^{i\omega_0 t\hat{\sigma}_z/2}|\Psi_S(t)\rangle = \hat{\mathrm{Z}}(-\omega_0 t)|\Psi_S(t)\rangle\,, \tag{6.11}$$

where $|\Psi_S(t)\rangle$ is the state vector in the Schrödinger picture. An operator $\hat{\mathrm{A}}_S$ of the Schrödinger picture transforms correspondingly to

$$\hat{\mathrm{A}}_I(t) = e^{i\hat{\mathrm{H}}_0 t/\hbar}\hat{\mathrm{A}}_S(t)e^{-i\hat{\mathrm{H}}_0 t/\hbar} = \hat{\mathrm{Z}}(-\omega_0 t)\hat{\mathrm{A}}_S(t)\hat{\mathrm{Z}}(\omega_0 t)\,. \tag{6.12}$$

In the rotating frame the time-evolution of the state vector,

$$i\hbar\frac{d}{dt}|\Psi_I(t)\rangle = \hat{\mathrm{W}}_I(t)|\Psi_I(t)\rangle\,, \tag{6.13}$$

is determined solely by the perturbation of the lattice $\hat{\mathrm{W}}_I(t)$.

6.3.1. Rotating wave approximation

First, the general case of shaking the lattice with a frequency $\omega = \omega_0 + \delta$ is considered, where the detuning from resonance δ shall be small compared to ω_0. The corresponding perturbation $\hat{\mathrm{W}} = \hat{\mathrm{V}}_{\mathrm{sh}} = f_{\mathrm{sh}}\hat{\mathrm{x}}\cos(\omega t - \varphi)$ in the rotating frame, $\hat{\mathrm{W}}_I = \hat{\mathrm{Z}}(-\omega_0 t)\hat{\mathrm{W}}\,\hat{\mathrm{Z}}(\omega_0 t)$, evaluates to

$$\hat{\mathrm{W}}_I = f_{\mathrm{sh}}\begin{pmatrix} \cos(\omega t+\varphi)\,\langle 0|\,\hat{\mathrm{x}}\,|0\rangle & \frac{1}{2}e^{i(t\delta+\varphi)}\left(1+e^{-2i(\omega t+\varphi)}\right)\langle 0|\,\hat{\mathrm{x}}\,|1\rangle \\ \frac{1}{2}e^{-i(t\delta+\varphi)}\left(1+e^{2i(\omega t+\varphi)}\right)\langle 1|\,\hat{\mathrm{x}}\,|0\rangle & \cos(\omega t+\varphi)\,\langle 1|\,\hat{\mathrm{x}}\,|1\rangle \end{pmatrix}.$$

In Sec. 5.2 the time evolution was mainly governed by the tunneling of the atoms due to the acceleration of the lattice. Here, the acceleration oscillates on time scales on the order of $1/\omega_0$ which is much to fast for tunneling to take place. Also the onsite wave function of the qubits can hardly react on perturbations that oscillate on these time scales. As usual, this behavior is accounted for by the rotating wave approximation, which neglects all terms that oscillate with high frequencies on the order of ω_0, giving

$$\hat{\mathrm{W}}_I \approx f_{\mathrm{sh}}\begin{pmatrix} 0 & \frac{1}{2}e^{i(t\delta+\varphi)}\,\langle 0|\,\hat{\mathrm{x}}\,|1\rangle \\ \frac{1}{2}e^{-i(t\delta+\varphi)}\,\langle 1|\,\hat{\mathrm{x}}\,|0\rangle & 0 \end{pmatrix}. \tag{6.14}$$

The time evolution of the qubit state according to Eq. (6.13) is given as $|\Psi_I(t)\rangle = \hat{\mathrm{U}}_I(t)|\Psi_I(0)\rangle$ with the time evolution operator $\hat{\mathrm{U}}_I(t) = \hat{\mathrm{Z}}(\delta t)\hat{\mathrm{R}}(t)$, where

$$\hat{\mathrm{R}}(t) = \begin{pmatrix} \cos\left(\frac{t\Omega_R}{2}\right) + i\frac{\delta}{\Omega_R}\sin\left(\frac{t\Omega_R}{2}\right) & -ie^{-i\varphi}\frac{\Omega}{\Omega_R}\sin\left(\frac{t\Omega_R}{2}\right) \\ -ie^{i\varphi}\frac{\Omega}{\Omega_R}\sin\left(\frac{t\Omega_R}{2}\right) & \cos\left(\frac{t\Omega_R}{2}\right) - i\frac{\delta}{\Omega_R}\sin\left(\frac{t\Omega_R}{2}\right) \end{pmatrix}. \tag{6.15}$$

Here, $\Omega = f_{\mathrm{sh}}|\langle 0|\hat{\mathrm{x}}|1\rangle|/\hbar$ and $\Omega_R = \sqrt{\Omega^2 + \delta^2}$ is the Rabi frequency.

The time evolution simplifies in the two limiting cases of small detuning $\delta \ll \Omega$ and large detuning $\delta \gg \Omega$. For $\delta \ll \Omega$ the evolution operator evaluates to

$$\begin{aligned} \hat{\mathrm{U}}_I(t) &= \hat{\mathrm{Z}}(\delta t)\begin{pmatrix} \cos\left(\frac{\Omega t}{2}\right) & -ie^{-i\varphi}\sin\left(\frac{\Omega t}{2}\right) \\ -ie^{i\varphi}\sin\left(\frac{\Omega t}{2}\right) & \cos\left(\frac{\Omega t}{2}\right) \end{pmatrix} \\ &= \hat{\mathrm{Z}}(\delta t)e^{-i\Omega t\left[\cos(\varphi)\hat{\sigma}_x + \sin(\varphi)\hat{\sigma}_y\right]/2}. \end{aligned} \tag{6.16}$$

As one can see on the right-hand side of Eq. (6.16), depending on the chosen phase φ the shaking on resonance ($\delta = 0$) enables performing qubit rotations about any axes in the $x-y$ plane of the Bloch sphere. In the following such a rotation is shortly denoted by

$$\hat{\mathcal{U}}_\varphi(\alpha) \equiv e^{-i\alpha\left[\cos(\varphi)\hat{\sigma}_x + \sin(\varphi)\hat{\sigma}_y\right]/2}. \tag{6.17}$$

On the other hand, for large detuning $\delta \gg \Omega$ where $\Omega_R = \delta(1+\epsilon)$ with $\epsilon \ll 1$ the evolution operator is given as

$$\hat{\mathrm{U}}_I(t) = \begin{pmatrix} e^{it\delta\epsilon/2} & 0 \\ 0 & e^{-it\delta\epsilon/2} \end{pmatrix} = e^{it\delta\epsilon\hat{\sigma}_z/2} = \hat{\mathrm{Z}}(-t\delta\epsilon). \tag{6.18}$$

Hence, an off-resonant shaking leads to slow rotations of the qubit around the z axis in the Bloch sphere but to no rotation about the x or the y axes.

6.3.2. Pulse envelope

In the previous discussion it has been assumed that the pulse envelope of the shaking $f_{\mathrm{sh}}(t)$ changes sufficiently slowly, such that it does not induce any additional dynamic behavior. For example, a rectangular pulse envelope could severely disturb the qubit rotations as its Fourier spectrum is broad and can also include frequencies on the order of ω_0. On the other hand, a very slow variation of the pulse envelope requires accordingly long operation times. A well chosen pulse envelope is therefore crucial in order to perform the operations with sufficient speed and fidelity. Compared to the rectangular pulse a Gaussian pulse has the advantage that its Fourier spectrum is also Gaussian, such that Fourier components with higher frequencies are exponentially suppressed. However, an ideal Gaussian pulse takes infinitely long. Hence, all pulses would overlap to some extend. Moreover, the qubit rotations would be slow in the wings of the pulse. To reach short operation times this requires a relatively large peak

intensity, which also enhances unwanted off-resonant couplings. Numerical calculations with different trial pulses showed that a "Hermite" pulse envelope offers a very good compromise between the rectangular and the Gaussian pulse in terms of the required peak intensity and the width of the Fourier spectrum. The "Hermite" pulse is defined by

$$f_{\mathrm{sh}}(t) = \begin{cases} H_2(\tau)e^{-\tau^2} & \text{for } t_{\mathrm{start}} \leq t \leq t_{\mathrm{end}} \\ 0 & \text{otherwise} \end{cases} \tag{6.19}$$

with $\tau = (1 - 2[t - t_{\mathrm{start}}]/t_{\mathrm{end}})/\sqrt{2}$ and H_2 the 2nd Hermite polynomial. In Fig. 6.4 the three pulses are compared in both the time and the frequency domain.

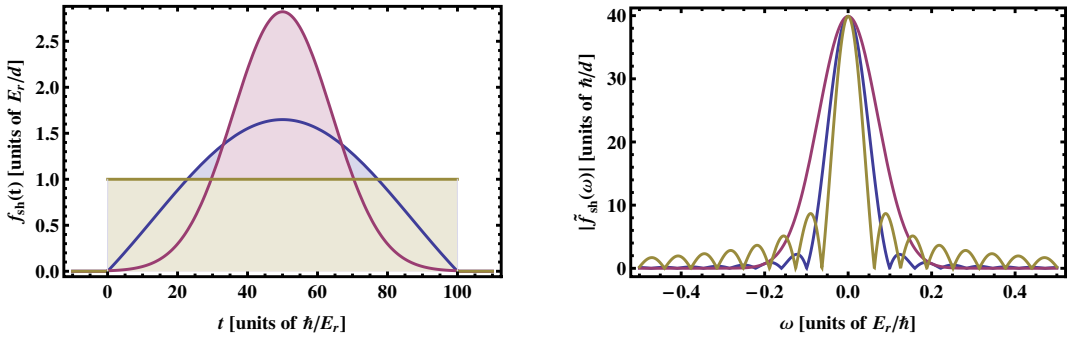

Figure 6.4: The "Hermite" pulse (blue) is compared to a Gaussian pulse (red) and a rectangular pulse (yellow) in both the time domain (left) and the frequency domain (right). The time integrals of all pulses, which span from $t_{\mathrm{start}} = 0$ to $t_{\mathrm{end}} = 100\hbar/E_r$, are the same. The Fourier spectrum of the rectangular pulse extends over a large frequency domain. While large ω components of the Gaussian pulse are exponentially suppressed, the central peak of the rectangular pulse is much narrower. The "Hermite" pulse combines a fast decay of high-frequency components with a relatively narrow central peak, which leads to a good addressability of the driven transition in the energy domain. Furthermore, the "Hermite" pulse has a smaller peak intensity than the Gaussian pulse.

6.4. Qubit operations in the optical lattice

6.4.1. Single-qubit operations

Driving a single-qubit operation at a certain lattice site necessitates that the energy difference between the corresponding qubit states $|0\rangle$ and $|1\rangle$ differs from that of other lattice sites. This can be achieved by shining a laser with a waist on the order of the lattice spacing perpendicular to the lattice, as was accomplished experimentally in

Ref. [23]. The perturbation by this laser can be assumed to have the Gaussian form

$$V_{\mathrm{Gauss}}(x) = -\gamma\, e^{\frac{(x-x_0)^2}{2\sigma^2}}\,. \tag{6.20}$$

The additional laser intensity changes the energy difference $\hbar\omega_0$ between the ground and excited state by some energy $\hbar\Delta$ [see Fig. 6.3 (c)]. Depending on the sign of the polarizability of the atoms, one has $\gamma > 0$ or $\gamma < 0$ (see also Eg. 4.1) and thus $\Delta > 0$ or $\Delta < 0$. By shaking with a frequency $\omega_{\mathrm{sh}} = \omega_0 + \Delta$ one is then able to drive single-qubit rotations on the marked lattice site.

6.4.2. Two-qubit operations

Before discussing how to deal with the additional z rotations that are also appearing during the single-qubit operation, the principle of a controlled two-qubit operation shall be introduced. Together with single-qubit operations, the ability to drive a controlled rotation (CROT) between adjacent lattice sites completes a universal gate set [113]. A CROT rotates one qubit (the target qubit) if and only if another qubit (the control qubit) is in state $|1\rangle$. The strategy to perform this operation between neighboring qubits is to deform the lattice, such that a repulsively bound state $\left\|{}^{02}_{00}\right\rangle$ comes into resonance with the state $|00\rangle = \left\|{}^{11}_{00}\right\rangle$. As sketched in Fig. 6.5, the coupling between the lattice sites leads to an avoided crossing in the energy spectrum. If one identifies the left qubit with the control qubit, any rotation on the form of Eq. (6.17) on the right target qubit becomes off-resonant and is inhibited if and only if the control qubit is initially in the excited state ($|0\rangle$). This enables the desired controlled rotation between neighboring qubits.

6.5. Dephasing and refocussing

6.5.1. Single qubit operations

In order to perform a rotation of a specific target qubit rather than on all qubits, a narrow-waist laser is used to change locally the energy separation of the qubit states by $\hbar\Delta$ [see Fig. 6.3 (c)]. This leads to an additional term $\frac{1}{2}\hbar\Delta\hat{\sigma}_z$ in the Hamiltonian and necessitates to shake with an adapted frequency $\omega_0 + \Delta$. Ignoring for the sake of simplicity the switching process of the narrow-waist laser, the perturbation of the lattice is

$$\hat{\mathrm{W}} = \frac{1}{2}\hbar\Delta\hat{\sigma}_z + f_{\mathrm{sh}}(t)\,\hat{\mathrm{x}}\cos([\omega_0 + \Delta]t + \varphi)\,. \tag{6.21}$$

On can easily determine the time evolution operator of the addressed qubit due to the perturbation $\hat{\mathrm{W}}$. In the frame rotating with frequency $\omega_0 + \Delta$ the time evolution of the wave function $|\Psi_{II}(t)\rangle$ is given again as $|\Psi_{II}(t)\rangle = \hat{\mathcal{U}}_\varphi(\Omega t)|\Psi_{II}(0)\rangle$ [see Eqs. (6.16) and (6.17)]. In order to transform back to the qubit frame rotating with ω_0, one has to add an additional frame rotation with frequency $-\Delta$. Hence, in the qubit frame the wave function is given as $|\Psi_I(t)\rangle = \hat{\mathrm{Z}}(\Delta t)|\Psi_{II}(t)\rangle = \hat{\mathrm{Z}}(\Delta t)\hat{\mathcal{U}}_\varphi(\Omega t)|\Psi_{II}(0)\rangle =$

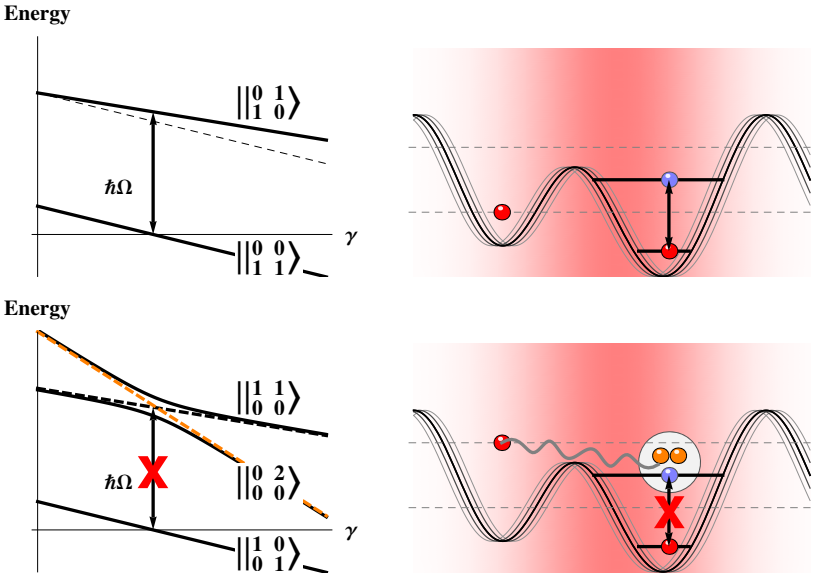

Figure 6.5: A laser (red shading in right images) is positioned slightly offset from the middle between two lattice sites so that both lattice sites are coupled and the energy of the right lattice site is lower than the one of the left site. **Top:** The lattice is shaken with frequency Ω resonantly to the transition $|10\rangle \leftrightarrow |11\rangle$ (i.e. $\left\|{}^{01}_{10}\right\rangle \leftrightarrow \left\|{}^{00}_{11}\right\rangle$), such that the right target qubit is rotated if the left atom is in the ground state $|1\rangle$. **Bottom:** If the control qubit is in the excited state $|0\rangle$, at a certain laser intensity the energy of the repulsively bound state $\left\|{}^{02}_{00}\right\rangle$ and that of the state $\left\|{}^{11}_{00}\right\rangle$ form an avoided crossing. At this avoided crossing the shaking is off-resonant to the transition $|00\rangle \leftrightarrow |01\rangle$ (i.e. $\left\|{}^{11}_{00}\right\rangle \leftrightarrow \left\|{}^{10}_{01}\right\rangle$). This enables rotations on the target qubit conditioned by the state of the control qubit.

$\hat{\mathrm{Z}}(\Delta t)\hat{\mathcal{U}}_\varphi(\Omega t)|\Psi_I(0)\rangle$. Therefore, the evolution operator in the qubit frame is simply $\hat{\mathrm{Z}}(\Delta t)\hat{\mathcal{U}}_\varphi(\Omega t)$.

What happens to other qubits during this operation? Since the waist of the addressing laser has a finite width, the other qubits experience a small perturbation $\frac{1}{2}\delta_i\hat{\sigma}_z$ where $\delta_i \ll \Delta$ depends on the distance from the target qubit and, hence, on the lattice site i. Consequently, the other qubits are shaken off-resonantly to their site-dependent energy difference $\hbar\omega_0 + \hbar\delta_i$ with a detuning $\Delta - \delta_i$. For a sufficiently weak shaking with $\Omega \ll \Delta$ this leads according to Eq. (6.18) to site-dependent z rotations of the qubits and thus to a general dephasing of the qubit register.

The total operation $\hat{\mathrm{U}}_R$ on the register after the operation time T with the target qubit on site $i = s$ can be written in general as

$$\hat{\mathrm{U}}_R(t) = \prod_i \hat{\mathrm{Z}}^{(i)}(\alpha_i)\hat{\mathcal{U}}_\varphi^{(s)}(\Omega T)\,, \tag{6.22}$$

where the upper indices denote on which qubit the operator acts. If all phases α_i were accurately known, one could account for the additional z rotations within the quantum calculation. However, one can also cancel unknown z rotations by applying a scheme similar to the refocussing technique well known from NMR quantum control [112]. For this purpose, one exploits the property that two π rotations about any axis in the $x-y$ plane invert any z rotation, i.e. $\hat{\mathcal{U}}_\varphi(\pi)\hat{\mathrm{Z}}(\alpha)\hat{\mathcal{U}}_\varphi(\pi) = \hat{\mathrm{Z}}(-\alpha)$. Hence, by inserting π rotations at the beginning and the middle of the z rotation any z rotation is cancelled, i.e. one has

$$\hat{\mathcal{U}}_\varphi(\pi)\hat{\mathrm{Z}}(\alpha/2)\hat{\mathcal{U}}_\varphi(\pi)\hat{\mathrm{Z}}(\alpha/2) = \hat{\mathrm{I}}\,. \tag{6.23}$$

Thus, inserting two global π pulses by shaking the lattice resonantly to ω_0 while no other perturbation of the lattice is active, allows to cancel the dephasing of the register. Only the z rotation of the target qubit itself cannot be cancelled by this procedure. In order to cancel the two z rotations $\hat{\mathrm{Z}}(\Delta T/2)$ of the target qubit between the π-pulses one can, e.g., adjust the operation time T, such that $\Delta T/2 = 2\pi$. Alternatively, one can adapt the phase φ of the first half of the operation to $\varphi - \Delta T/2$. Using the property that $\hat{\mathrm{Z}}(\alpha)\hat{\mathcal{U}}_\varphi(\beta) = \hat{\mathcal{U}}_{\varphi+\alpha}(\beta)\hat{\mathrm{Z}}(\alpha)$ together with Eq. (6.23) and the fact that rotations $\hat{\mathcal{U}}_\varphi(\alpha)$, $\hat{\mathcal{U}}_\varphi(\beta)$ with the same φ commute, one has

$$\begin{aligned}
&\hat{\mathcal{U}}_\varphi(\pi)\ \hat{\mathrm{Z}}(\Delta T/2)\,\hat{\mathcal{U}}_{\varphi-\Delta T/2}(\Omega T/2)\ \hat{\mathcal{U}}_\varphi(\pi)\ \hat{\mathrm{Z}}(\Delta T/2)\,\hat{\mathcal{U}}_\varphi(\Omega T/2) = \\
&\hat{\mathcal{U}}_\varphi(\pi)\qquad \hat{\mathcal{U}}_\varphi(\Omega T/2)\ \hat{\mathrm{Z}}(\Delta T/2)\ \ \hat{\mathcal{U}}_\varphi(\pi)\ \hat{\mathrm{Z}}(\Delta T/2)\,\hat{\mathcal{U}}_\varphi(\Omega T/2) = \\
&\hat{\mathcal{U}}_\varphi(\pi)\qquad \hat{\mathcal{U}}_\varphi(\Omega T/2)\qquad\qquad \hat{\mathcal{U}}_\varphi(\pi)\qquad\qquad \hat{\mathcal{U}}_\varphi(\Omega T/2) = \hat{\mathcal{U}}_\varphi(\Omega T)\,.
\end{aligned} \tag{6.24}$$

6.5.2. Controlled qubit operations

Altogether, the refocussing scheme allows to perform for example an x rotation $\hat{\mathrm{X}}(\pi) = \hat{\mathcal{U}}_0(\pi)$ one a specific qubit without inducing any additional z rotations. Equipped with these local π operations one is able to also refocus controlled qubit operation.

For the sake of concreteness the case of a controlled $\hat{\mathrm{X}}(\pi) = \hat{\mathcal{U}}_0(\pi)$ rotation with the control qubit at site 1 and the target qubit at site 2 shall be discussed. In terms of the projection operators $\hat{\mathrm{P}}_0 = |0\rangle\langle 0|$ and $\hat{\mathrm{P}}_1 = |1\rangle\langle 1|$ a controlled π rotation $\hat{\mathrm{C}}_\varphi$ about any angle φ can be expressed as

$$\hat{\mathrm{C}}_\varphi = \hat{\mathrm{P}}_0^{(1)}\hat{\mathrm{I}}^{(2)} + \hat{\mathrm{P}}_1^{(1)}\hat{\mathcal{U}}_\varphi^{(2)}(\pi)\,. \tag{6.25}$$

During the desired controlled qubit operation $\hat{\mathrm{C}}_0$ the control and target qubits are coupled, which leads effectively to an energy difference of the target qubit states at site $i = 2$ that depends on the state of the control qubit at site $i = 1$ (see Fig. 6.5). This state-dependent energy offset δE of the two qubits leads to a term $\delta E\ \hat{\mathrm{P}}_0^{(1)}\hat{\mathrm{P}}_0^{(2)} = \frac{\delta E}{4}\left(\hat{\mathrm{I}} + \hat{\sigma}_z^{(1)} + \hat{\sigma}_z^{(2)} + \hat{\sigma}_z^{(1)}\hat{\sigma}_z^{(2)}\right)$ in the Hamiltonian. Consequently, the complete two-qubit operation in the lattice is in general given as

$$\hat{\mathrm{U}}_{\mathrm{op}}(\varphi) = \exp\left(-i\hbar[c\hat{\sigma}_z^{(1)}\hat{\sigma}_z^{(2)} + a_1\hat{\sigma}_z^{(1)} + a_2\hat{\sigma}_z^{(2)} + a_3\hat{\sigma}_z^{(3)} + \cdots]\right)\hat{\mathrm{C}}_\varphi\,. \tag{6.26}$$

The coupled z rotations, which are induced by the term $\hat{\sigma}_z^{(1)}\hat{\sigma}_z^{(2)}$, cannot be refocussed

by global π pulses. Moreover, one may not rotate the control qubit during the refocussing without perturbing the controlled operation. The pulse sequence

$$\hat{\mathrm{X}}^{\mathrm{gl}}(\pi)\hat{\mathrm{X}}^{(1)}(\pi)\sqrt{\hat{\mathrm{U}}_{\mathrm{op}}(0)}\hat{\mathrm{X}}^{\mathrm{gl}}(\pi)\hat{\mathrm{X}}^{(1)}(\pi)\sqrt{\hat{\mathrm{U}}_{\mathrm{op}}(0)} \tag{6.27}$$

with

$$\hat{\mathrm{X}}^{\mathrm{gl}}(\pi) = \hat{\mathrm{X}}^{(1)}(\pi) + \hat{\mathrm{X}}^{(2)}(\pi) + \hat{\mathrm{X}}^{(3)}(\pi) + \cdots \tag{6.28}$$

does not perturb the controlled rotation. However, it only refocusses the phases of the qubits $3, 4, 5, \ldots$ As in the case of the single-qubit operation the phases of the control and target qubit can be controlled by either waiting for an appropriate time or by performing the π rotations at a different angle. Performing the single-qubit π rotations at an angle $\varphi = -2a_1$ and the controlled two-qubit operations at an angle $\varphi = 2(a_2 - c)$, where a_1, a_2, and c are defined in Eq. (6.26), the total pulse sequence

$$\hat{\mathrm{X}}^{\mathrm{gl}}(\pi)\hat{\mathcal{U}}^{(1)}_{-2a_1}(\pi)\sqrt{\hat{\mathrm{U}}_{\mathrm{op}}(2[a_2 - c])}\hat{\mathrm{X}}^{\mathrm{gl}}(-\pi)\hat{\mathrm{X}}^{(1)}(\pi)\sqrt{\hat{\mathrm{U}}_{\mathrm{op}}(0)} \tag{6.29}$$

evaluates to the desired operation $\hat{\mathrm{C}}_0$.

6.6. Simulation of the qubit operations

In order to validate the proposal for single and two-qubit operations by a numerical calculation, a lattice with unit filling described by a Wannier basis of the first three Bloch bands with periodic boundary conditions is considered. It is assumed that the lattice is sufficiently deep so that, as usual within the Bose-Hubbard model, only next-neighbor hopping and onsite interaction need to be considered. For the single-qubit rotation a system of two lattice sites suffices to estimate the influence of the operation on the remaining register and vice versa. For studying the two-qubit operation a third site has to be added. The third Bloch band is included to study possible excitations of atoms out of the qubit basis. In the following a lattice depth $V_{\mathrm{L}} = 2.7\,\hbar\omega_{\mathrm{L}} = 29.16$ is considered. For this lattice a relatively small interaction strength $g = 0.16\,\hbar\omega_{\mathrm{L}} = 1.87$ suffices to form a Mott insulator so that all qubit states are eigenstates of the unperturbed Hamiltonian.

As an example a single-qubit π rotation on the right site of a two-well lattice is considered. As stated above, the dephasing caused by terms of the form $\hat{\mathrm{W}} = a_1\hat{\sigma}_z^{(1)} + a_2\hat{\sigma}_z^{(2)}$ is inhibited by two global $\hat{\mathrm{X}}^{\mathrm{gl}}(\pi)$ rotations. However, the narrow-waist laser can also lead to a weak coupling $b\hat{\sigma}_z^{(1)}\hat{\sigma}_z^{(2)}$, which can only be cancelled by more complex sequences of refocussing pulses that would themselves require to perform single-qubit π rotations. To suppress this term during the operation the lattice depth V_{L} is temporarily enlarged to $V_{\mathrm{L}} + \delta V_{\mathrm{L}}$ before shining in the narrow-waist laser. Both perturbations are switched on and off adiabatically and are sufficiently small so that couplings to states above the third Bloch band are negligible. While the perturbations are active, $\hat{\mathrm{V}}_{\mathrm{sh}}$ drives resonantly the rotation $\hat{\mathrm{U}} = \exp(-i\Omega t\hat{\sigma}_x/2)$ on the right site, which for $\Omega t = \pi$ is the $\hat{\mathrm{X}}(\pi)$ rotation. Fig. 6.6 shows numerical simulations for the NOT operation including two $\hat{\mathrm{X}}^{\mathrm{gl}}_{\pi}$ operations for refocussing. For the chosen parameter set (see caption

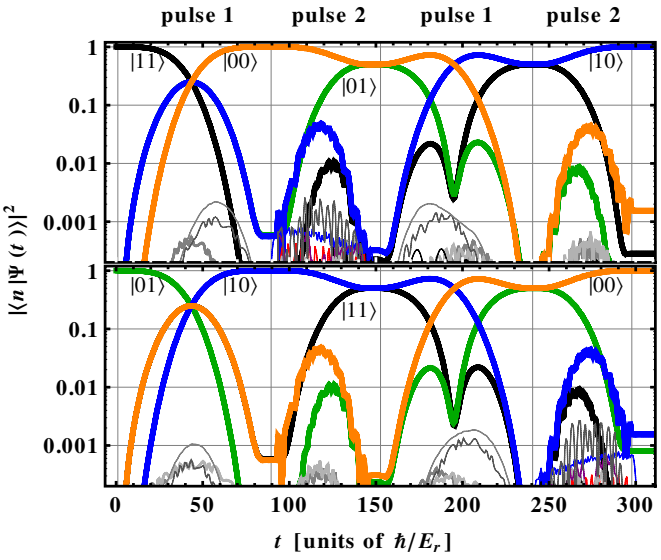

Figure 6.6: Admixtures of different eigenstates for the initial states $|11\rangle$ and $|01\rangle$ during an $\hat{\mathrm{X}}(\pi)$ rotation on the right qubit of a two-well lattice. Pulse 1 drives an $\hat{\mathrm{X}}^{\mathrm{gl}}(\pi)$ rotation. Pulse 2 starts by linearly increasing the lattice depth by $\delta V_{\mathrm{L}} = 0.17 V_{\mathrm{L}}$ during a ramping time of $5.9\,\hbar/E_r$. Then the Gaussian beam with waist $\sigma = \pi/2$ centered at the site of the target qubit is linearly ramped during a time of $0.4\,\hbar/E_r$ to the strength $\gamma = 2.62$. After a $\pi/2$ rotation $\hat{\mathrm{X}}(\pi/2)$ on the right qubit driven by shaking the lattice resonantly to the energy difference between $|11\rangle$ and $|10\rangle$, δV_{L} and γ are ramped off in reversed order. The simulations show a fidelity of 99.7% for a gate time of $300\hbar/E_r$.

of Fig. 6.6) the influence of the qubit state on the left side is negligible and an average fidelity of 99.7% is reached. Without refocussing (not shown) the fidelity would be only 33.2% due to dephasing.

For the CROT operation a system of three lattice sites is considered. The left site acts as the control qubit of an $\hat{\mathrm{X}}_{\pi}^{(2)}$ rotation on the central target qubit. Due to the periodic boundary conditions the right site can couple to both the control and the target qubit. Example results and parameters of the numerical simulations of the CROT are shown in Fig. 6.7. For a gate time of $400\,\hbar/E_r$ an average fidelity of 99.4% is reached. For the evaluation of the fidelity the individual z rotations and those z rotations coupled to the control qubit are neglected. This is possible since equipped with the global $\hat{\mathrm{X}}_{\pi}^{\mathrm{gl}}$ and local $\hat{\mathrm{X}}_{\pi}$ rotations these z rotation can be cancelled by using a refocusing scheme [see Eq. (6.29)].

Opposing to the single-qubit rotation an important source of infidelity of the CROT stems from the leakage to states out of the qubit basis, e.g., to states in the third Bloch band. Averaged over the computational basis the leakage probability after the operation is 0.27%. To diminish this, one can either use techniques of leakage elimination [117]

Table 6.1: Average fidelity of the CROT operation presented in Fig. 6.7 for uncontrolled errors of the interaction strength g, the strength of the gaussian laser γ, and the lattice depth V_{L}.

Parameter	g		γ		V_{L}		
Error	0.1%	1%	0.1%	1%	0.01%	0.1%	1%
Fidelity	99.4%	98.1%	98.9%	97.3%	99.2%	90.9%	31.4%

or one has to choose a deeper lattice. This leads to weaker couplings between the lattice sites and thus to longer gate times. For example, increasing the lattice depth V_{L} from $2.7\hbar\omega_{\mathrm{L}}$ to $2.8\hbar\omega_{\mathrm{L}}$ and the gate time to $540\hbar/E_r$ reduces the leakage probability to 0.15% and increases the fidelity by another 0.06%.

In order for the operations to be robust, any relative energy shift of the manipulated qubit states by some external perturbation must be small compared to the energy scale of the Rabi oscillations $\hbar\Omega$ which in the presented case is about $0.1\,E_r$. Since the energy differences are mainly influenced by the lattice potential itself, its uncontrolled perturbation can severely reduce the fidelity of the operation. Considering the CROT operation, which is more sensitive to perturbations than single-qubit operations, only a lattice laser intensity that is controlled on the 10^{-4} level leads to negligible fidelity reduction (see Tab. 6.1). On the other hand, perturbations of other parameters such as the intensity of the gaussian laser beam or the interaction strength g are much less severe.

6.7. Qubit readout

The last important ingredient for quantum computation is the possibility to read out qubit states. This can be done by removing atoms in the excited state $|0\rangle$ from the lattice and determining subsequently the atom distribution of the remaining atoms by fluorescence imaging with single-site resolution (see Fig. 6.1). The removal of excited atoms is related to an evaporative cooling of the system and corresponding strategies may be applied. One method is to accelerate the lattice in x direction. During an increasing acceleration atoms can go adiabatically through a Landau-Zener transition with a state in a higher Bloch band on the neighboring lattice site. For sufficiently deep lattices the large gap between the first and second Bloch bands inhibits Landau-Zener transitions between these bands, such that atoms in the ground state $|1\rangle$ are dragged by the lattice. On the other hand, atoms in the state $|0\rangle$ may tunnel to higher Bloch bands and eventually leave the lattice [118, 119]. The tunneling can be enhanced by first transferring atoms in state $|0\rangle$ to a higher Bloch band. As shown in Fig. 6.8 for the exemplary lattice depth of $V_{\mathrm{L}} = 2.7\,\hbar\omega_{\mathrm{L}}$ one can drive transitions from the 2^{nd} to the high-lying 5^{th} Bloch band by means of shaking the lattice with frequency $\Omega_{2,5}$ while transitions from the first Bloch band are inhibited due to a band gap. In the 5th Bloch band the atoms are quasi-free and leave the lattice even during slow accelerations.

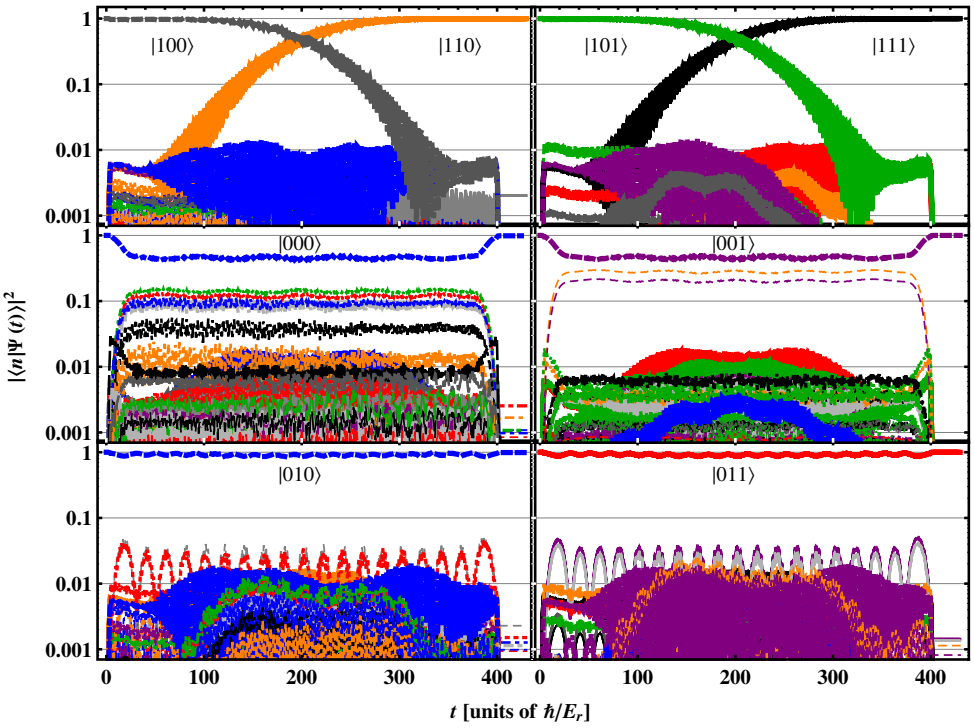

Figure 6.7: Admixtures of different eigenstates for six different initial states during a CROT on the left control qubit at $x = 0$ and the central target qubit at $x = \pi$. The Gaussian beam with waist $\sigma = \pi/2$ at $x_0 = 0.6\,\pi$ is linearly ramped to a strength of $\gamma = 0.224$ during a time of $2\hbar/E_r$. After waiting for $12\hbar/E_r$ the beam is linearly ramped for $16\hbar/E_r$ to the avoided crossing with the repulsively bound state at $\gamma = 0.204$ (see also Fig. 6.5). After shaking the lattice resonantly to the energy difference between $|111\rangle$ and $|101\rangle$ the gaussian beam is switched off in reversed order. For a gate time of $400\hbar/E_r$ a fidelity of 99.4% is reached neglecting phases, which can be cancelled by refocussing schemes.

In Ref. [120] a closely related scheme of a state-dependent removal of atoms from an optical lattice has been used experimentally for cooling a quantum gas. This supports the practicability of vibrationally encoded qubits and the proposed read-out scheme. In the experiment atoms in different excited states have been selectively removed by periodic variations of the depth of the optical lattice with a varying frequency.

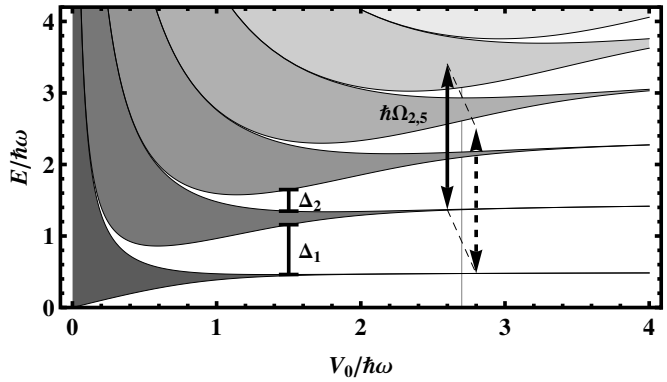

Figure 6.8: Energy extensions of the Bloch bands as a function of the lattice depth. For shallow lattices the band gap Δ_2 is much smaller than Δ_1. When moving the lattice this allows for Landau-Zener transitions out of the 2^{nd} band while atoms in the 1^{st} band are dragged by the lattice. At $V_{\text{L}} = 2.7\hbar\omega_{\text{L}}$ one may drive a transition from the 2^{nd} to the 5^{th} Bloch band with energy difference $\hbar\Omega_{2,5}$ while a transition from the first Bloch band is inhibited by a band gap.

6.8. Shor's algorithm in an optical lattice

One of the most prominent examples of a quantum-computer algorithm is Shor's algorithm, which enables to efficiently determine the prime factors of large integers. For the integer 15 the algorithm could be also experimentally demonstrated, e.g., using nuclear magnetic resonance [121], photonic qubits [122, 123] and lately also superconducting qubits [124]. So far the algorithm could not be performed using ultracold atoms in optical lattices.

In order to assess the practicability and speed of the presented approach, the very same case of a factorization of 15 is considered. The algorithm is discussed in the notation of a quantum circuit, which is introduced on the basis of a small exemplary quantum circuit in Fig. 6.9. In the following a time estimate of this quantum algorithm in different lattice setups is given. The quantum circuit of Shor's algorithm as used by Vandersypen et al. [121] is depicted in Fig. 6.10 (a). A specialized version of the factoring problem leading to a reduced quantum circuit was presented by Lu et al. [123] and is shown in Fig. 6.10 (b).

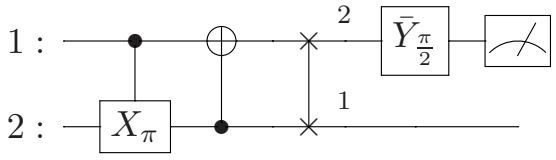

Figure 6.9: Sample of a small quantum circuit. The indices at the operations denote the angle of the rotation about the corresponding axis. An overbar indicates the inverse rotation. The following operations are performed from left to right on two qubits 1 and 2: (i) An x rotation of qubit 2 controlled by qubit 1. (ii) A NOT operation of qubit 1 controlled by qubit 2. (iii) A swap operation between the qubits. (This operation can be necessary since only next neighbors can undergo controlled operations in the lattice.) The exchange of the roles of the qubits is indicated by the numbering appearing after the swap operation. (iv) An unconditional y rotation of qubit 2. (v) A measurement of qubit 2 in the computational basis.

6.8.1. Time estimate for the quantum algorithm

The operation times for the various gates appearing in Fig. 6.10 need to be estimated in order to assess the speed of the complete algorithm in an optical lattice. The estimates are based on the numerical simulations of the single qubit rotation and the controlled two-qubit rotation (see Figs. 6.6 and 6.7).

Hadamard operation

The Hadamard gate can be decomposed as $H = X_\pi Y_{\frac{\pi}{2}} = \bar{Y}_{\frac{\pi}{2}} X_\pi$ and takes $\approx (300 + 250)\,\hbar/E_r = 550\,\hbar/E_r$.

(a)

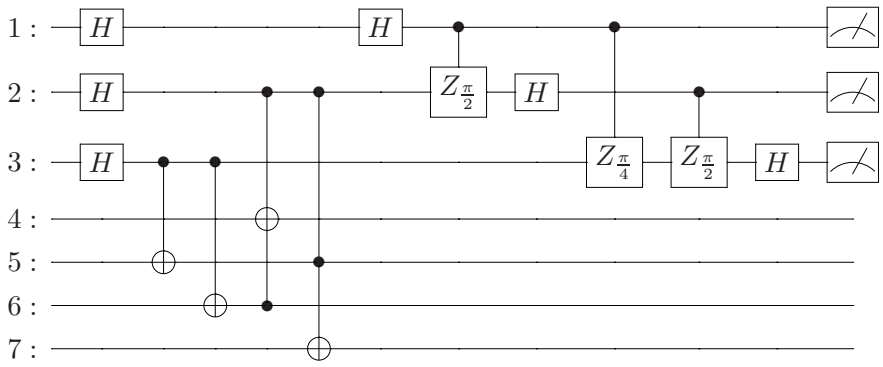

(b)

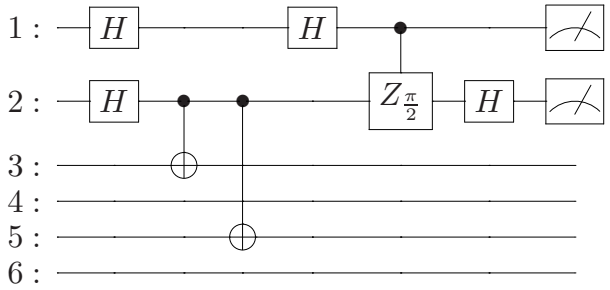

Figure 6.10: **(a)** Quantum circuit used by Vandersypen et al. [121] for factoring 15. **(b)** Quantum circuit used by Lu et al. [123] for factoring 15.

Refocussing two-qubit operations

According to the pulse sequence (6.29), a refocussed controlled π rotation $\hat{\mathrm{C}}_0$ requires to perform two (non-refocussed) local and two global π rotations. A global π rotation takes $\approx 100\hbar/E_r$ and the local one $\approx 120\hbar/E_r$. The additional switching times of the narrow-waist laser take $\approx 2 \times 30\hbar/E_r = 60\hbar/E_r$. Hence, the refocussing during a controlled two-qubit rotation takes an additional time of $\approx 500\hbar/E_r$.

CNOT

The CNOT operation can be decomposed into

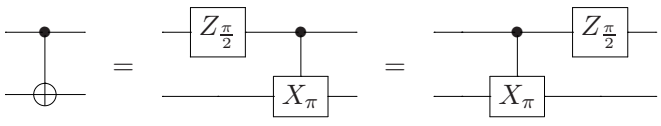

.

In the quantum circuits the $Z_{\frac{\pi}{2}}$ operations can be commuted through to the end of the circuit and do not lead to an increased computational effort (see Ref. [112] for details). The refocussed controlled X_π rotation takes $(400 + 500)\hbar/E_r = 900\hbar/E_r$.

Controlled Z operation

A controlled z rotation about the angle ϕ can be decomposed as

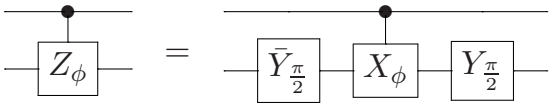

For $\phi = \pi$ this operation takes $\approx (2{\cdot}250{+}400{+}500)\hbar/E_r = 1400\hbar/E_r$, while for $\phi = \pi/2$ it takes $\approx (2 \cdot 250 + 200 + 500)\hbar/E_r = 1200\hbar/E_r$. An alternative way, which would be also potentially faster, is to drive a controlled, slightly off-resonant 2π rotation on the target qubit [see Eq. (6.16)]. In the following, however, the worst-case time estimates of $1400\hbar/E_r$ and $1200\hbar/E_r$, respectively, are used.

Doubly controlled CNOT

The doubly controlled CNOT operations can be implemented as

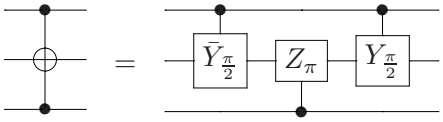

(see Methods section of Ref. [121]). The controlled y rotations take $(250 + 500)\, E_r = 750\, E_r$ resulting in a total operation time of $(2 \cdot 750 + 1400)\, \hbar/E_r = 2900\, \hbar/E_r$.

Swap operation

Since within the quantum computing scheme operations can be only performed between neighboring lattice sites, a swap operation is essential. The worst case overhead due to additional swapping operations is polynomial, i.e. one has to perform $\mathcal{O}$(Number of operations) $\times\, \mathcal{O}$(Number of qubits) swap operations[2]. Therefore, a polynomial quantum algorithm will still be polynomial if only controlled operations between next-neighbor are allowed.

The swap operation can be decomposed by three CNOT operations, which can be replaced (without additional computational effort) by three controlled X_π rotations

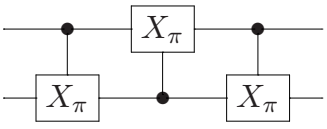

These operations can be performed by manipulating the lattice in the way it is done for the CROT operation (i.e. bringing the bound state $\left\|{}^{02}_{00}\right\rangle$ into resonance with the state

[2]Regarding the working horse of quantum computation, the quantum Fourier transform, the overhead can be reduced to just $\mathcal{O}$(Number of operations) by swapping the qubits after every two-qubit operation.

$\left\|{}^{11}_{00}\right\rangle$). Then three X_π transition between the states (i) $\left\|{}^{01}_{10}\right\rangle \leftrightarrow \left\|{}^{00}_{11}\right\rangle$, (ii) $\left\|{}^{10}_{01}\right\rangle \leftrightarrow \left\|{}^{00}_{11}\right\rangle$, (iii) $\left\|{}^{01}_{10}\right\rangle \leftrightarrow \left\|{}^{00}_{11}\right\rangle$ can be driven, which is equivalent to the above circuit. Together with switching and refocussing time the swap operation takes $\approx (2\cdot 30+3\cdot 340+500)\,\hbar/E_r \approx 1600\,\hbar/E_r$.

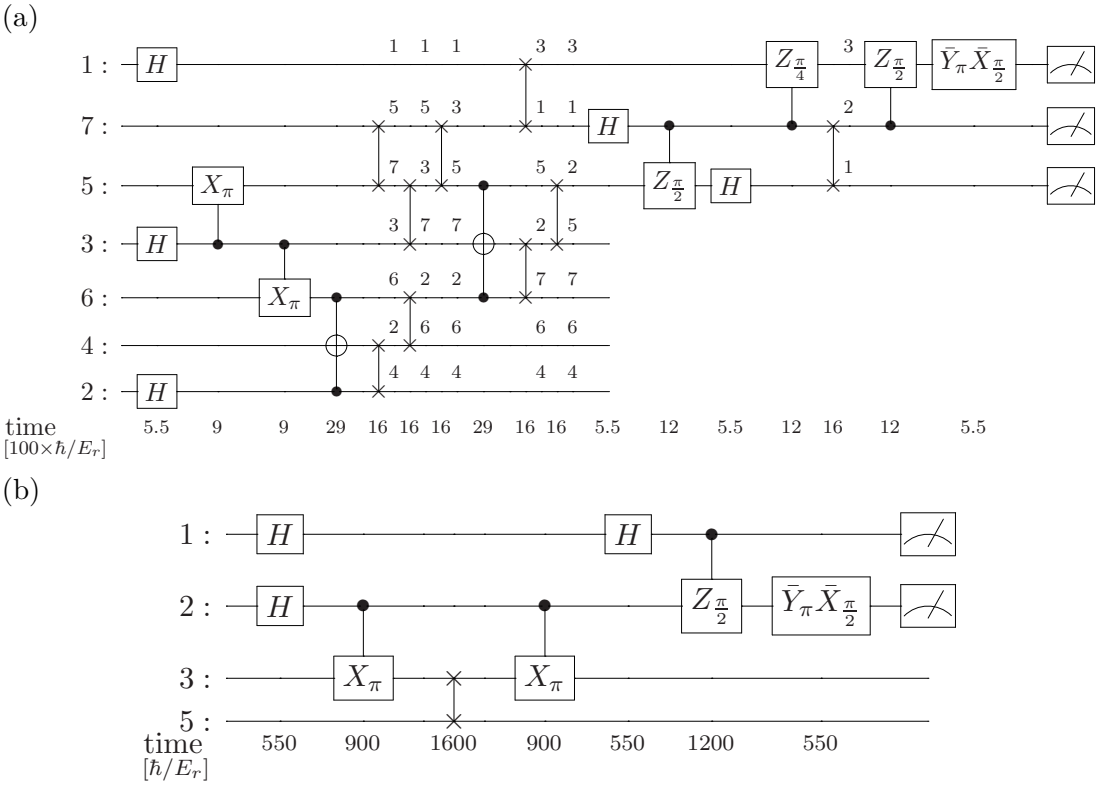

Figure 6.11: **(a)** Proposed realization of the quantum circuit of Fig. 6.10 (a) for the optical-lattice computation. The additional swap operations allow for qubit gates on next neighbors only. The total computation time (sum of last row) is $23\,000\,\hbar/E_r$ **(b)** Proposed realization of the circuit of Fig. 6.10 (b). The total computation time (sum of last row) is $6250\hbar/E_r$.

In summary, the total computation time of the large circuit is $23\,000\,\hbar/E_r$ and that of the reduced circuit is $6250\,\hbar/E_r$ (see Fig. 6.11). In different lattice systems this amounts to the computation times shown in Tab. 6.2.

6.8.2. Feasibility of quantum computation in optical lattices

In order to assess the feasibility of performing Shor's algorithm in the OL, different experimental error sources have to be considered.

One prominent error source in experiments with ultracold atoms is the scattering of photons of the lattice-laser beam with the atoms that lead to atom losses. The photon scattering happens on the order of several seconds and the life time of an atoms

Table 6.2: Time needed to perform a factorization of 15 for different atomic species and lattice spacings using the large and the small circuit shown in Fig. 6.11.

Setup	Large circuit	Small circuit
^{87}Rb, $d = 500\,\mathrm{nm}$	1.60 s	434 ms
^{7}Li, $d = 500\,\mathrm{nm}$	128 ms	35 ms
^{7}Li, $d = 300\,\mathrm{nm}$	46 ms	13 ms

is about 60 s [125]. Hence, photon scattering is negligible on the time scale of the quantum algorithm.

In the laboratory the greatest source of decoherence is usually the fluctuation of the magnetic field, which is hard to control. In the presented approach the qubits are not encoded by different spin states of the atoms, which react differently on the fluctuating magnetic field. Nevertheless, close to a Feshbach resonance magnetic field fluctuations could lead to fluctuations of the scattering length and thus of the interaction strength g. However, the interaction strength g can be quite small such that there is no need to go close to a Feshbach resonance. Furthermore, g can vary on the order of 0.1% without significantly affecting the fidelity (see Tab. 6.1). Hence, the sensitivity on magnetic field fluctuations should be negligible as well.

Most problematic is the so-called transversal decoherence due to the instability of the laser creating the lattice. Intensity fluctuations change most dramatically the energy difference between the qubit states and thus lead to uncontrolled z rotations of the qubits. So far this was not an issue in most of the optical lattice experiments and not too much effort has been made to reduce the transversal decoherence. Currently decoherence times of 30 ms are observed, which could be possibly pushed substantially higher to hundreds of milliseconds requiring a laser power stability at the 10^{-4} level [126].

In Ref. [120] Rabi oscillations between the ground and second excited state of ultracold atoms in an optical lattice were driven by intensity modulations of the laser creating the lattice. The good stability of the Rabi oscillations over some 120 ms (see Fig. 2 b) and c) in Ref. [120]) indicate that already a very good laser stability close to the 10^{-4} level is reached in the lab. As shown in Tab. 6.1 for a stability level of 10^{-4} the quantum operations would be robust against fluctuations of the laser intensity. Moreover, the dephasing that is induced by fluctuations that happen on time scales larger than $100\hbar/E_r$ can be partially compensated for by the refocussing pulses during the quantum computation, which could thus further enlarge the transversal decoherence time.

Assuming decoherence times on the order of several 100 ms especially when using ^{7}Li atoms (see Tab. 6.2) an experimental realization of the factoring algorithm appears to be within reach.

7. Conclusions

In the last years numerous experiments have shown that ultracold atoms are a fascinating object of research. They can be controlled and observed to a level of accuracy that allows, e.g., for high-precision measurements or the quantum simulation of complex physical phenomena. Eventually, ultracold atoms might enable the implementation of a quantum computer. Also from the viewpoint of a theorist ultracold atoms are fascinating objects. At short internuclear distances the full description of the interaction process requires to solve a coupled multi-channel (MC) differential equation. For specific external magnetic fields the atoms can experience a magnetic Feshbach resonance (MFR), i.e. a bound state comes into resonance and the atoms can scatter with an arbitrarily large cross section. The situation becomes even more interesting if the atoms are additionally confined and the coupling energy to the bound state is on the same order as the energy scale of the trap. Normally, the existence of two strong physical impacts on the same energy scale hinders an easy theoretical investigation since none of the impacts can be treated as a perturbation. However, as demonstrated in the first part of this thesis, approximations like the two-channel (TC) model of MFRs or the zero-range approximation of the interaction make it possible to obtain an accurate and even analytic description of free or confined ultracold atoms, which are strongly correlated due to the resonant interaction.

In Chapter 2 the enhancement of a photoassociation (PA) of two free atoms at an MFR by many orders of magnitude was investigated. The TC model allowed for a very simple, yet accurate description of the PA process independently of the complex nature of atomic interactions at short internuclear distances. The agreement to full coupled MC calculations was excellent. It was shown, that the enhancement of the transition rate is closely related to the position of vanishing transition rate. In general, the larger the detuning of the position of vanishing transition rate from the resonant magnetic field, the larger the enhancement of the transition rate.

In Chapter 3 the TC model and the zero-range approximation were applied in order to derive an analytic model of MFRs between atoms in isotropic and anisotropic harmonic traps. One of the important results of the model is the accurate parametrization of the energy-dependent scattering length in terms of parameters that are known for many MFRs. Since the obtained parametrization differs, especially for large background scattering lengths, from previous parametrizations, it was demonstrated by a comparison to a simple two-channel square-well model of an MFR that the parametrization is also correct for large background scattering lengths. Furthermore, the model was verified by full numerical calculations for ^{6}Li-^{87}Rb .

In addition to the energy-dependent scattering length the model allows one to determine the energy spectrum and the admixture of the resonant bound state. Their analysis revealed many fascinating effects of the interplay between the harmonic trap

and the MFR. For example, MFRs that are broad in free space can become narrow in sufficiently tight confinement. Other consequences of the model included a trap-induced shift of the resonance position, the appearance of stable molecules in excited trap states, and a maximal bound-state admixture away from the resonance position. As discussed, the latter could be important for the theoretical description of three-body loss processes.

In Chapter 4 a Bose-Hubbard model (BHM) was derived that enables an accurate determination of the eigenenergies of atoms in an optical lattice (OL) at an MFR. The model explicitly includes the coupling between unbound atoms in the lattice to bound states. Although the zero-range approximation is crucial for the simple description of the interaction between the atoms, it was demonstrated that it prevents the possibility to expand the two-atom wave function in single-atom basis states. As a consequence, the eigenenergies of the initially derived BHM did not converge to the correct eigenenergies. The problem was resolved by introducing dressed bound-state energies and coupling strengths that were based on the analytic model of MFRs in harmonic traps. In contrast to common regularization schemes of delta-like interactions, which require to expand the solution in Bloch functions or Wannier functions of many Bloch bands, the introduced method enabled the determination of accurate solutions with only a small number of Bloch bands included. The approach could be useful not only for OLs, but also for ultracold atoms in many other potential landscapes. In fact, the comparison with a full numerical solution was performed for two atoms in a double-well potential that significantly differed from an OL, showing nevertheless very good agreement.

In general, the understanding of the interplay between MFRs and the confinement of the atoms gained in the first part of the thesis could be useful for the interpretation of experimental results and for extending the possibilities of using ultracold atoms to simulate complex physical phenomena. For example, the introduced BHM revealed that states of unbound atoms can be in resonance with a plethora of bound states in different Bloch bands. These resonances would be experimentally visible by enhanced atom losses. Their exact localization is therefore important for the stability of the atomic system but also for the correct identification of other types of resonances, e.g., resonances with three-body bound states. Resonances with a repulsively bound state have also shown to be very useful for modelling spin systems with ultracold atoms and for investigating quantum phase transitions [21]. In this respect, the availability of an additional resonance to an *attractively* bound state at a narrow MFR could offer the flexibility to simulate a larger class of spin Hamiltonians.

In the second part of the thesis a theoretical approach for the full non-perturbative time-dependent description of two interacting particles in an OL was introduced. A comparison with analytical results showed that high-precision analyses of dynamical processes can be performed. Example calculations for ^{6}Li-^{7}Li in a three-well optical lattice demonstrated the possibility to analyze this complex six-dimensional system in terms of several expectation values. The use of a spectral method, i.e. expanding the time-dependent wavefunction in a basis of eigenfunctions of some underlying Hamiltonian, offers a large degree of flexibility. For example, by modifying the underlying Hamiltonian, the system of two neutral atoms can be easily generalized to other particles such as ions or dipoles. An example of this flexibility was the description of atoms

at an MFR by a square-well interaction potential. Replacing the Born-Oppenheimer potential by the square-well potential in the stationary Hamiltonian enabled a verification of the BHM introduced in the first part of the thesis for the treatment of atoms in non-adiabatically perturbed OLs. Moreover, the external potential is flexible enough to describe a large class of systems like quantum dots or one- and two-dimensional optical traps. Hence, the numerical approach can be used to analyse and develop schemes for the fast and high-fidelity manipulation of a plethora of small quantum systems.

In the last chapter of the thesis a scheme for the implementation of a quantum computer with Bosons in a one-dimensional OL was presented. The qubits were encoded in the spacial atomic wave function, which suppresses decoherence due to fluctuating magnetic fields. It was shown that by shaking the lattice one may drive single qubit operations and controlled qubit operations between neighboring qubits. As demonstrated the dephasing of the qubits can be prevented by using refocussing pulses known from nuclear magnetic resonance spectroscopy. The qubit readout can be performed by removing atoms in excited states from the lattice and determining the atom distribution by fluorescence imaging. Numerical simulations showed that for gate times on the order of milliseconds fidelities above 99% can be reached. It would be interesting to extend the approach to a two-dimensional OL in order to reduce the number of needed swap operations. However, considering ^{7}Li atoms in a 300-nm-period lattice, already within the one-dimensional approach a factorization of 15 using Shor's quantum algorithm would be feasible within about 50 ms with about 20 ms needed for swapping operations. Another interesting extension of the approach would be to consider atoms at an MFR, which could be theoretically described by the BHM derived in the first part of the thesis. Especially a narrow MFR could minimize the coupling of the lattice sites and Bloch bands leading to more robust qubit states.

Though the experimental implementation of a large-scale quantum computer with the presented approach would be currently very challenging, the presented techniques could be useful for a number of applications. For example, the preparation of a many-body system of atoms with different spacial excitations in an OL enables to mimic strongly correlated electronic matter. The experimental analysis of these systems could be relevant for the understanding of solid-state phenomena such as high-temperature superconductivity or colossal magnetoresistance [127]. The quantum-computation scheme demonstrates particularly how to control the spacial excitation of atoms at specific lattice sites while maintaining the coherence of the many-body system. The corresponding techniques could thus be very useful for performing quantum simulations in OLs.

A. Performing time propagations

A.1. Program sequence for time propagations

In order to provide others with the possibility to run time propagations with the code presented in Chap. 5, the necessary sequence of the numerical calculations is presented in more detail. The full program sequence for performing time propagations is sketched in Fig. A.1.

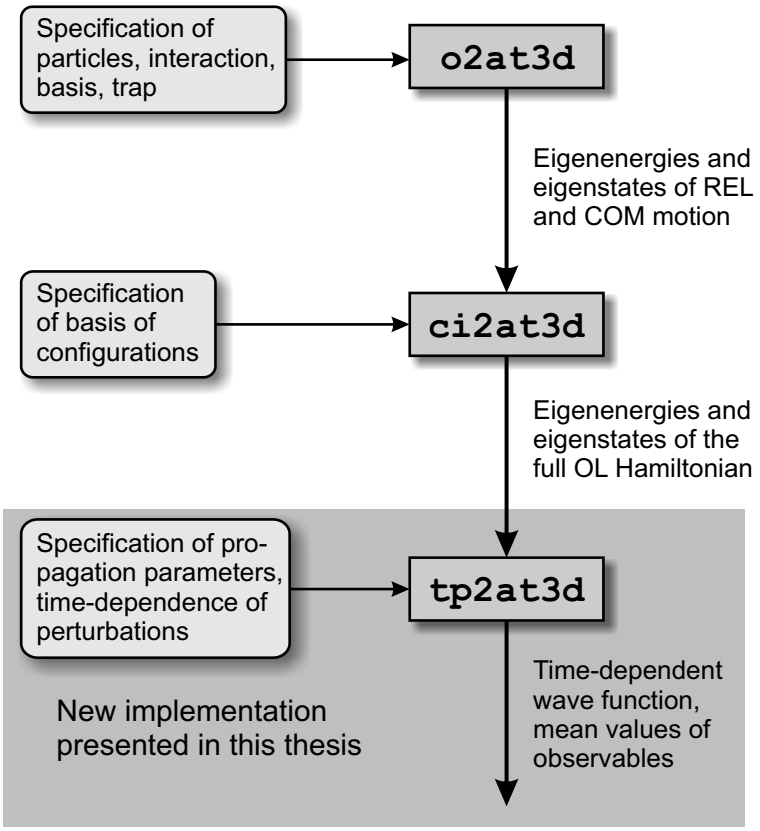

Figure A.1: Sketch of the program sequence of a time propagation. Arrows mark the inputs and outputs of the three programs `o2at3d`, `ci2at3d`, and `tp2at3d`. More details are given in the main text.

The first step of the calculation consists of the determination of the eigenstates and eigenenergies of the COM part $H_{\mathrm{COM}}(\vec{R})$ and REL part $H_{\mathrm{REL}}(\vec{r})$ of the full OL Hamiltonian (5.7) via a program called `o2at3d` (**o**rbit calculation of **2** **at**oms in a

3d OL). For this, atomic properties such as the mass, mutual interaction, and the polarizability have to be specified. Furthermore the properties of the basis and the OL must be provided.

In a second step the calculated eigenenergies and eigenstates are used to diagonalize the full Hamiltonian (5.7) in a configuration interaction procedure carried out by the program `ci2at3d` (**c**onfiguration **i**nteraction of **2 at**oms in a **3d** OL). To this end one has to specify, which REL and COM eigenstates are used to form the basis of configurations of the full solution (5.8).

In the last step, whose implementation is described in this thesis, the time propagation is performed by the program `tp2at3d` (**t**ime **p**ropagation of **2 at**oms in a **3d** OL) using the stationary basis of the full Hamiltonian (5.7). The program is controlled by declaring the initial state, the precision goal of the propagation, the energy range of states used for the propagation, the output, and, of course, the time-dependent perturbation of the OL. Usually, one wants to perform many different time propagations for the same system. Therefore, the time-demanding calculation of the perturbation matrix elements $\mathcal{P}_{mn}^{(\tau,\sigma)}$ of Eq. (5.14) is performed only once and the result is stored for further time propagations.

A.2. Sample calculation

As an example the dynamical behavior of two atoms in a double-well potential with strong transversal confinement is considered. That is, the potential consists of a $\cos^2(x)$ potential that is expanded to 12^{th} order, and $\sin^2(y)$ and $\sin^2(z)$ potentials that are expanded to second order. The two atoms shall have the mass of ^{7}Li. Their behavior at an MFR is simulated by a square-well potential, as it was introduced in Sec. 4.4. The parameters are chosen such that the program runs sufficiently fast. In order to obtain converged states, at least a larger maximal angular momentum has to be chosen and more states have to be included in the configuration-interaction step.

More information of the control of the program can be obtained from the script files that launch the programs and from other input files.

Calculation of REL and COM eigenstates

Program call

```
~/TwoAtInOL/d2h/orbit>o2at3d.csh Li7Li7_b_x9000_y3000_z3000_77rm8g6l10_65CM8g1L10
                      swave_sqw_60_100_1.456e-7_3.9095e-7
                      Li7a200_Li7a200_kx1000_ky1000_kz1000_ix1000_iy10000_iz10000
                      cos sin sin 12 2 2 D V m64 X none
```

Input files

1. Square-well interaction file `TwoAtInOL/d2h/orbit/input/trap/`

`swave_sqw_60_100_1.456e-7_3.9095e-7.pot` for the potential

$$V(r) = \begin{cases} -1.456 \cdot 10^{-7} & 0 \leq r \leq 60 \\ 3.9095 \cdot 10^{-7} & 60 < r \leq 100 \\ 0 & r > 100 \end{cases} \tag{A.1}$$

```
*******************************************************************************
*
   Dissociation energy (in E_h)                        :   0.0D+00
*
   Number of grid points (or type of model potential)  :   -5     !
*
   Square well potential radius : 60   100 !
*
   Square well depth            : -1.456e-7   3.9095e-7 !
*
*******************************************************************************
```

2. Basis file `TwoAtInOL/d2h/orbit/input/trap/Li7Li7_b_x9000_y3000_z3000_77rm8g6l10_65CM8g1L10.dba`

```
*******************************************************************************
*
 START
*-----
*
 BASIS SPECIFICATION:
*--------------------
*
* Relative-distance motion
*
 Maximum value of x                      : 9000   ! Box in x
 Maximum value of y                      : 3000   ! Box in y
 Maximum value of z                      : 3000   ! Box in z
 Order of the B-spline for r             : 8
 Number of B-splines for r               : 77
 Type of knot vector for r               : 6       ! 5 linear zones
*
*-----------------------------------------------------------------------------*
* B-spline knot sequence usefull for the square-well potential                *
* Format r_1,n_1,r_2,n_2,r_3,n_3,r_4,n_4 specifying that                      *
* n_i B splines are placed in the interval r_i < r < r_i+1                    *
*-----------------------------------------------------------------------------*
 Parameter for the grid specification    : 59.5,14,60.5,8,99.5,6,100.5,8
 Maximum value of the angular momentum l : 10
*
* Center-of-mass motion
*
 Order of the B-spline for R             : 8
 Number of B-splines for R               : 65
 Type of knot vector for R               : 1       ! 1 linear zone
 Parameter for the grid specification    : 20.99
 Maximum value of the angular momentum L : 10
*
```

```
 PARAMETERS OF THE ATOMS:
*-----------------------
 Statistics                        : 2             ! Bosons
 Name of the first element         : Li7
 Name of the second element        : Li7
 Mass of the first particle        : 7.0160040     ! In Daltons
 Mass of the second particle       : 7.0160040     ! In Daltons
*
 PARAMETERS OF THE MOLECULAR POTENTIAL:
*-------------------------------------
 Range of rotational quantum numbers J (begin, end)   : 0  0
 Electronic angular and spin momenta (projected on z) : 0  0
*
 END
*******************************************************************************
```

3. Trap file `TwoAtInOL/d2h/orbit/input/trap/Li7a200_Li7a200_kx1000_ky1000_kz1000_ix1000_iy10000_iz10000.dtr`

```
*******************************************************************************
*
 START
*-----
*
 ATOMIC CHARACTERISTICS:
*-----------------------
*
  Name of the first element         : Li7
  Name of the second element        : Li7
  Polarizability of first element   : 200
  Polarizability of second element  : 200
*
 LASER CHARACTERISTICS:
*----------------------
*
  Wavelength along x direction     : 1000
  Wavelength along y direction     : 1000
  Wavelength along z direction     : 1000
*
  Laser intensity along x direction : 1000
  Laser intensity along y direction : 10000
  Laser intensity along z direction : 10000
*
 END
*******************************************************************************
```

Calculation of eigenstates of the full OL Hamiltonian

Program calls

Calculation of A_g symmetry eigenstates:

```
~/TwoAtInOL/d2h/config>ci2at3d.csh Li7Li7_b_x9000_y3000_z3000_77rm8g6l10_65CM8g1L10
                       swave_sqw_60_100_1.456e-7_3.9095e-7
```

```
                    Li7a200_Li7a200_kx1000_ky1000_kz1000_ix1000_iy10000_iz10000
                    cos sin sin 12 2 2 Ag_vsLiLi_1-50 D V m64 X none
```

Calculation of B_{3u} symmetry eigenstates:

```
~/TwoAtInOL/d2h/config>ci2at3d.csh Li7Li7_b_x9000_y3000_z3000_77rm8g6l10_65CM8g1L10
                    swave_sqw_60_100_1.456e-7_3.9095e-7
                    Li7a200_Li7a200_kx1000_ky1000_kz1000_ix1000_iy10000_iz10000
                    cos sin sin 12 2 2 B3u_vsLiLi_1-50 D V m64 X none
```

Input files

1. Configuration file `TwoAtInOL/d2h/config/input/Ag_vsLiLi_1-50.dci` specifying, which basis states are used to form A_g configurations

```
*******************************************************************************
*
  ACTIVE ORBITALS:
*-----------------
*
 RELATIVE COORDINATE:
*--------------------
*
 ag:   [1->50] ! include Ag REL eigenstates 1 to 50
 b1g:  [1->6]  ! include B1g REL eigenstates 1 to 6
 b2g:  [1->6]
 b3g:  [1->6]
 au:   [0]
 b1u:  [0]
 b2u:  [0]
 b3u:  [0]
*
 CENTER-OF-MASS COORDINATE:
*--------------------------
*
 Ag:   [1->50] ! include Ag COM eigenstates 1 to 50
 B1g:  [1->6]  ! include B1g COM eigenstates 1 to 6
 B2g:  [1->6]
 B3g:  [1->6]
 Au:   [0]
 B1u:  [0]
 B2u:  [0]
 B3u:  [0]
*
 END
*******************************************************************************
```

2. Configuration file `TwoAtInOL/d2h/config/input/B3u_vsLiLi_1-50.dci` specifying which basis states are used to form B_{3u} configurations

```
*******************************************************************************
*
  ACTIVE ORBITALS:
*-----------------
```

```
*
 RELATIVE COORDINATE:
*--------------------
*
 ag:   [1->50] ! include Ag REL eigenstates 1 to 50
 b1g:  [1->6]  ! include B1g REL eigenstates 1 to 6
 b2g:  [1->6]
 b3g:  [1->6]
 au:   [0]
 b1u:  [0]
 b2u:  [0]
 b3u:  [0]
*
 CENTER-OF-MASS COORDINATE:
*--------------------------
*
 Ag:   [0] ! include no Ag COM eigenstates
 B1g:  [0] ! include no B1g COM eigenstates
 B2g:  [0]
 B3g:  [0]
 Au:   [1->6]
 B1u:  [1->6]
 B2u:  [1->6]
 B3u:  [1->50]
*
 END
*******************************************************************************
```

Time propagation

After the determination of the stationary eigenstates, a time propagation for an inclination (i.e. an acceleration) of the OL followed by a shaking shall be performed.

Program call

The initial state shall be the lowest eigenstate of A_g symmetry (`Ag1`). Alternatively, one can specify the name of an input file containing a specification of the initial state in terms of real and imaginary coefficients of its expansion in the basis states included in the time propagation. If the perturbation matrix elements $\mathcal{P}_{mn}^{(\tau,\sigma)}$ of Eq. (5.14) have been calculated before, the argument `both` (do **both**, calculate $\mathcal{P}_{mn}^{(\tau,\sigma)}$ and perform the time propagation) can be replaced by `prop` (do only the time **prop**agation).

```
~/TwoAtInOL/d2h/timeprop>tp2at3d.csh Li7Li7_b_x9000_y3000_z3000_77rm8g6l10_65CM8g1L10
                         swave_sqw_60_100_1.456e-7_3.9095e-7
                         Li7a200_Li7a200_kx1000_ky1000_kz1000_ix1000_iy10000_iz10000
                         cos sin sin 12 2 2 Ag_vsLiLi_1-50 B3u_vsLiLi_1-50
                         incline_shake sample_PP Ag1 both D m64 X
```

Input files

1. File `TwoAtInOL/d2h/timeprop/input/PropParams/sample_PP.pp` specifying propagation parameters and the output data

```
*******************************************************************************
*
* Precision in 10^-"Precision"
*---------------------
 Precision: 9.0 !
*
* Energy minimum in units of (hbar w_ho)
*--------------------------------------
 Energy minimum: -10.0 !*
*
* Energy cut-off in units of (hbar w_ho)
*--------------------------------------
 Energy cut-off: 15.0 !
*
* Time step of output in units of 1/w_ho
*--------------------------------------
 Time step : 50
*
* Output of matrix elements
*-----------------------------
*
* Units:   Lengths are given in units of a_ho
*          i.e. X   = CMLi  ->   CMLi/a_ho
*          i.e. x^2 = rmSq  ->   rmSq/a_ho^2
*
 Matrix elements: CMLi       ! others:  CMSq, rmSq, rmLi, rmCMLi
*
* Output of coefficients
*-----------------------
*
 Coeff Ag ImRe: 1, 1 ! min, max (real and imaginary part of coefficients)
 Coeff B3u Abs: 1, 1 ! min, max (absolute value of coefficients)
*
 End!
*
*******************************************************************************
```

2. File `TwoAtInOL/d2h/timeprop/input/TimeDep/incline_shake.tdp` specifying the time-dependent perturbation of the OL

```
*******************************************************************************
*
* Units:   Lengths are given in units of a_ho and are multipled by
*          hbar*w_ho in order to obtain a perturbation in energy units
*          i.e. X -> hbar w_ho X/a_ho,  X^2 -> hbar w_ho X^2/a_ho^2
*          Time and pulse lengths in units of 1/w_ho
*          a_ho and w_ho are taken for x-direction
*
* Pulse description (example)
*----------------------------
*
* Center-of-mass linear perturbation:
* (t=0 marks beginning of the single pulse, not beginning of whole sequence)
*
* X(t) = A + B*t + C Sin(w*t + p)
```

```
*
* Naming convention: A = ACMLi, B = BCMLi, C = CCMLi, ...
*
* Relative-motion quadratic perturbation:
*
* x^2(t) = A + B*t + C Sin(w*t + p)
*
* Naming convention: A = ArmSq, B = BrmSq, ...
*
* (Left out parameters are assumed to be zero.)
*
***********************************************
*
 Number of pulses: 2 !
*
********************
*
 Pulse length: 400.0 !
*
 ACMLi: 0.0 !
 BCMLi: 0.01 !
*
********************
*
 Pulse length: 400.0 !
*
 ACMLi: 4.0 !
 CCMLi: 0.1 !
 wCMLi: 1.0 !
*
********************
*
 End!
*
*******************************************************************************
```

Output file

The program produces the following output file in the folder
`TwoAtInOL/d2h/timeprop/out/state_vs_time/`

```
   tau    Re(  1Ag)    Im(  1Ag)    Abs(  1B3u)  X(tau)              Norm
   0.000  0.10000E+01  0.00000E+00  0.00000E+00  0.000000000000E+00 1.00000000
  50.000 -0.64777E+00  0.33323E+00  0.57702E+00 -0.129570224298E+01 1.00000000
 100.000  0.19299E+00 -0.49557E+00  0.51230E+00 -0.162005514867E+01 0.99999999
 150.000 -0.15717E+00 -0.46914E+00  0.48366E+00 -0.183380096550E+01 0.99999992
 200.000 -0.51080E+00  0.13781E+00  0.52038E+00 -0.182684043993E+01 0.99999988
 250.000 -0.41845E+00  0.34710E+00  0.54769E+00 -0.177302605143E+01 0.99999970
 300.000  0.22987E+00 -0.20234E+00  0.26912E+00 -0.206657537841E+01 0.99999954
 350.000 -0.13905E+00  0.39183E+00  0.39113E+00 -0.200373185351E+01 0.99999950
 400.000  0.14599E+00 -0.39041E+00  0.39343E+00 -0.205105328855E+01 0.99999958
 400.000  0.14599E+00 -0.39041E+00  0.39343E+00 -0.205105328855E+01 0.99999958
 450.000 -0.13974E+00 -0.23335E+00  0.23518E+00 -0.221711344589E+01 0.99999974
 500.000 -0.39989E+00  0.59112E-01  0.37334E+00 -0.199585154845E+01 0.99999989
 550.000 -0.12773E+00  0.29139E+00  0.29180E+00 -0.223479792206E+01 1.00000004
```

```
600.000  0.31940E+00  0.35629E+00  0.46005E+00 -0.197959457420E+01 1.00000019
650.000  0.30011E+00 -0.16461E+00  0.31432E+00 -0.214308065435E+01 1.00000035
700.000  0.12285E+00 -0.38485E+00  0.37639E+00 -0.206311659613E+01 1.00000050
750.000 -0.32364E+00 -0.16193E+00  0.33504E+00 -0.207882250258E+01 1.00000065
800.000 -0.34672E+00  0.45268E-01  0.32484E+00 -0.210391699076E+01 1.00000080
```

Abbreviations

Abbreviation	Description
BHM	Bose-Hubbard model
COM	Center of mass (coordinate specification)
MFR	Magnetic Feshbach resonance
MC	Multi channel (description of an MFR by multi-channel calculations)
NMR	Nuclear magnetic resonance
OL	Optical lattice
PA	Photoassociation
RBS	Resonant bound state
REL	Relative distance (coordinate specification)
TC	Two channel (approximation of an MFR by two channels)

Bibliography

[1] M. H. Anderson, J. R. Ensher, M. R. Matthews, C. E. Wieman, and E. A. Cornell. Observation of Bose-Einstein condensation in a dilute atomic vapor. *Science*, 269: 198, 1995.

[2] C. Bradley, C. Sackett, J. Tollet, and R. Hulet. Evidence of Bose-Einstein condensation in an atomic gas with attractive interactions. *Phys. Rev. Lett.*, 75:1687, 1995.

[3] K. B. Davis, M. O. Mewes, M. R. Andrews, N. J. van Druten, D. S. Durfee, D. M. Kurn, and W. Ketterle. Bose-Einstein condensation in a gas of sodium atoms. *Phys. Rev. Lett.*, 75:3969, 1995.

[4] D. Jaksch and P. Zoller. The cold atom Hubbard toolbox. *Ann. of Phys.*, 315:52, 2005.

[5] F. Dalfovo, S. Giorgini, L. P. Pitaevskii, and S. Stringari. Theory of Bose-Einstein condensation in trapped gases. *Rev. Mod. Phys.*, 71:463, 1999.

[6] M. Greiner, O. Mandel, T. Esslinger, T. Hänsch, and I. Bloch. Quantum phase transition from a superfluid to a Mott insulator in a gas of ultracold atoms. *Nature*, 415:39, 2002.

[7] W. S. Bakr, A. Peng, M. E. Tai, R. Ma, J. Simon, J. I. Gillen, S. Fölling, L. Pollet, and M. Greiner. Probing the superfluid-to-Mott insulator transition at the single-atom level. *Science*, 329:547, 2010.

[8] I. Bloch, J. Dalibard, and W. Zwerger. Many-body physics with ultracold gases. *Rev. Mod. Phys.*, 80:885, 2008.

[9] C. Chin, R. Grimm, P. Julienne, and E. Tiesinga. Feshbach resonances in ultracold gases. *Rev. Mod. Phys.*, 82:1225, 2010.

[10] A. Micheli, G. K. Brennen, and P. Zoller. A toolbox for lattice-spin models with polar molecules. *Nat. Phys.*, 2:341, 2006.

[11] P. Rabl, D. DeMille, J. M. Doyle, M. D. Lukin, R. J. Schoelkopf, and P. Zoller. Hybrid quantum processors: Molecular ensembles as quantum memory for solid state circuits. *Phys. Rev. Lett.*, 97:033003, 2006.

[12] G. Pupillo, A. Griessner, A. Micheli, M. Ortner, D.-W. Wang, and P. Zoller. Cold atoms and molecules in self-assembled dipolar lattices. *Phys. Rev. Lett.*, 100:050402, 2008.

[13] T. Zelevinsky, S. Kotochigova, and J. Ye. Precision test of mass-ratio variations with lattice-confined ultracold molecules. *Phys. Rev. Lett.*, 100:043201, 2008.

[14] C. Chin, T. Kraemer, M. Mark, J. Herbig, P. Waldburger, H.-C. Nägerl, and R. Grimm. Observation of Feshbach-like resonances in collisions between ultracold molecules. *Phys. Rev. Lett.*, 94:123201, 2005.

[15] T. V. Tscherbul and R. V. Krems. Controlling electronic spin relaxation of cold molecules with electric fields. *Phys. Rev. Lett.*, 97:083201, 2006.

[16] V. V. Ivanov, A. Alberti, M. Schioppo, G. Ferrari, M. Artoni, M. L. Chiofalo, and G. M. Tino. Coherent delocalization of atomic wave packets in driven lattice potentials. *Phys. Rev. Lett.*, 100:043602, 2008.

[17] C. Sias, H. Lignier, Y. P. Singh, A. Zenesini, D. Ciampini, O. Morsch, and E. Arimondo. Observation of photon-assisted tunneling in optical lattices. *Phys. Rev. Lett.*, 100:040404, 2008.

[18] M. Anderlini, P. J. Lee, B. L. Brown, J. Sebby-Strabley, W. D. Phillips, and J. V. Porto. Controlled exchange interaction between pairs of neutral atoms in an optical lattice. *Nature*, 448:452, 2007.

[19] U. Schneider, L. Hackermüller, S. Will, T. Best, I. Bloch, T. A. Costi, R. W. Helmes, D. Rasch, and A. Rosch. Metallic and insulating phases of repulsively interacting Fermions in a 3d optical lattice. *Science*, 322:1520, 2008.

[20] D. Jaksch and P. Zoller. The cold atom Hubbard toolbox. *Ann. of Phys.*, 315: 52–79, 2004.

[21] J. Simon, W. S. Bakr, R. Ma, M. E. Tai, P. M. Preiss, and M. Greiner. Quantum simulation of antiferromagnetic spin chains in an optical lattice. *Nature*, 472:307, 2011.

[22] S. Lloyd. Universal quantum simulators. *Science*, 273(5278):1073, 1996.

[23] C. Weitenberg, M. Endres, J. F. Sherson, M. Cheneau, P. Schausz, T. Fukuhara, I. Bloch, and S. Kuhr. Single-spin addressing in an atomic Mott insulator. *Nature*, 471:319, 2011.

[24] P.-I. Schneider and A. Saenz. Two-channel model of photoassociation in the vicinity of a Feshbach resonance. *Phys. Rev. A*, 80:061401, 2009.

[25] P.-I. Schneider, Y. V. Vanne, and A. Saenz. Feshbach resonances of harmonically trapped atoms. *Phys. Rev. A*, 83:030701, 2011.

[26] P.-I. Schneider and A. Saenz. Quantum computation with ultracold atoms in a driven optical lattice. *Phys. Rev. A*, 85:050304, 2012.

[27] P.-I. Schneider, S. Grishkevich, and A. Saenz. Nonperturbative theoretical description of two atoms in an optical lattice with time-dependent perturbations. *Phys. Rev. A*, 87:053413, 2013.

[28] P.-I. Schneider and A. Saenz. Two-channel Bose-Hubbard model of atoms at a Feshbach resonance. *Phys. Rev. A*, 87:052712, 2013.

[29] P.-I. Schneider, S. Grishkevich, and A. Saenz. Ab initio determination of Bose-Hubbard parameters for two ultracold atoms in an optical lattice using a three-well potential. *Phys. Rev. A*, 80:013404, 2009.

[30] S. Grishkevich, P.-I. Schneider, Y. V. Vanne, and A. Saenz. Mimicking multi-channel scattering with single-channel approaches. *Phys. Rev. A*, 81:022719, 2010.

[31] S. Sala, P.-I. Schneider, and A. Saenz. Inelastic confinement-induced resonances in low-dimensional quantum systems. *Phys. Rev. Lett.*, 109:073201, 2012.

[32] H. Friedrich. *Theoretical Atomic Physics*. Springer-Verlag, Berlin, 1991.

[33] B. Marcelis, E. G. M. van Kempen, B. J. Verhaar, and S. J. J. M. F. Kokkelmans. Feshbach resonances with large background scattering length: Interplay with open-channel resonances. *Phys. Rev. A*, 70:012701, 2004.

[34] T.-O. Müller, A. Kaiser, and H. Friedrich. s-wave scattering for deep potential with attractive tails falling off faster than $-1/r^2$. *Phys. Rev. A*, 84:032701, 2011.

[35] A. Derevianko, J. F. Babb, and A. Dalgarno. High-precision calculations of van der Waals coefficients for heteronuclear alkali-metal dimers. *Phys. Rev. A*, 63: 052704, 2001.

[36] K. Huang and C. N. Yang. Quantum-mechanical many-body problem with hard-sphere interaction. *Phys. Rev.*, 105:767, 1957.

[37] A. J. Moerdijk and B. J. Verhaar. Laser cooling and the highest bound state of the Na diatom system. *Phys. Rev. A*, 51:R4333, 1995.

[38] G. Breit and I. I. Rabi. Measurement of nuclear spin. *Phys. Rev.*, 38:2082, 1931.

[39] H. Feshbach. Unified theory of nuclear reactions. *Ann. of Phys.*, 5:357, 1958.

[40] P. Pellegrini, M. Gacesa, and R. Côté. Giant formation rates of ultracold molecules via Feshbach-optimized photoassociation. *Phys. Rev. Lett.*, 101:053201, 2008.

[41] P.-I. Schneider. Ultrakalte atome: Wechselwirkung und verhalten im optischen gitter, 2009. Diploma thesis.

[42] E. L. Bolda, E. Tiesinga, and P. S. Julienne. Effective-scattering-length model of ultracold atomic collisions and Feshbach resonances in tight harmonic traps. *Phys. Rev. A*, 66:013403, 2002.

[43] M. Wouters, J. Tempere, and J. T. Devreese. Feshbach resonances in a quasi-two-dimensional atomic gas. *Phys. Rev. A*, 68:053603, 2003.

[44] M. Krych and Z. Idziaszek. Controlled collisions of two ultracold atoms in separate harmonic traps. *Phys. Rev. A*, 80:022710, 2009.

[45] Z. Idziaszek and T. Calarco. Analytical solutions for the dynamics of two trapped interacting ultracold atoms. *Phys. Rev. A*, 74:022712, 2006.

[46] See C. Chin, R. Grimm, P. Julienne, and E. Tiesinga. Feshbach resonances in ultracold gases. *Rev. Mod. Phys.*, 82:1225, 2010 and references cited therein.

[47] A. J. Moerdijk, B. J. Verhaar, and A. Axelsson. Resonances in ultracold collisions of ^{6}Li, ^{7}Li, and ^{23}Na. *Phys. Rev. A*, 51:4852, 1995.

[48] F. A. van Abeelen, D. J. Heinzen, and B. J. Verhaar. Photoassociation as a probe of Feshbach resonances in cold-atom scattering. *Phys. Rev. A*, 57:R4102, 1998.

[49] P. Courteille, R. S. Freeland, D. J. Heinzen, F. A. van Abeelen, and B. J. Verhaar. Observation of a Feshbach resonance in cold atom scattering. *Phys. Rev. Lett.*, 81:69, 1998.

[50] S. Grishkevich and A. Saenz. Influence of a tight isotropic harmonic trap on photoassociation in ultracold homonuclear alkali-metal gases. *Phys. Rev. A*, 76: 022704, 2007.

[51] M. Junker, D. Dries, C. Welford, J. Hitchcock, Y. P. Chen, and R. G. Hulet. Photoassociation of a Bose-Einstein condensate near a Feshbach resonance. *Phys. Rev. Lett.*, 101:060406, 2008.

[52] K. Sando and A. Dalgarno. The absorption of radiation near 600 Å by helium. *Mol. Phys.*, 20:103, 1971.

[53] B. Deh, C. Marzok, C. Zimmermann, and P. W. Courteille. Feshbach resonances in mixtures of ultracold ^{6}Li and ^{87}Rb gases. *Phys. Rev. A*, 77:010701(R), 2008.

[54] T. Busch, B.-G. Englert, K. Rzazewski, and M. Wilkens. Two cold atoms in a harmonic trap. *Found. Phys.*, 28:549, 1998.

[55] M. G. Moore. Pseudopotential analog for zero-range photoassociation and Feshbach resonance. *Phys. Rev. Lett.*, 96:100401, 2006.

[56] D. B. M. Dickerscheid, U. A. Khawaja, D. van Oosten, and H. T. C. Stoof. Feshbach resonances in an optical lattice. *Phys. Rev. A*, 71:043604, 2005.

[57] K. Jachymski, Z. Idziaszek, and T. Calarco. Feshbach resonances in a nonseparable trap, 2013. arXiv:1302.0297.

[58] M. Abramowitz and I. Stegun. *Handbook of mathematical functions: with formulas, graphs, and mathematical tables.* Courier Dover Publications, 1965.

[59] F. W. J. Olver, D. W. Lozier, R. F. Boisvert, and C. W. Clark, editors. *NIST Handbook of Mathematical Functions.* Cambridge University Press, New York, NY, 2010.

[60] I. Gradshteyn and I. Ryzhik. *Table of Integrals, Series, and Products.* Academic Press, 2007.

[61] V. V. Flambaum, G. F. Gribakin, and C. Harabati. Analytical calculation of cold-atom scattering. *Phys. Rev. A*, 59:1998, 1999.

[62] K. Góral, T. Köhler, S. A. Gardiner, E. Tiesinga, and P. S. Julienne. Adiabatic association of ultracold molecules via magnetic-field tunable interactions. *J. Phys. B*, 37:3457, 2004.

[63] G. F. Gribakin and V. V. Flambaum. Calculation of the scattering length in atomic collisions using the semiclassical approximation. *Phys. Rev. A*, 48:546, 1993.

[64] J. W. Dunn, D. Blume, B. Borca, B. E. Granger, and C. H. Greene. Feshbach resonance cooling of trapped atom pairs. *Phys. Rev. A*, 71:033402, 2005.

[65] N. Nygaard, R. Piil, and K. Mølmer. Two-channel Feshbach physics in a structured continuum. *Phys. Rev. A*, 78:023617, 2008.

[66] M. Jona-Lasinio and L. Pricoupenko. Three resonant ultracold Bosons: Off-resonance effects. *Phys. Rev. Lett.*, 104:023201, 2010.

[67] T. Bourdel, J. Cubizolles, L. Khaykovich, K. M. F. Magalhães, S. J. J. M. F. Kokkelmans, G. V. Shlyapnikov, and C. Salomon. Measurement of the interaction energy near a Feshbach resonance in a ^{6}Li Fermi gas. *Phys. Rev. Lett.*, 91:020402, 2003.

[68] D. A. Butts and D. S. Rokhsar. Trapped Fermi gases. *Phys. Rev. A*, 55:4346, 1997.

[69] G. B. Partridge, K. E. Strecker, R. I. Kamar, M. W. Jack, and R. G. Hulet. Molecular probe of pairing in the BEC-BCS crossover. *Phys. Rev. Lett.*, 95:020404, 2005.

[70] N. Syassen, D. M. Bauer, M. Lettner, D. Dietze, T. Volz, S. Dürr, and G. Rempe. Atom-molecule Rabi oscillations in a Mott insulator. *Phys. Rev. Lett.*, 99:033201, 2007.

[71] N. N. Klausen, J. L. Bohn, and C. H. Greene. Nature of spinor Bose-Einstein condensates in rubidium. *Phys. Rev. A*, 64:053602, 2001.

[72] M. Erhard, H. Schmaljohann, J. Kronjäger, K. Bongs, and K. Sengstock. Measurement of a mixed-spin-channel Feshbach resonance in ^{87}Rb. *Phys. Rev. A*, 69: 032705, 2004.

[73] A. Widera, O. Mandel, M. Greiner, S. Kreim, T. W. Hänsch, and I. Bloch. Entanglement interferometry for precision measurement of atomic scattering properties. *Phys. Rev. Lett.*, 92:160406, 2004.

[74] R. B. Diener and T.-L. Ho. Comment on "Feshbach resonances in an optical lattice". *Phys. Rev. A*, 73:017601, 2006.

[75] D. B. M. Dickerscheid, D. van Oosten, and H. T. C. Stoof. Reply to "Comment on 'Feshbach resonances in an optical lattice' ". *Phys. Rev. A*, 73:017602, 2006.

[76] J. C. Sanders, O. Odong, J. Javanainen, and M. Mackie. Bound states of two bosons in an optical lattice near an association resonance. *Phys. Rev. A*, 83: 031607, 2011.

[77] L. D. Carr and M. J. Holland. Quantum phase transitions in the Fermi-Bose Hubbard model. *Phys. Rev. A*, 72:031604, 2005.

[78] V. G. Rousseau and P. J. H. Denteneer. Feshbach-Einstein condensates. *Phys. Rev. Lett.*, 102:015301, 2009.

[79] K. V. Krutitsky and D. V. Skryabin. Quantum lattice solitons in ultracold bosons near the Feshbach resonance. *J. Phys. B*, 39:3507, 2006.

[80] M. L. Wall and L. D. Carr. Microscopic model for Feshbach interacting Fermions in an optical lattice with arbitrary scattering length and resonance width. *Phys. Rev. Lett.*, 109:055302, 2012.

[81] L.-M. Duan. Effective Hamiltonian for Fermions in an optical lattice across a Feshbach resonance. *Phys. Rev. Lett.*, 95:243202, 2005.

[82] B. D. Esry and C. H. Greene. Validity of the shape-independent approximation for Bose-Einstein condensates. *Phys. Rev. A*, 60:1451, 1999.

[83] H. P. Büchler. Microscopic derivation of Hubbard parameters for cold atomic gases. *Phys. Rev. Lett.*, 104:090402, 2010.

[84] H. P. Büchler. Erratum: Microscopic derivation of Hubbard parameters for cold atomic gases [Phys. Rev. Lett. 104, 090402 (2010)]. *Phys. Rev. Lett.*, 108:069903, 2012.

[85] I. Brouzos and P. Schmelcher. Controlled excitation and resonant acceleration of ultracold few-boson systems by driven interactions in a harmonic trap. *Phys. Rev. A*, 85:033635, 2012.

[86] S. Grishkevich, S. Sala, and A. Saenz. Theoretical description of two ultracold atoms in finite three-dimensional optical lattices using realistic interatomic interaction potentials. *Phys. Rev. A*, 84:062710, 2011.

[87] W. Kohn. Analytic properties of Bloch waves and Wannier functions. *Phys. Rev.*, 115:809, 1959.

[88] E. Timmermans, P. Tommasini, M. Hussein, and A. Kerman. Feshbach resonances in atomic Bose-Einstein condensates. *Phys. Rev.*, 315:199, 1999.

[89] R. M. Cavalcanti. Exact Green's functions for delta-function potentials and renormalization in quantum mechanics. *Revista Brasileira de Ensino de Física*, 21(3): 336, 1999.

[90] J. von Stecher, V. Gurarie, L. Radzihovsky, and A. M. Rey. Lattice-induced resonances in one-dimensional Bosonic systems. *Phys. Rev. Lett.*, 106:235301, 2011.

[91] L. M. Jensen, H. M. Nilsen, and G. Watanabe. BCS-BEC crossover in atomic Fermi gases with a narrow resonance. *Phys. Rev. A*, 74:043608, 2006.

[92] H. Bachau, E. Cormier, P. Decleva, J. E. Hansen, and F. Martín. Applications of B-splines in atomic and molecular physics. *Rep. Prog. Phys.*, 64:1815, 2001.

[93] M. Bandyopadhyay and S. Dattagupta. Quantum mechanics of rapidly and periodically driven systems. *Pramana-Journal of Physics*, 70(3):381–398, 2008.

[94] F. D. Colavecchia, J. P. Burke, W. J. Stevens, M. R. Salazar, G. A. Parker, and R. T. Pack. The potential energy surface for spin-aligned $Li_3(1^4A')$ and the potential energy curve for spin-aligned $Li_2(a^3\Sigma_u^+)$. *J. Chem. Phys.*, 118:5484, 2003.

[95] I. Bloch. Quantum coherence and entanglement with ultracold atoms in optical lattices. *Nature*, 453:1016, 2008.

[96] D. Schrader, I. Dotsenko, M. Khudaverdyan, Y. Miroshnychenko, A. Rauschenbeutel, and D. Meschede. Neutral atom quantum register. *Phys. Rev. Lett.*, 93: 150501, 2004.

[97] M. Karski, L. Förster, J. M. Choi, W. Alt, A. Widera, and D. Meschede. Nearest-neighbor detection of atoms in a 1d optical lattice by fluorescence imaging. *Phys. Rev. Lett.*, 102:053001, 2009.

[98] W. S. Bakr, J. I. Gillen, A. Peng, S. Folling, and M. Greiner. A quantum gas microscope for detecting single atoms in a Hubbard. *Nature*, 462:74, 2009.

[99] J. F. Sherson, C. Weitenberg, M. Endres, M. Cheneau, I. Bloch, and S. Kuhr. Single-atom-resolved fluorescence imaging of an atomic Mott insulator. *Nature*, 467:68, 2010.

[100] L. K. Grover. A fast quantum mechanical algorithm for database search. In *Proceedings of the twenty-eighth annual ACM symposium on Theory of computing*, pages 212–219. ACM, 1996.

[101] P. W. Shor. Polynomial-time algorithms for prime factorization and discrete logarithms on a quantum computer, 1995. arXiv:quant-ph/9508027.

[102] M. A. Nielsen and I. L. Chuang. *Quantum Computation and Quantum Information*. Cambridge University Press, Cambridge, 2010.

[103] T. D. Ladd, F. Jelezko, R. Laflamme, Y. Nakamura, C. Monroe, and J. L. O'Brien. Quantum computers. *Nature*, 464:45, 2010.

[104] G. K. Brennen, C. M. Caves, P. S. Jessen, and I. H. Deutsch. Quantum logic gates in optical lattices. *Phys. Rev. Lett.*, 82:1060, 1999.

[105] D. Hayes, P. S. Julienne, and I. H. Deutsch. Quantum logic via the exchange blockade in ultracold collisions. *Phys. Rev. Lett.*, 98:070501, 2007.

[106] A. J. Daley, M. M. Boyd, J. Ye, and P. Zoller. Quantum computing with alkaline-earth-metal atoms. *Phys. Rev. Lett.*, 101:170504, 2008.

[107] A. Negretti, P. Treutlein, and T. Calarco. Quantum computing implementations with neutral particles. *Quantum Information Processing*, 10:721–753, 2011.

[108] K. Eckert, J. Mompart, X. X. Yi, J. Schliemann, D. Bruß, G. Birkl, and M. Lewenstein. Quantum computing in optical microtraps based on the motional states of neutral atoms. *Phys. Rev. A*, 66:042317, 2002.

[109] F. W. Strauch, M. Edwards, E. Tiesinga, C. Williams, and C. W. Clark. Tunneling phase gate for neutral atoms in a double-well lattice. *Phys. Rev. A*, 77:050304, 2008.

[110] A. Eckardt, C. Weiss, and M. Holthaus. Superfluid-insulator transition in a periodically driven optical lattice. *Phys. Rev. Lett.*, 95:260404, 2005.

[111] H. Lignier, C. Sias, D. Ciampini, Y. Singh, A. Zenesini, O. Morsch, and E. Arimondo. Dynamical control of matter-wave tunneling in periodic potentials. *Phys. Rev. Lett.*, 99:220403, 2007.

[112] L. M. K. Vandersypen and I. L. Chuang. NMR techniques for quantum control and computation. *Rev. Mod. Phys.*, 76:1037, 2005.

[113] M. J. Bremner, C. M. Dawson, J. L. Dodd, A. Gilchrist, A. W. Harrow, D. Mortimer, M. A. Nielsen, and T. J. Osborne. Practical scheme for quantum computation with any two-qubit entangling gate. *Phys. Rev. Lett.*, 89:247902, 2002.

[114] M. A. Nielsen. A simple formula for the average gate fidelity of a quantum dynamical operation. *Phys. Lett. A*, 303:249, 2002.

[115] L. H. Pedersen, N. M. Møller, and K. Mølmer. Fidelity of quantum operations. *Phys. Lett. A*, 367:47, 2007.

[116] T. Müller, S. Fölling, A. Widera, and I. Bloch. State preparation and dynamics of ultracold atoms in higher lattice orbitals. *Phys. Rev. Lett.*, 99:200405, 2007.

[117] M. S. Byrd, D. A. Lidar, L.-A. Wu, and P. Zanardi. Universal leakage elimination. *Phys. Rev. A*, 71:052301, 2005.

[118] Q. Niu, X.-G. Zhao, G. A. Georgakis, and M. G. Raizen. Atomic Landau-Zener tunneling and Wannier-Stark ladders in optical potentials. *Phys. Rev. Lett.*, 76: 4504, 1996.

[119] K. W. Madison, M. C. Fischer, R. B. Diener, Q. Niu, and M. G. Raizen. Dynamical Bloch band suppression in an optical lattice. *Phys. Rev. Lett.*, 81:5093, 1998.

[120] W. S. Bakr, P. M. Preiss, M. E. Tai, R. Ma, J. Simon, and M. Greiner. Orbital excitation blockade and algorithmic cooling in quantum gases. *Nature*, 480:500, 2011.

[121] L. M. K. Vandersypen, M. Steffen, G. Breyta, C. S. Yannoni, M. H. Sherwood, and I. L. Chuang. Experimental realization of Shor's quantum factoring algorithm using nuclear magnetic resonance. *Nature*, 414:883, 2001.

[122] B. P. Lanyon, T. J. Weinhold, N. K. Langford, M. Barbieri, D. F. V. James, A. Gilchrist, and A. G. White. Experimental demonstration of a compiled version of Shor's algorithm with quantum entanglement. *Phys. Rev. Lett.*, 99:250505, 2007.

[123] C.-Y. Lu, D. E. Browne, T. Yang, and J.-W. Pan. Demonstration of a compiled version of Shor's quantum factoring algorithm using photonic qubits. *Phys. Rev. Lett.*, 99:250504, 2007.

[124] E. Lucero, R. Barends, Y. Chen, J. Kelly, M. Mariantoni, A. Megrant, P. O'Malley, D. Sank, A. Vainsencher, J. Wenner, et al. Computing prime factors with a Josephson phase qubit quantum processor. *Nat. Phys.*, 8:719, 2012.

[125] S. Kuhr. private communication.

[126] J. Simon. private communication.

[127] G. Wirth, M. Ölschläger, and A. Hemmerich. Evidence for orbital superfluidity in the p-band of a bipartite optical square lattice. *Nat. Phys.*, 7:147, 2011.

List of Figures

List of Tables

Acknowledgments

The path from the first vague idea about the solution to a scientific problem to its more or less profound understanding is tedious and winding but, provided it is not a dead end, also exciting and satisfying. I am truly indebted to my supervisor PD Dr. Alejandro Saenz for his guidance, encouragement and inspiration along these paths. Whenever I got stuck in my scientific work or required support in practical affairs, he was instantly helping. I benefited a lot from his broad knowledge, practical ideas, and his commitment.

I would like to thankfully acknowledge three years of financial and personal support of the Telekom-Stiftung, which allowed me to take part in many interesting conferences and work shops. Prof. Dr. Wolfgang Nolting was actively supporting my application for scholarship including the one to the Telekom foundation. For this I am truly grateful.

I would also like to thank all members of the AMO group for the enjoyable time, for their help, and the stimulating work together. Special thanks go to Simon Petretti for his technical assistance and to Simon Sala for proofreading this thesis.

Last but not least, I am very grateful for the support and backup of my family especially of my beloved wife Joanna.